Carbon Dioxide Sequestration in Sedimentary Reservoirs: Fundamental and Applied Considerations

A DISSERTATION
SUBMITTED TO THE FACULTY OF THE GRADUATE SCHOOL
OF THE UNIVERSITY OF MINNESOTA
BY

Benjamin Michael Tutolo

IN PARTIAL FULFILLMENT OF THE REQUIREMENTS
FOR THE DEGREE OF
Doctor of Philosophy

William E. Seyfried, Jr. and Martin O. Saar, Advisers

May, 2015

Acknowledgements

This thesis represents four and a half very enjoyable years that I have spent as a PhD student in the Department of Earth Sciences at the University of Minnesota. Many people have helped to make this experience so fantastic, and I would like to acknowlege a number of them here. First and foremost, I would like to recognize the support of my wife, Julia Tutolo, whose love, personality, and companionship have always been the perfect complement to my own, and our daughter, Carlotta Francesca Tutolo, for so commonly leaving me in total awe. I would also like to express my most sincere and honest gratitude to my parents, Michael and Jeri Tutolo, for providing me with everything I have ever needed to succeed. I am additionally grateful to my brothers, Christopher and Nicholas Tutolo, and my many other wonderful family members for their encouragement and support. Of the many excellent friends I have been surrounded with in Minneapolis, I would particularly like to acknowledge Brian and Tiffany Bagley, Scott Bressers, the Burnetts, Annia Fayon, the Hansens, Andrew Haveles and Kit Resner, the Iredale-Foxes, Megan Kelly, Tim Kiesel, Xiang-Zhao Kong, Sharon Kressler, Anna Lindquist and Joe Myre, Andrew Luhmann, Will Nachlas, Paul McKinney, Amy Myrbo and Charles Gillett, Nicholas Pester, Peter Scheuermann, Drew Syverson, Laura Vietti, and Johnny Zhang.

I would additionally like to thank my advisers, Martin Saar and Bill Seyfried, for making this work possible. In particular, I thank Martin for granting me the freedom to explore an incredible spectrum of the Earth Sciences during my time at UMN, and Bill for exposing me to the fascinating field of geochemistry.

Chapter 2 Acknowledgements

Co-authors of this chatper include Xiang-Zhao Kong, Martin O. Saar, and William E. Seyfried, Jr. We gratefully acknowledge support from the Department of Energy (DOE) Geothermal Technologies Program under Grant Number EE0002764 for this contribution and related research. W.E.S. wishes to acknowledge funding from NSF

MGG-OCE under grant numbers 0751771 and 0813861. M.O.S. also thanks the George and Orpha Gibson endowment for its generous support of the Hydrogeology and Geofluids Research Group. The authors also thank the anonymous reviewers, Associate Editor Gleb Pokrovski, and Executive Editor Marc Norman for their helpful comments and handling of this manuscript.

Chapter 3 Acknowledgements

Co-authors of this chapter include Adam T. Schaen, Martin O. Saar, and William E. Seyfried, Jr. We gratefully acknowledge support for this publication and related research from the National Science Foundation (NSF) MGG-OCE program under Grant Numbers 0927615 and 1232704, from the U.S. Department of Energy (DOE) under Grant Number DE-EE0002764, and by a grant from the Initiative for Renewable Energy and the Environment (IREE), a signature program of the Institute on the Environment (IonE) at the University of Minnesota (UMN). Any opinions, findings, conclusions and/or recommendations expressed in this material are those of the authors and do not necessarily reflect the views of the NSF, DOE, IREE, IonE, or UMN. M.O.S. also thanks the George and Orpha Gibson endowment for its generous support of the Hydrogeology and Geofluids Research group in the Department of Earth Sciences, UMN. We additionally thank the guest editors of this Special Issue of Applied Geochemistry, "Geochemical Speciation Codes and Databases: Present Status and Future Needs" for inviting us to contribute this manuscript, which benefited considerably from the intelligent and thorough review of an anonymous reviewer.

Chapter 4 Acknowledgements

Co-authors of this chapter include Andrew J. Luhmann, Xiang-Zhao Kong, Martin O. Saar, and William E. Seyfried, Jr. We gratefully acknowledge support from the Department of Energy (DOE) Geothermal Technologies Program under Grant Number EE0002764 and from the Initiative for Renewable Energy and the Environment (IREE), a signature program of the Institute on the Environment (IonE) at the University of Minnesota (UMN) for this contribution and related research. XPS analyses were carried out by Dr. Bing Luo and SEM images were obtained by Nick Seaton, both of whom are part of the UMN Characterization Facility, which receives partial support from NSF through the MRSEC program. Kevin Roberts of the UMN

Nanofabrication Center assisted with the FIB-SEM analyses, and Rick Knurr performed the ICP-OES and IC analyses. Use of the Advanced Photon Source (APS) was supported by the U. S. Department of Energy, Office of Science, Office of Basic Energy Sciences, under Contract No. DE-AC02-06CH11357. We are grateful to beamline scientist Dr. Xianghui Xiao for assistance with APS tomographic data, and Glenn Hammond of Sandia National Laboratories for his assistance with PFLOTRAN applications. XRCT data processing and PFLOTRAN simulations were carried out in part using computing resources and software at the University of Minnesota Supercomputing Institute and software available through the UMN XRCT Laboratory. We also thank Anthony Runkel for providing the Eau Claire samples. WES would like to acknowledge support from NSF MGG-OCE under grant numbers 0927615, 1232704, and 1426695 for this contribution and related research. MOS also acknowledges support for this and related research from an NSF Sustainable Energy Pathways (SEP) grant, NSF SEP-1230691, and is grateful for the support of the Hydrogeology and Geofluids research group by the George and Orpha Gibson Endowment. BMT would also like to acknowledge the organizers and attendees of the NSF "Expanding the Role of Reactive Transport Models (RTMs) in the Biogeochemical Sciences" workshop for their interesting discussions of the data needs for successful application of RTMs. Any opinions, findings, conclusions, or recommendations in this material are those of the authors and do not necessarily reflect the views of the DOE, NSF, IREE, IonE, UMN, or ETH. The authors thank Associate Editor Carl Steefel, Nicholas Pester (LBNL), and two anonymous reviewers for their thorough, thoughtful reviews of this manuscript, which significantly improved its clarity and strengthened its impact.

Chapter 5 Acknowledgements

Co-authors of this chapter include Andrew J. Luhmann, Xiang-Zhao Kong, Martin O. Saar, and William E. Seyfried, Jr. We gratefully acknowledge support from the Department of Energy (DOE) Geothermal Technologies Program under Grant Number EE0002764, from the National Science Foundation (NSF) under Grant Number CHE-1230691, and from the Institute on the Environment (IonE) at the University of Minnesota (UMN) through its Initiative for Renewable Energy and the Environment (IREE). XRCT and SEM data were obtained at the X-ray Computed Tomography Laboratory and LacCore, respectively, at UMN. Opinions, findings, conclusions and/or recommendations expressed in this material are those of the authors and do

not necessarily reflect the views of the NSF, DOE, IREE, IonE, or UMN. MOS also thanks the George and Orpha Gibson Foundation for its support of the Geofluids Research Group. The authors thank two anonymous reviewers for their helpful comments and suggestions.

Chapter 6 Acknowledgements

Co-authors of this chapter include Xiang-Zhao Kong, William E. Seyfried, Jr., and Martin O. Saar. We gratefully acknowledge support from the Department of Energy (DOE) Geothermal Technologies Program under Grant Number EE0002764 and from the Initiative for Renewable Energy and the Environment (IREE), a signature program of the Institute on the Environment (IonE) at the University of Minnesota (UMN) for this contribution and related research. MOS also acknowledges support for this and related research from an NSF Sustainable Energy Pathways (SEP) grant, NSF SEP-1230691, and is grateful for the support of the Hydrogeology and Geofluids research group by the George and Orpha Gibson Endowment. MOS also thanks the Werner Siemens Foundation for its support of the Geothermal Energy and Geofluids group in the Institute of Geophysics, Department of Earth Sciences, ETH-Zürich, Zürich, Switzerland. BMT acknowledges receipt of the UMN Doctoral Dissertation Fellowship, which provided funding for a portion of this research. This work was carried out using computing resources at the University of Minnesota Supercomputing Institute (MSI). Any opinions, findings, conclusions, or recommendations in this material are those of the authors and do not necessarily reflect the views of the DOE, NSF, IREE, IonE, MSI, ETH-Zürich, or UMN. Glenn Hammond and Peter Lichtner are additionally acknowledged for their assistance with PFLOTRAN input files. Associate Editor Jens Birkholzer and two anonymous reviewers are gratefully thanked for their handling and helpful comments, which helped to improve the quality and impact of this manuscript.

Disclaimer

Dr. Martin Saar has a royalty and equity interest in, and serves as the Chief Scientific Officer for, TerraCOH, Inc., a company which may commercially benefit from the results of this research. Dr. Saar and the University of Minnesota have financial interests arising from the rights to receive royalty income under the terms of a license agreement withTerraCOH, Inc. These relationships have been reviewed and

managed by the University of Minnesota in accordance with its conflict of interest policies.

Contents

List of Tables

List of Figures

Chapter 1

Introduction

Greenhouse gas emissions and their associated changes to Earth's climate, hydrologic, and ecological systems are amongst the most pressing issues facing society in the twenty-first century. In this thesis, I explore fundamental and applied aspects of one of the proposed methods for transitioning from a fossil fuel-burning, greenhouse gas emitting society to a renewable energy-based society: Carbon Capture, Utilization, and Storage (CCUS). CCUS involves capturing carbon dioxide (CO_2) from point sources, such as coal-fired power plants, injecting it deep underground into permeable, porous geologic formations, and, potentially, *utilizing* the injected CO_2 to extract geothermal energy from the subsurface. CCUS is an inherently multi-faceted problem, with researchers and practioners ranging in fields from the Earth sciences to engineering, economics, and public policy, amongst other fields. Within the Earth sciences alone, researchers must focus on a variety of processes, including (but not limited to): the thermodynamics and kinetics of geochemical reactions; the flow and transport of CO_2, reservoir brines, dissolved solutes, and heat; and the evolution of porosity and permeability with the progression of geochemical reactions and mechanical stresses. Here, my co-authors and I offer perspectives and advancements within these sub-fields of the Earth sciences. Specifically, Chapters 2 and 3 focus on the thermodynamics of relevant chemical reactions; Chapters 4 and 5 focus on experimental observations of coupled fluid flow, chemical reactions, and porosity/permeability changes; and Chapter 6 focuses on placing laboratory-scale observations of these coupled processes into the reservoir scale. Together, these chapters offer a glimpse of the immensely multi-faceted nature of CCUS research.

Chapter 2

Internal consistency in aqueous geochemical data revisited: applications to the aluminum system

2.1 Summary

Internal consistency of thermodynamic data has long been considered vital for confident calculations of aqueous geochemical processes. However, an internally consistent mineral thermodynamic data set is not necessarily consistent with calculations of aqueous species thermodynamic properties due, potentially, to improper or inconsistent constraints used in the derivation process. In this study, we attempt to accommodate the need for a mineral thermodynamic data set that is internally consistent with respect to aqueous species thermodynamic properties by adapting the least squares optimization methods of Powell and Holland (1985). This adapted method allows for both the derivation of mineral thermodynamic properties from fluid chemistry measurements of solutions in equilibrium with mineral assemblages, as well as estimates of the uncertainty on the derived results. Using a large number of phase equilibria, solubility, and calorimetric measurements, we have developed a thermodynamic data set of 12 key aluminum-bearing mineral phases. These data are derived to be consistent with Na^+ and K^+ speciation data presented by Shock and Helgeson (1988), H_4SiO_4 data presented by Stefánsson (2001), and the Al speciation data set presented by Tagirov and Schott (2001). Many of the constraining phase equilibrium measurements are exactly the same as those used to develop other thermodynamic data, yet our derived values tend to be quite different than some of the others' due to our choices of reference data. The differing values of mineral thermodynamic properties have implications for calculations of Al mineral solubilities; specifically, kaolinite solubilities calculated with the developed data set are as much as 6.75 times lower

and 73% greater than those calculated with Helgeson et al. (1978) and Holland and Powell (2011) data, respectively. Where possible, calculations and experimental data are compared at low T, and the disagreement between the two sources reiterates the common assertion that low-T measurements of phase equilibria and mineral solubilities rarely represent equilibrium between water and well-crystallized minerals. As an ancillary benefit of the derived data, we show that it may be combined with high precision measurements of aqueous complex association constants to derive neutral species activity coefficients in supercritical fliuds. Although this contribution is specific to the aluminum system, the methods and concepts developed here can help to improve the calculation of water-rock interactions in a broad range of earth systems.

2.2 Background and motivation

Ongoing research in the fields of equilibrium and kinetic geochemistry and their applications to many geologic processes, including hydrothermal crustal alteration (Seyfried et al., 2011), equilibrium isotope fractionation (Syverson et al., 2013), geologic CO_2 utilization (Randolph and Saar, 2011a) and storage (DePaolo et al., 2013), soil formation (Brantley and White, 2009), and others, have illustrated the vital importance of accurate calculations of equilibrium solubilities of rock-forming minerals. In turn, accurate calculations of mineral solubilities are important for modeling kinetically controlled mineral-fluid reactions, particularly in the region very close to equilibrium where most natural systems exist over geologic time scales (Lasaga et al., 1994; White and Brantley, 2003; Maher et al., 2009). Importantly, because mineral solubility calculations require computation of both the thermodynamic properties of the mineral phases and aqueous species, mineral thermodynamic data must be consistent with calculations of aqueous species thermodynamic properties in order to ensure accurate aqueous geochemical simulations.

2.2.1 Internally consistent thermodynamic data

Extensive development of geochemical thermodynamic data since at least the 1960s has resulted in increasingly confident calculations of mineral solubilities, stabilities, and saturation indices in aqueous fluids. Since the derivation of the first large geochemical thermodynamic data sets, internal consistency has been a vital attribute for confident geochemical calculations (Robie and Waldbaum, 1968; Helgeson, 1969;

Robie et al., 1978; Helgeson et al., 1978; Halbach and Chatterjee, 1984; Nordstrom and Munoz, 1994; Gottschalk, 1997; Berman, 1988; Holland and Powell, 1998, 2011; Wolery and Sutton, 2013). Nonetheless, a particular data set can be *consistently incorrect* due to improper calorimetric constraints, misinterpreted phase relationships, or unknown crystal ordering (Helgeson et al., 1978; Robie and Hemingway, 1995). Moreover, internal consistency of a mineral data set does not imply consistency with aqueous species thermodynamic data because their respective derivation processes do not guarantee overarching consistency between the two data types. Likewise, mineral thermodynamic data assembled from different internally consistent data sources are not necessarily mutually consistent.

While internal consistency is of great importance, it is also important for geochemists to estimate uncertainties on calculations of fluid-mineral interaction. Compilers of thermodynamic data sets intended for metamorphic and petrologic applications have repeatedly emphasized the importance of estimating uncertainty on geochemical calculations (Powell and Holland, 1985; Holland and Powell, 1990; Powell and Holland, 1993; Robie and Hemingway, 1995), yet the concept has not pervaded the field of aqueous geochemistry. In this contribution, we intend to exhibit a method for deriving internally consistent thermodynamic data with estimates of uncertainties from aqueous geochemical data. The method is set apart from other methods because it: a) exclusively employs aqueous solution analyses to constrain mineral thermodynamic properties, thereby ensuring accurate calculations of fluid-mineral equilibria; and b) incorporates the thermodynamic properties of aqueous species in the derivation process, thereby ensuring internal consistency with respect to both mineral and aqueous species. To illustrate this method, we have chosen to correct longstanding inconsistencies in the aluminum mineral thermodynamic data reported by Helgeson et al. (1978) (referred to here as "the aluminum problem"), which has long been the subject of critical comments and revisions due to inconsistencies noticed by several researchers (Hemley et al., 1980; Hemingway et al., 1982; Sverjensky et al., 1991; Pokrovskii and Helgeson, 1995; Haselton et al., 1995; Arnórsson and Stefánsson, 1999).

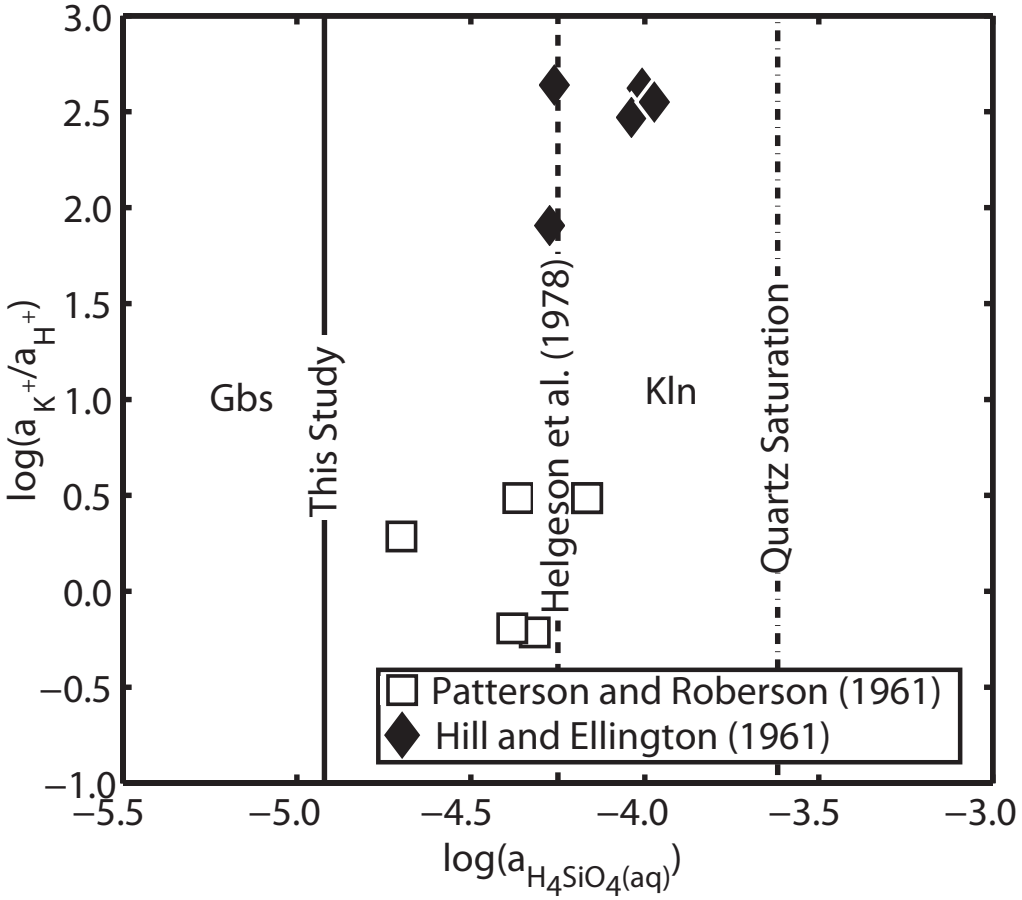

Figure 2.1: Pore water chemical compositions utilized by Helgeson et al. (1978) to constrain the thermodynamic properties of kaolinite based on calorimetrically determined thermodynamic properties of gibbsite. The equilibrium silica activity accepted by Helgeson et al. (1978) is shown (dashed line), as well as the activity predicted using the thermodynamic data set from this study (solid line).

2.2.2 The aluminum problem

Helgeson et al. (1978) utilized the reaction:

$$\text{kaolinite} + \text{H}_2\text{O} \rightleftharpoons 2 \text{ gibbsite} + 2 \text{ SiO}_2(\text{aq}) \tag{2.1}$$

to calculate the standard Gibbs free energy of formation, ΔG_f°, of the mineral kaolinite based on known values of ΔG_f° for gibbsite and SiO_2(aq). Kaolinite is an important mineral in this regard, because it can transition the Al reference state from gibbsite, a pure Al hydroxide, to kaolinite, an aluminosilicate which has been studied in a large number of phase equilibria experiments. Helgeson et al. (1978) calculated ΔG_f° of gibbsite based on enthalpy and entropy values reported by Hemingway and Robie (1977) and Robie and Waldbaum (1968), respectively. The standard molal Gibbs free energy at 1 bar and 25°C for the reaction in Eqn. 2.1 was obtained from Jamaican bauxite (Hill and Ellington, 1961) and weathered Hawaiian basalt (Patterson and Roberson, 1961) pore water compositions (Fig 2.1). These samples were interpreted by Bricker and Garrels (1967) and Garrels and Mackenzie (1967) to be in equilibrium with the minerals kaolinite and gibbsite, which permits calculation of the gibbsite/kaolinite equilibrium based on the buffered activity of SiO_2(aq). Helgeson et al. (1978) emphasized that by employing the gibbsite/kaolinite reaction, they could ensure that the thermodynamic properties of aluminosilicates anchored by these data are consistent with both experimental (Hemingway and Robie, 1977; Robie and Waldbaum, 1968) and geologic (Patterson and Roberson, 1961; Hill and Ellington, 1961) observations. However, this approach placed disproportionate weight on these low-T field measurements by defining the aluminum reference state based on the Reaction 2.1, and a number of researchers have suggested that the silica concentrations shown in Fig. 2.1 are too high to represent kaolinite-gibbsite equilibrium (Pačes, 1978; Hemley et al., 1980; Hemingway et al., 1982). It is likely that the silica concentration in the examined pore fluids could have developed a metastable equilibrium with amorphous silica, or was simply not equilibrated with the coexisting mineral assemblage.

Because the properties of kaolinite derived from the Reaction 2.1 were used as an Al reference in the evaluation of a large number of reactions, the thermodynamic data for many Helgeson et al. (1978) Al minerals are likely systematically offset from actual values (Hemingway et al., 1982). The questionable nature of the Helgeson et al. (1978) Al reference state has led researchers to devote significant effort to altogether

replacing this data set in geological applications (Holland and Powell, 1985, 1990, 1998, 2011; Berman, 1988; Hemingway and Haselton, 1994; Robie and Hemingway, 1995; Oelkers et al., 1995; Hemingway and Sposito, 1996; Arnórsson and Stefánsson, 1999), and to adjusting the Al minerals to bring them into consistency with experimental observations (Hemingway et al., 1982; Sverjensky et al., 1991; Saccocia and Seyfried, 1994). Hemingway et al. (1982) suggested a correction of -6.5 kJ/mol of Al (1.6 kcal/mol) to all Helgeson et al. (1978) Al minerals (except gibbsite) would bring them into agreement with collected experimental data. Similarly, Sverjensky et al. (1991) recommended subtracting 236 cal/mol from the Helgeson et al. (1978) K- and Na- bearing aluminum minerals, and Saccocia and Seyfried (1994) suggested subtracting 817 cal/mol from the Na-bearing Al minerals to bring the data into agreement with their respective experimental results. These corrections do not directly deal with the task of developing a new, internally consistent Al mineral data set, however, and errors with the erroneous kaolinite reference persist. Moreover, Hemingway and Haselton (1994) conclude that corrections of the type suggested by Sverjensky et al. (1991) are unwarranted based on calorimetric observations. Nonetheless, even with the widespread acknowledgment of these pervasive inconsistencies in the Helgeson et al. (1978) data set, the original Al mineral data are still being applied to a range of geologic systems, likely due to their inclusion in the data sets provided with popular geochemical simulation programs (e.g., Geochemist's Workbench (Bethke and Yeakel, 2012) and TOUGHREACT (Xu et al., 2006)).

2.3 Objectives and strategy

Aqueous geochemists require a database that provides an internally consistent means of calculating aluminum mineral and aqueous species thermodynamic properties over the wide range of crustal T and P, including not only the steam saturation curve, but also at the extreme conditions present in phase separation and hydrothermal alteration systems. In this study, we begin to develop this data set by taking advantage of both new and existing calorimetric measurements, phase equilibria, and aqueous species thermodynamic data. Throughout this study, we use the phrase "phase equilibria" to indicate measurements of an aqueous fluid in equilibrium with at least two mineral phases and "solubility" to indicate measurements of an aqueous fluid in equilibrium with a single mineral phase. We have strategically chosen anchor species so that the mineral thermodynamic properties derived here remain

Table 2.1: Mineral names and abbreviations, after Whitney and Evans (2010).

albite	$NaAlSi_3O_8$	Ab
andalusite	Al_2SiO_5	And
boehmite	$AlO(OH)$	Bhm
diaspore	$AlO(OH)$	Dsp
gibbsite	$Al(OH)_3$	Gbs
K-feldspar	$KAlSi_3O_8$	Ksp
kaolinite	$Al_2Si_2O_5(OH)_4$	Kln
muscovite	$KAl_2(AlSi_3O_{10})(OH)_2$	Ms
paragonite	$NaAl_2(AlSi_3O_{10})(OH)_2$	Pg
pyrophyllite	$Al_2Si_4O_{10}(OH)_2$	Prl
quartz	SiO_2	Qz

consistent with other thermodynamic data collections as well as aqueous Al speciation data presented by Tagirov and Schott (2001) and H_4SiO_4(aq) data presented by Stefánsson (2001). All phase equilibria chosen to constrain the relative thermodynamic properties of the produced data set rely on measurements of aqueous fluid concentrations and therefore can also be used to ensure agreement between aqueous speciation calculations and measured mineral-solution equilibria. Although the method of using experimental or field measurements of aqueous fluid concentrations has its complications–e.g., experimental artifacts, ion activity and aqueous speciation models, availability of high T,P speciation data– it should allow for more realistic calculations of fluid-mineral interaction because all constraining data is derived from measurements of fluid-mineral equilibria. Lastly, because a least squares optimization of mineral phase relations is employed to calculate standard state thermodynamic properties, the method enables estimation of uncertainties on derived properties and advances the ability of aqueous geochemists to estimate the accuracy of calculations of fluid-mineral interactions.

2.4 Methods

The standard states adopted in this study are a unit activity of an aqueous species in a hypothetical one molal solution referenced to infinite dilution, unit activity of pure minerals, and unit activity of pure liquid H_2O at all temperatures and pressures. Mineral abbreviations utilized in this study follow the recommendations of Whitney and Evans (2010) (Table 2.1).

2.4.1 Minerals

In the compilation of mineral thermodynamic data sets, it is often justifiably assumed that measurements or estimates of mineral heat capacities, $C^{\circ}_{P_r}$, standard molar volumes, V°, and third law entropies, S°, are obtained with suitable precision and accuracy to allow for accurate calculation of the T and P dependence of mineral standard state thermodynamic properties (Helgeson et al., 1978; Powell and Holland, 1985; Robie and Hemingway, 1995). However, calorimetric measurements of mineral enthalpies carry a more significant degree of uncertainty due to the means by which they must be calculated, even if the measurements themselves are exceedingly precise (Powell and Holland, 1985). Therefore, a reasonable and often chosen method to determine mineral standard state enthalpies, ΔH°_f, and Gibbs free energies of formation, ΔG°_f, is to derive them from measurements of phase equilibria at a range of T and P conditions through the relationship,

$$\Delta G^{\circ}_{r,P,T} = -RT \ln K, \tag{2.2}$$

where $\Delta G^{\circ}_{r,P,T}$ is the standard molal Gibbs free energy of reaction at the subscripted P and T, R is the ideal gas constant, and T is the temperature in Kelvin. By accepting known values of V°, $C^{\circ}_{P_r}$, and S° and inserting them into the equation:

$$\Delta\ G^{\circ}_{f,P,T} - \Delta\ G^{\circ}_{f,P_r,T_r} = -S^{\circ}_{P_rT_r}(T - T_r) + \int_{T_r}^{T} C^{\circ}_{P_r} dT - T \int_{T_r}^{T} C^{\circ}_{P_r} d\ln T + \int_{P_r}^{P} V^{\circ}_T dP, \tag{2.3}$$

the well-known T and P dependence of mineral thermodynamic properties can be subtracted from high-T experimental measurements, leaving only the contribution of $\Delta G^{\circ}_{f,P_r,T_r}$, the Gibbs free energy of formation from the elements at T_r (298.15 K) and P_r (1 bar).

We have chosen to use the Robie and Hemingway (1995) formulation for the calculation of heat capacity:

$$C^{\circ}_{P_r} = \mathrm{A}_1 + \mathrm{A}_2 T + \mathrm{A}_3 T^{-2} + \mathrm{A}_4 T^{-0.5} + \mathrm{A}_5 T^2, \tag{2.4}$$

where A_1 through A_5 are mineral-specific fitting parameters included in the Robie and Hemingway (1995) compilation. If desired, heat capacities can be calculated according to another polynomial (Robie and Hemingway, 1995; Nordstrom and Munoz, 1994).

Where required, ΔH_f°, can be calculated according to

$$\Delta H_f^\circ = \Delta G_f^\circ + T\Delta S_f^\circ, \tag{2.5}$$

where ΔS_f° is the standard entropy of formation from the elements, whose properties are obtained from Robie and Hemingway (1995).

The treatment of Al-Si disorder contributions to K-feldspar thermodynamic properties are dealt with by simply adopting heat capacity parameters from Helgeson et al. (1978), which allow for calculation of the thermodynamic properties of K-feldspar in its stable ordering state at all T relevant to this study. Accordingly, the value obtained for K-feldspar at T_r and P_r is that of maximum microcline, which is the ordered end-member of K-feldspar. To calculate standard state thermodynamic properties of sanidine, the disordered K-feldspar end-member, the corresponding entropy, enthalpy, and Gibbs free energy of disorder must be added and sanidine heat capacity coefficients must be adopted, as in, e.g., Helgeson et al. (1978) or Robie and Hemingway (1995). Because the only albite phase relations used to constrain albite's thermodynamic properties in this study correspond to low albite, the heat capacity coefficients for low albite were adopted directly from Robie and Hemingway (1995). Properties of albite in its stable state of order at elevated T and P can be calculated using the heat capacity and phase transition parameters from Helgeson et al. (1978), if desired.

2.4.2 Aqueous species and fluid speciation

Calculation of aqueous species thermodynamic properties relies on the revised Helgeson-Kirkham-Flowers (HKF) equations of state (Table 2.2), except for: 1) HCl(aq), KCl(aq), and KOH(aq), whose dissociation constants are calculated using both the parameters in Table 2.2 and empirical density-temperature relationships reported by Ho et al. (2001) and Ho and Palmer (1997) (see Sect. 2.5.2); and 2) NaCl(aq) and NaOH(aq) whose properties are calculated using only the equations of Ho et al. (1994) and Ho and Palmer (1996) (see Sect. 2.5.3). We utilize HKF parameters for H_4SiO_4(aq) from Stefánsson (2001), and parameters for $AlOH_4^-$ presented by Tagirov and Schott (2001). The H_4SiO_4(aq) parameters were obtained using quartz thermodynamic data from Robie and Hemingway (1995) and updated quartz (Rimstidt, 1997) and amorphous silica (Gunnarsson and Arnórsson, 2000) solubility measurements, and parameters for the Al system were derived from boehmite

and gibbsite solubility experiments (Wesolowski, 1992; Palmer and Wesolowski, 1992; Bénézeth et al., 2001). To remain consistent with the derived formulations, Robie and Hemingway (1995) data for quartz were used to anchor the least squares optimization (Sect. 2.5.1), and boehmite and gibbsite were not adjusted in the present study. This provision should allow for integration of the derived mineral thermodynamic data set and the Tagirov and Schott (2001) data set.

The B-dot extended Debye-Hückel equation (Hückel, 1925) is utilized in all speciation calculations for the calculation of charged species activity coefficients. At $T \geq 300°C$, activity coefficients calculated with the Debye-Hückel equation deviate negligibly from measured values, and therefore the deviation factor, B-dot, is set equal to zero (Helgeson, 1969). Although activity coefficients of neutral molecules are likely to be increasingly important at elevated ionic strengths, they are assumed to be unity here, as suggested by a number of researchers (e.g., Garrels and Christ, 1965; Helgeson, 1969; Helgeson et al., 1981), due to the lack of available data. Where required, fluid speciation calculations are facilitated by a Matlab implementation of the EQBRM package (Anderson and Crerar, 1993).

2.4.3 Least squares data optimization

Powell and Holland (1985) developed a method for optimizing mineral phase relations in the least squares sense to produce internally consistent thermodynamic data sets with estimates of uncertainties. Following the Powell and Holland (1985) method, standard state thermodynamic properties of minerals can be obtained from a least squares solution of the equation,

$$\mathrm{b} = \mathrm{Rg}, \tag{2.6}$$

where R is a matrix of reaction coefficients (Table 2.3, Columns 1-13), g is a vector of $\Delta G^{\circ}_{f,P_r,T_r}$ values for the minerals involved in the reactions, and b is a vector of $\Delta G^{\circ}_{r,P,T}$ values for the reactions in R (Table 2.3, Column 15). Because, in the application pertaining to the present study, the number of reactions able to be written between the minerals in vector g is limited, the least squares optimization requires "anchor minerals", or input values for certain members of g, to reduce the number of unknowns and ensure accurate results. For the vector of anchor minerals, c, to be included in the least squares solution, a matrix of synthetic, "identity" reactions, S, must be written.

Table 2.2: Revised Helgeson-Kirkham-Flowers (HKF) equation of state parameters and standard state thermodynamic properties used in this study.

Species	$\Delta G^\circ{}_f$	$\Delta H^\circ{}_f$	$S^\circ_{P_r,T_r}$	a_1 (10^1)	a_2 (10^{-2})	a_3	$a_4(10^{-4})$	c_1	$c_2(10^{-4})$	$\omega_{P_rT_r}(10^{-5})$
$Al(OH)_4^-$ [a]	-312,087.	-359,244.	24.748	8.4938	12.9576	0.6570	-3.3147	55.7265	-11.4047	1.0403
H^+	0.	0.	0.	0.	0.	0.	0.	0.	0.	0.
HCl(aq) [b]	-30,410.	-42,054.	3.2	1.2547	-4.7177	7.6043	-2.5840	16.7134	2.8727	-0.7000
H_4SiO_4 [c]	-312,920.	-348,676.	45.100	18.729	-21.2600	18.620	-1.200	58.031	-20.790	0.08690
K^+ [d]	-67,510.	-60,270.	24.15	3.5590	-1.4730	5.4350	-2.712	7.40	-1.791	0.1927
KCl(aq) [b]	-95,430.	-95,390.	42.25	6.9932	9.297	2.0889	-3.1633	0.9522	-4.7253	-0.038
KOH(aq) [b]	-104,423.	-113,197.	26.2	.704	-6.0623	8.1328	-2.5284	2.9855	-4.4605	0.100
Na^+ [d]	-62,591.	-57,433.	13.96	1.8390	-2.2850	3.2560	-2.726	18.18	-2.981	0.3306
OH^- [d]	-37,595.	-54,977.	-2.56	1.2527	0.0738	1.8423	-2.7821	4.15	-10.346	1.7246

[a] Tagirov and Schott (2001)
[b] Sverjensky et al. (1991)
[c] Stefánsson (2001)
[d] Shock and Helgeson (1988)

For example, the row of S corresponding to kaolinite is:

$$[0\ 1\ 0\ 0\ 0\ 0\ 0\ 0\ 0\ 0\ 0\ 0\ 0], \tag{2.7}$$

and its corresponding value in c is -907,624.3 cal/mol (Robie and Hemingway, 1995). The uncertainty on experimental measurements and anchor values can be written into two matrices, W_1 and W_2, respectively, to provide weights for the measured and anchored values. Here, as in Powell and Holland (1985), W_1 is a diagonal matrix of values equal to the inverse of a quarter of the reported or calculated uncertainty on each of the individual reactions in b (Table 2.3, Column 16), and W_2 is a diagonal matrix of the inverse of the uncertainties on the anchor minerals, water, and aqueous species. Continuing with the kaolinite example, its corresponding value in W_2 is 2.79×10^{-3} mol/cal, which is the inverse of the uncertainty reported by Robie and Hemingway (1995). Because the thermodynamic properties of aqueous species and water are fixed without refitting of equations of state, their weights are set to be large (0.21 mol/cal). Including the anchors and weights into the equation yields the final form,

$$\mathrm{g} = (\mathrm{R}^T\mathrm{W}_1^2\mathrm{R} + \mathrm{S}^T\mathrm{W}_2^2\mathrm{S})^{-1}(\mathrm{R}^T\mathrm{W}_1^2\mathrm{b} + \mathrm{S}^T\mathrm{W}_2^2\mathrm{c}). \tag{2.8}$$

The uncertainties of the solution can be estimated from

$$\mathrm{V_g} = (\mathrm{R}^T\mathrm{W}_1^2\mathrm{R} + \mathrm{S}^T\mathrm{W}_3^2\mathrm{S})^{-1}, \tag{2.9}$$

where $\mathrm{V_g}$ is the covariance matrix, and W_3 is the same as W_2, except with realistic values for the uncertainty of the aqueous species and water substituted into it. Uncertainties of aqueous species thermodynamic properties calculated using the HKF equations of state are variable dependent upon the T and P conditions of the calculation and the charge of the aqueous ion, but we estimate an average uncertainty of $\pm$500 cal/mol to calculate values for aqueous species in W_3 (Shock and Helgeson, 1988; Manning, 2013). Uncertainties on ΔH_f° of H_2O calculated using the Haar et al. (1984) equation of state, which is implemented in SUPCRT92, were estimated by Haar et al. (1984) to be on the order of 20 cal/mol. Because the uncertainty on ΔG_f° of water is expected to be on the same order of that of ΔH_f°, we adopt this value as an estimate of the uncertainty of ΔG_f° of H_2O when calculating estimates of uncertainty of properties optimized in the least squares solution. By including the matrix W_3 into Eqn. 2.9, the minerals can first be optimized to be internally consistent with

respect to the aqueous species through Eqn. 2.8, and then realistic estimates of the uncertainties on all derived values can be obtained from Eqn 2.9. The estimated uncertainty on the Gibbs free energy, $\sigma_{\Delta G_f^\circ}$, is equal to the square root of the diagonal of V_g.

2.5 Results

2.5.1 Anchor minerals: quartz, kaolinite, K-feldspar, and andalusite

Holland and Powell (1990) have shown that, for very large data sets, the relative size of the reaction matrix, R, and number of phases included in the vector g will reach a condition in which anchoring the matrix solution with input properties becomes unnecessary. However, the size of these data sets are much larger than the one presented here (e.g, >123 end-member phases (Holland and Powell, 1990)) and we therefore must employ anchor phases, as in their early studies (Powell and Holland, 1985; Holland and Powell, 1985). It is expected that additional reactions, such as: corundum + quartz = andalusite, could be added to the matrix in order to approach the critical relative size. However, until some critical number of phases was included, each additional reaction would require the inclusion of an additional phase (in this example, corundum) in the optimization. It is worth noting that, although anchor minerals have specified values in the vector c, which help to constrain the matrix solution, their final values in the vector g varies based on the optimization of the least squares solution. The choice of the number of anchor minerals and their thermodynamic properties has a significant weight on the outcome of the least squares optimization.

To determine the optimum anchor minerals, a solution to Eqn. 2.8 was attempted with a number of different anchor combinations. Quartz thermodynamic data from Robie and Hemingway (1995) is employed to anchor the data set so that the derived data may remain consistent with other data sets and the Stefánsson (2001) H_4SiO_4(aq) data. For the rest of the data set, it is clear that, to produce an acceptable solution of the reaction matrix, at least one K-containing or Na-containing mineral must be used to anchor the solution. For this purpose, ΔG_f° from Holland and Powell (1998) for K-feldspar was adopted. The decision to anchor the data with this value, which

Table 2.3: Reaction data utilized in the least squares optimization.

1	2	3	4	5	6	7	8	9	10	11	12	13	14	15	16	17	18	19
and	kln	qtz	H_2O	H_4SiO_4	Na^+	K^+	prl	dsp	alb	prg	ksp	msc	log(K)†	$\Delta G^\circ_{r,P,T}$ $^{\dagger,\sharp}$	$\sigma_{\Delta G^\circ_{r,P,T}}$ $^\sharp$	T† (°C)	P$^{\dagger,\flat}$	Ref.
0.0	1.0	0.0	-5.0	2.0	0.0	0.0	-1.0	0.0	0.0	0.0	0.0	0.0	-5.930	8,085	82	25	1	1
0.0	-1.0	0.0	-3.0	2.0	0.0	0.0	0.0	2.0	0.0	0.0	0.0	0.0	-9.290	12,665	136	25	1	1
1.0	0.0	0.0	-5.0	3.0	0.0	0.0	-1.0	0.0	0.0	0.0	0.0	0.0	-14.620	19,932	177	25	1	1
-1.0	0.0	0.0	-3.0	1.0	0.0	0.0	0.0	2.0	0.0	0.0	0.0	0.0	-0.690	941	14	25	1	1
0.0	0.0	3.0	0.0	0.0	1.0	0.0	0.0	0.0	-1.5	0.5	0.0	0.0	4.940	-12,947	786	300	500	2
-1.5	0.0	1.5	-1.5	0.0	0.0	0.0	0.0	0.0	0.0	0.0	-1.5	1.5	7.934	-10,817	205	25	1	3
0.0	0.0	0.0	0.0	0.0	1.0	-1.0	0.0	0.0	-1.0	0.0	1.0	0.0	2.087	-3,561	535	100	150	4
0.0	-1.5	3.0	1.5	0.0	0.0	0.0	0.0	0.0	0.0	0.0	-1.5	1.5	1.600	-4,193	393	300	1000	3
0.0	0.0	6.0	0.0	0.0	0.0	0.0	-1.5	0.0	0.0	0.0	-1.5	1.5	1.560	-4,088	393	300	1000	3

References: 1) Hemley et al. (1980), 2) Saccocia and Seyfried (1994), 3) Sverjensky et al. (1991), 4) Merino (1975).

†Where T and P are listed as 25°C and 1 bar, all reactions reported in the listed reference were used, and the reported $\sigma_{\Delta G^\circ_{r,P,T}}$ is their standard deviation.

$^\sharp$cal, $^\flat$bar

Table 2.4: Mineral thermodynamic parameters and heat capacity coefficients derived and utilized in this study.

Mineral	ΔG_f°	$\sigma_{\Delta G_f^\circ}$	ΔH_f°	S°	V°	A_1	A_2	A_3	A_4	A_5
	(cal/mol)	(cal/mol)	(cal/mol)	(cal/mol/K)	(cm^3/mol)		(K^{-1})	(K^2)	($K^{0.5}$)	(K^{-2})
albite	-887,370	1,178	-940,770	49.570	100.1	139.6	-0.0222	4.0105e+05	-1.5354e+03	5.4302e-06
andalusite	-583,160	316	-618,570	21.845	51.5	66.3	-0.0016	-4.5748e+05	-5.4149e+02	0
boehmite	-219,500[a]	526[a]	-238,150[a]	8.891	19.5	49.2	-0.0083	2.4546e+05	-6.2978e+02	0
dawsonite[b]	-425,910[c]	478[c]	-468,450[c]	31.310	59.3	8.2	0.0800	1.7839e+05	0	0
diaspore	-219,680	220	-238,460	8.437	17.8	14.4	0.0042	0	0	0
gibbsite	-276,030[a]	287[a]	-309,060[a]	16.348	32.0	8.7[d]	.00456[d]	0[d]	0[d]	0[d]
K-feldspar	-896,440	932	-950,300	51.195	108.9	76.6	0.0043	-2.9945e+06	0	0
kaolinite	-907,880	296	-984,530	48.518	99.3	341.8	-0.1885	1.9919e+06	-4.4264e+03	7.2514e-05
muscovite	-1,339,000	1,031	-1,429,900	69.790	140.8	219.3	-0.0194	6.7734e+05	-2.4737e+03	0
paragonite	-1,332,500	3,482	-1,423,600	65.966	132.1	159.8	0.0087	-4.4455e+05	-1.3901e+03	0
pyrophyllite	-1,258,400	561	-1,347,700	57.218	128.1	178.5	-0.0128	0	-1.8112e+03	4.7467e-06
quartz	-204,480	203	-217,480	9.919	22.7	19.4	0.0044	-4.3260e+04	-1.6695e+02	1.2921e-06

[a]Adopted from Robie and Hemingway (1995) [b]Dawsonite heat capacity coefficients reported in Table 2.4 differ from those reported by Robie and Hemingway (1995)– their reported values appear to have suffered from a typographical error in the decimal places of variables. [c] Bénézeth et al. (2007), [d]Robie and Waldbaum (1968)

is within the reported uncertainty but slightly different than that of Robie and Hemingway (1995), was made because it appears to accommodate the constraining data more effectively. This may be related to the small size of the reaction matrix, the Helgeson et al. (1978) K-feldspar heat capacity parameters, or order/disorder in the muscovite and K-feldspar samples, but investigations into this problem would require a larger produced data set or a more thorough characterization of the ordering states of experimental reaction minerals for sufficient resolution. Although the Holland and Powell (1998) value is accepted, we employ the uncertainty reported by Robie and Hemingway (1995), which is more characteristic of a calorimetric uncertainty, to weight its value.

Because kaolinite can exist in stable equilibrium with a large number of aluminum minerals, the choice of kaolinite thermodynamic properties can have a large effect on the calculated properties of the other minerals. Kaolinite has a long history of experimental and field data in the disciplines of high- and low- T geochemistry (A; Barany and Kelley (1961); Garrels and Christ (1965); Kittrick (1966); Hess (1966); Kittrick (1970); Hem and Lind (1974); Robie et al. (1978); Helgeson et al. (1978); Bassett et al. (1979); Hemley et al. (1980); Kittrick (1980); Hemingway et al. (1982); Halbach and Chatterjee (1984); Chatterjee et al. (1984); May et al. (1986); Berman (1988); Nagy et al. (1991); Robie and Hemingway (1995); Devidal et al. (1996); Hemingway and Sposito (1996); De Ligny and Navrotsky (1999); Fialips et al. (2001, 2003); Yang and Steefel (2008); Kiseleva et al. (2011)), and thermodynamic data derived from these data tend to differ considerably. Values of $\Delta G^{\circ}_{f,P_r,T_r}$ from data sets intended for use in metamorphic petrology applications tend to be more negative than those derived from low-T solubility studies. Holland and Powell (2011) present $\Delta G^{\circ}_{f,r}$ = -908.6 kcal/mol (virtually identical to that given by Holland and Powell (1998)), and Berman (1988) presented a value of -908.1668 kcal/mol[1]. Low-T solubility measurements yield a large range of values (Fig. 2.2)–most notably, Helgeson et al. (1978) derived a value of -905.614 kcal/mol from the data plotted in Fig. 2.1. The recent molten lead borate calorimetric measurements of De Ligny and Navrotsky (1999), Fialips et al. (2001), and Fialips et al. (2003) on both natural and synthetic crystals yield values converging on that of Chatterjee et al. (1984) (-907,624.3 cal/mol), which was also adopted by Robie and Hemingway (1995) and used here as an anchor value.

[1] Both of these values were derived from the unpublished data for the reaction kaolinite + quartz $\rightleftharpoons$ pyrophyllite from D.C. McPhail at the University of British Columbia), which, as noted by Berman (1988), underwent only minor amounts of reaction in most experiments.

The derived value (-907,874.6 cal/mol) is in excellent agreement with a large number of solubility and phase equilibria studies (Fig. 2.2), but yields a gibbsite/kaolinite equilibrium silica activity of $10^{-4.9}$ (Fig. 2.1), suggesting that, indeed, the water samples utilized by Helgeson et al. (1978) tended towards disequilibrium and were likely influenced by another silica-donating source. Fig. 2.2 additionally illustrates the difference between calculations performed using the presented data, Helgeson et al. (1978) data, and Holland and Powell (2011) thermodynamic data. Because the kaolinite solubility reaction was not employed in the reaction matrix (Table 2.3), this comparison offers a method for testing the results of our optimization. The line calculated using our optimized thermodynamic values for kaolinite (Table 2.4) combined with the requisite aqueous species thermodynamic properties and HKF parameters from Table 2.2 is in better agreement with the majority of the solubility studies than both of the other sources. Note that the width of the plotted line is proportional to the uncertainty on the calculated equilibrium constant, indicating that neither the Helgeson et al. (1978) nor the Holland and Powell (2011) calculations fall within the limits of the reported uncertainty. The agreement between the Helgeson et al. (1978) data and the low-T solubility studies illustrates the complications associated with the derivation of thermodynamic data from low-T solubility measurements. Although the low temperature kaolinite solubility measurements plotted in Fig. 2.2 tend to be in reasonably good agreement, they are all in substantial disagreement with solubilities calculated from the Holland and Powell (2011) data and our own. This disagreement has been noted by several researchers (e.g., Devidal et al., 1996; Oelkers et al., 1995), and it has therefore been suggested that solubility measurements at low temperature may be complicated by the formation of metastable Al hydroxide or Si-bearing phases, or the slow precipitation kinetics of kaolinite at low temperatures (Devidal et al., 1996).

A solution of Eqn 2.8 using only quartz, kaolinite, and K-feldspar as anchor minerals yielded acceptable results for all minerals, except andalusite, which was approximately 3 kcal/mol less negative than the calorimetric data reported by Robie and Hemingway (1995). This likely results from the tenuous connection between the anchor aluminosilicate phase, kaolinite, and andalusite. We therefore decided to anchor the solution with thermodynamic data for both kaolinite and andalusite from Robie and Hemingway (1995).

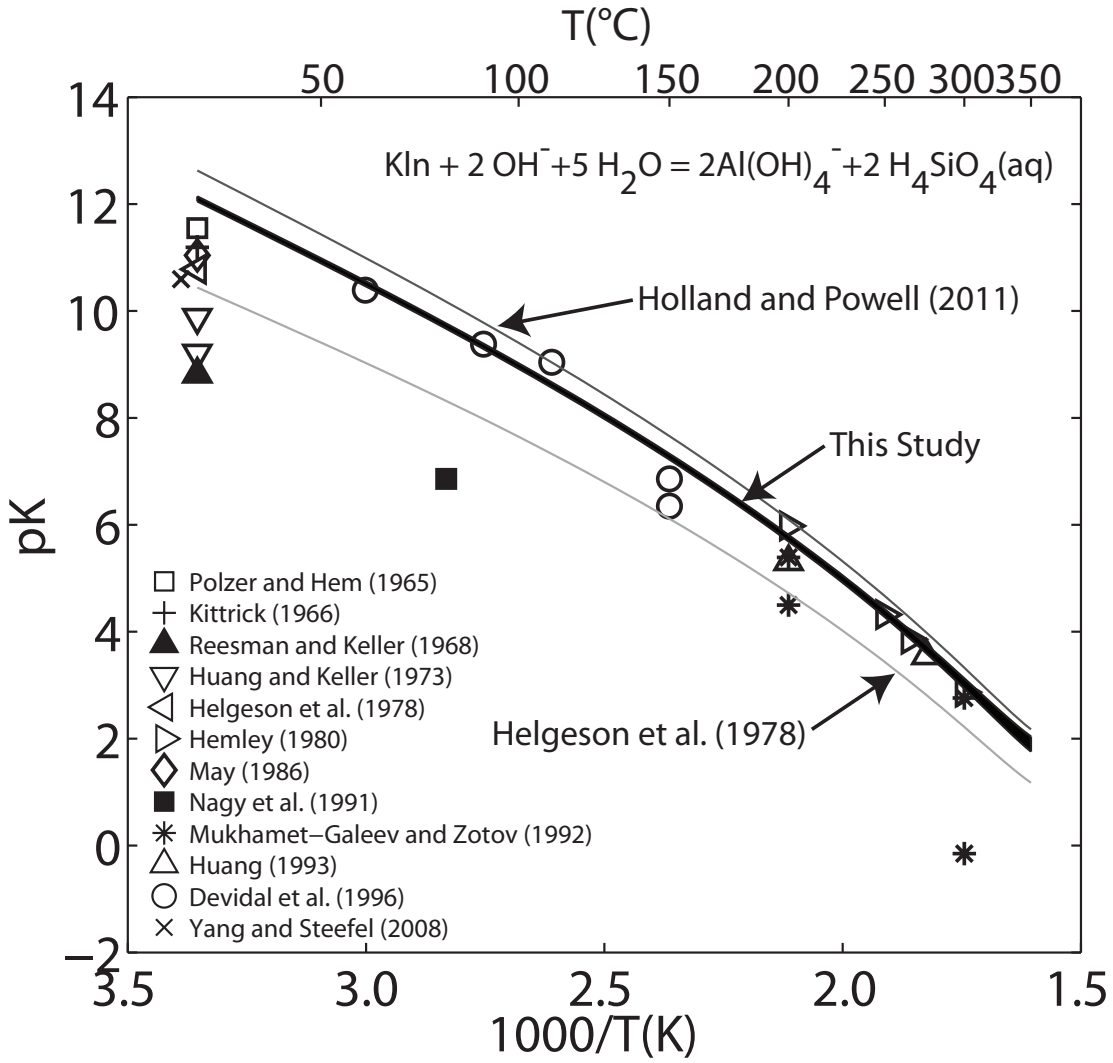

Figure 2.2: Kaolinite solubility values collected by Devidal et al. (1996) and taken from the literature compared with calculations performed using thermodynamic properties obtained and adopted in this study. Identical calculations performed using kaolinite data from Helgeson et al. (1978) and Holland and Powell (2011) are shown for comparison. The width of the line corresponding to this study is proportional to the uncertainty on the calculation.

2.5.2 K-feldspar, muscovite, pyrophyllite

The relative stability of muscovite in quartz-bearing systems compared to the aluminosilicates (pyrophyllite, kaolinite, andalusite), and K-feldspar has been the subject of a number of studies (A; Hemley (1959); Garrels and Howard (1959); Althaus et al. (1970); Usdowski and Barnes (1972); Shade (1974); Kerrick (1972); Montoya and Hemley (1975); Wintsch et al. (1980); Gunter and Eugster (1980); Haselton et al. (1988); Sverjensky et al. (1991); Haselton et al. (1995); Frank et al. (1998); Frank and Vaccaro (2012)) at various T, P, and chloride molalities. We have chosen to use data in this system provided by Sverjensky et al. (1991) because their experiments were almost entirely sampled using extraction techniques, as opposed to measurements on quenched fluids or determination of fluid compositions based on speciation calculations. Other sources, particularly Usdowski and Barnes (1972), Montoya and Hemley (1975), and Haselton et al. (1995), tend to be in agreement with the Sverjensky et al. (1991) measurements, but do not present measurements spanning as large of a T-P range. As suggested by Sverjensky et al. (1991), the natural muscovite sample used in their experiments shows signs of partial Al-Si disorder, and we have therefore set S° for muscovite to 69.80 cal/mol/K (Holland and Powell, 2011).

Sverjensky et al. (1991) presented values of equilibrium constants for the reactions:

$$\text{muscovite} + \text{H}^+ \rightleftharpoons 1.5\ \text{andalusite} + 1.5\ \text{quartz} + 1.5\ \text{H}_2\text{O} + \text{K}^+ \tag{2.10}$$

and

$$1.5\ \text{K-feldspar} + \text{H}^+ \rightleftharpoons 0.5\ \text{muscovite} + 3\ \text{quartz} + \text{K}^+. \tag{2.11}$$

Aqueous species can be entirely eliminated from Reactions 2.10 and 2.11 by "summing" the reactions to yield (Sverjensky et al., 1991):

$$1.5\ \text{K-feldspar} + 1.5\ \text{andalusite} + 1.5\ \text{H}_2\text{O} = 1.5\ \text{muscovite} + 1.5\ \text{quartz}, \tag{2.12}$$

which corresponds to the width of the stability field of muscovite in T - $\log \frac{K}{H}$ activity space (Fig. 2.3). Because the experimental fluid in Sverjensky et al. (1991) is a 1 molal chloride brine, the contribution of minor changes in K_{tot} and H_{tot} to solution ionic strength and ion activity coefficients are negligible and the widths of the muscovite stability field in $\text{K}_{\text{tot}}/\text{H}_{\text{tot}}$ and $\log(\text{aK}^+/\text{aH}^+)$ space are therefore equivalent (Sverjensky et al., 1991).

Similar to Reaction 2.10, equilibrium constants provided by Sverjensky et al. (1991) for the reaction,

$$\text{muscovite} + \text{H}^+ + 1.5\ \text{H}_2\text{O} \rightleftharpoons 1.5\ \text{kaolinite} + \text{K}^+ \tag{2.13}$$

can be combined with Reaction 2.11 to yield,

$$1.5\ \text{K-feldspar} + 1.5\ \text{kaolinite} \rightleftharpoons 1.5\ \text{muscovite} + 3\ \text{quartz} + 1.5\ \text{H}_2\text{O}. \tag{2.14}$$

Lastly, Sverjensky et al. (1991) presented values for the reaction:

$$\text{muscovite} + \text{H}^+ + 3.0\ \text{quartz} \rightleftharpoons 1.5\ \text{pyrophyllite} + \text{K}^+, \tag{2.15}$$

which can be combined with Reaction 2.11 to yield:

$$1.5\ \text{K-feldspar} + 1.5\ \text{pyrophyllite} \rightleftharpoons 1.5\ \text{muscovite} + 6\ \text{quartz}. \tag{2.16}$$

For Reaction 2.12, Sverjensky et al. (1991) included multiple measurements of equilibrium solution compositions. We have included all reported measurements in the least squares optimization by subtracting away the T-P contributions to the thermodynamic properties of the phases in the reactions through an appropriate statement of Eqn. 2.3, which leaves only the contribution of $\Delta G^\circ_{f,P_r,T_r}$ of the minerals to ΔG°_r. We then calculate the mean and standard deviation of these values of ΔG°_r at T_r and P_r. The calculated values are included in Table 2.3.

Experimentally measured values for Reactions 2.12, 2.14, and 2.16 at 1 kbar are plotted in Fig 2.3A. As shown in Figs. 2.3B and C, Reaction 2.13 is metastable compared to Reaction 2.15 at 300°C and 1 kbar, and therefore the calculated equilibrium constant for Reaction 2.14 is shown as a dashed line in Fig. 2.3A. This metastability is consistent with the nearly identical values of $\log(\text{K}_{\text{tot}}/\text{H}_{\text{tot}})$ determined by Sverjensky et al. (1991) for Reactions 2.13 (1.90 ± 0.15) and 2.15 (1.94 ± 0.15) at 300°C, but refinement of the boundary requires further determination of equilibrium ratios for these reactions in the range 250-350°C at 1 kbar.

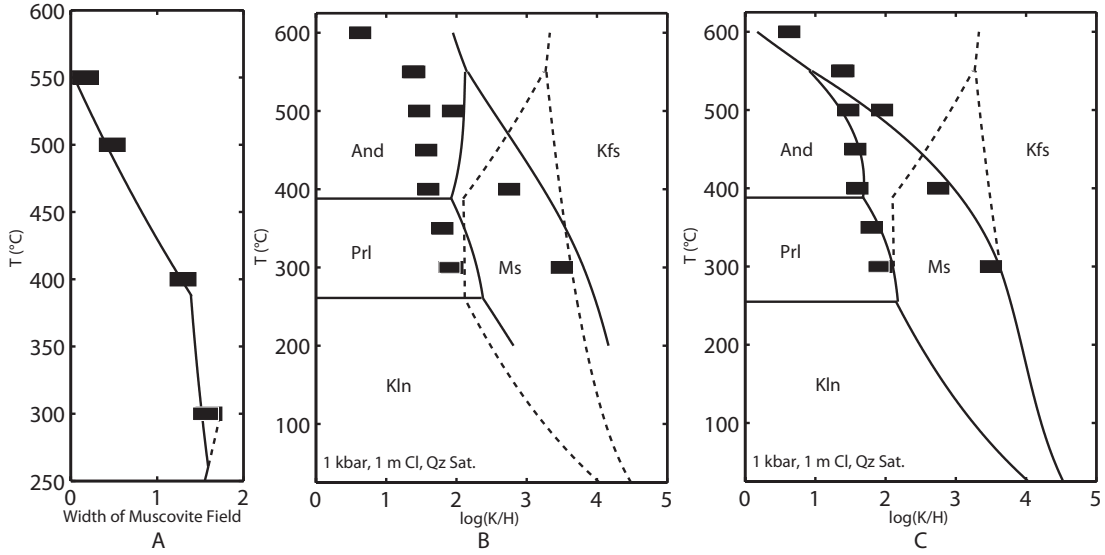

Figure 2.3: A. Width of the muscovite stability field in log(K/H)-temperature space, as measured by Sverjensky et al. (1991) at 1 kbar. The dashed line represents the metastable extension of the kaolinite-muscovite-quartz reaction. B. Calculations of equilibrium activity ratios, $\log(aK^+ / aH^+)$ (dashed lines), performed using the derived mineral thermodynamic data and equilibrium concentration ratios, $\log(K_{tot}/H_{tot})$ (solid lines), calculated using association constants derived from high-precision conductance data. C. Dashed lines are the same as in B, but solid lines indicate equilibrium $\log(K_{tot}/H_{tot})$ ratios calculated using aqueous complex data compiled and derived by Sverjensky et al. (1991).

2.5.3 Albite, paragonite

Analogous to muscovite, experimental measurements of compositions of fluids in equilibrium with paragonite and albite, quartz, and/or aluminosilicate minerals can constrain the relative stabilities of albite and paragonite using the anchor minerals andalusite, kaolinite, and quartz (Sverjensky et al., 1991). Equilibrium fluid concentrations for the reaction:

$$1.5 \text{ albite} + \text{H}^+ \rightleftharpoons 0.5 \text{ paragonite} + 3 \text{ quartz} + \text{Na}^+ \tag{2.17}$$

have been reported by a number of researchers (A; Montoya and Hemley (1975); Woodland and Walther (1987); Saccocia and Seyfried (1994); Tagirov et al. (2002)). This data, combined with measurements of solutions in equilibrium with paragonite, quartz, and an aluminosilicate phase can be used to create a system of "summed" reactions corresponding to the width of the paragonite field, analogous to that for the muscovite field. Unfortunately, however, results of only a limited number of phase equilibria studies are available to constrain the stability of paragonite relative to any of the aluminosilicates (Hemley and Jones, 1964; Ivanov and Gusynin, 1970; Chatterjee, 1972; Montoya and Hemley, 1975; Popp and Frantz, 1980; Shinohara and Fujimoto, 1994). Of these, Montoya and Hemley (1975) seems the most promising for the derivation of thermodynamic data. However, Sverjensky et al. (1991) suggest that the Montoya and Hemley (1975) phase boundaries may not reflect equilibrium measurements, due to problems with experimental equipment. The questionable accuracy of the Montoya and Hemley (1975) data has therefore forced us to abandon the paragonite field method, and utilize only the 300°C, 500 bar Saccocia and Seyfried (1994) albite-paragonite-quartz equilibrium measurement. Saccocia and Seyfried (1994) utilized a relatively low ionic strength fluid at relatively low P and T, which allows for more confident calculations of fluid speciation in the absence of detailed knowledge of the activity coefficients of NaCl(aq) and HCl(aq). The albite sample used in Saccocia and Seyfried (1994) was identified to be ordered albite by x-ray diffraction measurements, and we have therefore utilized heat capacity and entropy parameters for ordered albite from Robie and Hemingway (1995) here. Al-Si disorder in paragonite, on the other hand, was not reported, and we have therefore adopted S° for ordered paragonite from Robie and Hemingway (1995), consistent with other internally consistent datasets (Helgeson et al., 1978; Berman, 1988; Holland and Powell,

2011).

2.5.4 Albite, K-feldspar

Although the experimental measurements discussed in Sections 2.5.2 and 2.5.3 can suffice to produce accurate data for their individual systems, it is important to tie the involved minerals together with a coupling reaction. For this purpose, we have chosen the reaction:

$$\text{albite} + \text{K}^+ \rightleftharpoons \text{K-feldspar} + \text{Na}^+ \tag{2.18}$$

which has been studied by a number of researchers (e.g., Orville (1963); Kharaka (1971); Fournier and Truesdell (1973); Kharaka and Berry (1974); Merino (1975); Arnórsson et al. (1983); Giggenbach (1988)). Helgeson et al. (1978) used 100°C, 150 bars Na^+/K^+ ratios calculated by Merino (1975) from fluid chemistry samples presented by Kharaka (1971) to constrain the relative properties of low albite and K-feldspar. We have chosen to utilize the same data set here in order to incorporate field measurements without introducing conditions where alkali metal-chloride complexing becomes significant. The mean and standard deviation of the 41 equilibrium aNa^+/aK^+ values reported by Merino (1975) are 2.087 and 0.31, respectively.

2.5.5 Pyrophyllite, diaspore

A number of studies have been performed to constrain the relative thermodynamic properties of minerals in this system (Kerrick, 1968; Haas and Holdaway, 1973; Hemley et al., 1980; Theye et al., 1997). Of these, Hemley et al. (1980) presents the most complete set of measurements that fall in the range of applicability of this study. We use the Hemley et al. (1980) equilibria for the reactions:

$$\text{pyrophyllite} + 5\ \text{H}_2\text{O} \rightleftharpoons \text{kaolinite} + 2\ \text{H}_4\text{SiO}_4\text{(aq)}, \tag{2.19}$$

$$\text{kaolinite} + 3\ \text{H}_2\text{O} \rightleftharpoons 2\ \text{diaspore} + 2\ \text{H}_4\text{SiO}_4\text{(aq)}, \tag{2.20}$$

$$\text{andalusite} + 3\ \text{H}_2\text{O} \rightleftharpoons 2\ \text{diaspore} + \text{H}_4\text{SiO}_4\text{(aq)}, \tag{2.21}$$

and

$$\text{pyrophyllite} + 5\ \text{H}_2\text{O} \rightleftharpoons \text{andalusite} + 3\ \text{H}_4\text{SiO}_4\text{(aq)} \tag{2.22}$$

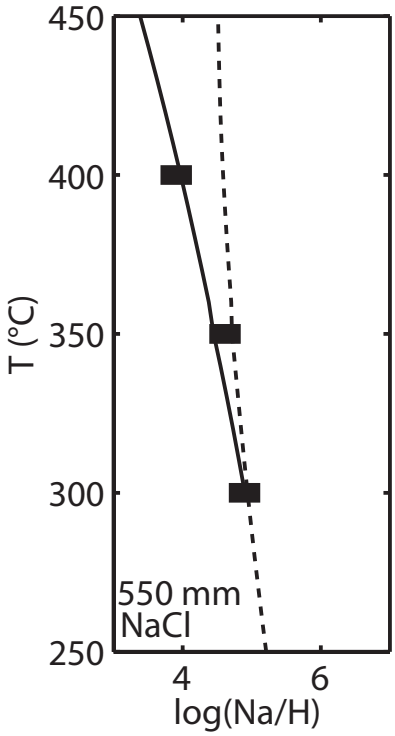

Figure 2.4: Equilibrium ratios of Na/H in fluids coexisting with albite, paragonite, and quartz measured by Saccocia and Seyfried (1994) at 500 bars and 3.2 wt% NaCl. The dashed line represents activity ratios calculated using the mineral thermodynamic data in Table 2.4 and the solid line represents calculations of Na_{tot}/H_{tot} based on the mineral data in Table 2.4 and aqueous complexing data for HCl, NaCl, and NaOH from Ho et al. (2001), Ho et al. (1994), and Ho and Palmer (1996), respectively.

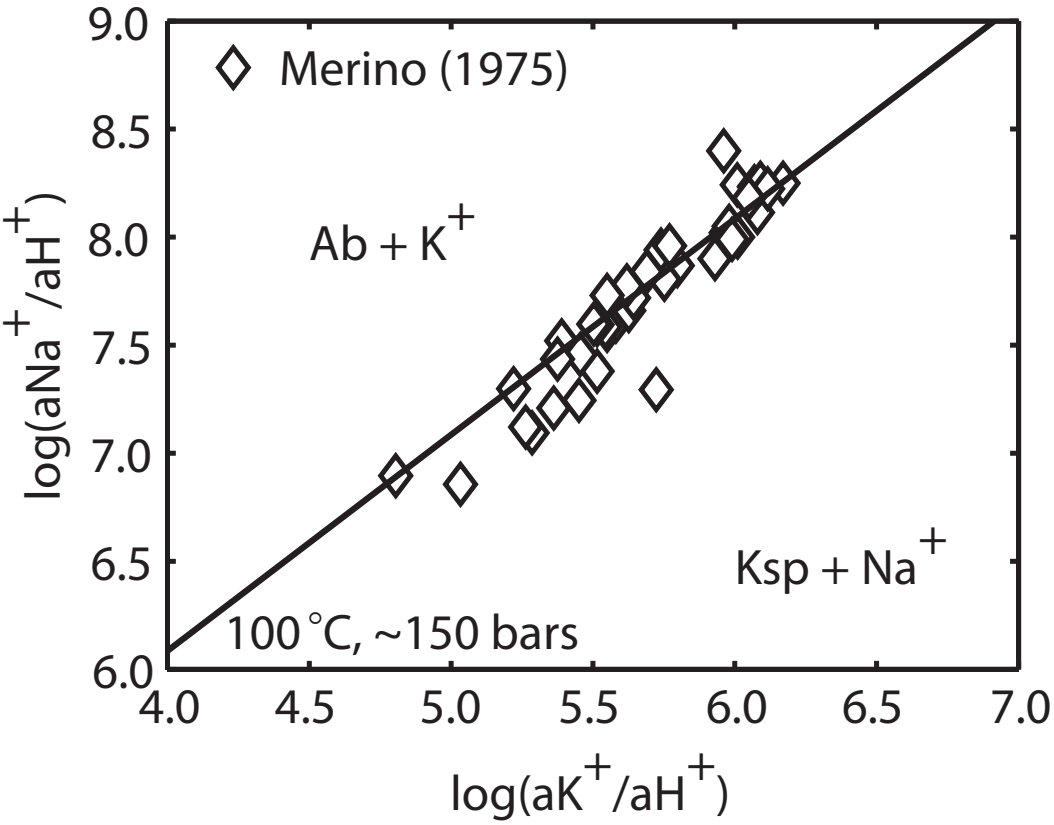

Figure 2.5: Na^+/K^+ ratios calculated using mineral thermodynamic data produced in this study compared with data presented by Merino (1975).

to constrain the relative properties of pyrophyllite, diaspore, kaolinite, and andalusite. For all of these reactions, Hemley et al. (1980) reported measurements at several T-P conditions. We have included all reported measurements in the least squares optimization using the method outlined for Reaction 2.12 above.

2.5.6 Important phases not included in the optimization: boehmite, gibbsite, dawsonite

Boehmite, gibbsite, and dawsonite may be important Al-bearing minerals in a range of geological settings (e.g., Apps et al., 1989; Kaszuba et al., 2011), but they were excluded from the reaction matrix because few accurate experimental measurements of phase equilibria exist to constrain their thermodynamic properties relative to other minerals examined in this study. Boehmite and gibbsite phase equilibria measurements are often questionable due to the metastability of Al hydroxides at

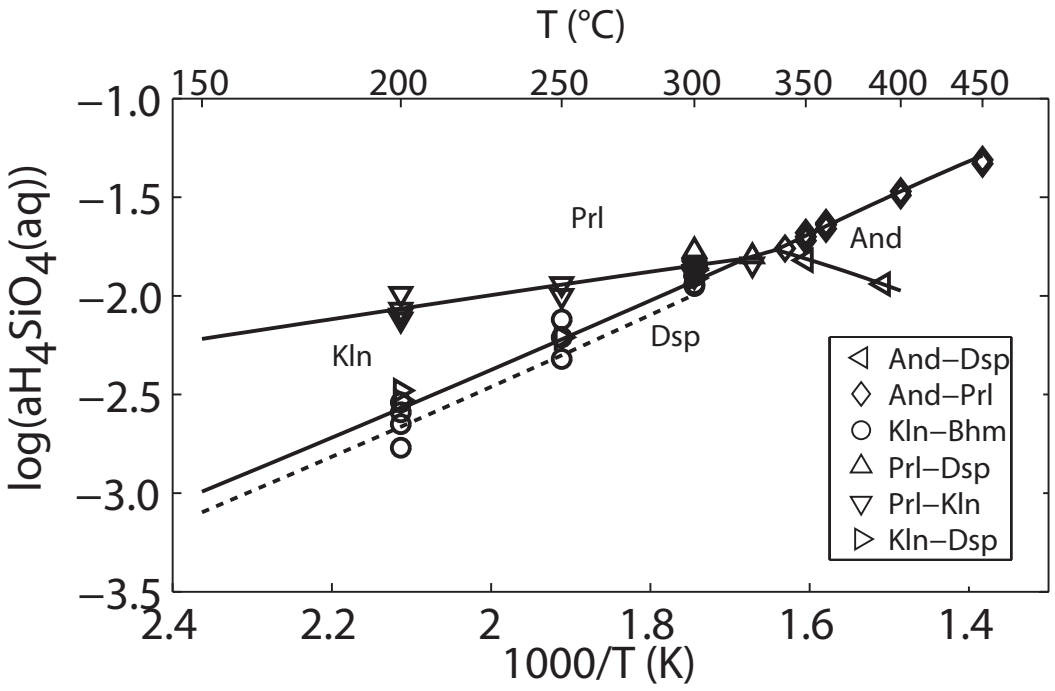

Figure 2.6: Mineral phase relations calculated from thermodynamic properties retrieved in this study are shown as lines (with the dashed line indicating the kaolinite-boehmite phase boundary). Experimentally determined values of equilibrium aqueous silica concentrations from Hemley et al. (1980) are shown as symbols.

various T and P (Kennedy, 1959; Hemley et al., 1980; Huang, 1993; Königsberger et al., 2011), and dawsonite has only recently begun to be studied in solubility experiments (Bénézeth et al., 2007; Hellevang et al., 2010). Furthermore, optimizing the thermodynamic properties of boehmite and gibbsite in the present study may have the unwanted consequence of producing mineral thermodynamic properties that are inconsistent with respect to the adopted Al aqueous speciation data set. Nonetheless, the respective thermodynamic properties of boehmite and gibbsite (Parks, 1972; Apps et al., 1988; Palmer and Wesolowski, 1992; Pokrovskii and Helgeson, 1995; Tagirov and Schott, 2001), and, to a lesser degree, dawsonite (Ferrante et al., 1976; Bénézeth et al., 2007) appear to be relatively well constrained (A). Because of the lack of phase equilibria, and the apparent agreement between calculations employing the values listed in Table 2.4 and experimental measurements, the inclusion of thermodynamic data for these three phases in the present study is justified. Dawsonite thermodynamic properties were taken from Bénézeth et al. (2007) and Ferrante et al. (1976), boehmite properties were taken from Robie and Hemingway (1995), and gibbsite thermodynamic properties were taken from Robie and Hemingway (1995) and Robie and Waldbaum (1968).

It is important to point out that, although reactions between boehmite and kaolinite reported by Hemley et al. (1980) were excluded from the solution of Eqn. 2.8, calculations performed using the accepted and derived data are still in excellent agreement with the experimental measurements (dashed line in Fig. 2.6). Moreover, the decision to accept the gibbsite and boehmite data directly from the literature does not appear to affect the internal consistency of the presented data set with respect to the Tagirov and Schott (2001) Al speciation data set, as exemplified by the agreement between calculated and measured kaolinite solubilities shown in Fig. 2.2.

2.6 Discussion

At its most basic level, the aluminum problem is truly a kaolinite problem, due to the improper reference state adopted by Helgeson et al. (1978) through Reaction 2.1 and the data shown in Fig. 2.1. By deriving and adopting thermodynamic data for 12 key Al minerals, including kaolinite, we have attempted to correct this longstanding problem. The ΔG_f° we derive for kaolinite is 2.3 kcal/mol more negative than that reported by Helgeson et al. (1978), and, compared to the data provided here, the Helgeson et al. (1978) kaolinite data predict equilibrium Al concentrations 6.75 times

higher at 25°C (Fig. 2.2). The Holland and Powell (2011) data set yields predictions in much better agreement with those derived in this study, at most 73% less soluble than our calculations. From this analysis, it is clear that use of the Helgeson et al. (1978) thermodynamic data will yield calculations of Al mass fluxes and mineral alteration that are at serious odds with experimental measurements. These significantly higher calculated solubilities likely persist across calculations performed with many of the Helgeson et al. (1978) Al minerals because of the improper reference state, and, therefore, continued use of their Al mineral data is discouraged.

2.6.1 Internal consistency in aqueous geochemical thermodynamic data

Interestingly, many of the phase equilibria adopted in this study to constrain the relative thermodynamic properties of the minerals (e.g., data plotted in Figs. 2.5 and 2.6) are *exactly the same* as those employed by Helgeson et al. (1978). Yet, the adoption of key Al reference values here has resulted in the derivation of dramatically different derived thermodynamic properties, which are more consistent with calculations of mineral solubilities. This conclusion–that calculations using a particular mineral thermodynamic data set can be in excellent agreement with measurements of mineral-mineral-fluid *phase equilibria* yet in substantial disagreement with measurements of mineral *solubilities*–is a key reason for adopting the methods and data developed in this study. Furthermore, as has been noted elsewhere, equilibrium is more easily demonstrated at higher temperatures, particularly with Al-bearing minerals, and higher temperature equilibrium measurements should be given preference over lower temperature measurements. Although we have only demonstrated this phenomenon for the mineral kaolinite, it is expected, based on the differing properties of much of the mineral thermodynamic data derived here, that such discrepancies pervade the Al system.

2.6.2 Estimated uncertainties on derived data

As shown in Figs. 2.2-2.6, agreement between solubility and phase equilbria calculations performed with thermodynamic properties accepted and derived in this study are in excellent agreement with a large number of experimental and field measurements. Because all equilibria included in the least squares optimization were

specifically related to measurements of fluid compositions, the presented method and data are specifically suited to aqueous geochemical applications. The values derived here are additionally in overall agreement with calorimetrically derived properties compiled by Robie and Hemingway (1995), as well as the feldspar solubility data set collected by Arnórsson and Stefánsson (1999). As was to be expected, the error on individual mineral phases is closely linked to the error reported for its accompanying phase relations. Some uncertainties, particularly those calculated by averaging and taking the standard deviations of reactions at a range of pressures, are much lower than those where only one experimental measurement was employed. Ideally, all of the reaction values could be made more certain by combining reactions in this way; however, it could become complicated if the mineral samples used within the experiments have differing states of order.

2.6.3 Implications for neutral species activity coefficients

Based on the analysis conducted in this contribution, it appears that phase equilibria, mineral thermodynamic data, and high-precision measurements of association constants can be used to constrain aqueous species activity coefficients. Fig. 2.3A shows some of the data we used to constrain the relative thermodynamic properties of the minerals exclusive of those of the aqueous species through Reactions 2.12, 2.14, and 2.16. The fact that the mineral thermodynamic data, which is in excellent agreement with the experimental measurements (Fig. 2.3A), is independent of the aqueous speciation model enables comparison between calculated and measured fluid compositions and examination of the effects of aqueous complex association constants on speciation calculations. The calculations of K_{tot}/H_{tot} in Figs. 2.3B and C differ quite significantly due to the difference between association constants calculated using equations consistent with recent high-precision conductivity measurements (Fig. 2.3B), and those derived and utilized by Sverjensky et al. (1991) (Fig. 2.3C). It appears that, at least for the specific 1 molal chloride system represented by the Sverjensky et al. (1991) data, the two sources of association constants can be brought into approximate mutual agreement using a simple density-activity coefficient relationship (Fig. 2.7), where the effective activity coefficient of the KCl component becomes increasingly greater than that of the HCl component with decreasing fluid density. Such behavior is not at all unrealistic, and differing neutral species-specific activity coefficients have long been acknowledged (Randall and Failey, 1927; Markham and Kobe, 1941;

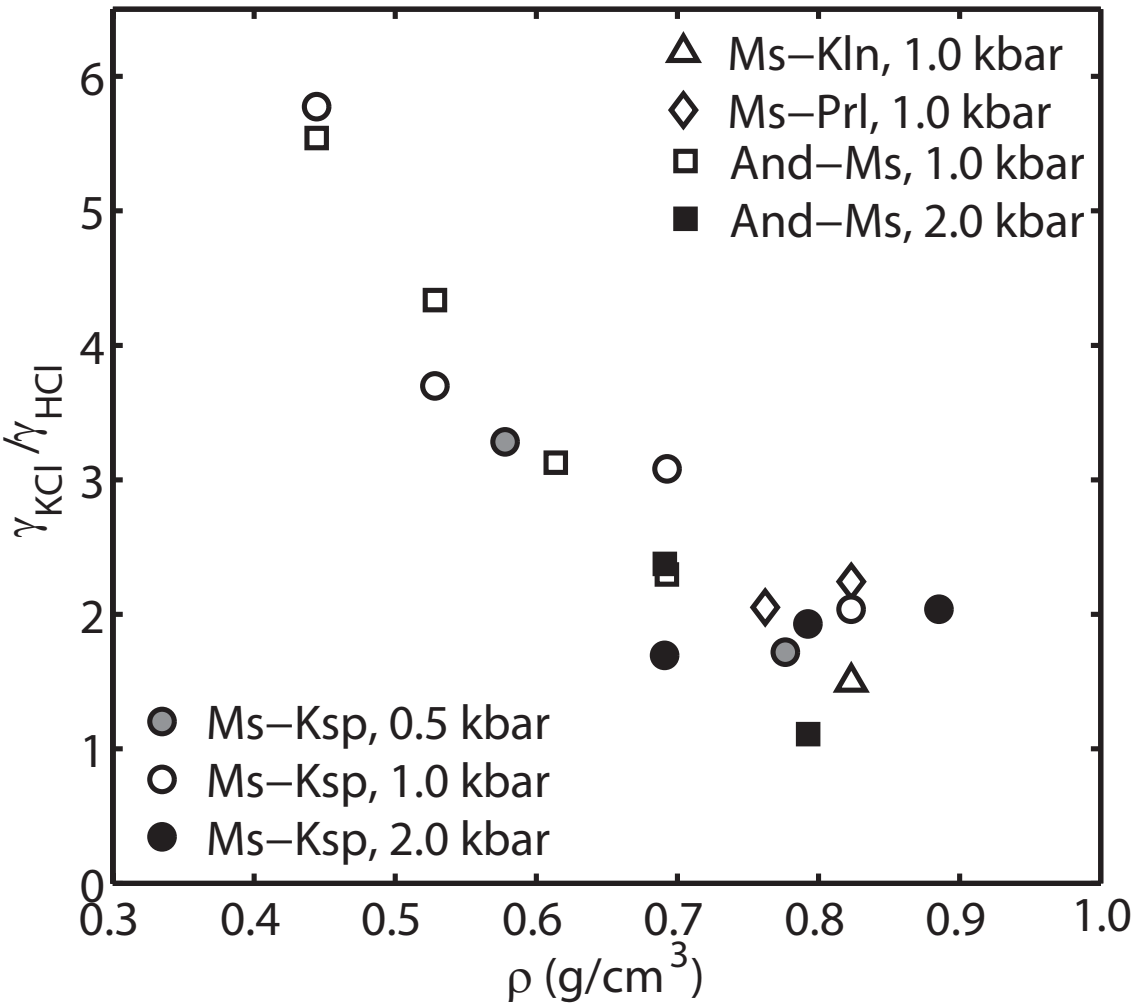

Figure 2.7: Ratio of the activity coefficients for the components KCl and HCl required to bring mineral solubilities calculated using high-precision conductance data for the aqueous species into agreement with the experimental measurements of Sverjensky et al. (1991).

Garrels and Christ, 1965; Drummond, 1981; Ding and Seyfried Jr., 1990; Oelkers and Helgeson, 1991; Pokrovskii and Helgeson, 1997), although calculations of neutral species activity coefficients in supercritical solutions remain uncertain (Oelkers and Helgeson, 1991; Seyfried et al., 1991).

Fig. 2.7 illustrates that a new model is required to simulate mineral solubilities and chemical speciation in supercritical H_2O. Although this development cannot be effectively resolved in the present contribution, we can discuss a few important notes, particularly regarding the HCl(aq) complex, which can dramatically affect the pH and hence speciation of supercritical fluids. Ho et al. (2001) presented high-precision conductance measurements of dilute (10^{-5}-10^{-3} molal) HCl solutions with densities from 0.27 to 0.96 g/cm^3 over the range 100 to 410°C, along with an equation calibrated using their presented data and that of Franck (1956) and Wright et al. (1961) to calculate the association of HCl(aq) to 600°C. Association constants calculated with this equation are in good agreement with most experimental results at densities >0.5 g/cm^3, but up to 2.5 log units lower than those measured by Frantz and Marshall (1984) or calculated using the equation of state parameters presented by Sverjensky et al. (1991) and Pokrovskii (1999) (Ho et al., 2001). The HCl(aq) dissociation constants presented by Sverjensky et al. (1991), on the other hand, were derived from high ionic strength fluids (Cl molality = 1) assuming that activity coefficients for all neutral species are unity, which, by definition, makes them "effective" association constants (Pokrovskii and Helgeson, 1997). Moreover, the Sverjensky et al. (1991) HCl(aq) association constants are only internally consistent with the association constants for KCl(aq) and KOH(aq) they use in their fluid speciation calculations. These observations may be able to explain the discrepancy between the Sverjensky et al. (1991) and Ho et al. (2001) association constants and hence the discrepancy between the calculations in Figs. 2.3A and B, but it implies that the Sverjensky et al. (1991) data is only specifically applicable to KCl system from which it was derived. Calculations of mineral solubilities in hydrothermal fluids with lower or higher ionic strengths (e.g., subseafloor, phase separated vapors and brines) require more general values of the association constants and the ability to calculate species-specific activity coefficients to adapt the data to the particular system. Figs. 2.3 and 2.7, along with the above discussion, illustrate one potentially promising method for developing such an activity model. This method, combined with a recently developed set of high-precision conductivity measurements of association constants (Ho et al., 1994;

Ho and Palmer, 1996, 1997; Ho et al., 2001) and new and existing measurements of mineral-fluid equilibria, may be able to provide the generality and accuracy required to improve our ability to model these systems.

2.6.4 Future Needs

It has been shown here (Figs. 2.1 and 2.2) and elsewhere (e.g., Freyer and Voigt, 2003) that measurements of low-T fluids coexisting with minerals rarely represent equilibrium with well-crystallized mineral phases . Therefore, it is important that low-T aqueous solubility data are not employed in the derivation of mineral thermodynamic properties. Instead, a great wealth of phase equilibria data at elevated T-P conditions exits, and this data can be confidently employed in the derivation of mineral and aqueous species thermodynamic data. In this regard, several experimental equilibria used in this study could be made more robust with the addition of new experimental results. Specifically, a systematic experimental approach to the "paragonite field" system similar to the contributions of Sverjensky et al. (1991) for the "muscovite field" system would improve the strength of the derived data for Na-bearing aluminosilicates. New experimental measurements in this system, as well as a systematic observation of mineral phase equilibria and aqueous speciation in supercritical fluids with a range of compositions can help in the examination of neutral species activity coefficients in concentrated supercritical solutions.

2.7 Conclusion

Ongoing aqueous geochemical research has shown the critical significance of accurate calculations of rock-forming mineral solubilities, which, in turn, form the foundation of models of kinetically controlled mineral-fluid reactions. These calculations require a thermodynamic data set that is internally consistent with respect to both minerals and aqueous species. In this contribution, we have exhibited a method for deriving internally consistent thermodynamic data with estimates of uncertainties from aqueous geochemical data. Because we exclusively employ measurements of fluids coexisting with minerals to constrain the derivation process, the method is optimized to produce data for aqueous geochemical applications. To illustrate this method, we have applied it to the aluminum system, which has had a long history of experimental and theoretical advances in the field of geochemistry. The

developed data set includes derived and adopted thermodynamic properties and uncertainties for 12 key aluminum-bearing mineral phases, which are consistent with calculations of thermodynamic properties for a large number of aqueous species (e.g., Na^+ and K^+ from Shock and Helgeson (1988), H_4SiO_4 from Stefánsson (2001), and Al species from Tagirov and Schott (2001)). Many of the constraining phase equilibrium measurements are *exactly the same* as those used to develop other thermodynamic data sets, yet our derived values tend to be quite different than theirs due to our choices of anchor phases from the literature. The differing absolute values of mineral thermodynamic properties can strongly affect the calculation of mineral solubilities. Specifically, we have demonstrated that kaolinite solubility predicted with the developed data set is more consistent with experimental measurements at $T > 50$ °C than two other popular data sets. The calculations and experimental data at $T \leq 25$ °C significantly disagree, however, which reiterates the assertion that low-T phase equilibria and mineral solubilities rarely represent equilibrium between water and well-crystallized Al-bearing mineral phases. By inference, the observed trends in calculations of kaolinite solubility should apply to calculations of the solubilities of many of the other Al minerals, due to the prevalence of kaolinite as a reaction mineral in phase equilibria experiments used to constrain internally consistent data sets. As an ancillary benefit of the derivation process, we have shown that our data set may be combined with high precision measurements of aqueous complex association constants to derive neutral species activity coefficients in supercritical fluids.

The methods and data developed in this study can form the foundation for a new standard in aqueous geochemical calculations. As we refine our models for aqueous speciation, mineral solubility, and phase equilibria in many earth systems, it is likely that discrepancies between mineral thermodynamic data and aqueous speciation models will continue to be discovered. For example, Bénézeth et al. (2013) have recently shown that geochemical simulators mispredict dolomite solubility in elevated T solutions. At the same time, Stefánsson et al. (2013) have begun to develop new thermodynamic data for carbonate speciation, which may hold the key to the resolution of this miscalculation. Thus, although the current contribution is specific to the aluminum system, the methods and concepts developed here can help to improve the calculation of water-rock interactions in a broad range of earth systems.

Chapter 3

Implications of the redissociation phenomenon for mineral-buffered fluids and aqueous species transport at elevated temperatures and pressures

3.1 Summary

Aqueous species equilibrium constants and activity models form the foundation of the complex speciation codes used to model the geochemistry of geothermal energy production, extremophilic ecosystems, ore deposition, and a variety of other processes. Recently, researchers have shown that a simple three species model (i.e., Na^+, Cl^-, and NaCl(aq)) can accurately describe conductivity measurements of concentrated NaCl and KCl solutions at elevated temperatures and pressures (Sharygin et al., 2002). In this model, activity coefficients of the charged species (e.g., Na^+, K^+, Cl^-) become sufficiently low that the complexes must redisocciate with increasing salt concentration in order to meet equilbrium constant constraints. Redissociation decreases the proportion of the elements bound up as neutral complexes, and thereby increases the true ionic strength of the solution. In this contribution, we explore the consequences of the redissociation phenomenon in albite-paragonite-quartz (APQ) buffered systems. We focus on the implications of the redissociation phenomenon on mineral solubilities, particularly the observation that, at certain temperatures and pressures, calculated *activities* of charged ions in solution remain practically constant even as element *concentrations* increase from <1 molal to 4.5 molal. Finally, we note that redissociation has a similar effect on pH, and therefore aqueous speciation, in APQ-hosted systems. The calculations and discussion presented here are not limited to APQ-hosted systems, but additionally apply to many others in which the dominant cations and anions can form neutral complexes.

3.2 Motivation

High-temperature hydrothermal systems embody many scientifically, societally, and economically important processes. These systems can host a variety of extremophilic organisms (Jørgensen and Boetius, 2007); are proposed to be exploited for both CO_2- and water-based geothermal energy (Barbier, 2002; Fridleifsson and Elders, 2005; Pruess, 2006; Randolph and Saar, 2011a); and concentrate significant amounts of valuable metals (Simmons and Browne, 2000; Yardley, 2005; Williams-Jones and Heinrich, 2005; Williams-Jones et al., 2012). The aqueous fluids involved in these processes generally contain chlorine as their dominant anion, and many common cations tend to form charged and/or neutral complexes with chlorine at elevated temperatures and pressures. Because cation-chloride complexing tends to increase the solubility of minerals and elements in geological fluids, it is one of the most fundamental processes controlling mass transfer in high temperature hydrothermal systems (e.g., Helgeson, 1964; Quist and Marshall, 1968; Helgeson, 1969; Gunter and Eugster, 1980; Helgeson, 1992; Sverjensky et al., 1997; Ho et al., 1994; Ho and Palmer, 1997; Ho et al., 2001; Yardley and Bodnar, 2014, and sources therein).

One of the most striking examples of the importance of cation-chloride complexing in geologic systems is the control that complex formation exerts on solution pH. Measurements of in situ pH in seafloor hydrothermal vents on the Juan de Fuca Ridge and East Pacific Rise indicate "near-neutral" values of 4.35-5.4, but measurements of the pH of these fluids at ambient temperatures indicate much more acidic fluids, in the range of 3.2-3.9 (Ding et al., 2005). The difference between these in situ and ambient values (up to 2 orders of magnitude in the activity of H^+) can be attributed almost entirely to the complete dissociation of the HCl(aq) complex at ambient temperature. The fact that the in situ values are only weakly acidic places constraints on mineral solubilities and elemental speciation and fluxes through these systems. In turn, these effects play a role in the formation of ore deposits (Reed, 1997; Yardley and Bodnar, 2014) and development of diverse, geologically-fueled ecosystems (Jørgensen and Boetius, 2007).

3.3 Background

3.3.1 Ionic strength and cation-chloride complexing

Because of their ability to regulate mineral and gas solubility and transport processes in a wide range of geological solutions, the association constants of certain chloride complexes (e.g., NaCl, KCl, HCl) and their activity coefficients and those of their constituent ions have been extensively studied (Quist and Marshall, 1968; Helgeson, 1969; Helgeson et al., 1981; Frantz and Marshall, 1984; Pitzer and Pabalan, 1986; Pabalan and Pitzer, 1987; Sverjensky et al., 1991; Archer, 1992; Oelkers and Helgeson, 1993a,b; Pokrovskii and Helgeson, 1997; Ho and Palmer, 1997; Tagirov et al., 1997; Pokrovskii, 1999; Ho et al., 2001; Sharygin et al., 2002; Zimmerman et al., 2012; Tutolo et al., 2014a). Commonly, chloride complex association constants are obtained using conductance measurements in static or flow-through cells (e.g., Quist and Marshall, 1968; Frantz and Marshall, 1984; Ho and Palmer, 1997; Ho et al., 2001; Sharygin et al., 2002; Zimmerman et al., 2012), although some researchers have attempted to use mineral-fluid equilibria to extract association constants and activity coefficients from supercritical solutions (e.g., Frantz and Popp, 1979; Gunter and Eugster, 1978; Popp and Frantz, 1979, 1980; Sverjensky et al., 1991; Xie and Walther, 1993; Aranovich and Newton, 1996, 1997; Walther, 1997; Tutolo et al., 2014a). Overall, measurements and calculations indicate substantial association of the chloride complexes at elevated temperature, although the degree to which these complexes form is dependent upon the temperature and pressure and concentration of the solution.

Ionic strength is the measure of the amount of charged solutes dissolved in a solvent. There are two methods for calculating ionic strength: "stoichiometric ionic strength", I, which assumes that all complexes in solution are completely dissociated, and "true ionic strength", $\bar{I}$, which takes speciation and complex association into account. $\bar{I}$ is calculated according to:

$$\bar{I} = \frac{1}{2} \sum_i m_i z_i^2, \tag{3.1}$$

where m_i and z_i are the molality and charge, respectively, of the i^{th} charged species. Because the formation of neutral chloride complexes tends to decrease the number of charged species in solution, $\bar{I}$ is typically considerably smaller than I. Importantly,

however, calculations and experimental measurements indicate that, at certain temperatures and pressures, $\bar{I}$ actually begins to increase relative to I with increasing NaCl molality such that the two can become nearly equivalent.

3.3.2 Modeling the aqueous speciation of cation-chloride complexes

Extensive effort has been devoted towards developing and utilizing thermodynamic models to understand and predict the behavior of cation-chloride complexing at elevated temperatures and pressures. The goal of these models is to utilize a simplistic microscopic description to capture important macroscopic phenomena, such as the effects of cation-chloride interactions on solution pH, ionic strength, fluid density, and boiling and freezing points. In the case of the NaCl(aq) system, there are an infinite number of individual species that may exist in solution at the molecular scale (e.g., NaCl(aq), Na^+, Cl^-, Na_2Cl^+, $NaCl_2^-$, ...), but it is both impractical and unnecessary to produce measurements and thermodynamic descriptions of the behavior of each of these individual species. Indeed, researchers have shown that the behavior of NaCl in solution can be accurately modeled at many commonly encountered temperatures, pressures, and NaCl concentrations using only three species (NaCl(aq), Na^+, and Cl^-) and an appropriate activity model. Thus, thermodynamic models are a "useful fiction" in this regard, because, although they may not necessarily capture the molecular-scale phenomena occurring in a system, they can be calibrated to reproduce and accurately predict processes occurring in natural systems.

Although they have been studied in extensive detail, several aspects of the thermodynamics of chloride complex association remain uncertain. One specific example relates to the neutral and charged species activity model and the number of species that need to be included in the model in order to capture the relevant processes. Based upon examination of a large volume of experimental conductance data, Oelkers and Helgeson proposed, in the early 1990s, a model for cation-chloride complexes at elevated temperatures and pressures that involved substantial activity coefficients of the neutral complex and formation of polynuclear and triple ion complexes (e.g., Na_2Cl^+, $NaCl_2^-$) (Oelkers and Helgeson, 1990, 1991, 1993a,b). Additionally, Driesner et al. (1998) presented molecular dynamics simulation results that support the extensive multi-ion clustering proposed by Oelkers and Helgeson. In the latter case, the authors note that their study is somewhat preliminary, and Sharygin et al. (2002)

have pointed out that the modeling results hinge on potentially uncertain parameters. Furthermore, it is important to note that the Oelkers and Helgeson analysis was based upon data obtained at chloride molalities <0.1 molal, and therefore calculations at higher ionic strengths had to be based upon model extrapolations.

The advent of field and experimental devices for measuring the in situ speciation and pH of hydrothermal solutions has increasingly provided the requisite data for discerning the thermodynamics of chloride complexes at elevated temperatures, pressures, and concentrations. A more recent reexamination of the Oelkers and Helgeson model by Sharygin et al. (2002) indicates that the observed phenomena can potentially be explained using a simpler model than that suggested by Oelkers and Helgeson. Notably, Sharygin et al. (2002) suggest that: a) based upon statistical mechanical calculations, the high neutral chloride complex activity coefficients proposed by Oelkers and Helgeson (1991) yield distances of closest approach that are physically unrealistic, and b) the Oelkers and Helgeson speciation model involving a number of multi-ion complexes cannot match their (Sharygin et al., 2002) conductance measurements of NaCl and KCl solutions up to 4.5 molal without the use of the unphysically large salting out coefficients. Based on this analysis, they suggest that the activity coefficient of the neutral complex can be assumed equal to 1 and a simple speciation model involving only Na^+, Cl^-, and NaCl(aq) can fit the measurements within the experimental uncertainty, except in solutions with exceptionally low dielectric constants. Their proposed speciation model uses the extended Debye-Hückel equation (Helgeson et al., 1981) with extended parameters calculated using the revised Helgeson-Kirkham-Flowers (HKF) equation of state (Tanger and Helgeson, 1988) by Oelkers and Helgeson (1990) to calculate the charged species (Na^+, K^+, Cl^-) activity coefficients.

At certain temperatures and pressures, this aqueous speciation model calculates low charged species activity coefficients, which, combined with constraints placed upon the fluid by aqueous species association constants, yields an increasing degree of redissociation of the chloride complexes with increasing chloride molalities. Sharygin et al. (2002) show that their model is able to fit their conductivity measurements with a high degree of accuracy for all but one of their measurements, which was obtained at an extreme condition where the fluid was very close to phase separation behavior (397°C, 280 bar) and the solute interactions are calculated to be the strongest. The overall agreement of their proposed model with their experimental data indicates that

it has robust capacity for calculating charged species activity coefficients and fluid speciation over a wide range of conditions. Nonetheless, the effects of redissociation processes on geochemical fluxes have not been thoroughly examined, likely because of the historical uncertainty surrounding their occurrence. Here, we attempt to stimulate thought and continued experimental study by producing calculations and hypotheses that explore the consequences of redissociation in geological systems.

3.4 Methods

3.4.1 Aqueous Speciation

Sharygin et al. (2002) only reported association constants at a number of discrete points and did not produce a parameterization for extrapolating their measurements to other conditions. Nonetheless, their reported association constants are in good agreement with those calculated according to the Ho et al. (1994) density model, suggesting that the latter (which was calibrated using considerably more dilute solutions) has robust calculation capabilities. Therefore, we use the Ho et al. (1994) model to calculate NaCl association constants in the present study. Density is calculated using a Matlab implementation (Junglas, 2009) of the IAPWS-95 formulation (Wagner and Pruss, 2002). Additionally, although their effects are minor compared with those of NaCl association, the association constants of water and HCl(aq) are calculated according to Marshall and Franck (1981) and Ho et al. (2001), respectively. Mineral hydrolysis constants are calculated according to the Tutolo et al. (2014a) thermodynamic data set. Where required, speciation calculations are performed using a Matlab implementation of the EQBRM package (Anderson and Crerar, 1993).

3.4.2 Activity coefficients of charged aqueous species

Activity coefficients are typically utilized to account for departures from the thermodynamic reference state resulting from increasing ionic strength of the solvent. The activity coefficient of an aqueous species, γ_i, may be defined as:

$$\gamma_i = \frac{a_i}{m_i}, \tag{3.2}$$

where a_i and m_i are its activity and molality, respectively. Two main types of models exist for calculating activities of solutes in geological fluids: "Pitzer-style" formulations, which are based on specific ion interaction approaches (e.g., Pitzer, 1973; Harvie et al., 1984), and formulations based on Debye-Hückel theory and its extensions (e.g., Helgeson, 1969; Helgeson et al., 1981). Both styles of models have their limitations, but, generally, "Pitzer-style" formulations are better suited to the calculation of ion activities in concentrated electrolyte solutions. Nonetheless, the "Pitzer-style" models are typically characterized by their complexity, and large amounts of data are required for their implementation. Due to the relative lack of the requisite data to parameterize "Pitzer-style" models at elevated temperatures and pressures, their applications in geochemical modeling are generally limited to near-ambient conditions (e.g., Harvie et al., 1984; Møller, 1988; Duan and Sun, 2003; Zhang et al., 2006).

Thus, because of its generality and versatility, many geochemical models utilize the extended Debye-Hückel equation to calculate the activity coefficients of charged aqueous species. The mean ionic activity coefficient[1] of a charged ion in an electrolyte solution, $\gamma^*_\pm$, can be approximated according to Helgeson et al. (1981):

$$\log \gamma^*_\pm = -\frac{z_i^2 A_\gamma \bar{I}^{1/2}}{1 + \mathring{a} B_\gamma \bar{I}^{1/2}} + b_{\gamma,i}\bar{I} + \Gamma_\gamma, \tag{3.3}$$

where z_i is the charge of the i^{th} electrolyte, $\mathring{a}$ is the ion size parameter for the solution, Γ_γ is mole fraction to molality conversion factor:

$$\Gamma_\gamma = -\log(1 + 0.180153 m^*), \tag{3.4}$$

where m^* is the sum of molalities of all species in solution, A_γ and B_γ are T-, P-specific constants, and $\mathrm{b}_{\gamma,i}$ is an electrolyte-specific "extended term parameter". Values of A_γ and B_γ can be calculated according to (Helgeson and Kirkham, 1974):

$$A_\gamma \equiv \frac{(2\pi N)^{1/2} e^3 \rho^{1/2}}{\ln(10)(1000)^{1/2}(\epsilon k T)^{3/2}} = \frac{1.825 \times 10^6 \rho^{1/2}}{(\epsilon T)^{3/2}}, \tag{3.5}$$

and

$$B_\gamma \equiv \left(\frac{8\pi N \rho e^2}{1000 \epsilon k T}\right)^{1/2} = \frac{5.029 \times 10^9 \rho^{1/2}}{(\epsilon T)^{1/2}}, \tag{3.6}$$

[1] The "mean" ionic activity coefficient represents the activity coefficients of all charged species in the NaCl solutions considered here (Helgeson et al., 1981; Oelkers and Helgeson, 1990). In mixed electrolytes, other forms of this equation must be employed (Helgeson et al., 1981).

where N is Avogadro's number, e is the absolute electron charge, k is the Boltzmann constant, and ρ and ϵ are the density and dielectric constant of pure water, respectively, at the T and P of the calculation. Here, values of ϵ are calculated according to equations Johnson and Norton (1991) implemented in SUPCRT92, and the ion size parameter is calculated according to the HKF equation of state (Oelkers and Helgeson, 1990; Shock et al., 1992). For NaCl solutions, $\mathring{a}$ is calculated as the sum of the effective electrostatic radii of Na^+ and Cl^-, which can be calculated according to equations and parameters presented by Shock et al. (1992). At most pressures, values of the electrostatic radii of both Na^+ and Cl^- in liquid water remain constant to at least 300°C, and therefore $\mathring{a}$ differs negligibly from 3.72 Å at these conditions (Shock et al., 1992). Nonetheless, $\mathring{a}$ does deviate slightly from this value at some of the conditions considered here (Shock et al., 1992), and we have therefore included a provision to calculate its value using the HKF equation of state here.

Due to the high probability that most geologic solutions contain NaCl as the dominant electrolyte, $b_{\gamma,i}$ is often taken equal to $b_{\gamma,NaCl}$. Versions of Eq. 3.3 for NaCl solutions have been parameterized by several researchers. For example, Helgeson (1969) utilized a simplified version of Eq. 3.3) in which Γ_γ was assumed to be equal to 0 to calculate activity coefficients of charged aqueous species. Helgeson (1969) calculated values of $b_{\gamma,i}$ from 0-300°C based upon data and extrapolations and the assumption that γ for NaCl(aq) could be taken as equal to values of γ calculated from experimental measurements of CO_2 solubility in NaCl solutions (thus putting it at odds with the Sharygin et al. (2002) model). Helgeson (1969) suggested that solutions deviate negligibly from Debye-Hückel theory at T>300°C and that $b_{\gamma,i}$ should therefore be set to 0. Values of $b_{\gamma,NaCl}$ over the entire range of applicability of the HKF were later recalculated by Helgeson et al. (1981) using a full implementation of Eq. 3.3. More recently, Oelkers and Helgeson (1990) recalculated values of $b_{\gamma,NaCl}$ to reflect revisions to the HKF equation of state (Tanger and Helgeson, 1988; Shock et al., 1992). A validation of the implementation of our activity coefficient model is included in Appendix B. In this study, we employ Eq. 3.3 with $b_{\gamma,NaCl}$ values presented by Oelkers and Helgeson (1990) parameters for all relevant calculations.

3.5 Implications of neutral complex redissociation for mineral solubilities

3.5.1 Aqueous chemistry of mineral-buffered systems

The redissociation phenomenon can affect the evolution of water-rock-gas interactions and elemental fluxes in a variety of geologic settings. One important example (and the one that we will rely upon here) involves silicate-fluid interactions, which are ubiquitous throughout Earth's crust and upper mantle. Geologic formations containing felsic mineral assemblages such as those plotted in Fig. 3.1 (i.e., alkali feldspar-mica-quartz) host a plethora of geothermal energy and hydrothermal ore deposition systems (e.g., Hemley, 1959; Hemley and Jones, 1964; Montoya and Hemley, 1975; Merino, 1975; Giggenbach, 1988; Sverjensky et al., 1991; Yardley and Bodnar, 2014). When these assemblages interact with chloride brines, Na^+ and K^+ are the dominant cations and Cl^- is the dominant anion. Based on charge balance constraints, therefore, $Na^+ + K^+ = Cl^-$, and the total solubility of the alkali feldspar-mica-quartz assemblage is fixed by the chlorinity of the fluid. Furthermore, dependent upon the equilibrium mineralogical assemblage, the ratio of the activities of Na^+ and/or K^+ relative to the activity of H^+ will be fixed by the equilibrium constants forming the boundaries of the stability fields in Fig. 3.1. Thus, because the equilibrium constant is fixed by the temperature and pressure conditions, the pH should decrease with increasing Cl concentration. Furthermore, because pH fixes the speciation and fluxes of many of the more minor solutes, this combined chlorinity-activity constraint plays an important role in the fluxes of elements through many geological systems.

3.5.2 An example: the albite-paragonite-quartz system

Importantly, the "chlorinity constraint" discussed above fixes Na and K *concentrations*, but the "equilibrium constant constraint" fixes Na^+, K^+, and H^+ *activities*. The difference between these values is affected not only by the departures from ideality resulting from the elevated ionic strength of the solution (accounted for by activity coefficients), but also by the degree of association of neutral ion pairs. As redissociation processes increasingly dominate the speciation of the system, the activity of Na^+ becomes increasingly independent of the NaCl concentration. In other words, at certain temperatures and pressures, the activity of Na^+ remains virtually constant,

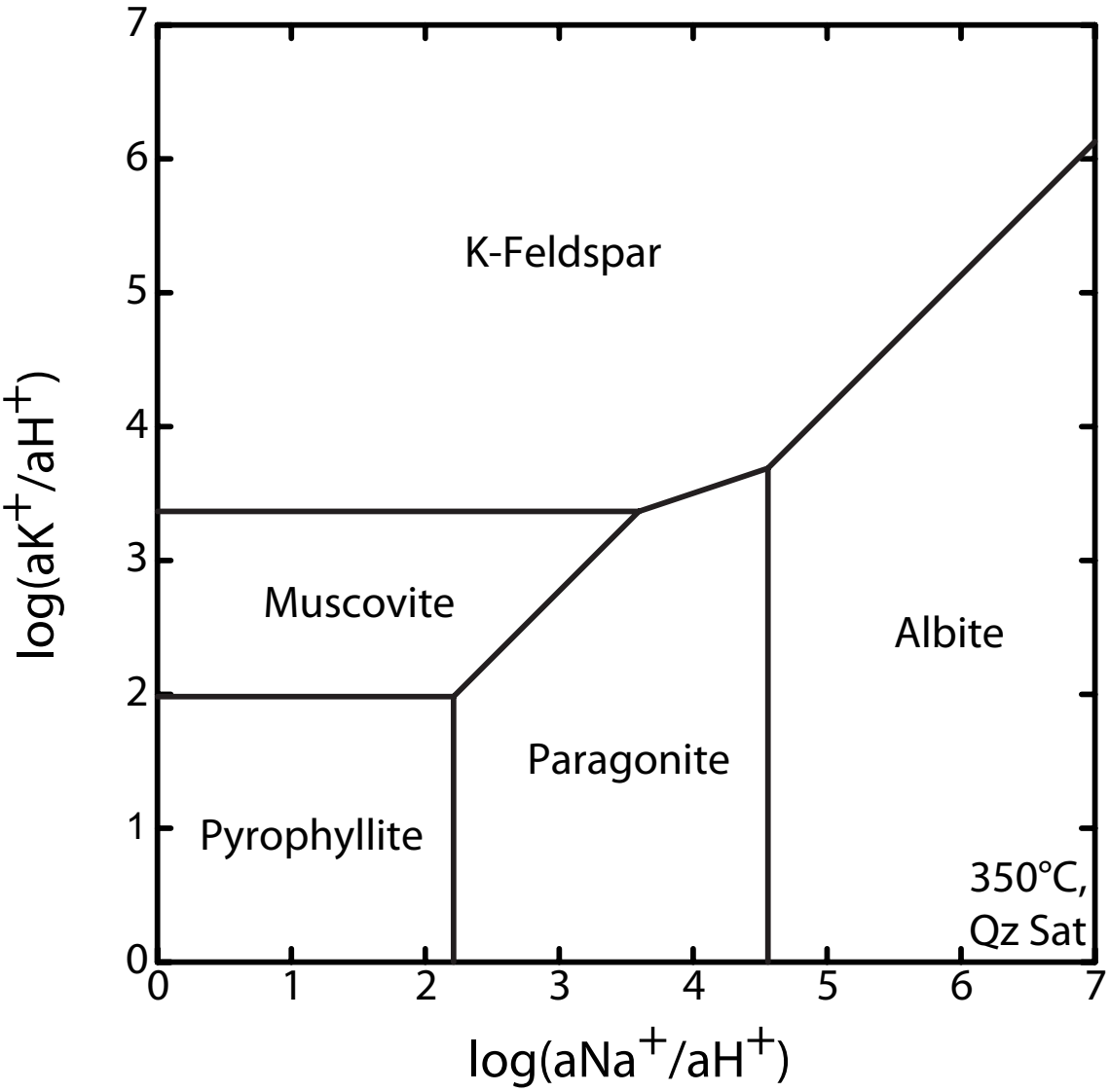

Figure 3.1: Activity diagram showing silicate mineral buffering of fluid compositions at 350°C and steam saturation pressure, calculated using the thermodynamic data set presented by Tutolo et al. (2014a).

even when the Na molality is greatly increased. We can examine the temperature and pressure conditions at which this behavior will occur by using the example of the albite-paragonite-quartz equilibrium:

$$1.5 \text{ albite} + \text{H}^+ \rightleftharpoons 0.5 \text{ paragonite} + 3 \text{ quartz} + \text{ Na}^+, \tag{3.7}$$

which is not only a common fluid-buffering assemblage in the field but is also commonly employed to fix pH in hydrothermal experiments (e.g., Woodland and Walther, 1987; Saccocia and Seyfried, 1994; Tagirov et al., 2002). The fact that this reaction may be metastable at some of the conditions examined here is irrelevant for the purposes of the present discussion; we could have just as easily used any reaction represented in Fig. 3.1 to portray these phenomena.

In order to exhibit the redissociation phenomenon, we calculate the fraction of NaCl in solution present as neutral complexes, $\alpha_{\text{NaCl(aq)}}$, according to:

$$\alpha \equiv \frac{m_{\text{NaCl(aq)}}}{m_{\text{NaCl,tot}}}, \tag{3.8}$$

where $m_{\text{NaCl(aq)}}$ is the calculated molality of the neutral complex and $m_{\text{NaCl,tot}}$ is the total NaCl molality. Accordingly, the fraction of NaCl in solution that does not exist as a charged species is equivalent to one minus α. At steam saturation pressures and NaCl concentrations from 0-4.5 molal (the limit of the Sharygin et al. (2002) measurements), the redissociation phenomenon is only evident (i.e., α peaks and begins to decline within our modeled range of concentrations) at temperatures greater than $\sim$300°C (Fig. 3.2a). However, at 1 kbar pressure and those same NaCl molalities, redissociation processes begin to dominate NaCl speciation at significantly higher temperatures, greater than $\sim$400°C. Furthermore, below these temperature cutoffs in both scenarios, the molality of Na^+ in solution increases with a near-constant slope with increasing NaCl molality. However, above this temperature, the calculated Na^+ molalities demonstrate increasingly positive slopes with increasing NaCl molality, with higher temperatures exhibiting more dramatic slope increases (Fig. 3.3a,b). Unlike their molalities, the activities of Na^+ and Cl^- remain linear with increasing NaCl molality at all modeled temperatures and pressures. This behavior results from the constraints placed upon the activities of these individual ions by the equilibrium constant for NaCl association, which is only a function of temperature and pressure,

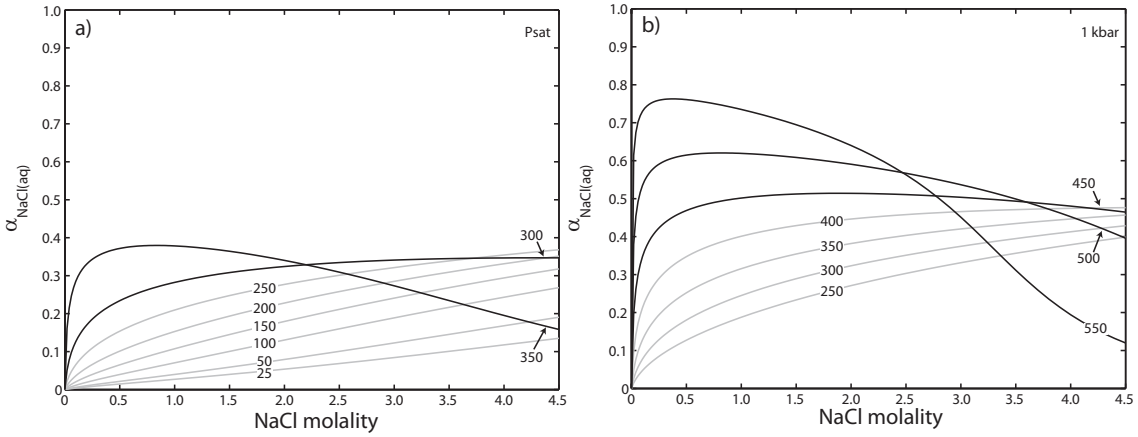

Figure 3.2: Fraction of total NaCl in solution present as NaCl(aq) (α, see Eq. 3.8) in 0-4.5 molal NaCl solutions at: a) 25°C-350°C and pressures along the steam saturation curve, and b) 250-550°C and 1 kbar. Lines colors represent temperature and pressure conditions where redissociation does (black) or does not (gray) occur.

and not NaCl concentration. Importantly, in the solutions where significant redissociation is calculated to occur, the activities of these ions remain virtually constant with increasing NaCl molality.

The calculations presented in Figs. 3.2 and 3.3 demonstrate that the redissociation phenomenon is a result of the competing effects of activity coefficient decreases and molality increases. The high NaCl molalities, combined with the fact that a larger proportion of the total NaCl in solution is present as the charged ions Na^+ and Cl^-, lead to elevated values of $\bar{I}$ and therefore lower values of the activity coefficient (Eq. 3.3). Nonetheless, it is additionally apparent that the redissociation phenomenon is not only tied to the salinity of the fluid, but also closely linked to both temperature and pressure (Figs. 3.2 and 3.3). Based on the experimental observations of Sharygin et al. (2002) and the calculations performed here, redissociation predominantly occurs in solutions with relatively low densities and dielectric constants. As these values decrease, the salinity at which the fluid begins to demonstrate redissociation behavior also becomes lower, such that, at 350°C and steam saturated pressure, where the density of pure water is 0.57 g/cm^3, redissociation begins to occur at ∼0.5 molal NaCl (Fig. 3.2a). However, at 1 kbar, the redissociation phenomenon does not occur in 0-4.5 molal NaCl solutions at this same temperature (Fig. 3.2b). At 1 kbar and 550°C, where the density of pure water is 0.44 g/cm^3 however, solutions under 0.5 molal NaCl are very strongly associated and become increasingly dissociated with

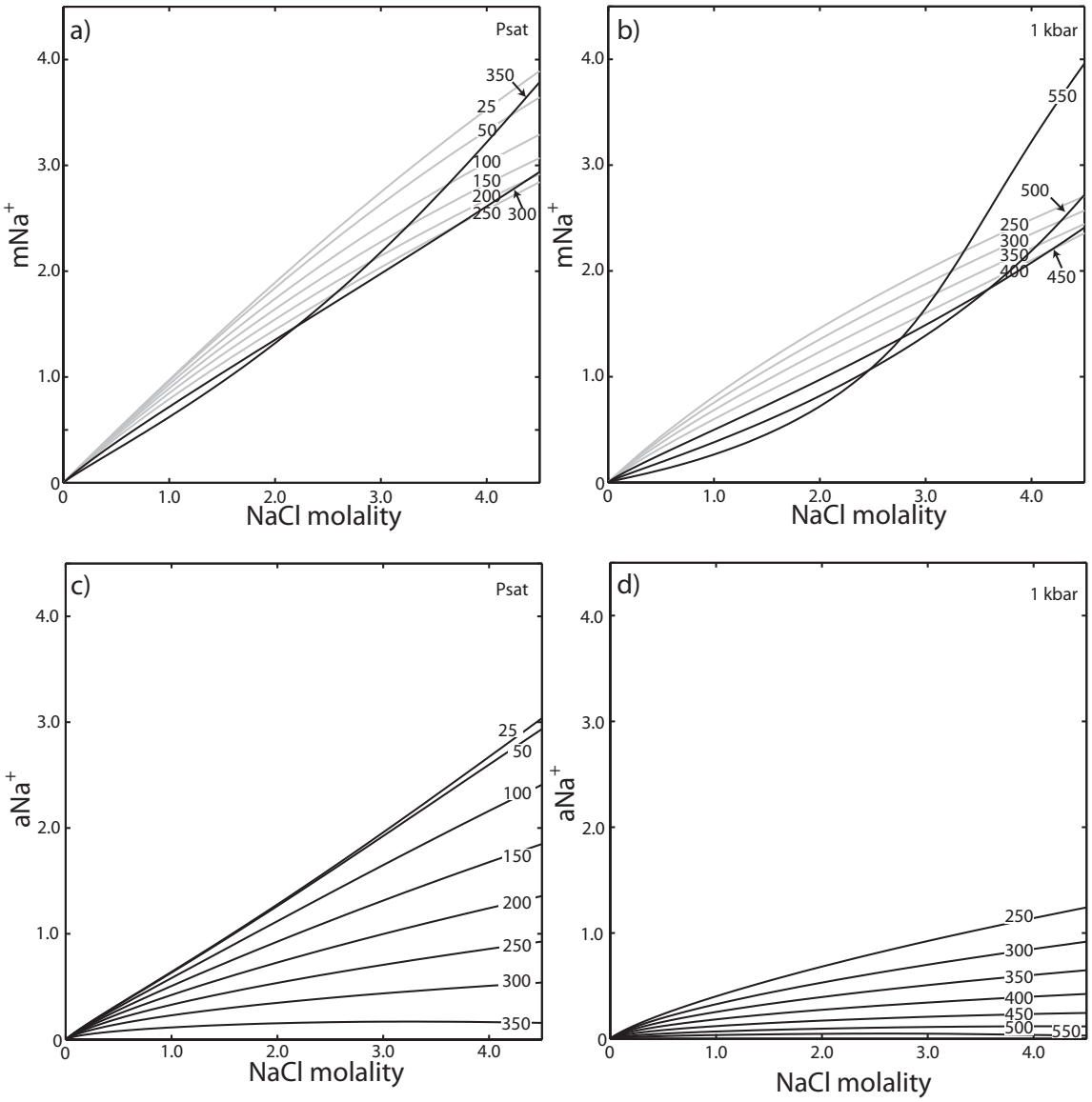

Figure 3.3: Molality (a,b) and activity (c,d) of Na^+ in 0-4.5 molal NaCl solutions up to 350°C at steam saturation pressures calculated using the speciation model discussed in Section 3.4. The panels on the left side (a,c) illustrate calculations performed at 25°C-350°C at pressures along the steam saturation curve, and the panels on the right side (b,d) illustrate calculations performed at 250-550°C at 1 kbar.

increasing NaCl concentration.

If we now assume, as discussed above, that the fluids plotted in Figs. 3.2 and 3.3 are in equilibrium with the mineral assemblage represented by Reaction 3.7, we can examine how the pH may vary as a function of salinity at these temperatures and pressures. As may be expected from a direct relationship between NaCl concentration and fluid pH, fluids at relatively low temperatures generally decrease in pH as salinity increases (Fig. 3.4). This style of behavior occurs in fluids at steam saturated pressures and temperatures up to ∼250°C, and in fluids at 1 kbar at temperatures up to ∼400°C. However, at elevated temperatures, where redissociation begins to have a major effect on the fluid speciation, the increasing salinity has very little, and, for the most part, immeasurable effect on pH, even as NaCl molality increases from <0.25 to 4.5 molal NaCl.

The concept that solutions with cation-chloride concentrations up to (and likely greater than) 4.5 molal can have approximately the same activity of their dominant cation, and, in our example, pH, as a solution containing <1 molal of the same elements (Fig. 3.3) is counter-intuitive if redissociation processes are not considered. These calculations suggest that solutions existing along any of the mineral-mineral boundaries in Fig. 3.1 can have concentrations of [Na + K] and Cl anywhere over the range from <1 to >4.5 molal and still have virtually the same pH. These calculations therefore suggest that, in instances where substantial redissociation is calculated to occur, the solubility of the aluminosilicate assemblages plotted in Fig. 3.1 and others is, indeed, dependent upon the concentration of the Cl ligand, but pH is not. Thus, in situations where a phase-separated vapor and brine equilibrate with an equivalent mineral assemblage at temperatures and pressures where redissociation is calculated to occur, it is likely that both fluids will have equivalent pH. This has implications for the chemistry of fluids sampled at seafloor hydrothermal vents (e.g., Ding et al., 2005; Pester et al., 2014) as well as in active geothermal systems (e.g., Reed, 1997; Simmons and Browne, 2000).

3.5.3 Extension to other systems and trace element transport

Although we have specifically focused on the albite-paragonite-quartz equilibrium, it is likely that analogous considerations apply to the K-feldspar-muscovite-quartz system and many others in which redissociation can affect the speciation of the dominant

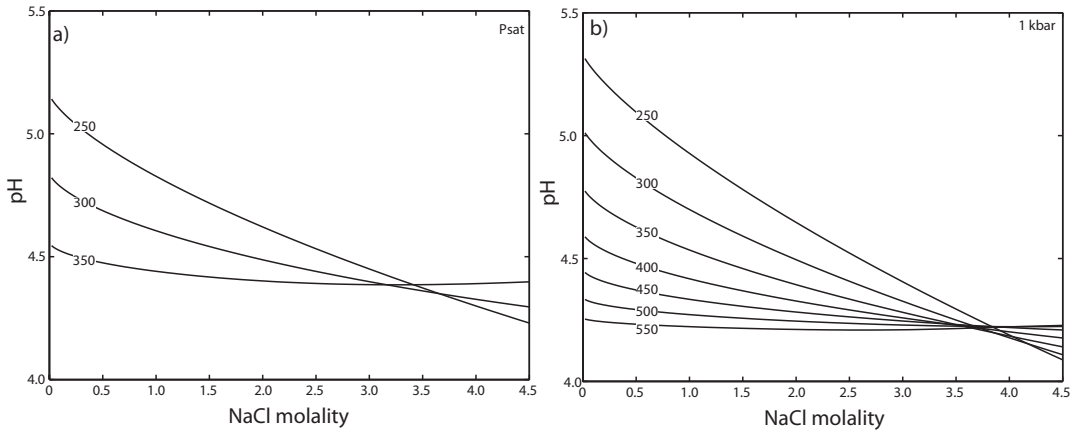

Figure 3.4: Calculated pH in equilibrium with an albite-paragonite-quartz assemblage (Reaction 3.7) in 0-4.5 molal NaCl solutions at: a) 250-350°C and steam saturation pressures, and b) 250-550°C and 1 kbar.

cations and anions in solution. Furthermore, the speciation of many geologically important trace elements, such as Al and B, is strongly pH-dependent. Therefore, the considerations discussed above regarding the pH-independent nature of redissociated solutions can affect the transport and flux of these elements in geological environments.

3.6 Uncertainties and future work

Although the redissociation phenomenon has a number of important implications for describing elemental fluxes through geologic systems, its effects and applicability vary depending on the temperature and pressure conditions of the system. It must therefore be emphasized that the results reported here are dependent upon the accuracy of the model that we have employed. The experimental measurements of Sharygin et al. (2002) show that this model can effectively match the conductivities that they have observed experimentally. However, they also provide measurements at temperature and pressure conditions where the model employed here cannot account for the behavior of the solution. Considering that Sharygin et al. (2002) made this observation based upon conductivity measurements of solutions with up to 1.0 molal NaCl at 397°C, 280 bar, where the density and dielectric constant of water are calculated to be 0.3 g/cm^3 and $\sim$5, respectively, indicates that some relationship between density, dielectric constant, and model applicability must exist. Tutolo et al. (2014a) offer further evidence of regions where the transition from single ion pair to multiple

ion association may occur. Using measurements of mineral-buffered solutions at elevated temperatures and pressures, Tutolo et al. (2014a) have shown that the single ion pair model with the assumption of $\gamma_{KCl(aq)}=\gamma_{HCl(aq)}=1$ cannot reproduce the measured solubilities to an increasing degree with increasing temperature and decreasing density. Notably, the solutions that deviate most significantly from the single ion pair model have similar densities and dielectric constants to the measurement by Sharygin et al. (2002), suggesting that similar processes (i.e., multiple ion clustering or salting out/in of neutral species) are governing solution chemistry. Further experimental work will be required to improve our ability to model these processes. The approaches advocated by both Sharygin et al. (2002) and Tutolo et al. (2014a) can likely be used in tandem to further advance our understanding of redissociation processes.

3.7 Conclusion

Consideration of the experimental measurements of Sharygin et al. (2002) and the simple calculations that we have performed here suggest the redissociation phenomenon is important to consider in a variety of geological systems. Specifically, because, at certain temperatures and pressures, calculated *activities* of ions in solution remain practically constant even as element *concentrations* increase from <1 molal to 4.5 molal, this phenomenon could significantly affect mineral and gas solubilities as well as elemental fluxes. In turn, these effects play a role in the formation of ore deposits (Reed, 1997; Yardley and Bodnar, 2014) and development of diverse, geologically-fueled ecosystems (Jørgensen and Boetius, 2007). Nonetheless, the full region of applicability of the types of calculations performed here is not yet clear. Our hope is that the calculations and hypotheses included herein will stimulate continued experimental and numerical study examining the limits of the the speciation model employed here in order to improve the certainty with which geochemical speciation codes may be applied to geological problems.

Chapter 4

CO_2 sequestration in feldspar-rich sandstone: Coupled evolution of fluid chemistry, mineral reaction rates, and hydrogeochemical properties

4.1 Summary

To investigate CO_2 Capture, Utilization, and Storage (CCUS) in sandstones, we performed three 150°C flow-through experiments on K-feldspar-rich cores from the Eau Claire formation. By characterizing fluid and solid samples from these experiments using a suite of analytical techniques, we explored the coupled evolution of fluid chemistry, mineral reaction rates, and hydrogeochemical properties during CO_2 sequestration in feldspar-rich sandstone. Overall, our results confirm predictions that the heightened acidity resulting from supercritical CO_2 injection into feldspar-rich sandstone will dissolve primary feldspars and precipitate secondary aluminum minerals. A core through which CO_2-rich deionized water was recycled for 52 days decreased in bulk permeability, exhibited generally low porosity associated with high surface area in post-experiment core sub-samples, and produced an Al hydroxide secondary mineral, such as boehmite. However, two samples subjected to ∼3 day single-pass experiments run with CO_2-rich, 0.94 mol/kg NaCl brines decreased in bulk permeability, showed generally elevated porosity associated with elevated surface area in post-experiment core sub-samples, and produced a phase with kaolinite-like stoichiometry. CO_2-induced metal mobilization during the experiments was relatively minor and likely related to Ca mineral dissolution. Based on the relatively rapid approach to equilibrium, the relatively slow near-equilibrium reaction rates, and the minor magnitudes of permeability changes in these experiments, we conclude that CCUS systems with projected lifetimes of several decades are geochemically feasible

in the feldspar-rich sandstone end-member examined here. Additionally, the observation that K-feldspar dissolution rates calculated from our whole-rock experiments are in good agreement with literature parameterizations suggests that the latter can be utilized to model CCUS in K-feldspar-rich sandstone. Finally, by performing a number of reactive transport modeling experiments to explore processes occurring during the flow-through experiments, we have found that the overall progress of feldspar hydrolysis is negligibly affected by quartz dissolution, but significantly impacted by the rates of secondary mineral precipitation and their effect on feldspar saturation state. The observations produced here are critical to the development of models of CCUS operations, yet more work, particularly in the quantification of coupled dissolution and precipitation processes, will be required in order to produce models that can accurately predict the behavior of these systems.

4.2 Introduction

Greenhouse gases, predominantly carbon dioxide (CO_2), emitted to the atmosphere at currently projected rates for the duration of the twenty-first century will cause immense changes to Earth's climate, hydrologic, and ecologic systems and will lead to dramatic reductions in the quality of life for many of its human inhabitants (IPCC, 2014). As society increasingly embraces these facts, researchers and policymakers are exploring CO_2 Capture, Utilization, and Storage (CCUS) as a method of reducing anthropogenic CO_2 emissions while transitioning to more efficient and less polluting energy sources. CCUS involves capturing CO_2 from point sources and injecting it deep underground into geological formations (DePaolo and Cole, 2013). Researchers have additionally proposed to utilize the injected CO_2 as a working fluid to extract geothermal heat from the subsurface and offset some of the costs of the capture and injection operations (e.g., Pruess, 2006; Randolph and Saar, 2011a).

Because of their favorable flow and storage properties and relative abundance, siliciclastic reservoirs comprise a significant proportion of the reservoirs proposed for CCUS operations (e.g., U.S.G.S., 2013). As CO_2 is injected into these reservoirs, it will dissolve into formation fluids, form carbonic acid, lower solution pH, and react with the reservoir minerals (e.g., Kaszuba et al., 2003; Andreani et al., 2008; Busch et al., 2008; Luquot et al., 2012; Carroll et al., 2011; Karamalidis et al., 2012; Liu et al., 2012; Carroll et al., 2013b; Tutolo et al., 2014b; Luhmann et al., 2014). The acidification process will lead to an associated evolution of important hydrogeochemical

parameters (e.g, porosity, permeability, and reactive surface area). Most researchers performing CCUS studies on feldspar and clay mineral-bearing sandstones note primary silicate and (if present) carbonate cement dissolution coupled to secondary mineral growth (Gunter et al., 1997; Andreani et al., 2008; Fu et al., 2009; Kampman et al., 2009; Scislewski and Zuddas, 2010; Lu et al., 2010, 2011; Luquot et al., 2012; Liu et al., 2012; Luhmann et al., 2013; Carroll et al., 2013b; Lu et al., 2013; Kirsch et al., 2014). Generally, this progression of reactions (i.e., primary feldspars weathering to clays) is expected to reduce CCUS reservoir injectivity, but these effects have been difficult to quantify over laboratory time scales.

4.2.1 Numerical simulation of CCUS in sandstones

Researchers have developed and applied increasingly sophisticated simulators to investigate and predict the long-term, coupled chemical and physical response of siliciclastic reservoirs to CO_2 injection (Xu et al., 2003; Johnson et al., 2004; Gaus et al., 2005; Zerai et al., 2006; Xu et al., 2006, 2007; Gaus et al., 2008; Hangx and Spiers, 2009; Balashov et al., 2013; Carroll et al., 2013b). These reactive transport simulators–i.e., those that couple fluid and heat flow and kinetically controlled geochemistry to predict reservoir behavior at a range of spatial and temporal scales–carry with them unique and difficult-to-quantify sources of uncertainty. One of the most significant sources of these relates to the reactive surface area parameter, which is used to constrain rates of mineral dissolution and precipitation. Mineral reactive surface areas within natural geologic samples are generally poorly constrained (Helgeson et al., 1984; White and Peterson, 1990; Nagy et al., 1999; Washton et al., 2008; Peters, 2009; Landrot et al., 2012; Luhmann et al., 2014) and potentially incomparable to surface areas measured on laboratory samples (White and Peterson, 1990; Hajash et al., 1998; Li et al., 2014; Luhmann et al., 2014). However, because laboratory-measured rates are typically normalized to reactant mineral surface areas using gas sorption methods (e.g., B.E.T. (Brunauer et al., 1938)) or geometric measurements (e.g., White and Peterson, 1990), modelers must know natural samples' reactive surface areas in order to simulate kinetically controlled mineral-fluid reactions. Furthermore, although a plethora of studies focuses on mineral-specific dissolution rates (see e.g., the Palandri and Kharaka (2004) compilation), significantly fewer laboratory studies examine mineral precipitation rates, and even fewer yet have explored the complexities of whole rock reaction kinetics in the context of previously published, mineral-specific kinetic

studies (e.g., White et al., 1999; White and Brantley, 2003; Gong et al., 2012; Tutolo et al., 2014b; Li et al., 2014; Luhmann et al., 2014). Notably, in whole rock samples, quantifying surface area of the reacting minerals is particularly challenging due to the heterogeneous distribution of minerals and pore space.

4.2.2 Rate laws for K-feldspar dissolution and secondary mineral precipitation

Feldspars are one of the more reactive groups of minerals present in siliciclastic formations. Rates of feldspar dissolution have been repeatedly shown to be a complex function of solution pH and composition, temperature, chemical affinity, and secondary mineral precipitation rate (Lagache, 1965; Aagaard and Helgeson, 1982; Helgeson et al., 1984; Knauss and Wolery, 1986; Schweda, 1990; Rafal'skiy et al., 1990; Burch et al., 1993; Hellmann, 1994; Gautier et al., 1994; Blum and Stillings, 1995; Alekseyev et al., 1997; White and Brantley, 2003; Maher et al., 2009). Mineral dissolution rates are typically calculated using a rate law of the form:

$$r = \mathrm{A}\mathrm{T}_K \mathrm{e}^{\left(\frac{\Delta H^{\ddagger}}{R\mathrm{T}_K}\right)} a_{\mathrm{H}^+}^n (1 - \Omega^p)^q, \tag{4.1}$$

where A is a pre-exponential factor and $\Delta H^{\ddagger}$ is the activation enthalpy[1] of feldspar dissolution, a_{H^+} is the activity of H^+ in solution, n describes the pH dependence of the dissolution rate, p and q are empirical parameters describing the dependence of the dissolution rate on the saturation index (Ω), which is calculated according to:

$$\Omega = \left(\frac{IAP}{K_{eq}}\right), \tag{4.2}$$

where IAP and K_{eq} represent the ion activity product and equilibrium constant, respectively.

The pH dependence of feldspar dissolution rates has been studied extensively (Helgeson et al., 1984; Schweda, 1990; Knauss and Wolery, 1986; Hellmann, 1994; Blum and Stillings, 1995; Fenter et al., 2014), but consensus has not been reached regarding the value of n in Eqn. 6.4. Because a_{H^+} can range up to ∼5 orders of magnitude in the region where acidic rate laws apply (Helgeson et al., 1984), the value of n can contribute up to several orders of magnitude of uncertainty to a calculated

[1] $\Delta H^{\ddagger}$ may be related to activation energy (E_A) by: $\mathrm{E}_\mathrm{A} = \mathrm{RT}_K + \Delta H^{\ddagger}$ (Helgeson et al., 1984; Hellmann, 1994)

rate, especially at very low solution pH. Fortunately, in the pH range attributed to most natural and engineered systems (e.g., pH $\gtrsim$ 3), the value of n has less of an effect than at lower pH. Hellmann (1994) reports values of n ranging from 0.2 to 0.6, based on experimental calibration over the range of 100-300°C; Schweda (1990) reports values of 0.52 and 0.45 for microcline and sanidine at 25°C, respectively; Blum and Stillings (1995) give 0.5 (which was adopted in the Palandri and Kharaka (2004) compilation); and Helgeson et al. (1984) and Knauss and Wolery (1986) both give values of $n = 1$, calibrated over a range of temperatures (25°-200°C and 25°-70°C, respectively). More recently, Fenter et al. (2014) presented x-ray reflectivity measurements that indicate a transition from n=1 at acidic pH > 2.5 to $n = 0.37$ at pH <2.5, which suggests that the range of reported values of n may be attributed to the pH range over which the formulations were calibrated.

Considerable scatter also exists for derived values of the activation energy (E_A), which is used to approximate the temperature dependence in Eqn. 6.4. Helgeson et al. (1984) and Hellmann (1994) derive values in remarkably close agreement with each other, yet both values are in substantial disagreement with studies deriving E_A from lower temperature experiments (Knauss and Wolery, 1986; Bevan and Savage, 1989; Sverdrup, 1990; Schweda, 1990; Blum and Stillings, 1995). Importantly, however, in spite of the lack of inter-study similarity in these important rate parameters, these various formulations tend to calculate high temperature rates within reasonable agreement with each other. The latter consideration indicates that calibration of E_A is subject to uncertainties associated with the rate law formulation, particularly in the value of n, and that values of E_A should only be used with the rate law and parameters with which they were derived.

The final important parameters for calculating the feldspar dissolution rate are related to the chemical affinity, which has been studied for feldspars mostly in the basic region (Burch et al., 1993; Gautier et al., 1994; Alekseyev et al., 1997; Hellmann and Tisserand, 2006). All of these studies indicate that the classical Transition State Theory formulation, in which p and q are assumed equal to 1, tends to overestimate near-equilibrium rates. Essentially, when values of p=q=1 are utilized, calculated rates are only affected by chemical affinity in the region very close to equilibrium, which is generally inconsistent with laboratory and field observations (e.g., Lasaga et al., 1994; Alekseyev et al., 1997; Kampman et al., 2009; Lu et al., 2013).

In addition to these direct, solution controls on feldspar dissolution rates, several

researchers (Alekseyev et al., 1997; Maher et al., 2009; Zhu and Lu, 2009) have noted that sluggish secondary Al mineral precipitation rates may help to fix the feldspar saturation state close to equilibrium and, consequently, slow down the dissolution rate of primary feldspars. This mechanism is difficult to explore, however, because rate laws for secondary Al mineral precipitation are relatively sparse. One of the most important–and perhaps the most difficult to quantify–parameters required to investigate the rates of secondary mineral formation is the reactive surface area of the secondary phase (Nagy and Lasaga, 1993; Nagy et al., 1999). The surface area of secondary phases is difficult to quantify both because it will start at or near zero and increase exponentially and also because measurable changes in surface area must somehow be separated to account for both secondary phase growth and primary phase dissolution. Some researchers employ the bulk surface area of all minerals in the system (e.g., Zhu et al., 2010) as an estimate of precipitating mineral surface area, or simply normalize rates to the fluid volume (e.g., Alekseyev et al., 1997), both of which yield lower bound estimates of mineral precipitation rates.

In this study, we experimentally observe CO_2-induced dissolution and precipitation reactions in three K-feldspar-rich sandstone cores at 150°C. We monitor permeability changes, analyze fluid and solid chemistry, and evaluate mineral volume and surface area evolution using synchrotron X-Ray Computed Tomography (XRCT)-based methods. Because our core samples were cut to preserve the naturally complex spatial distribution of mineral grains and flow pathways, they allow for comparison between previously published, laboratory-measured reaction rates and whole rock dissolution kinetics. Importantly, we compare the products of experiments run under both single-pass and recirculating flow regimes with each other and "pristine" samples from the same rock in order to evaluate CO_2-water-sandstone interactions as a function of solution composition and reaction progress.

4.3 Methods

4.3.1 Experimental Configuration

Three CO_2-charged flow-through experiments were conducted at 150°C with an outlet pressure of 200 bar using a flow-through apparatus previously employed in a number of complementary studies (Luhmann et al., 2013; Tutolo et al., 2014b; Luhmann et al., 2014). The experimental apparatus (Fig. 4.1) makes use of four

pumps: Pumps A, B, and C are Teledyne ISCO 260D pumps, and Pump D is a 500D pump. The apparatus can be run in either "recycling" (RC, Fig. 4.1A) or "single-pass" (SP, Fig. 4.1B) mode, and both configurations were employed in this study. To prevent brine corrosion of the interiors of the syringe pumps, recycling mode requires the use of deionized water as a reaction fluid. In single-pass mode, however, titanium separators described by Luhmann et al. (2014) isolate the experimental fluid from the pumps and therefore allow for high ionic strength reaction fluids to simulate reservoir brines. Due to these differences, the two configurations yield the unique opportunity to examine the effects of fluid saturation state (i.e., "far-from-equilibrium" (SP) versus approaching equilibrium (RC)) and solution composition (i.e., deionized water (RC) vs. high ionic strength brine (SP)). The confining pressure in all experiments was set at 240 bar.

During the single experiment run in recycling mode, a 0.86 mol CO_2/kg, deionized H_2O solution was continually circulated through the core sample for 52 days. This CO_2 concentration is ∼74% of saturation at these temperature, pressure, and ionic strength conditions (Duan et al., 2006). A flow rate of 0.1 mL/min was used for the first 19 hours, but was then increased to 0.5 mL/min for the remainder of the experiment in order to improve the resolution of real-time permeability measurents. During several brief periods, flow rates were additionally cycled to obtain improved permeability measurements (gray points in Fig. 5.1). The recycling experiment began with ∼510 mL of fluid, but finished with ∼460 mL due to sample collection. During the two experiments run in single-pass mode, a 0.75 mol CO_2/kg brine solution (0.94 mol NaCl/kg) was injected into each core at a constant flow rate of 0.1 mL/min. This CO_2 concentration is ∼80% of saturation at these temperature, pressure, and ionic strength conditions (Duan et al., 2006). The two single-pass experiments lasted 3.20 (SP1) and 2.74 days (SP2), yielding total injected volumes of 460 and 395 mL of CO_2-charged brine, respectively.

In the recycling experiment, either Pump A or B continuously pumped fluid into the core while the other refilled. Computerized valves alternated the roles of the pumps as they became full/empty. It is not possible for the refilling pump to refill in a constant pressure mode in the dual-pump configuration mode. For this reason, Pump C operated in a constant pressure capacity to set the outlet pore-fluid pressure. The refill rate in either Pump A or B was twice the flow rate to facilitate mixing of experimental fluid. Pump C was sufficiently full at the beginning of each cycle to

provide half of the fluid volume to the pump that was refilling. During the first half of each cycle, Pump C was partially emptied as Pump A or B was refilled; during the second half of each cycle, Pump C partially refilled as Pump A or B paused after becoming full. This experimental provision allows for homogenenization of the reaction fluid after successive passes through the core and therefore permits calculation of full-core mineral reaction rates based upon flow rates and measured concentrations.

In the single-pass experiments, the 0.94 mol NaCl/kg solution was injected from the upstream titanium separator into the core and then either sampled or collected in the downstream titanium separator (Fig. 4.1B). In order to simulate the reducing brines that may be encountered in CCUS reservoirs (e.g., Lammers et al., 2015), oxygen was purged from the upstream separator before the brine solution was added. This was done by opening the separator to three cycles of ∼60 bar of CO_2 pressure that was later released. Additionally, nitrogen was bubbled through the brine for more than two hours to purge oxygen before it was pumped into the separator. CO_2 was then added to attain the desired CO_2 concentration. As noted previously (Luhmann et al., 2014), the Teflon sheaths in which the cores are housed during experimental reaction, while non-reactive, are susceptible to CO_2 diffusion from the pore fluids into the confining fluid. Therefore, we wrapped 0.005 cm stainless steel foil around the Teflon sheaths in all three experiments. Nontheless, CO_2 concentration in the sampled solutions evolves somewhat over the course of the experiments, particularly during the initial stages when the confining fluid surrounding the core is CO_2-free.

In all experiments, pressure transducers placed in the fluid circulation line just upstream and downstream of the core permit determination of in situ bulk permeability through Darcy's Law. However, due to the relatively high permeability of the sandstone samples and the relatively small, and thus difficult to measure, pressure gradients resulting from our fixed injection rates, the in situ permeability data is relatively noisy. Therefore, we produced more precise permeability measurements by cycling through a series of injection rates at periodic intervals during the recycling experiment and before and after the single-pass experiments while deionized water flowed through the cores at experimental temperature and pressure.

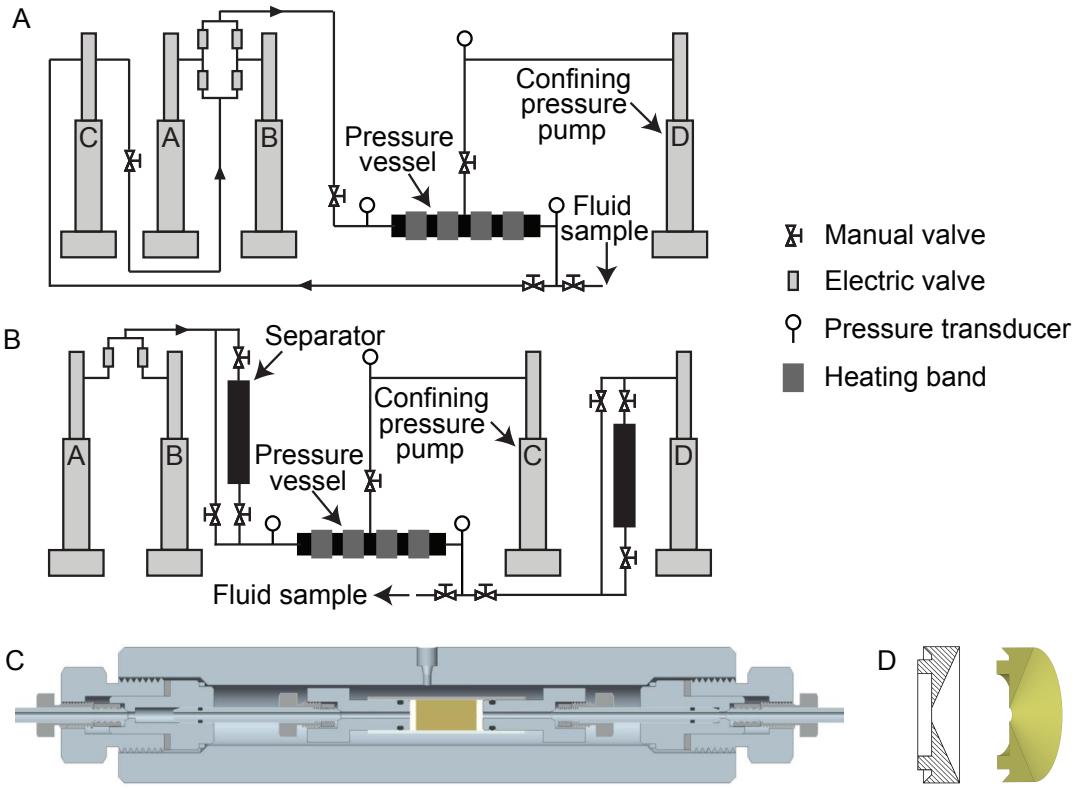

Figure 4.1: Hydrothermal flow system used for recycling (A) and single-pass (B) experiments. Fluid-rock reaction occurs in the pressure vessel (C) and the cone in PEEK retainer rings (shown in both 2D and 3D) allows fluids to access and exit all potential flow paths in experimental cores (D).

Table 4.1: Chemical and Physical Properties of Eau Claire Arkose Samples

Oxide[§]	Al_2O_3	BaO	CaO	Fe_2O_3	K_2O	MgO	Na_2O	SiO_2	TiO_2	total
Wt. %	12.1	0.119	0.261	0.67	10.0	0.217	0.125	75	0.32	99
Mineral[‡]	Orthoclase	Quartz	Total Specific Surface Area[♭] (m^{-1})					Porosity[♭] (%)		
Wt. %	50.7±6.6	49.3±4.3	2.36×10^5					21		

[§]Analyzed by ICP-OES, [‡]Analyzed by XRD, [♭]Calculated from XRCT, subject to uncertainties discussed in Sect. 4.3.2.

4.3.2 Characterization Methods

The Eau Claire arkose sample (Table 4.1) and the fluid samples listed in Tables 4.2 and 4.3 were analyzed using inductively coupled plasma-optical emission spectrometry (ICP-OES) for major dissolved cations and major oxides, and ion chromatography was used for anions. Experience dictates that 2σ accuracies are generally better than 3%, and the number of significant figures given for individual analyses in Tables 4.1-4.3 is indicative of their individual precision. Core masses were measured before and after the experiment by drying at 60°C and repeatedly weighing until no change in core mass was detected. Mineral abundances of a powdered sample of the Eau Claire taken adjacent to the experimental cores were determined by X-ray diffraction (XRD). X-ray Photoelectron spectroscopy (XPS) was performed on four samples (the upstream face of the three experimental cores and a pristine sample) using an SSX-100 (Surface Science Laboratories, Inc.) system equipped with a monochromated Al K_α X-ray source, a hemispherical sector analyzer, and a resistive anode detector. XPS system base pressure was 5.3 $\times 10^{-8}$ Pa and $\sim$1.3 $\times 10^{-6}$ Pa during data collection. XPS was performed using a 1 $\times$ 1 mm^2 spot size (corresponding to an X-ray power of 200 W) to determine elemental abundances of the materials to a maximum depth of $\sim$10 nm. Atomic percentages were calculated using the ESCA 2005 software provided with the XPS system. Both the XRD and XPS analyses were performed in the Characterization Facility at the University of Minnesota. A Quanta 200 3D DualBeam Focused Ion Beam-Scanning Electron Microscope (FIB-SEM) housed in the Minnesota Nano Center, employing both a scanning electron beam and a Ga ion beam, was used to image (electron and Ga beam) as well as mill into (Ga beam) samples from the recycling experiment core. Additional SEM imagery was obtained in the UMN Characterization Facility on a JEOL 6700F Field Emission Gun Scanning Electron Microscope (FEG-SEM). Samples for FIB-SEM and FEG-SEM imaging were adhered to carbon tape and coated in Au-Pd to reduce charging and improve image quality.

Full-core X-ray Computed Tomography (XRCT) imaging was performed pre- and post-experiment at 8 μm voxel size at the University of Minnesota XRCT laboratory. The small size of the sediment particles prevented imaging of individual grains, but larger features, such as the presence and absence of shells, were observable. Higher resolution, smaller sample size, XRCT imaging was performed on post-experiment sub-samples at the Advanced Photon Source (APS) at Argonne National Laboratory

at the 2-BM-B beamline. Images were reconstructed at 0.75 μm voxel size. Each tomographic volume is 2048 x 2048 x 2048 voxels, allowing for maximum imaged sample sizes on the order of 1.5 mm x 1.5 mm x 1.5 mm. The cylindrical cores were initially sawed length-wise to create two half cylinders. One of these half cylinders was further subsectioned to provide samples within the allowable size range for the high resolution, synchrotron XRCT imaging. These samples, along with several pristine samples, were prepared for imaging by mounting $\sim$4 mm x 1.5 mm x 1.5 mm sub-samples to wooden toothpicks using epoxy to prevent sample shifting during the imaging process.

The reconstructed higher resolution XRCT images provide 3D observations of pore-scale mineral orientations and therefore allow for calculation of specific surface area and sample porosity. Reconstructed samples were analyzed using the Avizo® software package. All data sets were cropped to remove edge artifacts introduced by the imaging and reconstruction procedure, then passed through a non-local means filter to reduce image noise. The data sets were then thresholded to separate pore space from solid grains using a watershed filter. In order to attempt to remove artifacts introduced by the sample preparation, imaging, or reconstruction processes, "holes" in the solid less than 6 total voxels (2.5 μm^3) were filled in on a slice-by-slice basis, and "solid particles" less than 40 total voxels (17 μm^3) were removed on a 3D basis. Note that these "holes" and "particles" may actually be holes or particles, but may also be artifacts or noise that were not removed during the cropping and filtering procedure or were inadvertently assigned to solid or pore space during the thresholding procedure. In either case, holes in the solid would not be accessible to flowing fluids and therefore do not represent reactive surface area or effective porosity. The decision to employ the slice-by-slice and 3D artifact removal operations was made for computational efficiency and not necessarily for improved accuracy, which did not vary greatly between 3D and 2D methods. For each data set, this thresholding method yielded one large connected object (i.e., the sandstone) and numerous, much smaller (e.g., $>1\times10^5$ smaller), disconnected "particles", which may be the result of slight disaggregation during preparation, artifacts, or noise. After this procedure was completed, the resulting image data set was a binary representation of the bulk rock, and all analyses were based upon calculations performed on this binary data set. Specific surface area in units of m^{-1} was calculated by summing the pore-solid

interfacial area of the large, connected object and dividing by its volume. The uncertainty in the actual surface area calculation (i.e., the summation step) is estimated to be less than a few percent, based on similar calculations performed upon digitized objects of known dimensions. The uncertainty on the entire XRCT analytical process (i.e., from imaging through thresholding and artifact removal) is more difficult to constrain, however, because analogous samples of known dimensions have not been imaged at the APS and surface area is, of necessity, a relative parameter subject to the size of the "ruler" used for the measurement (e.g., White and Peterson, 1990). Notably, Porter and Wildenschild (2010) calculate absolute errors of <1.5% and <10-40% on porosity and surface area, respectively, relative to "spherical cap" analytical estimates of these properties generated through several XRCT processing schemes performed on capillary tube XRCT data sets with around an order of magnitude lower resolution. These researchers additionally suggest that improvements in accuracy could potentially be made with enhanced filtering and thresholding techniques, which we have attempted to employ here. For comparison, the standard deviations of all specific surface area and porosity analyses presented in this study (including both pristine and post-experiment samples) are 5.3×10^4 m^{-1} and 3%, respectively, which represent 22% and 15% of the pristine values.

4.3.3 Reservoir Sample

The feldspar-rich arkose sandstone used in this study was sampled from drill core obtained in the city of St. Paul, Minnesota, USA (Minnesota Unique Well Number 185810). In order to preserve predominant permeability encountered by flowing basin fluids in CCUS reservoirs, experimental cores (12.8 mm diameter × 24.9 mm length) were extracted from the 246 m borehole interval by drilling parallel to bedding. All three cores were obtained within 30 mm of stratigraphic depth in order to facilitate comparison between experimental results. Clay-rich sections of the Eau Claire formation have been studied as a caprock for the underlying Mt. Simon formation (Liu et al., 2012; Carroll et al., 2013b; Swift et al., 2014; Shao et al., 2014), yet the samples used here are considerably more permeable, feldspar-rich, and clay/mica-poor and were chosen to serve as a reduced-complexity analogue for CCUS injection formations. Arkose sandstones generally contain a maximum of ∼60% feldspar (greater contents would require a source in which feldspar was more abundant than quartz (Selley, 1982)), and XRD analyses indicate that the cores used in our

experiments are near the top of this range, with 50.7±6.6% orthoclase and 49.3±4.3% quartz, and mica contents less than a few percent. Therefore, these samples are ideal for studying the role of K-feldspar dissolution in CCUS environments without the added complexity of clays and other accessory phases. Electron microprobe (EMP) analyses show that the feldspar is K-rich (96% K-feldspar), with approximately 4% albite and trace amounts of anorthite (Luhmann et al., 2013). SEM, XRCT, and petrographic observations indicate that a variety of types and morphologies of micas are present within the sample. Small grains of TiO_2, identified by EMP, are also seen in small proportions in XRCT and SEM imagery. XRCT and SEM images additionally reveal minor amounts of shells within the bedding layers, and EMP analyses show that these shells are predominantly composed of $CaPO_4$, consistent with other researchers' analyses of the Eau Claire formation (Klemic and Mrose, 1972). The initial porosity and surface area of the Eau Claire arkose (Table 4.1) were obtained by calculating these parameters for two "pristine" samples that were not exposed to the experimental fluid. The two measured samples yielded porosities that agreed within less than 0.5% and specific surface areas that agreed within less than 0.02%. The values included in Table 4.1 are the average of the two measured values for each parameter, which are assumed to be representative of the pristine sandstone. Imagery of the pristine arkose sample indicates that the K-feldspar and quartz grains are relatively unweathered (Fig. 4.2).

4.3.4 Numerical Methods

The Geochemist's Workbench (GWB, Bethke and Yeakel, 2012) version 9.0.9 with a 150°C, 200 bar database created using the DBCreate software package (Kong et al., 2013) was employed for speciation calculations, and PFLOTRAN (Hammond et al., 2012; Lichtner et al., 2013), outfitted with an appropriately formatted thermodynamic database containing identical equilibrium constants, was utilized for reactive transport analyses of the single-pass experimental results. The Drummond (1981) formulation was used to calculate activity coefficients of CO_2(aq), and internally consistent thermodynamic data presented by Tutolo et al. (2014a) was employed for Al-bearing minerals and aqueous species, quartz, and H_4SiO_4(aq). Silicic acid ionization constants and SiO_2(am) thermodynamic data came from Busey and Mesmer (1977) and Gunnarsson and Arnórsson (2000), respectively. Data for the remaining aqueous species and minerals are consistent with the standard SUPCRT92 (Johnson

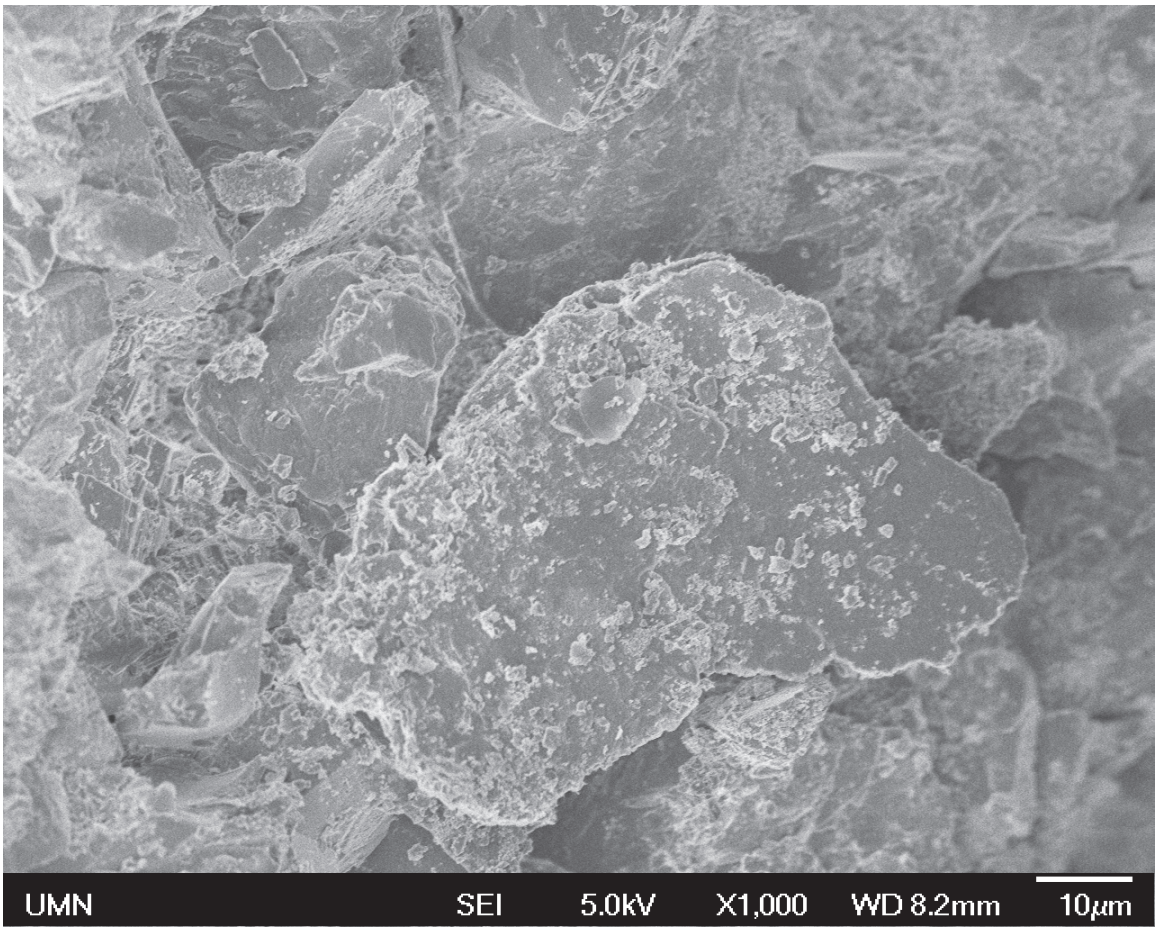

Figure 4.2: SEM image of a sample taken from the pristine sandstone near where the experimental cores were drilled. Note the relatively smooth grain surfaces and lack of fibrous secondary minerals.

et al., 1992) data set. At the temperatures, pressures, and ionic strengths relevant to this study, the extended Debye-Hückel formulation (Helgeson, 1969), which was used in both GWB and PFLOTRAN calculations, is able to accurately calculate charged species activity coefficients (Tutolo et al., 2015b). In calculations of saturation indices for the single-pass experiments, Cl concentrations were set equal to analytical Na concentrations, which is consistent with brine preparation by NaCl addition to deionized water. The chemical affinity, ΔG_r, was calculated according to:

$$\Delta G_r = -\mathrm{RT_K} \ln(\Omega), \tag{4.3}$$

where R is the ideal gas constant (8.314 kJ/mol/K) and $\mathrm{T_K}$ is the temperature in Kelvin. In the one-dimensional PFLOTRAN simulations, the experimental core, which was assumed to be composed of 50% K-feldspar and 50% quartz, was divided into 15 elements, and fluid flowed through the core at a uniform velocity equivalent to the fixed 0.1 mL/min flow rate in these experiments. The core temperature was set to 150°C, and fluid flow was only allowed through its upstream and downstream faces.

The reaction rate, r, in units of mol/cm^2/s for the dissolution of K-feldspar in a well-mixed, flow-through reaction system may be calculated according to (e.g., Dove and Crerar, 1990; Hellmann, 1994; Tutolo et al., 2014b):

$$r = \frac{\Delta C Q}{\nu P S_{ksp}}, \tag{4.4}$$

where ΔC is the measured change in concentration in mol/kg, Q is the flow rate in kg/s, ν is the stoichiometric number of the element in the K-feldspar structure, P is the integer number of passes through the core that the fluid has undergone between fluid sampling (calculated by multiplying the experimental time by the fluid flow rate and dividing by the fluid volume), and S_{ksp} is the K-feldspar surface area in cm^2, calculated according to:

$$S_{ksp} = S_{tot}(1-\phi)V_{core}X_{ksp}, \tag{4.5}$$

where S_{tot} is the XRCT-calculated total specific surface area, ϕ is the XRCT-calculated porosity (both obtained from the pristine samples), V_{core} is the core volume, and X_{ksp} is the XRD-determined K-feldspar volume fraction. The decision to employ a constant value of S_{ksp} in Eqn. 4.4 introduces some uncertainty into the calculated value

of r, but a lack of knowledge about the temporal evolution of this parameter combined with an inability to effectively separate primary and secondary phases within the post-experiment images and the already potentially large uncertainty on the surface area measurement itself precludes a more specific, time-dependent quantification (see Sect. 4.5.5). The average calculated absolute change in total (i.e., all minerals in the sample) surface area in post-experiment samples relative to the pre-experiment samples is 22%.

In all plots of rates versus time, the rates are plotted at the mid-point between each successive sampling time. In calculations of recycling experiment K-feldspar dissolution rates between 15.8 and 45.7 hours and 353.5 and 695.5 hours, the 15.8 and 526.3 hour samples were smoothed using a cubic spline interpolation that was fit to all data except those at 15.8 and 526.4 hours in order to prevent calculation of negative and/or unrealistic rates of K-feldspar dissolution. The sample at 15.8 hours contains comparatively high concentrations due to the slower flow rate (0.1 mL/min) and longer fluid residence time in the preceding time, but no explanation for the high Al, Si, and K concentrations measured at 526.3 hours is known. Details of these calculations are included in Appendix C. Based upon the error in the surface area calculations, XRD measurements, and ICP-OES measurements discussed above, the uncertainty in the calculated rates is expected to be less than several tens of percent (the symbols in Figs. 4.5 and 4.6 are roughly $\pm 5\%$), with the largest portion of the uncertainty attributed to the surface area calculation. More precise estimation of this parameter would have benefited from acquisition of tomographic images of analogous materials of known surface area and porosity at the APS.

4.4 Results

4.4.1 Fluid chemistry and reaction progress

Fluid chemistry samples taken from both the recycling and single-pass experiments exhibit higher rates of element release during the initial stages relative to later stages (Tables 4.2 and 4.3). In all samples, measured Al concentration is much lower ($\lesssim 5\%$) than would be expected from stoichiometric K-feldspar dissolution (i.e., [Al] = [K] = [Si]/3). Saturation indices (Ω) calculated from these analyses indicate that the outlet fluids were very close to equilibrium with respect to quartz ($-0.4 < \Omega < 0.1$) throughout all experiments, and generally undersaturated with respect to primary K-feldspar

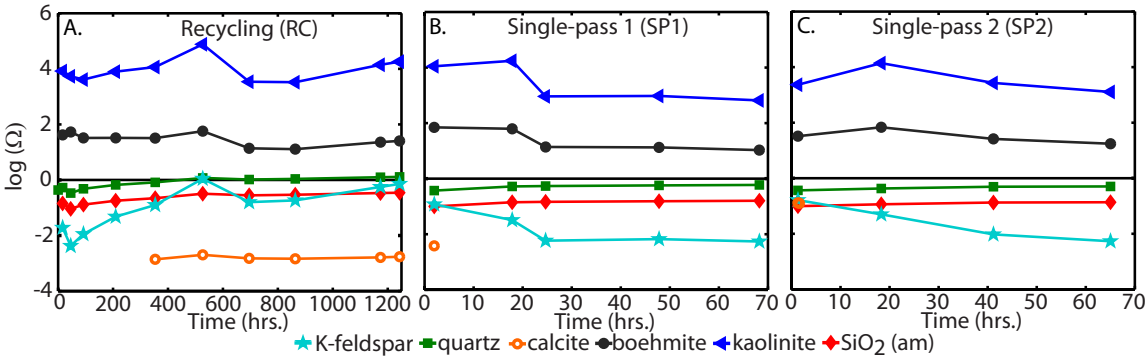

Figure 4.3: Saturation indices (Ω) calculated for the recycling (A) and single-pass (B and C) experiments.

and supersaturated with respect to both kaolinite and boehmite (Fig. 4.3) and a suite of other Al-bearing secondary phases (e.g., paragonite, muscovite, gibbsite, and diaspore). Because of the large supersaturations of these minerals, the trace micas present within the experimental cores are not expected to have contributed to dissolution processes occurring within the core. Ca concentrations in the sampled fluids increase initially and either reach a steady state (recycling) or drop off substantially (single-pass) as the experiments progress. Changes in trace metal concentrations tend to be correlated with these changes in Ca concentrations. Fluids sampled from the single-pass experiments indicate an overall approach to a Si/K ratio of 2, whereas the recycling experiment tends to have Si/K ratios between 3 and 3.5 (Fig. 4.4A). All samples from all experiments are within the kaolinite stability field (Fig. 4.4B), although single-pass fluid samples progressively move further into the kaolinite stability field and recycling fluid samples tend to approach the K-feldspar stability field.

4.4.2 K-feldspar dissolution

Rates of K-feldspar dissolution calculated using Eqn. 4.4 are plotted in Figs. 4.5 and 4.6 and included as a supplementary file. In all three experiments, reaction rates decrease with reaction progress. All samples obtained from all experiments have approached equilibrium with respect to K-feldspar relative to the initial solution composition, and demonstrate chemical affinities ranging from -22 kJ/mol to -1.2 kJ/mol (Fig. 4.6). In the recycling experiment, the K-feldspar dissolution rate approached a mean (i.e., average of K- and Si-based rates) value of 1.2×10^{-14} mol/cm^2/s from

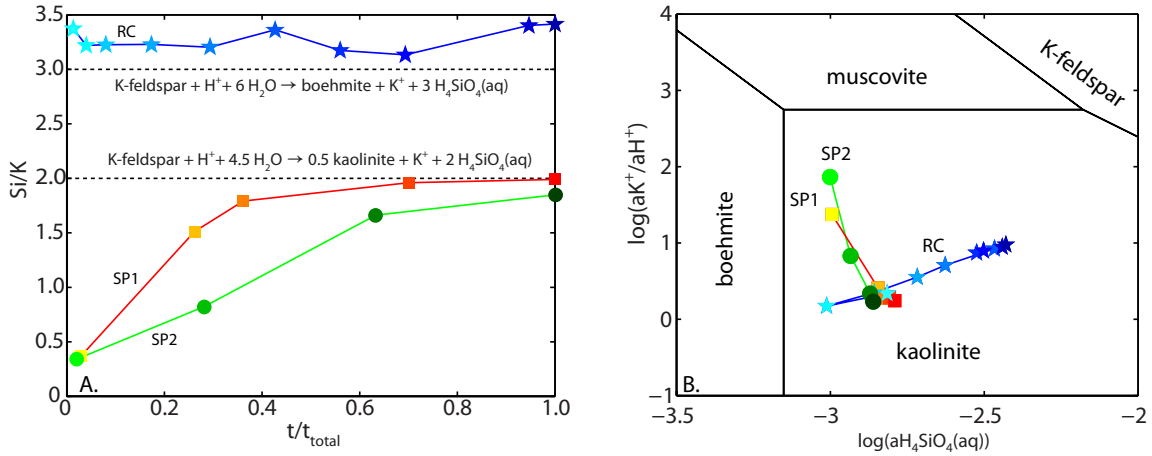

Figure 4.4: A. Evolution of the ratio of Si to K in the experimental fluid with reaction progress. Two potential reactions governing this ratio are included for reference (See Sect. 4.5.3) B. Activity diagram for the K_2O-Al_2O_3-SiO_2-H_2O system at 150°C, 200 bar. Darker symbol colors represent samples taken later in the experiment.

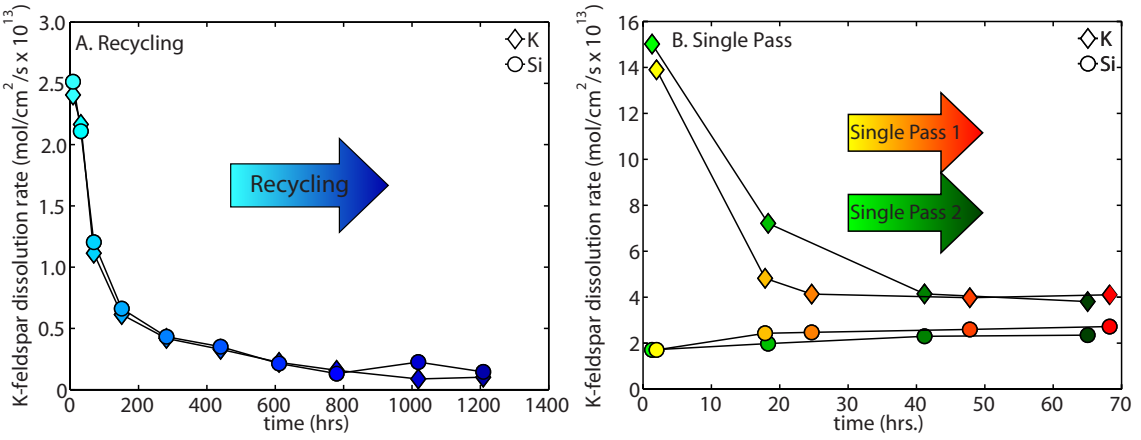

Figure 4.5: K-feldspar rate calculated through time during the recycling (A) and single-pass (C) experiments. Rates are calculated for both K and Si release from the K-feldspar structure. Importantly, the recycling experiment utilized a CO_2-rich, deionized H_2O solution and the single-pass experiments utilized a CO_2-rich, 0.94 mol NaCl/kg brine. Darker symbol colors represent samples taken later in the experiment.

an initial mean value of 2.5×10^{-13} mol/cm^2/s as the fluid was repeatedly passed through the sandstone core. The single-pass experiments yield a final mean K-based[2] K-feldspar dissolution rate of 4.0×10^{-13} mol/cm^2/s, which is similar in magnitude to the initial rates calculated from the recycling experiment. Interestingly, these samples also have aK^+/aH^+ ratios and silica activities similar to the initial sample taken from the recycling experiment (Fig. 4.4B), although their Si/K molal ratios are considerably lower (Fig. 4.4A).

4.4.3 Secondary phase precipitation

FIB-SEM, SEM, and XRCT imagery reveal significant changes in mineral surface area and core porosity in post-experiment samples relative to their pristine counterparts (Figs. 4.2, 4.7, 4.8, 4.9, 5.2). Images of the upstream face of the recycling core show both etching of grain surfaces as well as significant growth of secondary phases (Fig. 4.7). By milling into the surface of one of the grains using the focused Ga ion beam on the FIB-SEM (Fig. 4.7B), we determined that the alteration/precipitation coating on a single sandstone grain from the recycling experiment, which is characterized by a round, massive texture, is approximately 500-600 nm thick. Significantly less precipitation is apparent in SEM images of the single-pass experiments (Fig. 4.8), which were run for considerably less time (∼3 days vs. 52 days). In these images, clay-type minerals with needle-like morphology appear to have formed in discrete clusters, and nano-scale nuclei appear to have formed on many mineral surfaces. It additionally appears that certain lamellae within the K-feldspar crystal structure preferentially dissolved. XPS analyses of the upstream faces of all experiments indicate increases in the relative amount of Al and depletion of K relative to identical analyses performed on a pristine sample (Table 4.4). The Si/K and Si/Al ratios from the XPS data can potentially be helpful for the identification of the precipitating phases, particularly in the case of the recycling experiment where the secondary phase appears to coat the entire grain surface for a considerable thickness.

4.4.4 Physical property evolution

Core mass and bulk permeability decreased in both the recycling and single-pass experiments (Table 4.6). Mass decreased by approximately the same amount (∼2.1%)

[2] In the single-pass experiments, the K-based rate is likely a more accurate representation of the rate of K-feldspar dissolution due to the precipitation of a Si-containing phase (see Sect. 4.5.3).

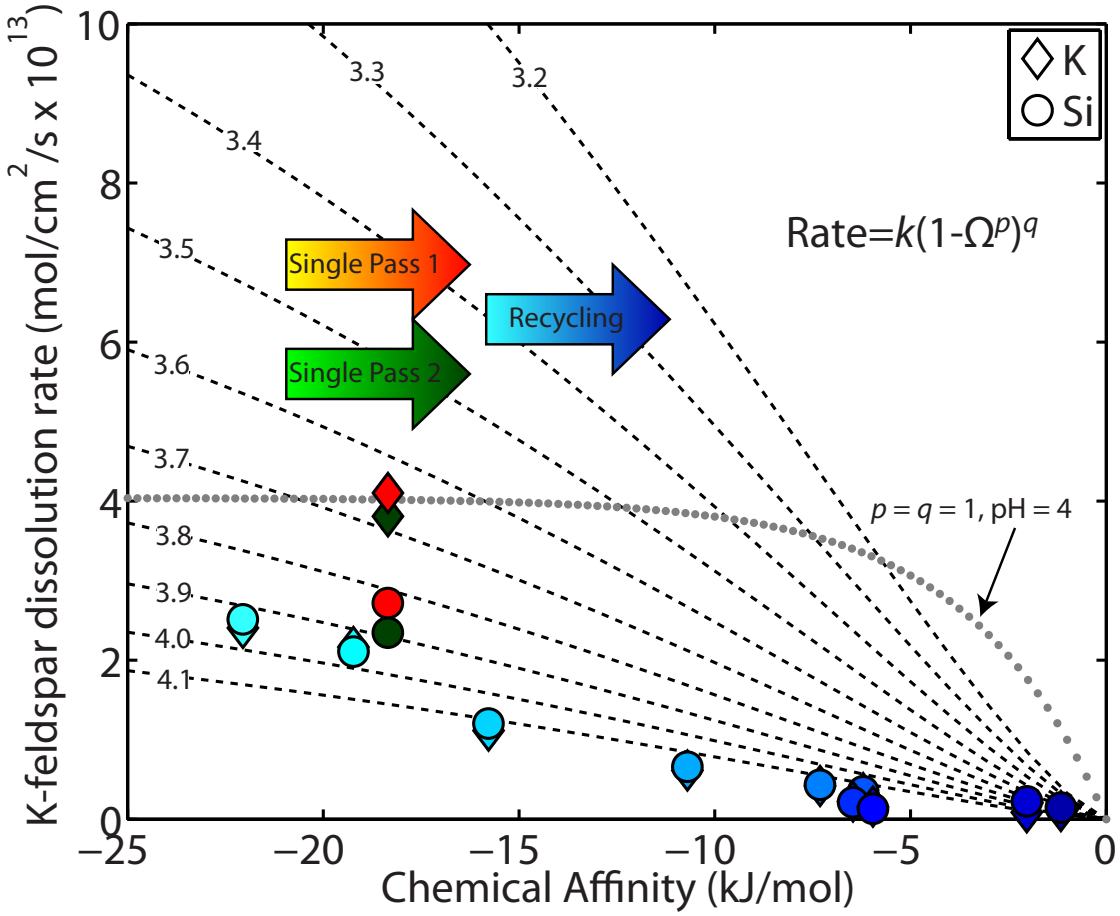

Figure 4.6: K-feldspar rate plotted as a function of chemical affinity for the three whole-rock arkose experiments. Chemical affinities and rates for the experimental samples are calculated according to methods presented in Sect. 4.3.4. Symbol colors are the same as in Fig. 4.5, but only the final, "steady-state" rates are plotted for the single-pass experiments. Dashed lines are calculated using the pH- and temperature-dependent alkali feldspar rate formulation presented by Helgeson et al. (1984) and chemical affinity parameters p=0.16 and q=1.4 (Alekseyev et al., 1997) (see Sect. 4.2.2) at pH values of 3.2-4.1, which approximately corresponds to the range of pH calculated for the sampled fluids (Tables 4.2 and 4.3). Dotted line is the rate calculated using the Helgeson et al. (1984) formulation and $p = q = 1$ in Eqn. 6.4 at pH = 4, which is the pH calculated for the final 5 samples of the recycling experiment.

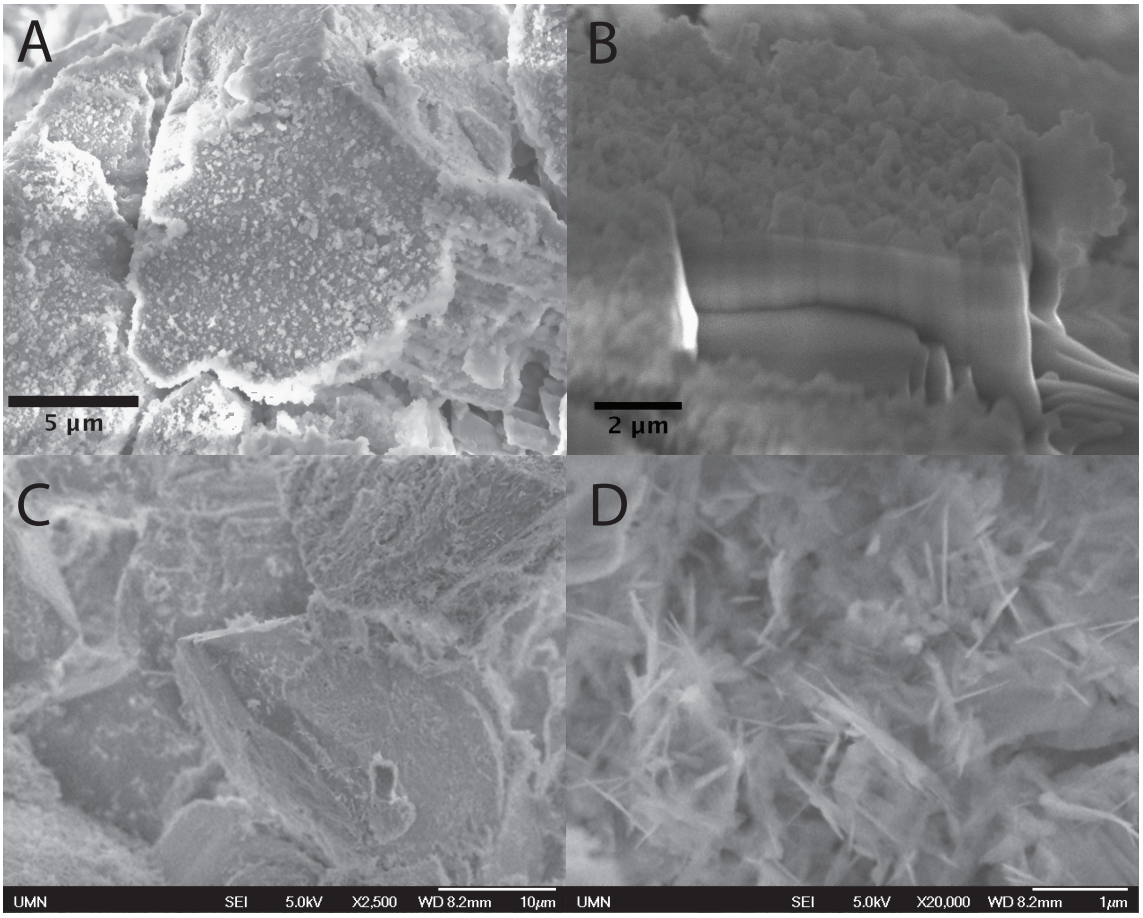

Figure 4.7: FIB-SEM (A, B) and SEM (C, D) images of samples taken from the upstream face of the recycling core. A) Secondary mineral coating on a sandstone grain; B) Image showing thickness of the altered layer, revealed by milling into the grain with the FIB- note that the lighter-colored material on the grain surface, considered to be an alteration/precipitation layer, was measured to be 500-600 nm thick; C) fibrous secondary phases coating unetched sandstone grains; D) Fibrous secondary phase within the pore space.

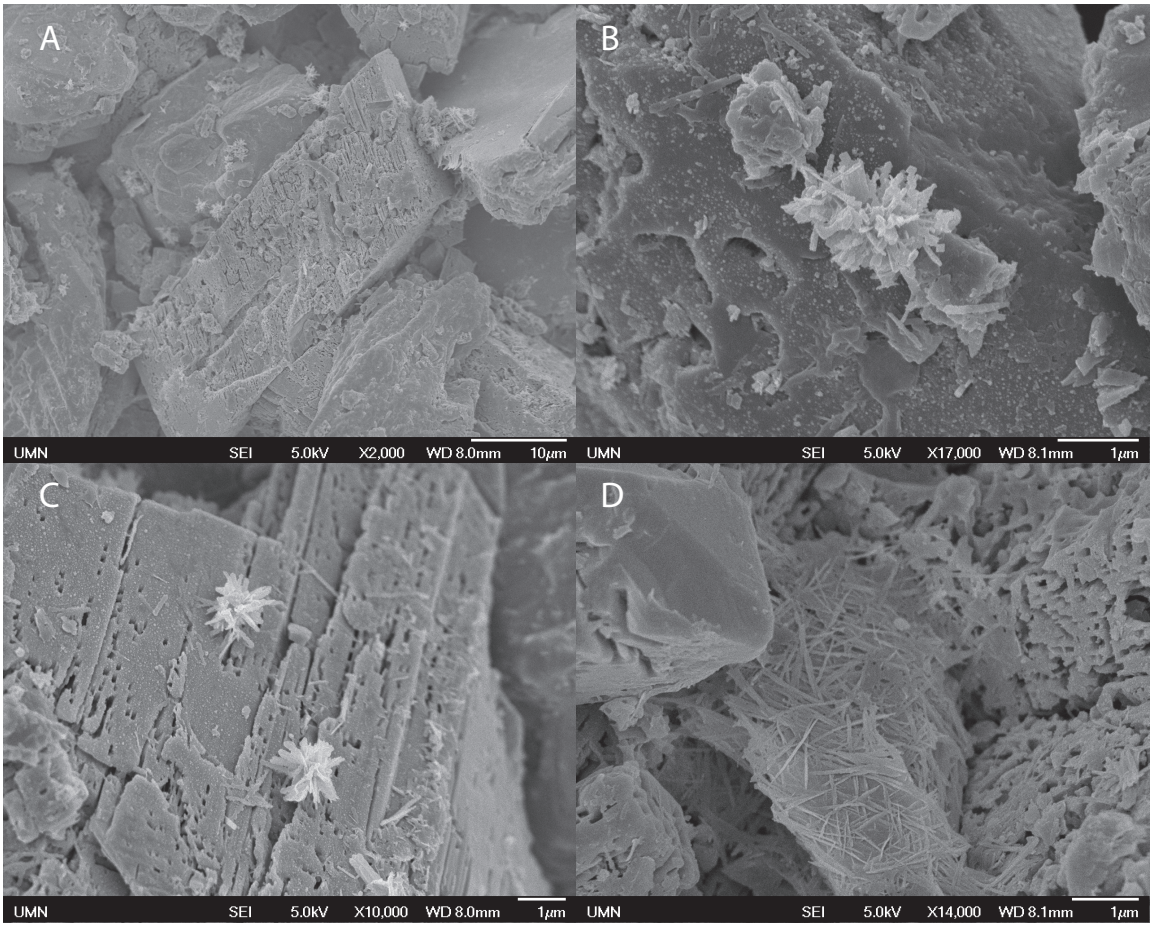

Figure 4.8: SEM images of samples taken from the upstream face of single-pass experiment 2 post-experiment. A) Deeply etched feldspar grain sparsely covered by clusters of secondary minerals; B) One of the secondary phase clusters and ubiquitous, nanometer-size nuclei on a pitted feldspar surface; C) Preferential dissolution of certain lamellae within the feldspar structure as well as secondary phase clusters on the mineral surface; D) Large secondary mineral bundle near a deeply etched and relatively unaltered mineral.

Table 4.2: Recycling Experiment: flow rate= 0.1 and 0.5 mL/min

Sample #	Time hrs.	pH†	$CO_2(aq)^{\sharp}$ m	Al^{+3} μm	Ba^{+2} μm	Ca^{+2} mm	Fe^{+2} μm	K^{+} mm	Li^{+} μm	Mg^{+2} μm	Mn^{+2} μm	Na^{+} μm	P μm	Si mm	Sr^{+2} μm	F^{-} μm	Cl^{-} μm	NO_3^{-2} μm	SO_4^{-2} μm	PO_4^{-3} μm
0	Pre	3.2	0.86	2.6	0.17	0.019	18	<DL	1.8	<DL	1.5	<DL	<DL	0.105	0.22	-	92	-	<DL	7
1	15.8	3.7	0.75	7.8	0.31	0.129	21.6	0.44	1.8	<DL	2.42	20	11	1.48	0.67	16	10	-	79	8
2	45.7	3.7	0.79	8.9	0.298	0.249	10.8	0.293	2.01	53	4.3	30	<DL	0.94	0.69	9	30	1.5	151	4
3	92.0	3.7	0.79	5.5	0.33	0.214	8.8	0.42	2.2	39	3.9	20	<DL	1.34	0.6	7	13	-	123	4
4	209.3	3.8	0.79	5	0.07	0.253	14.3	0.57	0.9	60	4.9	<DL	3	1.85	<DL	9	11	-	116	-
5	353.5	3.9	0.78	4.5	0.04	0.281	23.1	0.71	0.97	59	5.4	130	5	2.28	<DL	13	13	4.2	108	-
6	526.3	4.0	0.76	7.3	0.25	0.294	36	0.97	0.4	46	7.3	<DL	7	3.3	0.56	15	19	-	110	5
7	695.5	4.0	0.74	1.8	0.092	0.25	49	0.91	0.8	45	6.9	60	5	2.89	0.13	14	18	-	96	-
8	863.3	4.0	0.76	1.7	0.106	0.238	65	0.97	1.2	44	7.5	40	7	3.04	0.14	14	14	3.8	93	-
9	1173.3	4.0	0.75	3	0.1	0.244	85	1.03	0.08	37	8.4	42	4	3.5	0.14	15	15	-	94	-
10	1243.2	4.0	0.72	3.2	0.13	0.244	89	1.05	0.18	36	8.6	34	5	3.6	0.12	15	16	-	93	-

†Calculated by speciation. ♯Measured using the manometric method (Luhmann et al., 2013). <DL = Below the detection limit.

Table 4.3: Single-pass experiments

Sample #	Time hrs.	pH† -	$CO_2^\sharp$ m	Al^{+3} μm	Ba^{+2} μm	Ca^{+2} mm	Co μm	Cr μm	Cu μm	Fe^{+2} μm	K^+ mm	Li^+ μm	Mg^{++} mm	Mn^{+2} μm	Na^+ mm	Ni μm	Si mm	Sr^{+2} μm	Zn μm
single-pass 1, flow rate = 0.1 mL/min																			
Initial		3.4	0.75												940				
1	1.65	4.2	0.64	11	3.4	1.12	7.1	2	36	600	2.54	30.6	0.175	20.1	920	72	0.93	5.9	35
2	17.54	3.7	0.69	41	0.5	0.211	<DL	2	45	149	0.88	26.7	0.04	2.9	910	32	1.33	1.1	41
3	24.36	3.6	0.71	12	0.19	0.175	<DL	<DL	21	125	0.76	26	0.029	1.9	910	9	1.36	0.82	32
4	47.49	3.7	0.7	11	0.08	0.225	<DL	<DL	7	102	0.73	25	0.017	1.3	920	9	1.43	0.61	56
5	67.93	3.6	0.68	11	0.1	0.095	<DL	<DL	<DL	88	0.75	24	0.016	1	920	9	1.49	0.56	63
single-pass 2, flow rate = 0.1 mL/min																			
Initial		3.4	0.75												940				
1	1	4.7	0.58	6	9	5.2	10	3	24	200	2.71	<DL	3.2	137	890	67	0.92	10.1	30
2	18	4.0	0.73	18	1.4	0.8	<DL	4	<DL	200	1.3	<DL	0.3	8	910	2	1.07	2.5	29.2
3	40.85	3.7	0.72	17	0.14	0.32	<DL	4	<DL	100	0.75	<DL	0.07	0.8	920	<DL	1.24	1.3	50
4	64.72	3.6	0.69	15	<DL	0.178	<DL	2	<DL	74	0.69	<DL	0.026	<DL	920	2	1.27	0.77	55

†Calculated by speciation. ♯Measured using the manometric method (Luhmann et al., 2013). <DL = Below the detection limit.

Table 4.4: XPS analyses of pristine and experimental samples

Element Ratio	Pristine	RC	SP1	SP2
Si/K	6.8	55	10.	15
Si/Al	5.1	3.3	1.9	2.0

Table 4.5: Potential Reactions Governing Fluid Composition

	Reaction	Si(aq)/K(aq)	Si(aq)/Al(aq)
(4.6)	K-feldspar + 4 H^+ + 4 H_2O → Al^{+++} + K^+ + 3 H_4SiO_4(aq)	3	3
(4.7)	K-feldspar + H^+ + 6 H_2O → boehmite + K^+ + 3 H_4SiO_4(aq)	3	-
(4.8)	K-feldspar + H^+ + 4.5 H_2O → 0.5 kaolinite + K^+ + 2 H_4SiO_4(aq)	2	-
(4.9)	1.5 K-feldspar + H^+ + 6 H_2O→ 0.5 muscovite* + K^+ + 3 H_4SiO_4(aq)	3	-

*Note that muscovite is not expected to form in our experiments (too low of temperature (Montoya and Hemley, 1975; Aja et al., 1991)), but is used here to represent idealized clay stoichiometry.

in both cores for which measurements are available, even though these cores were subjected to significantly different experimental durations and solution compositions ((i.e., 52 days, deionized water, approaching equilibrium (recycling) vs. ∼3 days, far-from-equilibrium NaCl brine (single-pass)). Permeability decreased by about a third in all three experiments, with the permeability reduction in the recycling experiment, the only one for which real-time measurements are available, being the most dramatic and tending to mostly occur during the initial stages of the experiment (Fig. 5.1). Calculations of porosity along the length of the experimental cores give values that are both greater than and less than the pristine value (Fig. 5.2). Interestingly, measurements of local core porosity are generally greater than the pristine value in the single-pass experiment samples and generally less than the pristine value in the recycling experiment samples. The single-pass experiment cores show their highest XRCT-calculated specific surface areas near their upstream faces, where the experimental fluid was farthest from equilibrium and most capable of dissolving primary minerals and producing secondary phases (Fig. 4.8, 4.9). The greater specific surface area values tend to be associated with larger calculated porosities, although several of the single-pass analyses indicate higher surface area linked to lower porosity. The lowest porosities in the recycling experiment core were calculated from samples obtained near its upstream face; however, in this core, nearly all measurements demonstrate low porosity associated with high surface area. Unfortunately, the XRCT image grayscale contrast between primary and secondary phases does not allow for separation and quantification of the relative amounts of primary versus secondary phases (Fig. 4.9).

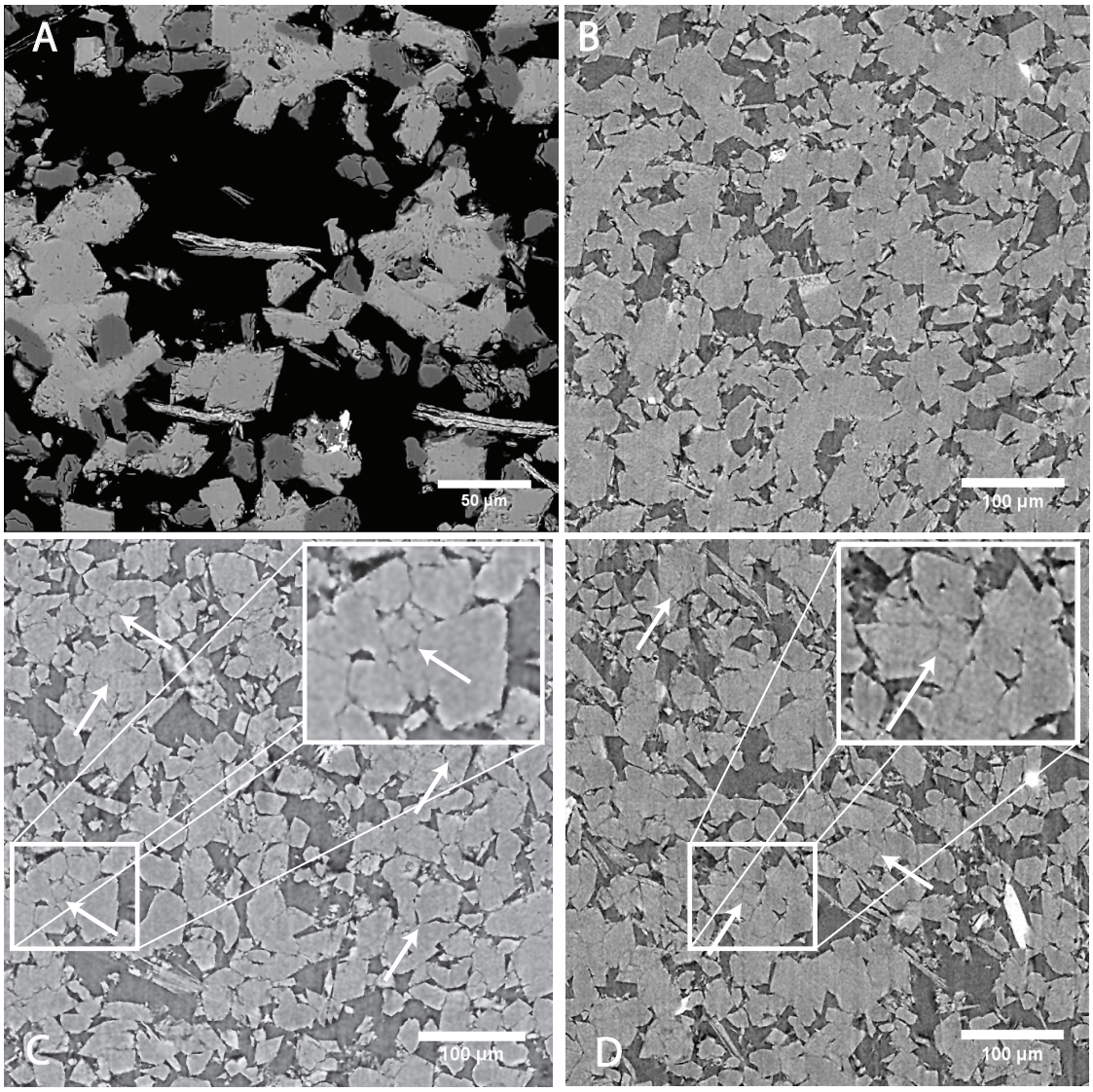

Figure 4.9: Imagery showing core mineralogy, porosity, and grain-binding cement dissolution. A) Backscatter SEM image showing distribution of K-feldspar (light), quartz (dark), and micas (sheets) in the sample prior to experiment. Note that individual sediment particles are made up of both K-feldspar and quartz. Comparing the SEM image with synchrotron XRCT images of the pristine sandstone sample (B) and samples taken near the upstream faces of cores taken from the recycling experiment (C) and single-pass experiment 2 (D) reveals that minerals separated along grain boundaries (indicated by arrows) as a result of experimental dissolution. Note that the dissolution appears to occur between K-feldspar and quartz grains.

Table 4.6: Summary of parameters measured on the three cores before and after the experiments

	Mass (g)			Permeability (10^{-14} m^2)		
Experiment	Pre	Post	Change	Pre	Post	Change
recycling	5.632	5.509	-2.2%	5.7	3.6	-37%
single-pass 1	-	-	-	2.3	1.6	-30%
single-pass 2	5.659	5.538	-2.1%	4.7	3.5	-26%

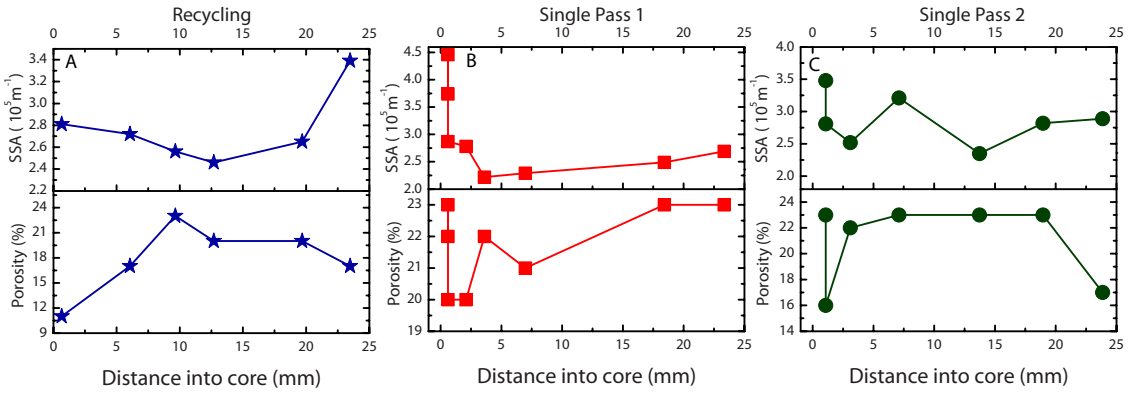

Figure 4.10: Total specific surface area (SSA) and porosity calculated from synchrotron XRCT imagery of ~1.5 × 1.5 × 1.5 mm^3 sandstone subsamples (full-core diameter = 12.8 mm) that were subjected to recycling (A) and single-pass (B,C) experiments. For comparison, values of SSA and porosity calculated from pristine samples are 2.36 m^{-1} and 21%, respectively.

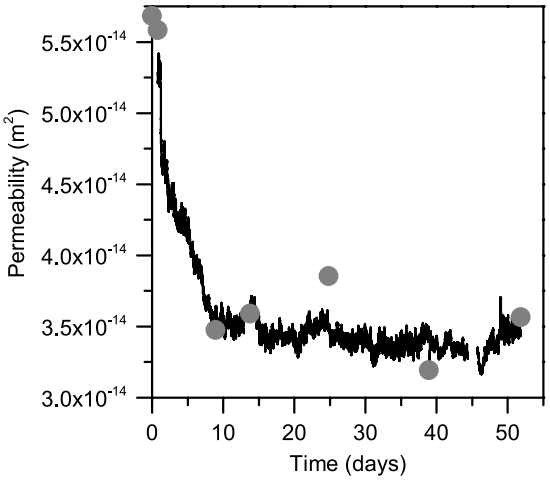

Figure 4.11: Permeability evolution during the recycling experiment. Data has been smoothed by taking an hourly average of the measured values. Gray symbols represent permeabilities obtained by cycling through a series of flow rates.

4.5 Discussion

4.5.1 K-feldspar dissolution

K-feldspar dissolution rates plotted as a function of chemical affinity are in relatively good agreement with rates calculated using the Helgeson et al. (1984) rate constant formulation and affinity parameters $p = 0.16$ and $q = 1.4$ reported by Alekseyev et al. (1997) (Fig. 4.6). Although the chemical affinities plotted in Fig. 4.6 were calculated from fluids sampled after exiting the reaction vessel and therefore represent the nearest-to-equilibrium status exhibited by the fluid, the agreement between the calculated lines and experimental measurements tends to be quite good, particularly when considering the uncertainty associated with calculating rates from our experiments. In particular, it appears that the shape of the K-feldspar dissolution curve plotted for the recycling experiment is approximated well by the Alekseyev et al. (1997) parameters. For comparison, we have additionally plotted a form of Eqn. 6.4 assuming that p=q=1 for pH = 4 (the calculated pH for the final 5 recycling experiment samples (Table 4.2)) in Fig. 4.6. This form of the equation tends to considerably overestimate the reaction rates calculated from not only the recycling experiment, but also the single-pass experiments: an equivalent curve calculated at pH = 3.6 (the calculated pH for the final single-pass experiment samples (Table 4.3)) would be around twice as fast as the K-based rates plotted in Fig. 4.6, and an equivalent curve calculated at pH = 3.4 (the inlet solution pH) would be around 4 times as fast. It is important to note here that, although the K-feldspar dissolution rate data that we have collected appear to provide an opportunity for regression of new parameters for use in Eqn. 6.4, we have chosen not to perform such a regression due to the uncertainty in the rate calculations.

The relatively good agreement between these measured and calculated K-feldspar dissolution rates is interesting because our values were measured on full rock cores rather than powdered samples. Conventional wisdom may have postulated that they would differ from laboratory values by several orders of magnitude due to the classic "field-lab rate discrepancy," problems with quantifying reactive surface area, and potential controls of secondary mineral precipitation on surface area and chemical affinity. However, it appears that our combined XRCT/XRD method of surface area quantification yields one potential method of avoiding these classic problems. It is

important to note, however, that the sandstone employed here is composed of abundant, well-connected pores surrounded by relatively well-mixed minerals. Other, more carbonate-rich samples, such as the monomineralic limestone (Luquot and Gouze, 2009; Gouze and Luquot, 2011), dolomite (Luhmann et al., 2014), and the dual mineral calcite-dolomite (Smith et al., 2013; Hao et al., 2013; Carroll et al., 2013a) and quartz-magnesite systems (Salehikhoo et al., 2013; Li et al., 2014) typically appear to be less well-behaved. This discrepancy may be due to the fact that carbonates tend to have relatively high reaction rates and heterogeneous distributions of pores and minerals. Nevertheless, the XRCT methods employed here can likely aid in the resolution of this problem by examining, in 3D, the dimensions of connected pore space.

4.5.2 Metal release from sandstones

Mobilization of trace metals has been noted as a potential concern in CCUS reservoirs (e.g., Siirila et al., 2012; Karamalidis et al., 2012; Navarre-Sitchler et al., 2013; Kirsch et al., 2014; Shao et al., 2014). The initially rapid rates of Ca addition to the experimental fluids and subsequent leveling off or absence of Ca in fluid samples, suggests that Ca-bearing materials (i.e., carbonate cement or shells) dissolve predominantly during the initial stage of both the single-pass and recycling experiments. The elevated fluid concentrations of Ca, Mg, Mn, Ni, Sr, Ba, Co, Cu, and Fe in the early phases of the single-pass experiments (Table 4.3) suggest that CO_2 injection into the subsurface can mobilize metals trapped within reservoir minerals. The association of the mobilization of these metals with the elevated concentrations of Ca suggests that these elements are likely included in the structure of the carbonate cements within the sample, which is in agreement with other studies of CO_2-H_2O-sandstone interactions (e.g., Kirsch et al., 2014). The short duration of their appearance in the experimental fluid and the rapid decline in calcite saturation state suggests that the mobilization of these metals is unlikely to be a major concern in sandstone reservoirs over the time scale of CCUS operations. Nonetheless, fluid concentrations of Zn show the opposite trend of other measured metals, suggesting that perhaps mobilization of this element is related to a different dissolution process that may be of concern over longer time scales.

4.5.3 Alteration mineral precipitation

A summary of potential reactions governing fluid composition are listed in Table 4.5. These end-member reactions assume the dissolution and precipitation of pure, stoichiometric phases, which inherently ignores the formation of Al- or Si-rich leached layers and the various phyllosilicates (e.g., illites, smectites) for which reliable thermodynamic data and accurate formulas are unavailable. Furthermore, these reactions suggest that K-feldspar, and not quartz, is dominating the fluid chemistry during the experiments. We show below that this is a reasonable approximation and that the reactions in Table 4.5 can accommodate the non-stoichiometric nature of the experimental fluid concentrations.

By simultaneously considering the solid and fluid chemical data sets presented in Tables 4.2, 4.3, and 4.4 and the potential reactions listed in Table 4.5, we can attempt to discern the stoichiometry and mineralogy of the alteration phases precipitating in our experiments. Specifically, in the recycling experiment, a Si/K ratio of slightly more than 3 persists throughout all chemistry samples (Fig. 4.4A). This observation, alongside the consideration that aluminum concentrations are invariably low in the analyzed fluids (Table 4.2), suggests either Reaction 4.7 or 4.9 is controlling the evolution of the fluid chemistry in the recycling experiment. In the case of the recycling experiment, where the secondary mineralization appears to fully coat the grain surfaces to a depth of a few hundred nm (Fig. 4.7), the XPS measurements can help to discern the composition of the precipitated phase. The XPS data show enrichment of Al and Si and strong depletion of K in the post-experimental measurements (Table 4.4), which can effectively preclude the formation of a K-rich (i.e., muscovite-like) phase according to Reaction 4.9. We therefore assume that boehmite, which is more stable than gibbsite at 150°C (Tutolo et al., 2014a), is the dominant alteration phase formed during the recycling experiment, according to Reaction 4.7. Boehmite has been shown elsewhere to form from feldspars at similar temperatures in pure water, KCl-bearing, and HCl-bearing solutions (Lagache, 1965; Fu et al., 2009; Lu et al., 2015, respectively).

Unlike the recycling experiments, the single-pass experiments do not approach stoichiometric, 3:1 release of Si and K from K-feldspar at any point during the experimental runs (Fig. 4.4A). Initially, the solution chemistry indicates that K is being released at a rate significantly faster than Si (Fig. 4.4A, 4.5), which is consistent with the approach to steady-state feldspar hydrolysis rates shown elsewhere (e.g.,

Schweda, 1990; Hellmann, 1994). After approximately 25-30 hours of the experimental run, fluid samples asymptotically approach a Si/K value of 2, indicating a tendency towards Reaction 4.8 governing fluid chemistry. The apparent immobility of Al and Si compared to K during the early time of the single-pass experiments suggests that initial acidic brine attack of the feldspar surface preferentially leaches K^+ ions. As the experiments progress, the rate of K release slows to a similar rate in both experiments, as Si release increases (Figs. 4.5B,C) to approach a Si/K release rate of 2:1, consistent with the production of kaolinite according to Reaction 4.8. Other researchers have experimentally demonstrated a Si/K ratio of ∼2:1 in NaCl-bearing K-feldspar dissolution experiments at similar conditions (Rafal'skiy et al., 1990; Alekseyev et al., 1997), and Rafal'skiy et al. (1990) suggest that kaolinite precipitation was coupled to feldspar hydrolysis in their experiments.

The morphological characteristics of the precipitates formed in each experimental style tend to agree with the conclusion that different minerals are forming in the two experiments (Figs. 4.7, 4.8). Specifically, the recycling experiment tends to exhibit small, rounded minerals that coat the entire grain surface (Fig. 4.7 A,B), whereas the single-pass experiments form both discrete clusters of lath-shaped minerals as well as nano-scale, surface-coating nuclei (Fig. 4.8). Clay minerals can manifest themselves in an array of morphologies, which makes positive identification by these image data sets difficult. However, the dominance of the rounded precipitates in the recycling experiment and lath-shaped crystals in the single-pass experiments is generally consistent with the formation of boehmite and kaolinite, respectively, in these two experiments.

All samples from all experiments are continually supersaturated with respect to both kaolinite and boehmite (Fig. 4.3) and remain within the kaolinite stability field throughout the experimental runs (Fig. 4.4B). However, the recycling experiment appears to have precipitated boehmite metastably, whereas the single-pass experiments appear to have produced kaolinite, the more supersaturated phase. Several factors differ between the single-pass and recycling experiments, but it appears that the addition of 0.94 mol/kg NaCl, which substantially increases the ionic strength of the experimental solution, may be the main driving force causing the difference in precipitating phases. Specifically, although one may hypothesize that this difference was related to either the flow rate or duration of the two experiment styles, these seem to be less likely to be able to explain the difference. The first sample from the

recycling experiment, which was obtained after 15.8 hours of flowing at 0.1 mL/min, has a Si/K ratio in excess of 3, whereas both single-pass experiments, which were both run at 0.1 mL/min, had asymptotically approached a Si/K ratio of ∼2 after a similar amount of run time. Thus, it appears unlikely that the difference in flow rates or experimental durations can account for the difference in precipitating phases. Furthermore, other aspects of solution chemistry, such as pH and CO_2 concentration, were in fact quite similar between the two experimental types. Thus, we suggest that the NaCl concentration, which is very different between the two experimental types, is the most likely reason for the difference in precipitating phases.

The mechanism by which the addition of NaCl to the experimental solution can enhance the formation of kaolinite relative to boehmite is not entirely clear, but some research suggests that NaCl may have an effect on the strength of Si-bearing bonds at the feldspar surface. Particularly, Strandh et al. (1997) used quantum chemical studies to show that NaCl strengthens the siloxane bonds within dissolving silicate minerals. Therefore, we suggest that, as K was being released from the feldspar structure during our NaCl-bearing single-pass experiments, the greater strength of the siloxane bonds relative to the K-bonds allow K to be preferentially released to the solution and for the remaining Al-Si-O-bearing feldspar structure to be converted to kaolinite. Alternatively, the precipitation of kaolinite could potentially be catalyzed by the presence of NaCl, which has been shown to catalyze kaolinite dissolution (Kline and Fogler, 1981). Both of these proposed mechanisms are admittedly tenuous extrapolations that would benefit from a more focused mechanistic study of the coupled dissolution and precipitation process. Nonetheless, both mechanisms could potentially account for the difference in the Si/K ratios observed in the fluids sampled from the single-pass and recycling experiments.

4.5.4 The effect of experimental alteration on hydrogeochemical properties

The measured mass and permeability decrease in all cores supports the net efflux of certain mobile elements (e.g., K and Si) and the production of the Al-rich secondary phases deduced above. The similar measured changes in mass between the two experiment types (Table 4.6) suggests that approximately the same amount of dissolution and precipitation occurred in all experiments in spite of their different durations. This similarity is consistent with the fact that the single-pass brine remained

far from equilibrium and highly reactive over the entire experimental runs, and the recycling experiment fluid became gradually less reactive as the experiment went on. Local porosity generally increased in the single-pass experiments and decreased in the recycling experiments, which suggests a transition from a dissolution-dominated regime to a precipitation-dominated regime with reaction progress.

Qualitatively, the porosity and permeability data show that porosity decreases in certain areas of the core have the ability to decrease the bulk permeability of the entire core, regardless of porosity increases in other sections of the core. This finding is consistent with the concept that the bulk permeability of materials in series is dominated by the lowest permeability layer and may be calculated according to the harmonic mean of their individual permeabilities (e.g., Saar and Manga, 2004; Alexander and Saar, 2012). Considerable scatter does exist, however, in the XRCT-based calculations, and it is therefore important to reiterate that the data plotted in Fig. 5.2 were calculated on XRCT data sets obtained from samples $<1.5\times1.5\times1.5$ mm^3, and thus represent a small sub-sample of the full-core cross section (core diameters are 12.8 mm). Ideally, several samples would have been analyzed at each interval such that the averaged result would be more representative of the full-core cross section. However, due to the limited synchrotron beamtime and the large quantities of data involved in these calculations (each of the points plotted in Fig. 5.2 represents $\sim$40 GB of data), we were unable to produce such a rich data set. The calculated porosity changes may have been caused solely by coupled dissolution and precipitation reactions, but it is also possible that the flow rates utilized here (which are considerably higher than those which the core samples would have experienced in situ in the sample reservoir) caused fine particles within the sample to migrate into pore throats during the initial stages of the experiment. In either case, each of the three experiments only demonstrated about a one third total reduction in permeability, and the majority of the permeability changes in the 52-day recycling experiment occurred during the initial, far-from-equilibrium stage of reaction, where natural and engineered systems are only expected to exist for relatively brief periods of time. Therefore, based on these observations, it seems likely that CO_2-induced feldspar weathering will negligibly affect fluid injectivity at CCUS reservoir scales.

Table 4.7: Rate parameters utilized in analysis and reactive transport simulations.

Mineral	$\log_{10}(k_{25})^{\dagger}$ (mol/cm^2/s)	E_A (kJ/mol)	n	p	q	Ref.
K-Feldspar	-8.39*	-	1	0.16	1.4	1 + 2
Kaolinite$^{\sharp}$	-15.31	65.9	0.777			3
Quartz	-17.40	90.9				3

1: Helgeson et al. (1984) 2: Alekseyev et al. (1997) 3: Palandri and Kharaka (2004)
*In order to avoid confusion between $\Delta H^{\ddagger}$ and E_A (see Sect. 4.2.2), we report the value calculated at 150°C
$^{\dagger}k_{25}$ = Mineral dissolution rate constant computed at pH=0 and 25°C (see, e.g., Palandri and Kharaka (2004)).
$^{\sharp}$We have approximated the kaolinite precipitation rate constant as being equivalent to its dissolution rate due to the lack of an appropriate parameterization at our pH and temperature conditions.

4.5.5 The coupled evolution of fluid chemistry, mineral reaction rates, and hydrogeochemical properties

The primary mineral surface area that is created and destroyed by dissolving along grain boundaries, forming etch pits, or precipitating secondary phases will affect the overall reactivity of sandstone minerals. Furthermore, as evidenced by the gradient in solid phase changes along the length of the experimental cores (Fig. 5.2), and the observed evolution of reaction rates and saturation states with reaction progress (Fig. 4.6), the core-scale reaction rates we calculate above and the sampled fluid chemistry are a bulk average of processes that occur as the experimental fluid is transported through and partially equilibrates with the experimental core. Parameterization of the coupled effects of dissolution and precipitation reactions on the evolution of porosity, permeability, and specific surface area in our Eau Claire samples for incorporation into continuum-scale models will require direct, in situ observations of the coupled evolution of these parameters. Time-resolved techniques such as "4D" XRCT experiments or pore-scale reactive transport simulations based upon 3D data sets of the type presented here will be particularly useful in the development of these parameterizations (e.g., Navarre-Sitchler et al., 2009; Molins et al., 2012; Steefel et al., 2013).

In spite of their inability to produce these direct parameterizations, simple, continuum-scale reactive transport simulations can help us to gain a better understanding of the progression of reaction rates and fluid chemistry as the fluid travels along the length of the experimental core. To this end, we have conducted five reactive transport simulations to examine the effects of quartz reactivity and kaolinite surface area on K-feldspar dissolution rate, fluid chemistry, and core porosity during the single-pass experiments (Table 6.3). For these numerical experiments, we have chosen to

only simulate the single-pass experiments in order to avoid the added complications brought about by the recycling process. Nonetheless, the general observations produced from these numerical simulations additionally apply to the analysis of the progression of reactions and solution chemistry as the fluid flowed through the recycling experiment core.

The first of the five simulations was performed to validate our PFLOTRAN model implementation by using the average K-based K-feldspar dissolution rates from the two single-pass experiments, and the other four utilize the Helgeson et al. (1984) pH-dependent K-feldspar dissolution rate parameterization coupled to the Alekseyev et al. (1997) affinity factors (Table 4.7), which we have shown above to be in reasonably good agreement with our experimental values. In all simulations, core porosity was assumed to be the average, pristine value measured by synchrotron XRCT (Table 4.1), and rate parameters for quartz and kaolinite were obtained from the literature (Table 4.7). One set of two simulations was run by assuming that kaolinite surface area was equivalent to K-feldspar surface area (a conservative overestimate), and a second set of two simulations was run assuming that kaolinite covers 10% of the surface area of the K-feldspar. This value (10%) is an arbitrary approximation that is simply intended to test the effect of imposed reactive surface area changes on outlet fluid chemistry. It is made even more arbritrary by the fact that we are approximating the kaolinite precipitation rate constant as being equivalent to its dissolution rate constant (Table 4.7), which is potentially an overestimate (Nagy et al., 1991; Devidal et al., 1997). Furthermore, the starting mineral composition in all simulations is fixed at 50% K-feldspar and 50% quartz, which, in practice, means that, in these reduced surface area simulations: 1) 10% of the K-feldspar surface is non-reactive; 2) kaolinite is effectively allowed to precipitate over 10% of the K-feldspar surface; but 3) kaolinite is not present at the beginning of the simulation. In each simulation set, quartz was either "reactive" (i.e., quartz surface area = 50% of the total core surface area) or completely inert. As with the kaolinite surface area, these two end members were chosen arbitrarily to test the effect of quartz reactivity on fluid chemistry. All simulations were run for 72 hours, which is approximately the average duration of the two single-pass experiments, in order to evaluate the effect of these steady-state reactions on core-scale porosity.

A number of observations can be made based upon the results of these five numerical experiments (Fig. 4.12). The simulation employing the rate derived in this study

Table 4.8: Summary of reactive transport simulations

#	Description†	ksp SA 10^5 m^{-1}	qz SA 10^5 m^{-1}	kln SA 10^5 m^{-1}
1	kln SA = ksp SA Derived Rate	1.18	1.18	1.18
2	kln SA = ksp SA H84+A97	1.18	1.18	1.18
3	kln SA = 10% ksp SA H84+A97	1.062	-	0.118
4	kln SA = ksp SA, qz inert H84+A97	1.18	1.18	1.18
5	kln SA = 10% ksp SA, qz inert H84+A97	1.062	-	0.118

†kln = kaolinite; ksp = K-feldspar; qz = quartz; H84 = Helgeson et al. (1984); A97 = Alekseyev et al. (1997)

produces outlet K concentrations in excellent agreement with those measured at the conclusion of both single pass experiments (diamonds in Fig. 4.12C). However, the outlet Si/K ratios (∼2.4), and the outlet Al concentration (∼4 μmol/kg) are greater than and less than, respectively, those measured during the experimental runs, which suggests that Si-donating quartz and Al-sequestering kaolinite are reacting faster in the simulation than in the experiments. Furthermore, as noted above, this derived rate is the bulk average of processes occurring along the length of the core and inherently ignores the effect of pH increases and chemical affinity decreases caused by K-feldspar dissolution, which clearly have the capacity to influence the K-feldspar dissolution rate (Figs. 4.6, 4.12A).

The simulations that incorporate the pH and chemical affinity dependency into the K-feldspar rate calculations all produce outlet K concentrations in relatively good agreement with the experimentally measured values. However, similar to the simulation run with the derived rate, these simulations produce Si/K ratios higher than measured if quartz is allowed to react and Al concentrations lower than measured if kaolinite surface area is assumed to be equivalent to K-feldspar surface area. Notably, quartz reactivity has practically no effect on K-feldspar reaction rate (Fig. 4.12A). However, if kaolinite is assumed to cover 10% of the K-feldspar surface as discussed above, both K-feldspar and kaolinite are slower to react. K-feldspar's reaction rate along the core is slower partially because its surface area is 10% blocked[3], but mostly because sluggish kaolinite precipitation rates allow more Al and Si to remain in solution and maintain the solution closer to K-feldspar saturation. The slower reaction rate causes the outlet K concentration to be ∼25% lower than in the higher surface

[3] An additional simulation run with kln surface area = 10% ksp surface area, but ksp SA = 50% core surface area (1.18×10^5m^{-1}), yielded an outlet K concentration and Si/K ratio that were very similar to simulations with Ksp surface area = 40% core surface area (1.062×10^5m^{-1}), but outlet Al concentrations that were ∼10 μmol higher. This simulation was not included in Fig. 4.12 for clarity. Nonetheless, the relatively small effect of a 10% reduction in K-feldspar surface area on measured K concentrations suggests that our decision to employ the pristine surface area for all rate calculations above is a reasonable approximation.

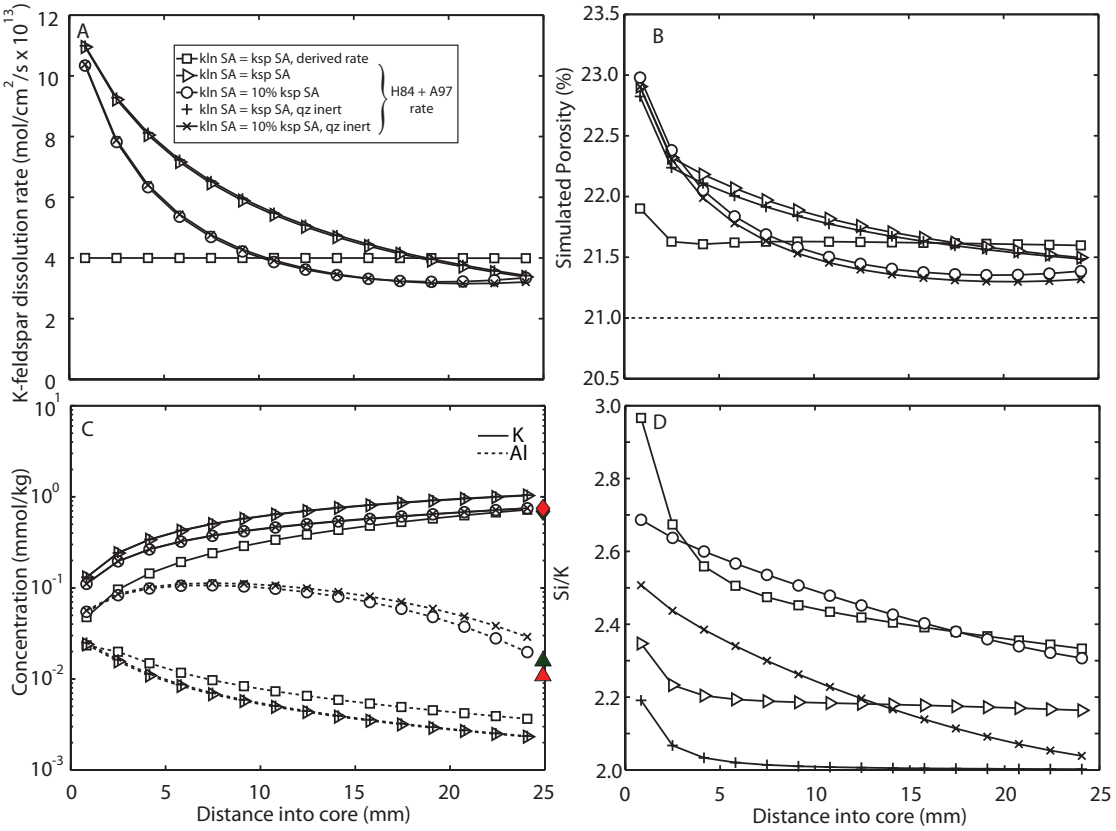

Figure 4.12: Five reactive transport simulations were run in order to explore the coupled evolution of fluid chemistry, mineral reaction rates, and hydrogeochemical properties during the single-pass experiments. One simulation was run using the average K-based K-feldspar dissolution rate derived from the two single-pass experiments presented in this study. Four other simulations were run using the temperature- and pH-dependent feldspar rate parameterization presented by Helgeson et al. (1984) (H84) and affinity factors (p and q in Eqn. 6.4) presented by Alekseyev et al. (1997) (A97). These four scenarios were designed to test the effect of quartz (qz) reactivity and kaolinite precipitation rate on the K-feldspar dissolution rate and composition of the sampled fluids. We have plotted K-feldspar dissolution rate (A), porosity (B), Al and K concentrations in the fluid (C), and Si/K ratio (D) as a function of distance along the core from inlet to outlet. Measured "steady-state" concentrations of K (diamonds) and Al (triangles) from the single-pass experiments are plotted in C for comparison.

area simulations, and therefore in excellent agreement with the measured results. The outlet concentrations of Al in these reduced surface area simulations are also in better agreement with our measured values. Together, these observations suggest that, at steady state in the single-pass experiments, the kaolinite reaction rate and the effect of kaolinite precipitation on K-feldspar surface area and reaction rates are more similar to this scenario. Thus, these numerical experiments show that kaolinite precipitation during the single-pass experiments is occurring fast enough such that >95% of the Al liberated from the feldspar structure is precipitated before exiting the core, but slow enough such that it cannot be approximated as instantaneous. The kaolinite precipitation rate clearly has a large effect on the calculated K-feldspar saturation state and dissolution rate and therefore suggests that renewed effort into the quantification of Al mineral precipitation rates is warranted. In particular, a more advanced understanding of the association between secondary mineral precipitation rates and primary feldspar dissolution rates will greatly benefit from targeted isotope spiking of experimental materials (e.g., Gruber et al., 2013; Oelze et al., 2015).

The simulations run under the assumption that quartz is completely inert both produce Si/K concentrations in considerably better agreement with the experimental results than those run assuming that quartz is highly reactive. Therefore, these numerical experiments demonstrate that the imposed quartz rate constant and reactive surface area combine to produce a reaction rate that is higher than occurred during our experiment. The quartz reaction rates employed in these simulations were derived from measurements performed in pure water, which should allow for reasonable approximation of the rates observed in our experiments because quartz is apparently independent of cation concentration below pH $\approx$ 4 (Dove, 1995). Nonetheless, quartz is very unlikely to be fully non-reactive within our samples, and the fact that the observed Si/K ratio is slightly more than 3 in the recycling experiments (Fig. 4.4A) does suggest that quartz can contribute Si to the experimental solutions at these temperatures. All samples from all experiments, however, were close to equilibrium with respect to quartz (Fig. 4.3) and, therefore, it is likely that an appropriate affinity relationship for quartz dissolution would produce outlet fluid chemistry in better agreement with the experimental results.

In all five simulations, the core porosity increases along the entire length of the core, with the most dramatic changes occurring near the upstream face (Fig. 4.12).

These results qualitatively agree with the XRCT analyses of the single-pass experiments discussed above. Nonetheless, the fact that no porosity reductions are calculated to occur suggests that some of the porosity-reducing processes are not being captured in this simplfied model. Therefore, the classical porosity-permeability relationships implemented in many reactive transport models would in fact predict permeability increases in the single-pass experimental cores. As noted above, the porosity reductions that occurred during our flow-through experiments may have been a function of coupled dissolution/precipitation processes, or, alternatively, the mechanical transport of grains within the sandstone matrix. The model is incapable of simulating this latter process, and the tentative nature of the kaolinite precipitation parameterization used in these experiments precludes a definitive analysis as to which of these two processes is dominating the observed permeability reductions.

4.6 Conclusions

In this study, we have presented single-pass and recirculating flow-through experiments conducted on K-feldspar-rich sandstone cores at 150°C and 200 bar. By characterizing fluid and solid samples from these experiments using a suite of analytical and numerical techniques, we have explored the coupled evolution of fluid chemistry, mineral reaction rates, and hydrogeochemical properties during CO_2 sequestration into feldspar-rich sandstone. In general, our experimental, analytical, and numerical results confirm predictions that the heightened acidity resulting from supercritical CO_2 injection into feldspar-rich sandstone will dissolve primary feldspars and precipitate secondary aluminum minerals. A core through which CO_2-rich deionized water was recycled for 52 days decreased in bulk permeability, exhibited generally lower porosity associated with higher surface area in post-experiment core sub-samples, and produced an Al hydroxide secondary mineral, such as boehmite. However, two samples subjected to $\sim$3 day single-pass experiments run with CO_2-rich, 0.94 molal NaCl brines decreased in bulk permeability, showed generally elevated porosity associated with elevated surface area in post-experiment core sub-samples, and produced a phase with kaolinite-like stoichiometry. Notably, boehmite remained two orders of magnitude less supersaturated than kaolinite in all samples from all experiments, and we have proposed that the presence of NaCl in the single-pass experimental fluids is the most likely explanation for the difference in precipitating phases. In the single-pass experiments, we observed only limited CO_2-induced metal mobilization, which

we have suggested is most likely related to Ca mineral dissolution. By considering the relatively rapid approach to equilibrium, the relatively slow near-equilibrium reaction rates, and the minor magnitudes of permeability changes in these experiments, we can conclude that CCUS systems with projected lifetimes of several decades are geochemically feasible, even in the feldspar-rich sandstone end-member examined here.

An overall goal of this study was to use our experiments to assess and improve the certainty with which reactive transport models may be applied to CCUS systems. To do this, we calculated K-feldspar dissolution rates using changes in K and Si concentrations sampled from our experiments and K-feldspar surface area calculated from synchrotron X-Ray Computed Tomography (XRCT) analyses. The observation that these full-core rates are in relatively good agreement with literature parameterizations suggests that the latter can be confidently utilized to model CCUS in K-feldspar-rich sandstone. This realization is especially evident when one considers the overall uncertainty involved in applying reactive transport simulations to geologic systems, particularly related to thermodynamic data, diffusion/dispersion effects, and hydrogeochemical heterogeneities. Finally, by performing a number of reactive transport modeling experiments to explore processes occurring as the fluids traveled through the experimental cores, we have found that the overall progress of feldspar hydrolysis is negligibly affected by quartz dissolution, but more strongly impacted by the rates of secondary mineral precipitation and their effect on K-feldspar saturation state. The observations produced here are critical to the development of models of CCUS operations, yet more work, particularly in the quantification of coupled dissolution and precipitation processes, will be required in order to produce models that can accurately predict the behavior of these systems.

Chapter 5

Experimental observation of permeability changes in dolomite at CO_2 sequestration conditions

5.1 Summary

Injection of cool CO_2 into geothermally warm carbonate reservoirs for storage or geothermal energy production may lower near-well temperature and lead to mass transfer along flow paths leading away from the well. To investigate this process, a dolomite core was subjected to a 650-hour , high pressure, CO_2 saturated, flow-through experiment. Permeability increased from $10^{-15.9}$ to $10^{-15.2}$ m^2 over the initial 216 hours at 21 °C, decreased to $10^{-16.2}$ m^2 over 289 hours at 50°C, largely due to thermally-driven CO_2 exsolution, and reached a final permeability of $10^{-16.4}$ m^2 after 145 hours at 100°C due to continued exsolution and the onset of dolomite precipitation. Theoretical calculations show that CO_2 exsolution results in a maximum pore space CO_2 saturation of 0.5, and steady state relative permeabilities of CO_2 and water on the order of 0.0065 and 0.1, respectively. Post-experiment imagery reveals matrix dissolution at low temperatures, and subsequent filling-in of flow passages at elevated temperature. Geochemical calculations indicate that reservoir fluids subjected to a thermal gradient may exsolve and precipitate up to 200 cm^3 CO_2 and 1.5 cm^3 dolomite per kg of water, respectively, resulting in substantial porosity and permeability redistribution

5.2 Background

Deep geologic storage of the increasingly prevalent greenhouse gas carbon dioxide, CO_2, is a proven technology with promising prospects for mitigating the damaging

effects of climate change Bachu (2003); Lackner (2003); Pacala and Socolow (2004); McGrail et al. (2006); Friedmann (2007); Oelkers and Cole (2008); Benson and Cole (2008). In order for this technology to meaningfully impact global atmospheric greenhouse gas concentrations, however, the global population will need to dramatically increase the quantity of subsurface CO_2 injection operations Pacala and Socolow (2004). Of the geologic formations considered for geologic carbon storage (GCS), siliciclastic and carbonate basins have received the majority of the attention due to their size, abundance, flow properties, and storage capabilities Benson and Cole (2008). Both reservoir types have significant potential for storing CO_2, but carbonate reservoirs, which are typically composed of limestone or dolomite, abundant, and prevalent as depleted hydrocarbon reservoirsLi et al. (2006); Jobard et al. (2013), will be the focus of the present study.

Injection of surface-temperature CO_2 into geothermally warm reservoirs for GCS or geothermal energy production may result in depressed temperatures near the injection well and thermal gradients and mass transfer along flow paths leading away from the well Randolph and Saar (2011a). GCS reservoirs may develop a range of thermal gradients, depending on the temperature of injected CO_2, background reservoir temperature, and reservoir permeability Lu and Connell (2008); André et al. (2010); Rayward-Smith and Woods (2011). Operations that inject low-temperature CO_2 into warm reservoirs (e.g.,$\gtrsim$100°C), are especially likely to develop severe thermal gradients. Of particular concern are CO_2-based geothermal systems (e.g., CO_2-based Enhanced Geothermal Systems (CO_2-EGS)Pruess (2006) or CO_2 Plume Geothermal (CPG) systems Randolph and Saar (2011a)), where lowering the heat rejection temperature for power generation increases heat extraction efficiencies Randolph and Saar (2011a).

A number of studies have highlighted the effects of temperature, partial pressure of CO_2, and salinity on the solubilities of both CO_2 and carbonate minerals. Particularly, experiments and theoretical calculations illustrate the heightened solubility of carbonates in high pCO_2 solutions and the inverse dependence of CO_2 and carbonate solubility on temperature (Duan and Sun, 2003; Allen et al., 2005; Spycher and Pruess, 2005; Noiriel et al., 2009; Luquot and Gouze, 2009; Gouze and Luquot, 2011; André et al., 2007; Smith et al., 2012; Jobard et al., 2013). Additionally, the reservoir salinity has been noted as a factor affecting the solubilities of both CO_2 and carbonates in reservoir fluids (Duan and Sun, 2003; Allen et al., 2005; Drummond, 1981). The

inverse solubility of CO_2 and carbonates is expected to dissolve primary carbonates and increase permeability in the cool, near-well region and re-precipitate carbonates and decrease permeability as CO_2 and carbonates are exsolved and precipitated, respectively, in the geothermally heated reservoir André et al. (2010); Jobard et al. (2013). These chemical processes can affect reservoir *intrinsic* permeability through redistribution of solid phase volume, as well as the *relative* permeabilities of water and CO_2 through the evolution of free phase CO_2. As the pore space continuously fills with CO_2, the relative permeabilities of water and CO_2 with respect to to the intrinsic permeability will decrease and increase, respectively. The magnitudes of the relative permeability changes are rock- and regime-dependent, and changes in relative permeabilities resulting from thermally-driven CO_2 exsolution in GCS reservoirs has only been discussed in a limited number of studies Luhmann et al. (2013).

To date, research has primarily focused on the dissolution regime, but the precipitation and exsolution of carbonates and CO_2 as reservoir fluids flow up thermal gradients are similarly important Oldenburg (2007); Han et al. (2010); Rayward-Smith and Woods (2011). Because little experimental data regarding the precipitation of carbonate phases in high pCO_2 solutions exists, simulations of the formation of solid carbonate phases and the resulting flow property changes in GCS reservoirs remain uncertain. Precipitation rates of some carbonates have been measured at a variety of temperatures applicable to geologic CO_2 sequestration Plummer et al. (1979); Shiraki and Brantley (1995); Lebron and Suarez (1998); Teng et al. (2000), but data for dolomite precipitation remain considerably more sparse Arvidson and Mackenzie (1997, 1999), and experimental confirmation of dolomite precipitation in high pCO_2 fluids at temperature and pressure relevant to GCS has not been demonstrated. While the data presented by Arvidson and Mackenzie Arvidson and Mackenzie (1999) indicate that a dolomite-equilibrated fluid traveling away from the low-temperature, near-well region may overcome the substantial activation energy required to precipitate dolomite, their range of investigated concentrations needs to be expanded to determine the applicability to GCS. Experimental observations of the relationship between temperature, mineral volume changes, CO_2 dissolution/exsolution, and flow properties are required to address the long-term security and sustainability of GCS and CO_2-based geothermal energy reservoirs.

In this study, we used a flow-through experiment to observe the permeability and porosity effects of dolomite dissolution and precipitation and CO_2 exsolution at GCS

and CO_2-based geothermal energy reservoir conditions. We measured permeability changes in a dolomite rock core at a series of temperatures encountered in GCS reservoirs and examined, using high resolution X-Ray Computed Tomography (XRCT) and Scanning Electron Microscopy (SEM), the *in situ* development of flow pathways and precipitation of dolomite crystals within the experimental core. To expand upon the experimental results, we performed theoretical calculations to show the exsolution and precipitation capacities for a variety of geologic CO_2 storage conditions.

5.3 Experimental Design

The experiment described here is unique in that the reacting fluid was continually recirculated through a cylindrical (3.6 cm length $\times$ 1.31 cm diameter) Madison dolomite core, allowing it to approach equilibrium with the core mineralogy at each imposed temperature condition, unlike other, single-pass experiments, which maintain a fixed input fluid concentration (e.g., Noiriel et al. (2009); Luquot and Gouze (2009); Gouze and Luquot (2011); Jobard et al. (2013)). Although the flow rates employed in the experiment are somewhat elevated relative to natural flow rates (see SI) to facilitate accurate permeability measurement, recirculation of the reaction fluid allows for cumulative fluid-mineral reaction times that are more consistent with those encountered in field settings. The comparably long reaction times therefore allow the system to more closely approximate long-term CO_2 injection reservoir behavior. The flow-through experimental apparatus (Fig. S1) has previously been used to show thermally-induced exsolution processes in rock and sediment samples Luhmann et al. (2013). The experimental setup approximates an open thermodynamic system with respect to CO_2 by recirculating the fluid through a room temperature (21 °C), high pressure (110-126 bars) separator containing H_2O and supercritical CO_2 before each pass through the reaction vessel. Stainless steel screened Teflon endcaps at each end of the core prevent solid material from migrating into or out of the core, and a set of two computer-controlled Teledyne Isco syringe pumps recirculat $\sim$400 mL of deionized water through the core. Two additional syringe pumps maintain the pressure vessel assembly at a confining pressure of 200 bars and an outlet pressure of 110 bars, respectively.

To explore a range of temperatures that may reasonably be encountered in geologic CO_2 sequestration and geothermal energy production reservoirs, the experiment was sequentially run at 21, 50, and 100°C. The experiment proceeded at room temperature

(21°C) for the first 216 hours. The pressure vessel was then heated to 50°C from 216-505 hours and to 100°C from 505-650 hours using four independently controlled Watlow band heaters surrounding the pressure vessel. The abrupt transition from 21°C to the elevated experimental temperatures are somewhat more dramatic than those encountered in GCS reservoirs where heat can travel through advective and diffusive processes, but more gradual gradients would be difficult to apply on the small core sample employed here. Fluid flow rates were fixed at a series of constant values (see SI) and two high-precision Heise pressure transducers allowed for real-time measurement of pressure differential across the sample. Together, these two values provide the requisite data for calculation of permeability using Darcy's Law.

5.4 Geochemical Formulation

A module with a similar structure to SUPCRT92 Johnson et al. (1992) was assembled and employed in the calculation of equilibrium constants for reactions between dolomite, CO_2, and H_2O. Where required, a Matlab implementation of the EQBRM code Anderson and Crerar (1993) enabled speciation calculations at the temperature and pressure of interest based on equilibrium constant and mass balance constraints for the dolomite system. We included an explicit provision for the calculation of temperature-, pressure-, and ionic strength-dependent activity and fugacity coefficients in the speciation code. CO_2 solubility calculations performed with this assembled model are in good agreement with independent calculations performed using the virial equations of Duan and Sun Duan and Sun (2003). The Matlab scripts employed in the fluid chemistry calculations are included in the Supporting Information.

5.5 Results and Discussion

Permeability changes throughout the experiment were distinctly tied to the geochemical processes of CO_2 exsolution and dolomite dissolution and precipitation (Fig. 5.1). Permeability changes throughout the 21°C stage can be divided into three distinct periods: 1) a 5-hour period during which permeability rapidly increased from $\sim 10^{-15.9}$ m^2 to $\sim 10^{-15.5}$ m^2; 2) a 100-hour period during which permeability gradually increased to $\sim 10^{-15.2}$ m^2, and 3) a stabilized period that lasted until temperature was raised. The rapidly increasing period suggests that initial exposure of the dolomite

to the experimental fluid dissolved material along critical pathways and likely short-circuited portions of the core. The limited permeability increases during the subsequent, gradually increasing period suggests that further exposure to the experimental fluid only continued to enlarge preexisting flow pathways, but did not cause further critical path breakthroughs. The final, stabilized period indicates that any further dissolution that occurred had no measurable effect on permeability. Although the reaction regime may have evolved as the flow rate was cycled through a range of values during this period, theoretical considerations and a fluid sample taken near the end of the 21°C stage indicate that the experimental fluid remained far from dolomite saturation during the 21°C stage of the experiment (Fig. S3). At the end of the 21°C stage of the experiment, the concentration of fluid being injected into the reaction vessel was nearing the 50°C dolomite saturation concentration, ∼12 mmolal (see SI for modeled 21°C concentration), and it therefore likely reached equilibrium with respect to the Madison dolomite at 50°C. These theoretical calculations suggest that dissolution primarily occurred before core temperature was raised above room temperature, removing approximately 7% (0.8 g) of the core mass, if stoichiometric dissolution of crystalline dolomite is assumed.

Post-experiment, X-ray Computed Tomography (XRCT) imagery of the core reveals the development of large dissolution passages during the 21°C stage (Fig. 5.2). As shown in Fig. 5.2A, two connected, ∼1 cm long, conical passages were formed at the upstream end of the core. The total volume of these two passages calculated from the XRCT data is ∼0.066 cm^3 (∼ 2% mass, assuming well-crystallized dolomite), which is in agreement with the mass removal calculations described above when considering the proportion of the post-experiment pore volume they occupy (Fig. 5.2B). Figure 5.2B shows that the volume of the identified passages drops rapidly within the initial 0.2 cm of the core, then remains at 0.8×10^{-4} cm^3 for about 0.75 cm, and finally drops quickly to zero approximately one third of the way through the core. Similarly, the total pore volume drops dramatically and reaches a stable value of 0.5×10^{-4} cm^3 approximately one third of the way through the core. The spatial profiles of passage volume and total pore volume suggest that dissolution mainly occurred near the injection point. However, permeability is mainly determined by the narrowest pore throat along the flow pathways, such that these much larger passages have only minor contributions to the bulk permeability. By recalling the three periods of permeability changes at 21°C, it seems likely that these passages at the upstream end of the core

were predominantly enlarged during the third, stable period.

Upon raising core temperature to 50 °C, permeability rapidly fell to $\sim 10^{-15.9}$ m^2 , approximately the initial permeability, within 20 hours. As temperature was maintained at 50°C for 289 hours, permeability continued to fall to a minimum of $\sim 10^{-16.2}$ m^2. From 21°C to 50°C, the theoretical CO_2 exsolution capacity for CO_2-saturated deionized water calculated using the methods described in the CO_2 Solubility and Exsolution Capacity section below is 34.4 cm^3/kg. The total pore volume calculated from the XRCT data is 0.23 cm^3, which is equivalent to a porosity of $\phi \approx 0.047$. This implies that each pass of fluid through the core will generate $\sim 8 \times 10^{-3}$ cm^3 of free phase CO_2, and, if it remains within the core, CO_2 will totally fill the pore space in approximately 2 hours. Therefore, because both phases continued to flow through the core for the entirety of the experiment, most of the exsolved CO_2 must pass out of the core. By assuming that exsolved CO_2 and water within the core behaves according to the modified Darcy's law for two-phase flow Stauffer et al. (2009), and that water relative permeability behaves according to the Brooks-Corey model (Brooks and Corey, 1966), the relative permeabilities of water (k_{rw}) and CO_2 (k_{rCO_2}), the Leverett function, and the capillary pressure can be calculated (see SI). Results of these calculations show that both CO_2 saturation and relative permeability reach quasi-steady state within 10 hours of raising core temperature (Inset (b) of Fig. 5.1). Researchers have demonstrated similar behavior for a number of rock types and exsolution scenarios Luhmann et al. (2013); Zuo et al. (2012). At steady state, the calculated values for free-phase CO_2 saturation of the pore space (S_{CO_2}), k_{rw}, and k_{rCO_2} reach ∼0.5, ∼0.1, and ∼0.0065, respectively. Inset (a) in Fig. 5.1 shows the relative permeabilities as a function of pore space water saturation, S_w, which are in general agreement with values measured in similar exsolution experiments Zuo et al. (2012).

Temperature was raised once more to 100°C, causing dolomite and CO_2 to precipitate and exsolve, respectively, and reduce permeability to $\sim 10^{-16.4}$ m^2, half of an order of magnitude lower than the initial measured permeability. The calculated CO_2 exsolution capacity for the fluid flowing from the room temperature separator into the 100°C core is ∼146 cm^3/kg, but due to the combined effects of CO_2 exsolution and dolomite precipitation, it is not possible to examine relative permeabilities, as was done above for the 50°C period. Nonetheless, because the drop in permeability seems to occur directly after raising the core temperature to 100°C, it is likely that

the majority of the observed permeability decrease can be attributed to further CO_2 exsolution within the core.

At 100°C, dolomite precipitation from a CO_2-saturated fluid equilibrated with dolomite at 50°C is thermodynamically (Fig. 5.4) and kinetically Arvidson and Mackenzie (1999) favorable and can lead to substantial crystal growth, on the order of 0.44 cm^3/kg. X-Ray Diffraction measurements confirm that crystalline dolomite indeed formed during the experiment (see SI), but calculations of the total volume of dolomite precipitated in the largest passage (Fig. 5.2A), which should comprise the majority of the overall precipitated volume, is only 0.04 cm^3. It is not expected that the entire precipitation capacity could be met during the experiment due to the kinetics of dolomite precipitation at low degrees of supersaturation; however, the calculated precipitation capacity is on the same order of magnitude as the pore volume within the core and, therefore, supersaturation of both CO_2 and dolomite can dramatically affect sample permeability.

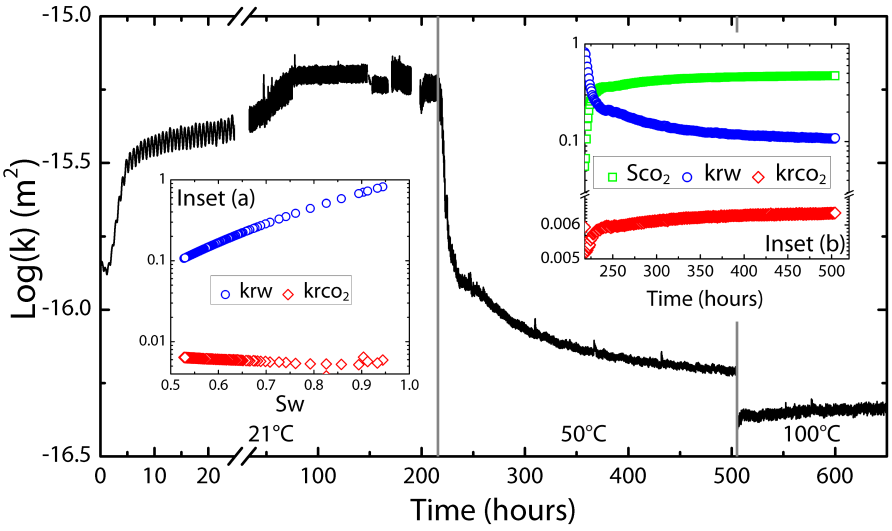

Figure 5.1: Logarithm of permeability, k, through time during a temperature series experiment on a dolomite rock core. Temperature was increased from 21°C to 50 °C at 216 hours and from 50°C to 100°C at 505 hours. Inset (a) Measured water relative permeability (k_{rw}) and calculated CO_2 relative permeability (k_{rCO_2}), as a function of water saturation (S_w). Inset (b) Calculated CO_2 saturation (S_{CO_2}), k_{rw}, and k_{rCO_2} as a function of time for the 50° stage.

The comparison between SEM micrographs of the host dolomite and the precipitated dolomite within the experimental sample (Fig. 5.3) allows further interpretation

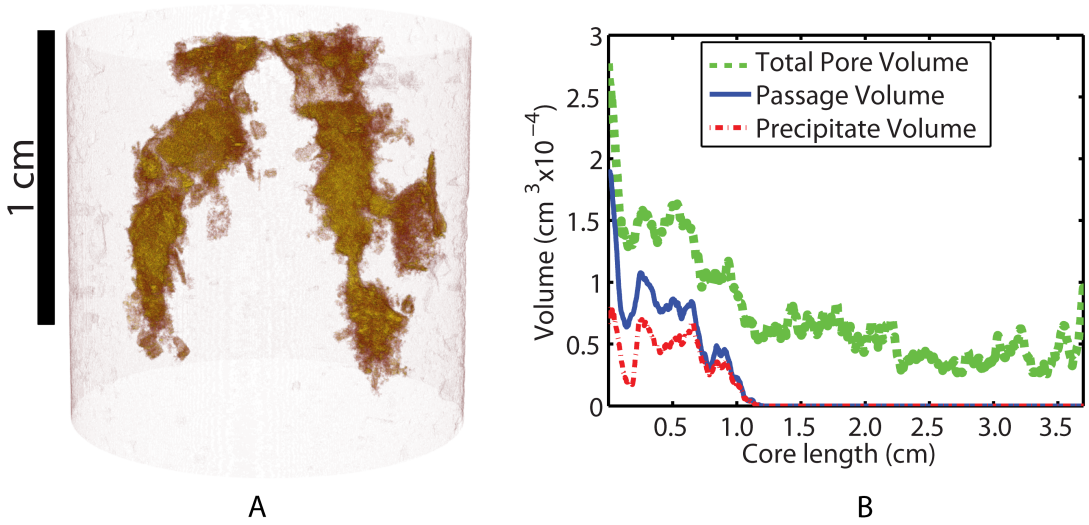

Figure 5.2: A) Post-experiment XRCT reconstruction of the upstream end of the Madison dolomite core (total core length is 3.6 cm). The largest connected flow path has been extracted, and precipitated dolomite within this passage is colored yellow. B) Total pore volume, passage volume, and the volume of the precipitated phase within the passage shown in A.

of the style of dissolution and precipitation dominating at different stages of the experiment. Notably, large crystals are apparent within a finer, cemented matrix in the sample prior to the experiment, and it appears that large dissolution passages formed by dissolving both the large crystals and fine-grained cement from selective flow pathways (Figs. 5.2, 5.3(a), and 5.3(c)) during the low-temperature stage of the experiment. These passages have been repeatedly shown to form and increase the permeability of carbonate samples exposed to acidic fluids Hoefner and Fogler (1988); Luquot and Gouze (2009); Gouze and Luquot (2011); Smith et al. (2012). The crystals shown in Fig. 5.3(c) must have become deeply etched during the lower temperature stage, because dolomite solubility dramatically decreases with increasing temperature. The lack of signs of growth on the crystal surface therefore suggest an absence of nucleation sites on the etched surface, or, alternatively, CO_2 trapped in the surrounding pore space prevented the supersaturated fluid from crystallizing dolomite in that region.

Although the crystals imaged in Fig 5.3(c) appear to have only experienced extensive dissolution and no subsequent growth, large, unetched dolomite crystals appear throughout the dissolution passage (Fig. 5.3(a), (d)-(f)). These crystals show signs characteristic of growth, including micron-scale dolomite crystals on their faces (e.g., Fig. 5.3 (a), (d)-(f)) and potential growth planes at step dislocations (e.g., Fig. 5.3(f)). Some of the crystals near the flow passage walls may have grown by enlarging preexisting dolomite crystals, but dolomite precipitation in the Teflon orifice downstream of the stainless steel screen (Fig. S2) and in the central parts of the enlarged flow passages requires that a significant portion of the dolomite crystals nucleated and grew from the supersaturated fluid. Areas of large voids separating precipitated dolomite, such as the one visible near the top of the right flow passage in Fig. 5.2A, suggest that dolomite growth is sensitive to the duration of fluid-mineral contact. This is emphasized by Fig. 5.2B, which shows that the precipitated dolomite almost entirely fills the final 0.5 cm of the dissolution passage, where the fluid than in upstream portions of the passage. Over the passage length, the precipitated volume and passage volume tend to covary, showing a tendency to decrease in total volume as the fluid travels away from the injection point. However, the fraction of the passage volume occupied by the precipitated dolomite tends to increase over this same distance as the fluid approaches the passage termination, again highlighting the dependency of dolomite growth on the duration of fluid-mineral contact. The substantial growth that occurred during the experiment suggests a potential rate-enhancing effect associated with the exsolution of CO_2 from carbonate-saturated fluids. In such a reaction regime, dolomite supersaturation and precipitation rate would be enhanced not only by the decreasing dolomite solubility with increasing temperature, but also by the evaporation of a portion of the water into the free CO_2 phase. In the presented experiment, this mechanism would be further exacerbated by the continued exsolution of fresh, water-undersaturated CO_2 as 21 °C, CO_2-saturated fluid is pumped into the core. The concentration of precipitated dolomite near the upstream end of the core, where the bulk of the CO_2 exsolution is expected to occur, lends support to this hypothesis. However, a more systematic study of dolomite precipitation rates at these conditions is required for accurate measurement and simulation of these processes.

In a similar experiment performed on a limestone rock core, Luquot and Gouze Luquot and Gouze (2009) noted a dependence of the rate of change of bulk permeability on proximity to the sample's critical porosity threshold, ϕ_c. Below this percolation

threshold, sample porosity is disconnected at the scale of the sample and the sample is effectively impermeable Saar and Manga (1999). Although the change in intrinsic permeability (as opposed to relative permeability effects during two-phase flow) with time in the presented experiment appears to evolve more gradually, dolomite formation in selective portions of the previously formed flow passages suggests that these considerations may be important at the sub-core scale. Progressive dolomite growth in certain locations within the bulk material may, as suggested by Luquot and Gouze Luquot and Gouze (2009) , lead to formation clogging over longer timescales associated with GCS and CO_2-based geothermal energy operations. Nonetheless, such effects were not directly observed in the present experiment, and the most dramatic permeability decreases appear to result from the relative permeability effects of CO_2 exsolution. The relatively small effect of dolomite precipitation on measured permeability is likely related to the fact that the majority of the precipitation occurred in the large dissolution passages that formed during the lower-temperature stages of the experiment, consequently allowing the porosity to remain far above ϕ_c.

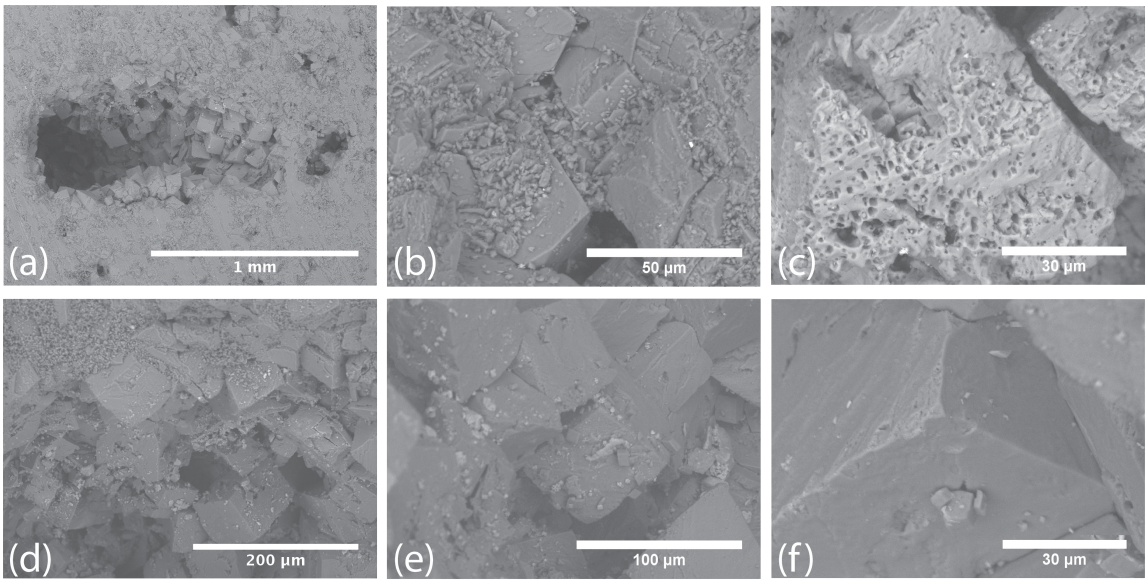

Figure 5.3: Post-experiment electron micrographs of the Madison dolomite core. (a) One of the large flow passages filled in with precipitated dolomite; (b) A minimally altered section of the core, between flow passages; (c) Deeply etched dolomite crystal at the edge of one of the flow passages; (d) Extensive crystal growth extending from the edge of a passage; (e) Large crystals showing signs of growth; and (f) Micron-scale crystals growing on the surface of a large crystal at the edge of the flow pathway.

5.5.1 CO_2 Solubility and Exsolution Capacity

The experiment illustrates processes that may occur in GCS and CO_2-based geothermal energy reservoirs as a result of an induced thermal gradient, but is limited to one set of temperature-pressure conditions. To expand upon this experiment, we calculate CO_2 exsolution and dolomite precipitation capacities for a range of reservoir conditions. These calculations, because they are derived from equilibrium solubility data, represent theoretical maxima. For the kinetically rapid CO_2 system, these calculations can be reasonably applied to natural systems; however, for the kinetically controlled dolomite system, the calculations may overestimate the amount of material that will precipitate over the lifetime of a CO_2 injection reservoir.

Because the Henry's Law constant and activity and fugacity coefficients are temperature- and pressure-, and in the case of activity coefficients, ionic strength- dependent, and P_{CO_2} is set by the reservoir pressure, the solubility of CO_2 in the subsurface is ultimately set by reservoir temperature, pressure, and fluid ionic strength. Figure 5.4A-C shows CO_2 solubility and exsolution capacity in 0.01 and 1 molal NaCl fluids at temperature and pressure conditions applicable to GCS The 0.01 molal curves are shown to illustrate the effect of ionic strength and salting out on CO_2 solubility. In reality, reservoirs with such low salt concentrations (i.e., <10,000 ppm) would not be considered for GCS Benson and Cole (2008); U.S.G.S. (2013).

It is apparent that CO_2 solubility slightly increases with pCO_2. For each investigated pressure (100, 150, and 200 bars), CO_2 solubility shows two temperature-dependent segments: a low-temperature, rapidly decreasing segment, and a high-temperature, increasing segment. The corresponding temperature at minimum CO_2 solubility decreases from ∼140°C for 100-bar pCO_2, to ∼130°C for 150-bar pCO_2, and to ∼120°C for 200-bar pCO_2. Furthermore, for higher pCO_2, CO_2 solubility appears to more strongly increase in the high-temperature stage. This diverging behavior mostly results from the increased nonideality and resulting low fugacity coefficients of CO_2 at the higher pressure and low temperature conditions Duan et al. (1992). This behavior, combined with the relatively high molar volume of CO_2 at 100 bars and all calculated temperatures leads to a dramatic difference in the calculated "CO_2 exsolution capacity", or the volume of CO_2 that will exsolve from a 25°C or 50°C solution during transfer to a higher temperature. The CO_2 exsolution capacity at 100 bars is significantly larger than at 150 and 200 bars, and thus would likely cause the most dramatic permeability reductions due to the presence of a nonaqueous CO_2

phase, similar to our experimental observations. The 200 bar exsolution capacities are relatively minor and will likely result in substantially less CO_2 exsolution and permeability reduction. This is an important consideration, because pressures >200 bars may commonly be encountered in conjunction with the high reservoir temperatures required for CO_2-based geothermal energy production Randolph and Saar (2011a).

These calculations provide a useful conceptualization of the CO_2 concentration of a fluid in a reservoir with an induced temperature gradient. Because fluids in regions near CO_2 injection wells will likely be saturated with respect to CO_2, CO_2 and carbonate mineral solubility are closely linked through the range of CO_2 sequestration conditions. If a fluid reaches equilibrium with respect to CO_2 at low temperature and then only experiences temperature increases along its flow path, the maximum concentration at a higher temperature will likely be the equilibrium solubility at that temperature, except in high pressure systems at temperatures $\gtrsim$ 100 °C, where the solubility reaches a minimum and can only increase if the fluid remains in contact with a nonaqueous CO_2 phase.

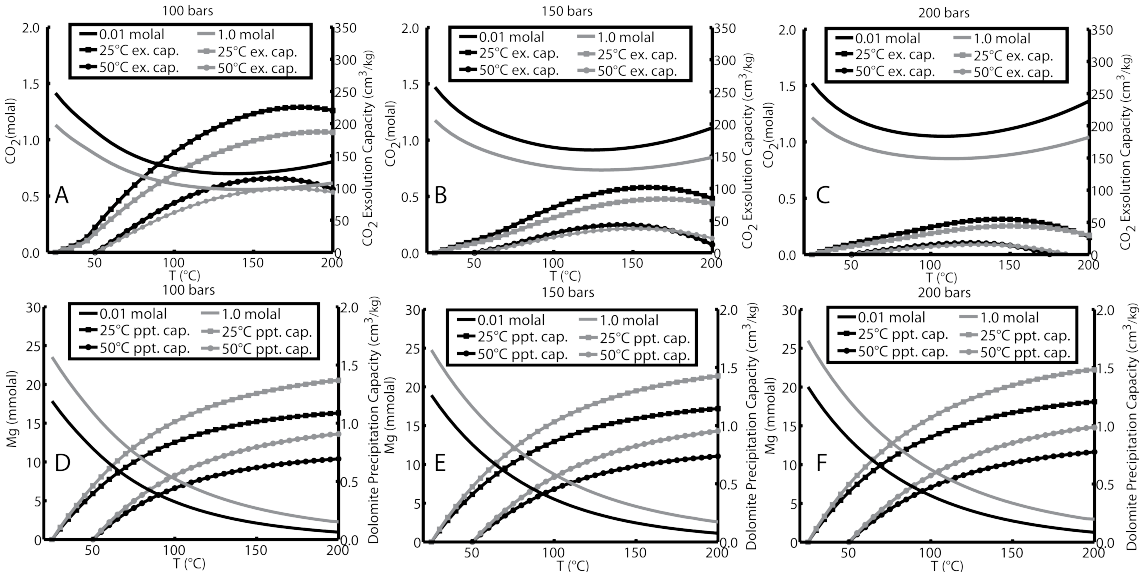

Figure 5.4: Calculations of CO_2 solubility and exsolution capacity (A-C) and dolomite solubility and precipitation capacity (D-F) at CO_2 sequestration and CO_2-based geothermal energy extraction temperatures and pressures of 100, 150, and 200 bars. Lines for 0.01 molal and 1.0 molal NaCl are plotted to illustrate the effects of ionic strength.

5.5.2 Dolomite Solubility and Precipitation Capacity

Another useful measure of potential permeability effects on GCS reservoirs is the calculation of dolomite solubility and precipitation capacity. Although the precipitation capacities are theoretical maxima, because dolomite growth is kinetically controlled, these calculations are useful to conceptualize the degree to which dolomite precipitation may affect permeability in GCS reservoirs. We assume stoichiometric dissolution/precipitation of dolomite:

$$\text{dolomite} + 4H^+ = Ca^{++} + Mg^{++} + 2CO_2(aq) + 2H_2O, \tag{5.1}$$

which may not occur in all systems due to kinetic constraints and the formation of, e.g., magnesian calcite Arvidson and Mackenzie (1999). The dolomite precipitation capacity is calculated by assuming that all of the reduction in dolomite solubility between the near-injection well temperature and the elevated reservoir temperature is accommodated by precipitating stoichimetric, crystalline dolomite with a molar volume of 64.365 cm^3/mol Robie and Waldbaum (1968). Precipitation capacity is calculated per kg of fluid, and these calculations again assume that the fluid is at CO_2 saturation at the temperature and pressure of the calculation. The results of these calculations are illustrated in Fig. 5.4D-F.

For all considered values of pressure (100, 150, and 200 bars), dolomite solubility increases with increasing ionic strength over the entire temperature range, whereas, under the same conditions, CO_2 is increasingly salted out of solution with increasing ionic strength. Dolomite's higher solubility in the higher ionic strength fluids results from lower ion activities and metal-chloride complexing in solution. Dolomite solubility is also proportional to pressure over the modeled conditions, consistent with higher CO_2 solubilities at elevated pressure (Fig. 5.4). The 200 °C dolomite solubilities are less than 5 mmolal for all considered pressures, which, for all cases, results in maximum precipitation capacities in the range ∼0.7-∼1.5 cm^3/kg, with the precipitation capacity increasing with increasing pressure. Therefore, in reservoirs where a significant thermal gradient is allowed to develop, this precipitation capacity, coupled with the exsolution capacity discussed above, can result in redistribution of system permeability and altered injectivities due to the substantial transfer of mass away from the injection well region.

5.6 Implications

These experimental results, considered alongside other researchers' numerical and laboratory results Allen et al. (2005); Pokrovsky et al. (2005, 2009); Luquot and Gouze (2009); André et al. (2010); Gouze and Luquot (2011); Luhmann et al. (2013); Jobard et al. (2013); Yoo et al. (2013) illustrate the importance of considering carbonate-fluid and CO_2-fluid interactions in GCS and CO_2-based geothermal energy reservoirs, particularly thermal gradient effects on carbonate and CO_2 solubilities and reservoir flow properties. In natural systems with less abrupt thermal gradients than exhibited in our experiment, the CO_2 will exsolve more progressively, such that the total volume represented by the "exsolution capacity" (Fig. 5.4) would be accommodated over a larger spatial domain than in our experiment. Therefore, permeability decreases in natural systems will likely occur more gradually, and potentially lead to smaller overall permeability reductions than those shown here. Nonetheless, we have illustrated that dolomite may be produced in abundant proportions provided that fluid supersaturation and temperature are sufficiently high. The substantial dolomite growth that occurred during the experiment suggests that further experimental investigation of carbonate precipitation from high pCO_2 solutions is warranted, particularly because the mechanisms of dolomite precipitation have been notoriously difficult to determine Land (1998); Arvidson and Mackenzie (1999). In particular, future research will need to examine carbonate precipitation rate enhancements unique to the CO_2 exsolution regime, such as rapid pH increases associated with CO_2 exsolution and the potentially elevated supersaturations created by water evaporating into supercritical CO_2. Moreover, the observed 100°C dolomite precipitation points to substantial possibilities for permanent storage of CO_2 as solid carbonate phases in reservoirs where the heightened pCO_2 causes primary silicates to contribute cations to the reservoir fluid. Equilibrating a fluid with cation-donating silicates near a low-temperature injection well and transporting the fluid to higher temperature may enhance the kinetics of mineral precipitation in such a way as to overcome the substantial activation energy required for permanent CO_2 storage as a solid carbonate phase. Furthermore, geochemical calculations of dolomite and CO_2 solubility and exsolution capacity at GCS and CO_2-based geothermal conditions indicate substantial mass transfer resulting in increased and decreased porosity/permeability near to and away from the injection well, respectively. At pressures >200 bars, however, CO_2 exsolution capacity is minor,

indicating that conditions commonly encountered in conjunction with the high reservoir temperatures required for CO_2-based geothermal energy production Randolph and Saar (2011a) will result in minor contributions of CO_2 exsolution to decreases in CO_2 injectivity.

Chapter 6

High performance reactive transport simulations examining the effects of thermal, hydraulic, and chemical (THC) gradients on fluid injectivity at carbonate CCUS reservoir scales

6.1 Summary

Carbonate minerals and CO_2 are both considerably more soluble at low temperatures than they are at elevated temperatures. This inverse solubility has led a number of researchers to hypothesize that injecting low-temperature (i.e., less than the background reservoir temperature) CO_2 into deep, saline reservoirs for CO_2 Capture, Utilization, and Storage (CCUS) will dissolve CO_2 and carbonate minerals near the injection well and subsequently exsolve and re-precipitate these phases as the fluids flow into the geothermally warm portion of the reservoir. In this study, we utilize high performance computing to examine the coupled effects of cool CO_2 injection and background hydraulic head gradients on reservoir-scale mineral volume changes. We employ the fully coupled reactive transport simulator PFLOTRAN with calculations distributed over up to 800 processors to test 21 scenarios designed to represent a range of reservoir depths, hydraulic head gradients, and CO_2 injection rates and temperatures. In the default simulations, 50°C CO_2 is injected at a rate of 50 kg/s into a 200 bar, 100°C calcite or dolomite reservoir. By comparing these simulations with others run at varying conditions, we show that the effect of cool CO_2 injection on reservoir-scale mineral volume changes tends to be relatively minor. We conclude that the low heat capacity of CO_2 effectively prevents low-temperature CO_2 injection from decreasing the temperature across large portions of the simulated carbonate

reservoirs. This small thermal perturbation, combined with the low relative permeability of brine within the supercritical CO_2 plume, yields limited dissolution and precipitation effects directly attributable to cool CO_2 injection. Finally, we calculate that relatively high water-to-rock ratios, which may occur over much longer CCUS reservoir lifetimes or in materials with sufficiently high brine relative permeability within the supercritical CO_2 plume, would be required to substantially affect injectivity through thermally-induced mineral dissolution and precipitation. Importantly, this study shows the utility of reservoir scale-reactive transport simulators for testing hypotheses and placing laboratory-scale observations into a CCUS reservoir-scale context.

6.2 Introduction

Geological Carbon Capture, Utilization, and Storage (CCUS) has the potential to prevent large volumes of the heat-trapping greenhouse gas carbon dioxide (CO_2) from entering the atmosphere and exacerbating global climate change (e.g., Pacala and Socolow, 2004; IPCC, 2005; Benson and Cole, 2008; DePaolo et al., 2013; IPCC, 2014). Although deep geologic CO_2 storage has been considered for some time as a tactic for mitigating the detrimental effects of climate change, the scale of its implementation has been largely limited by its high associated costs (Eccles et al., 2009; Randolph and Saar, 2011b). Researchers have suggested that both its economic feasibility and degree of implementation can be dramatically improved if the stored CO_2 is *utilized* for ancillary benefits, such as Enhanced Oil Recovery (EOR, e.g., Gozalpour et al. (2005); Saar et al. (2014b)), CO_2-based hydraulic fracturing (e.g., Tao and Clarens (2013); Zhou and Burbey (2014)), and/or energy extraction (e.g., CO_2-Enhanced Geothermal Systems (CO_2-EGS, e.g., Brown (2000); Pruess (2006); Lo Ré et al. (2014)) and CO_2 Plume Geothermal (CPG, Randolph and Saar (2011a); Saar et al. (2012, 2013, 2014a,b)).

A range of reservoir lithologies are considered for CCUS installation. To date, hydrocarbon reservoirs comprised of siliciclastics and/or carbonate minerals have been a large focus of CCUS research, particularly because of their widespread occurrence, known ability to securely trap light, non-aqueous phases, and the economic benefits of CO_2-EOR (e.g., Blunt et al., 1993; Malik et al., 2000). Moreover, researchers have proposed combined CPG and EOR in feasible reservoirs, which could offset some of the CO_2 emissions associated with hydrocarbon extraction and refining processes while

producing heat and/or electricity (Randolph, 2011; Freifeld et al., 2013; Adams et al., 2014). Nonetheless, if CCUS is going to make an impact on global CO_2 emissions, all feasible reservoirs–including those that did not previously contain an economically viable hydrocarbon resource– must be considered for CCUS installation.

Because CCUS reservoir temperatures are inherently elevated with respect to surface conditions (e.g., Saar, 2011), thermal gradients are likely to develop as cool CO_2 is injected (Lu and Connell, 2008; André et al., 2010; Han et al., 2010; Rayward-Smith and Woods, 2011; Randolph and Saar, 2011a; Singh et al., 2012; Jobard et al., 2013; Luhmann et al., 2013; Ruan et al., 2013; Tutolo et al., 2014b; Garapati et al., 2015). Although cool CO_2 may exchange energy with the geothermally warm material surrounding the well casing as it flows down the injection borehole and undergo Joule-Thomson heating and cooling upon compression and decompression, respectively, calculations show that bottomhole CO_2 temperatures typically remain significantly depressed relative to the reservoir (Oldenburg, 2007; Lu and Connell, 2008; Rayward-Smith and Woods, 2011; Garapati et al., 2015). Moreover, in some instances, particularly in the case of CO_2-based geothermal energy systems, lower injection wellhead CO_2 temperatures are actually sought in order to boost system power output (e.g., Pruess, 2006; Randolph and Saar, 2011a; Adams et al., 2014). In all cases, the lower temperatures near the injection well can lead to solubility gradients and coupled redistribution of reservoir porosity and permeability (e.g., Luhmann et al., 2013; Jobard et al., 2013; Tutolo et al., 2014b).

Deep, geothermally-heated, subsurface reservoirs are characterized by a range of background hydraulic head gradients and groundwater flow velocities (e.g., Saar, 2011). The magnitude, direction, and length scales of these natural flow regimes are dependent upon the permeability, porosity, and pressure and temperature structure of the particular reservoir. The presence of background hydraulic head gradients in subsurface aquifers can also determine the effectiveness of supercritical CO_2 storage, particularly by the capillary trapping mechanism (MacMinn et al., 2010). Furthermore, where required, CO_2-based geothermal energy reservoir operators may also engineer hydraulic head gradients by pumping fluids into or out of the reservoir to manage the flow of CO_2 in the subsurface and its thermal exchange with the reservoir (Buscheck et al., 2011, 2012; Elliot et al., 2013).

Ideal CCUS reservoirs have optimized permeability structures that will allow for sufficient CO_2 injectivities and/or promote efficient extraction of geothermal heat

from the subsurface. Ideal reservoirs for CO_2-based geothermal operations will maintain high enough permeabilities to ensure sufficient CO_2 injectivities and heat extraction from the subsurface without creating short-circuit, high permeability flow paths between injection and production wells (e.g., Harlow and Pracht, 1972; Randolph and Saar, 2011c; Tutolo et al., 2015a). However, as cool CO_2 is injected into CCUS reservoirs, it will displace and dissolve into formation waters, reduce reservoir temperature and pH, and enhance mineral reactivity (Kharaka et al., 2006; Benson and Cole, 2008; Kong and Saar, 2013). In CCUS formations containing carbonate minerals, their unique quality of decreasing solubility with increasing temperature, combined with similar behavior for CO_2 solubility, will tend to redistribute porosity and permeability as formation waters flow away from the injection well (André et al., 2010; Tutolo et al., 2014b). Depending on the spatial distribution of these mass and flow property changes, they may lead to positive or negative feedbacks on geothermal energy production from a particular reservoir (Adams et al., 2014).

A number of experimental studies have been conducted in order to examine the effects of low-temperature CO_2 injection into CCUS reservoirs (e.g., Luhmann et al., 2013; Jobard et al., 2013; Tutolo et al., 2014b). Experimental results generally illustrate that thermally-induced changes in CO_2 and carbonate solubility can substantially reorganize porosity and permeability in laboratory-scale samples. Reductions in CO_2 solubility appear to have a more pronounced effect, and can lead to considerable (i.e., up to several orders of magnitude in unconsolidated sediments (Luhmann et al., 2013)) reductions in permeability as a result of CO_2 exsolution, grain displacement, and the onset of two-phase flow. Reductions in carbonate solubility and the resultant precipitation tend to have a markedly less pronounced effect, with porosity typically being reduced by several percent (Jobard et al., 2013; Tutolo et al., 2014b).

Although these studies suggest a potentially significant impact of cool CO_2 injection on CCUS reservoir injectivity, the effects of injection, dissolution, precipitation, and exsolution, when coupled at the reservoir scale, may differ from the results of these studies conducted at much smaller scales, particularly in the context of CO_2-EOR, CO_2-EGS, and CPG. For example, in the experiments presented by both Luhmann et al. (2013) and Tutolo et al. (2014b), CO_2-rich H_2O was injected into experimental cores, and their observed permeability reductions were predominantly the result of thermally-driven CO_2 exsolution. In CCUS reservoirs, only a small fraction of the injected CO_2 will dissolve into the reservoir brine, and much of it will remain in the

supercritical phase, with the specific dissolution behavior depending on the permeability heterogeneity structure of the reservoir (Farajzadeh et al., 2011; Kong and Saar, 2013). Any CO_2 exsolution from the water phase will therefore likely occur in close proximity to the free CO_2 phase, and CO_2 will be able to coalesce with the larger CO_2 plume, depending on the capillary forces it experiences. In consequence, the permeability reduction associated with the transition from one- to two-phase flow observed in the core-scale experiments of Luhmann et al. (2013) and Tutolo et al. (2014b), which was the result of thermally-driven CO_2 exsolution, may be less significant at the CCUS reservoir scale.

Several numerical investigations have attempted to place the effects of cool CO_2 injection into a reservoir-scale context (e.g., André et al., 2010; Singh et al., 2012; Zhao and Cheng, 2014). Specifically, André et al. (2010) used the reactive transport simulator TOUGHREACT (Xu et al., 2006) in order to explore the effect of low-temperature CO_2 injection into the Dogger Aquifer, France. Their simulations illustrated the sensitivity of carbonate mineral and CO_2 solubilities to cool CO_2 injection, and showed that significant amounts of carbonates may dissolve and re-precipitate in CCUS reservoirs. They attributed much of their observed precipitation to desiccation processes (i.e., H_2O dissolution into supercritical CO_2), rather than thermal processes, however. Their simulations employed a three-dimensional (3D) but radially symmetric domain, which allowed for reduced, two-dimensional computational complexity but, unfortunately, lacked the ability to capture processes such as background hydraulic head gradients and changes in parameters (e.g., mineral composition and volume, porosity, permeability) in the third dimension.

Until recently, the computationally intensive nature of large-scale, 3D simulations of CCUS reservoirs has effectively prohibited researchers from performing them. The recent development of the massively parallel reactive transport simulator PFLOTRAN (Hammond et al., 2012; Lichtner et al., 2013) for simulating CCUS reservoirs has made such simulations increasingly feasible, particularly whenever researchers have access to high-performance supercomputing clusters (e.g., Lu and Lichtner, 2005; Mills et al., 2009; Navarre-Sitchler et al., 2013). In this study, we slightly modify and utilize PFLOTRAN to examine the hydrogeochemical effects of thermal and hydraulic head gradients in carbonate CCUS reservoirs. We specifically focus on the effects of cool (50°C) CO_2 injection into geothermally warm (100°C) reservoirs with uniform

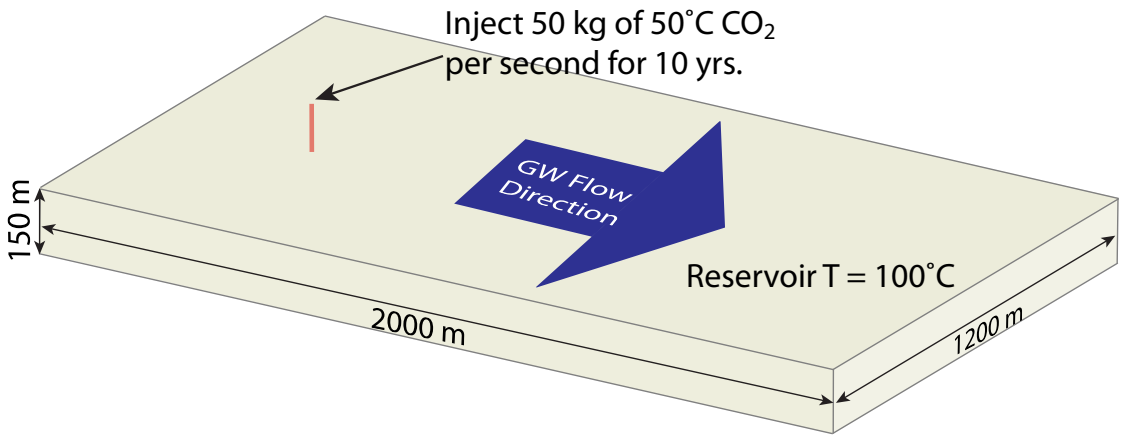

Figure 6.1: Reactive transport simulations illustrate the effects of cool CO_2 injection into 100°C calcite and dolomite CCUS reservoirs with background hydraulic head gradients of 0.01, 0.05, and 0.1 m/m. All simulated reservoirs have a constant permeability of 10^{-13} m^2, which translates to Darcy velocities of 1.1, 5.5, and 10.9 m/yr, respectively, for these hydraulic head gradients. Here, a schematic demonstrates the dimensions of the simulated reservoir for the 0.05 and 0.1 m/m hydraulic head gradient scenarios. Due to broader CO_2 plume dimensions caused by lower flow velocities, the dimensions of the reservoir in the 0.01 m/m hydraulic head gradient scenario are more square-shaped, at 1600 m in the primary flow direction and 1500 m in the direction perpendicular to flow. Although we indicate that 50 kg of 50°C CO_2 is injected per second into this schematic reservoir, simulations employing lower injection rates (4 kg/s) and higher injection temperatures (100°C) are also presented (Table 6.3). In all simulations presented in this study, the reservoir volume is 3.6×10^8 m^3. Scenarios with an injection rate of 50 kg/s employ 90,000 20 m x 20 m x 10 m elements and simulations with an injection rate of 4 kg/s employ 48,000 20 m x 20 m x 18.75 m elements (See Sect. 6.3.1).

background hydraulic head gradients. We quantify the volumes and spatial distribution of carbonate mineral dissolution and precipitation as well as the coupled spatial, temporal, and thermal evolution of the injected supercritical CO_2 plume and reservoir fluid. The simulations presented here allow us to place prior experimental and numerical observations into a reservoir-scale context while constraining the potential impacts of both thermal and hydraulic head gradients on important reservoir hydrogeochemical parameters.

6.3 Methods

6.3.1 Model Formulation

The simulations we present here utilize the reactive transport simulator PFLOTRAN (Hammond et al., 2012; Lichtner et al., 2013), which employs the integrated finite volume approach to discretize the spatial domain and fully-implicit backward-Euler time differencing (Hammond et al., 2007). In all simulations, the domain volume is set to 3.6×10^8 m^3, which is divided into 90,000 elements with horizontal dimensions of 20 m x 20 m and vertical dimensions of 10 m for the 50 kg/s injection simulations (Fig. 6.1). In the 4 kg/s injection simulations, the number of elements is reduced to 48,000 by changing the vertical grid spacing to 18.75 m. Reservoir thickness in all simulations is fixed at 150 m along the vertical coordinate, but the horizontal coordinates are varied to accommodate CO_2 plume flow paths and shapes characteristic of the applied hydraulic head gradient. Specifically, because their higher flow velocities tend to significantly elongate the CO_2 plume in the down-gradient direction, the 0.1 m/m and 0.05 m/m simulations contain 100 elements in the dominant flow direction and 60 elements perpendicular to flow. Likewise, because the 0.01 m/m simulations tend to yield CO_2 plumes that expand both latitudinally and longitudinally throughout the reservoir, they contain 80 elements in the dominant flow direction and 75 elements perpendicular to flow. In addition, the injection well is placed according to the hydraulic head gradient employed, in order to attempt to prevent injected CO_2 from escaping through the upstream boundary of the reservoir. This provision is necessary because the boundary conditions employed here dictate that once CO_2 exits the system, it will not return. In the 0.01, 0.05, and 0.1 m/m hydraulic head gradient reservoirs, CO_2 is injected 700, 400, and 200 m from the upstream boundary, respectively. The upper and lower domain boundaries are assigned no-flow boundary conditions to simulate impermeable caprock layers, but fluid and heat are allowed to flow through the hydrostatically equilibrated side boundaries of the modeled domain.

Several dolomite reservoir simulations (not presented here) were additionally performed with 10 m x 10 m grid spacing in the horizontal direction to ensure that relevant processes could be captured using the coarser grid spacing. These simulations are in general agreement with the results presented here, except for slight differences in the calculated volumes of minerals dissolved and precipitated. We conclude that, because these differences likely arise from the accumulation of very small differences

in mineral volume changes over the many thousands more time steps required by the high-resolution simulation, the grid spacing that we have chosen is adequate for the objectives of the present study.

Simulations were mostly run on Itasca, an HP Linux cluster maintained by the University of Minnesota Supercomputing Institute (MSI). A small proportion of the simulations were additionally run on the MSI "lab" Linux clusters. Individual simulations were run on up to 800 cores and took on the order of 5-10 CPU-years (i.e., the number of processors employed multiplied by the amount of calendar time required to complete the simulations) to reach 50 years of simulated time. In total, the simulations performed here generated over 1 TB of output files, with dolomite simulations requiring generally shorter timesteps than calcite simulations and simulations with lower hydraulic head gradients typically requiring smaller timesteps than higher hydraulic head gradient simulations.

6.3.2 Physical properties

Physical properties of reservoir materials are representative of material properties measured for carbonate reservoir rocks (Table 6.1). In our simulations, capillary pressure is calculated according to (Van Genuchten, 1980):

$$P_c = \frac{1}{\alpha}\left((s_{l,e})^{1/m} - 1\right)^{(1-m)}, \tag{6.1}$$

where α and m are fitting parameters and $s_{l,e}$ is the effective saturation of the wetting phase, defined by:

$$s_{l,e} = \frac{s_l - s_{l,r}}{1 - s_{l,r}}, \tag{6.2}$$

where $s_{l,r}$ is the residual saturation of the liquid phase. Relative permeability of the liquid phase, k_r, is then calculated according to the Mualem (1976) relative permeability function:

$$k_r = \sqrt{s_{l,e}}\left(1 - (1 - s_{l,e}^{1/m})^m\right)^2. \tag{6.3}$$

Relative permeability properties are approximated to be those of the Dogger aquifer presented by André et al. (2007), except residual CO_2 saturation is set to 0, instead of the reported value of 0.05. The different residual CO_2 saturation is used here both because PFLOTRAN time steps become prohibitively small when a residual CO_2 saturation greater than 0 is employed, and because the nature of our study dictates

that fresh brine will flood CO_2-saturated zones relatively rapidly and redissolve CO_2 trapped in large pores. Permeability is set to 1×10^{-13} m^2, which is approximately two orders of magnitude higher than core-scale dolomite permeabilities measured by Tutolo et al. (2014b) and Luhmann et al. (2014), in order to account for the fact that carbonate aquifers deemed feasible for CCUS operations are likely considerably more permeable at the simulated scale (e.g., André et al., 2007, 2010; Randolph and Saar, 2011c; U.S.G.S., 2013).

Table 6.1: Fluid and Heat Flow Parameters

Parameter	Value
Permeability (m^2)	1×10^{-13}
Aqueous species diffusion coefficient (m^2/s)	1×10^{-9}
Porosity	$0.07^{\S}$
Van Genuchten m	$0.6^{\dagger}$
Van Genuchten α	$1.9\times10^{-6\dagger}$
H_2O Resid. Sat. ($s_{l,r}$)	$0.2^{\dagger}$
CO_2 Resid. Sat.	0^{*}
Max. P_c (bar)	$100^{\dagger}$
Formation Density (g/cm^3)	$2.65^{\sharp}$
Formation Thermal Conductivity (W/(m.K))	$2.5^{\dagger}$
Rock specific Heat (kJ/(kg.K)	$1.0^{\sharp}$

§Computed from XRCT data (Luhmann et al., 2014) and only accounts for pores $\gtrsim 8\mu$m in diameter
†André et al. (2010). Dry and wet values are assumed to be identical
*See Sect. 6.3.2
$^{\sharp}$Randolph and Saar (2011a)

For all simulations, an initially uniform temperature of 100°C is assigned to the simulated domain. This fixed temperature corresponds to a relatively high geothermal gradient of ∼50°C/km for a 200 bar reservoir pressure and an extreme geothermal gradient of ∼100°C/km for a 100 bar pressure, although we show below that mineral solubilities are relatively pressure-independent. Thus, to reduce further expansion of the parameter space, we have decided to maintain the same temperature for both simulated pressures. For reference, the continental average geotherm is ∼25-30°C, and geothermal reservoir locales range from ∼24-76°C/km (Tester et al., 2006). The designated reservoir pressure (e.g., 100 or 200 bars) is assigned to the top row of elements at the furthest upstream end of the simulated reservoir and the rest of the reservoir is allowed to hydrostatically equilibrate according to the designated hydraulic head gradient prior to initialization. At these temperatures and pressures,

CO_2 is in a supercritical state and therefore has a more liquid-like density than at surface temperatures and pressures (e.g., Benson and Cole, 2008) and a more gas-like dynamic viscosity, resulting in a considerably higher mobility (i.e., lower kinematic viscosity) than water (Randolph and Saar, 2011a). These properties allow supercritical CO_2 to more efficiently fill subsurface pore space and more efficiently extract heat from the subsurface, respectively (Randolph and Saar, 2011a; Adams et al., 2014). It is important to note here that temperature and pressure both increase according to the regional geothermal gradient, such that real-world CCUS reservoirs at different depths are very likely to have different temperatures.

6.3.3 Chemical properties

In PFLOTRAN, equilibrium between the solution and supercritical CO_2 is assumed in elements where supercritical CO_2 exists, which is reasonable due to the rapid kinetics of CO_2 dissolution and exsolution at the modeled temperature and pressure conditions (Hirai et al., 1997; Takemura and Yabe, 1999). Likewise, the distribution of aqueous species is assumed to be kinetically rapid and at equilibrium according to the aqueous species equilibrium constants within the thermodynamic database. Simulated reservoir brines contain 1 mol/kg NaCl, which allows for simulation of the effects of reservoir ionic strength on aqueous species transport while remaining within the limits of applicability of the extended Debye-Hückel equation employed by PFLOTRAN (Tutolo et al., 2015b). In addition, the reservoir brines are equilibrated with the host mineralogy prior to initalizing the simulations. Initial compositional conditions for the calcite and dolomite reservoirs are listed in Table 6.2.

Kinetic considerations

Classically, carbonate dissolution and growth rates have been fit to the empirical relation (Lasaga, 1981; Shiraki and Brantley, 1995; Arvidson and Mackenzie, 1999; Teng et al., 2000):

$$r = k(\Omega - 1)^n, \tag{6.4}$$

where r is the reaction rate, k is the reaction rate constant, Ω is saturation index (i.e., the ratio of ion activity product to the equilibrium constant for the specified reaction), and n is the affinity factor, set by the reaction mechanism (Lasaga, 1981; Nielsen,

Table 6.2: Reservoir Composition

Component	Dolomite Conc. (mol/kg)	Calcite Conc. (mol/kg)
Ca	1.539×10^{-4}	4.52×10^{-4}
Cl	1.0	1.0
CO_2(aq)	3.089×10^{-4}	4.52×10^{-4}
Mg	1.539×10^{-4}	-
Na	1.0	1.0
pH	8.24*	8.35*
Mineral volume fraction	0.93	0.93
Reactive surface area (cm^2/g)	70.5	70.5
Porosity	0.07	0.07

*pH is set by equilibrium with respect to reservoir mineral

1984; Shiraki and Brantley, 1995). The temperature dependence of k is approximated according to the Arrhenius relationship (e.g., Lasaga, 1981):

$$k = k_{25} \exp\left(- \frac{E_A}{R} \left(\frac{1}{T_K} - \frac{1}{298.15} \right) \right), \tag{6.5}$$

where E_A is the activation energy, k_{25} is the 25°C reaction rate constant, and T_K is absolute temperature in Kelvin. Because one of the focus minerals in the present study is dolomite, the often-made approximation in which mineral dissolution rate constants are equivalent to their precipitation rate constants cannot be employed. By comparing calculated results with the experimental dolomite precipitation rate data of Arvidson and Mackenzie (1999), Hellevang et al. (2013) have shown that this approximation dramatically overestimates dolomite precipitation rates at CCUS reservoir temperatures, especially at relatively high dolomite saturation indices. To accommodate this behavior, we modified the PFLOTRAN source code to accept separate values of r, E_A, and n for both the dissolution and precipitation regimes, and the Arvidson and Mackenzie (1999) parameterization of Eqn. 6.4 is employed to describe dolomite precipitation rates. Specifically, we set $k_{25} = 4.48\times10^{-19}$ mol/m^2/s, $E_A = 133.47$ kJ/mol, and $n = 2.26$. At the elevated temperatures investigated in this study, calcite dissolution and precipitation and dolomite dissolution are sufficiently rapid (see, e.g., Pokrovsky et al., 2009; Hellevang et al., 2013) such that the fluid and mineral equilibrate between time steps, and kinetics therefore do not need to be

explicitly considered. However, because PFLOTRAN requires kinetic parameters for each phase included in the simulations, we set rate parameters for these reactions to be sufficiently high such that equilibrium is achieved during each time step. In practice, absolute values of Ω for these reactions never deviate more than a few tenths of a percent from unity.

In order to facilitate the separation of "primary" calcite and dolomite from "reprecipitated" calcite and dolomite (i.e., minerals that precipitated as a result of the system perturbation by CO_2 injection), the PFLOTRAN thermodynamic database we employ contains a secondary mineral with identical thermodynamic properties to the primary phase. The primary phase is given an extreme affinity threshold in order to effectively prevent its re-precipitation. The secondary phase, however, is allowed to dissolve if it becomes undersaturated during the course of the simulation.

Specific surface area for both calcite and dolomite is assumed to be 70.5 cm^2/g, which is the value determined by Tutolo et al. (2014b) for whole-core dolomite dissolution rates, based on low-T dissolution rate parameters provided by Pokrovsky et al. (2009). For the kinetically rapid reactions listed above, the magnitude of this parameter is insignificant. However, surface area plays a major role in the calculated volumes and rates of dolomite precipitation, as discussed in Sect. 6.5.1. The value we employ (70.5 cm^2/g) is approximately half of the geometric surface area calculated by Pokrovsky and Schott (2001) for powdered dolomite, which is consistent with the fact that Tutolo et al. (2014b) derived this value from intact dolomite cores, where preferential flow paths prevent homogenously distributed reactions. Similarly, Li et al. (2014) have shown that mineral effective surface area can be orders of magnitude lower than measured specific surface area.

6.3.4 Model runs

A total of 21 simulations designed to examine the effect of thermal and hydraulic head gradients in carbonate CCUS reservoirs are presented in this contribution (Table 6.3). Three hydraulic head gradients (0.01, 0.05, and 0.1 m/m, corresponding to Darcy velocities of 1.1, 5.5, and 10.9 m/yr, respectively, for the permeability utilized in this study) are examined for both calcite and dolomite reservoirs with an initial temperature of 100°C. In each of these scenarios, 50 kg/s (1.6 MT/year) of 50°C CO_2 is injected into the 100°C reservoir for 10 years and the reservoir is allowed to recover for an additional 40 years. The effect of pressure (i.e., depth) is investigated

by repeating simulations at reservoir pressures of both 100 and 200 bars. The three 200 bar calcite reservoir simulations are additionally repeated with a CO_2 injection temperature identical to the reservoir temperature in order to delineate the effects of thermal perturbations on calculated mineral volume changes. In addition, the effect of CO_2 injection rate is examined by repeating the three 200 bar calcite reservoir simulations with an injection rate of 4 kg CO_2/s (0.13 MT CO_2/yr). Finally, we present the results of three simulations that examine the effects of reactive surface area and porosity on our presented conclusions (Sect. 6.5.1).

Table 6.3: Summary of model runs

Mineral	Reservoir T (°C)	Injection T (°C)	Injection Rate (kg/s)	Reservoir P (bar)	Hydraulic Head Gradient (m/m)
Calcite	100	50	50	100	0.1
					0.05
					0.01
				200	0.1
					0.05
					0.01
			4		0.1
					0.05
					0.01
		100	50		0.1
					0.05
					0.01
Dolomite	100	50	50	100	0.1
					0.05
					0.01
				200	0.1*
					0.05
					0.01

*An additional 3 simulations are run at this condition in order to examine the effects of reactive surface area and porosity on the calculated results (Sect. 6.5.1.)

6.4 Results

6.4.1 Thermal perturbation

The thermal evolution of the simulated carbonate CCUS reservoirs over the 10 years of injection time illustrate that injected CO_2 tends to thermally equilibrate with the host reservoir before traveling large distances from the injection well (Fig. 6.2). This is indicated by the fact that the region outlined by the translucent gray in these figures, which represents the portion of the reservoir containing >1% CO_2 saturation, is, for the most part, outside of the depressed-temperature, near-well region. At the early stages of injection, as the CO_2 plume is approaching its steady-state configuration, the injected CO_2 approaches thermal equilibrium with respect to

the background reservoir temperature before it is transported more than a few meters away from the injection well. CO_2 dissolution into the reservoir brine is an exothermic process, which tends to increase the temperature in elements at the plume boundary by up to $\sim$2°C. The small magnitude of this temperature increase is consistent with the results of other researchers (e.g., André et al., 2010). Joule-Thomson cooling is less apparent than the exothermic dissolution reactions, but is documented below in Sect. 6.4.3. Once the plume is established, the lower relative permeability of water resulting from the increased CO_2 pore space saturation allows the injected CO_2 plume to "self-insulate" against the advecting, high-temperature fluids, such that the region of the reservoir with temperatures lower than the initial temperature expands slowly with time. Nonetheless, even at the end of the ten-year injection period, the region in which the injection of cool CO_2 appreciably decreases (i.e., >10°C lower than the initial reservoir temperature) the reservoir temperature is confined to a near-well region that grows to a maximum of several tens of meters in diameter over the 10-year injection period. After the conclusion of the 10-year CO_2 injection period, the CO_2 migrates down-gradient out of the reservoir. During this period, the reservoir is relatively quick to recover to its initial, unperturbed temperature, as illustrated by the temperature distribution after 50 years of simulated time (Fig. 6.2). During this recovery period, the low-temperature region is attenuated as it advects down-gradient.

Although we have only illustrated the thermal perturbation for the 0.05 m/m hydraulic head gradient scenario, these conclusions are largely representative of all simulations performed in this study. In all simulations, the actual thermal depression created by injecting the 50°C CO_2 at 50 kg/s in the reservoir is limited to this near-well region.

6.4.2 Magnitude and spatial distribution of the CO_2 plume and mineral precipitation

The magnitudes and spatial distributions of the CO_2 plume and mineral precipitation are affected by the pressure and hydraulic head gradient present within the reservoir. In order to quantify the spatial distribution of the precipitated minerals as well as the CO_2 plume, we calculate the horizontal distance between each of their centers of mass and the location of the injection well. It is important to reiterate that the injection wells in the 0.01, 0.05, and 0.1 m/m hydraulic head gradient reservoirs are placed 700, 400, and 200 m, respectively, from the upstream boundary. For this

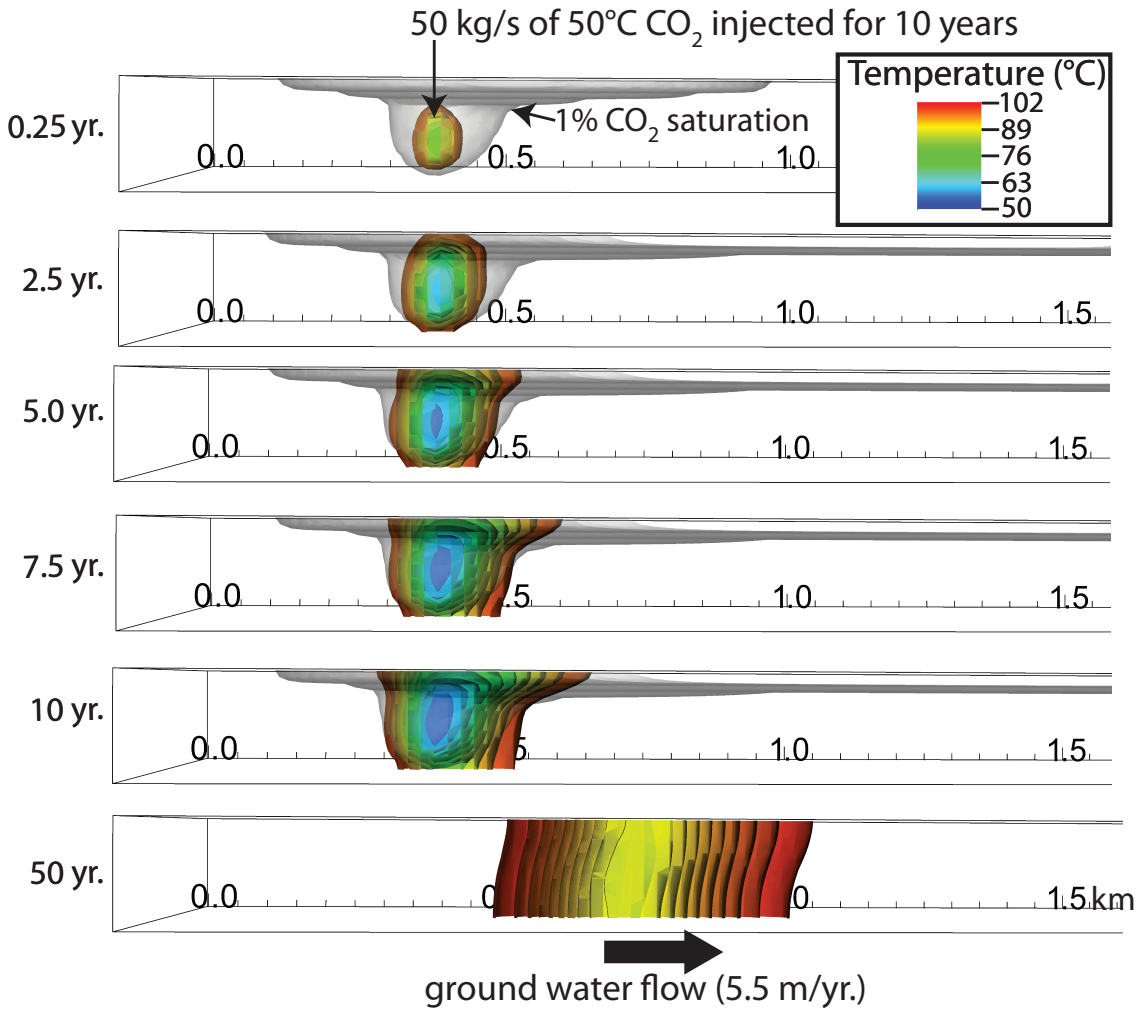

Figure 6.2: Snapshots of a simulated dolomite CCUS reservoir with a hydraulic head gradient of 0.05 m/m at 0.5, 2.5, 5, 7.5, 10, and 50 years showing the evolution of temperature as a result of injecting 50 kg of 50°C CO_2 per second into a 100°C reservoir for 10 years and allowing the reservoir to recover for an additional 40 years. Temperature isosurfaces are cut half way through the simulated reservoir in order to show internal temperatures, and the isosurface for CO_2 saturation >1% is shown in translucent gray. Note that the simulated reservoir is 2 km in length but has been cut off in these images for clarity.

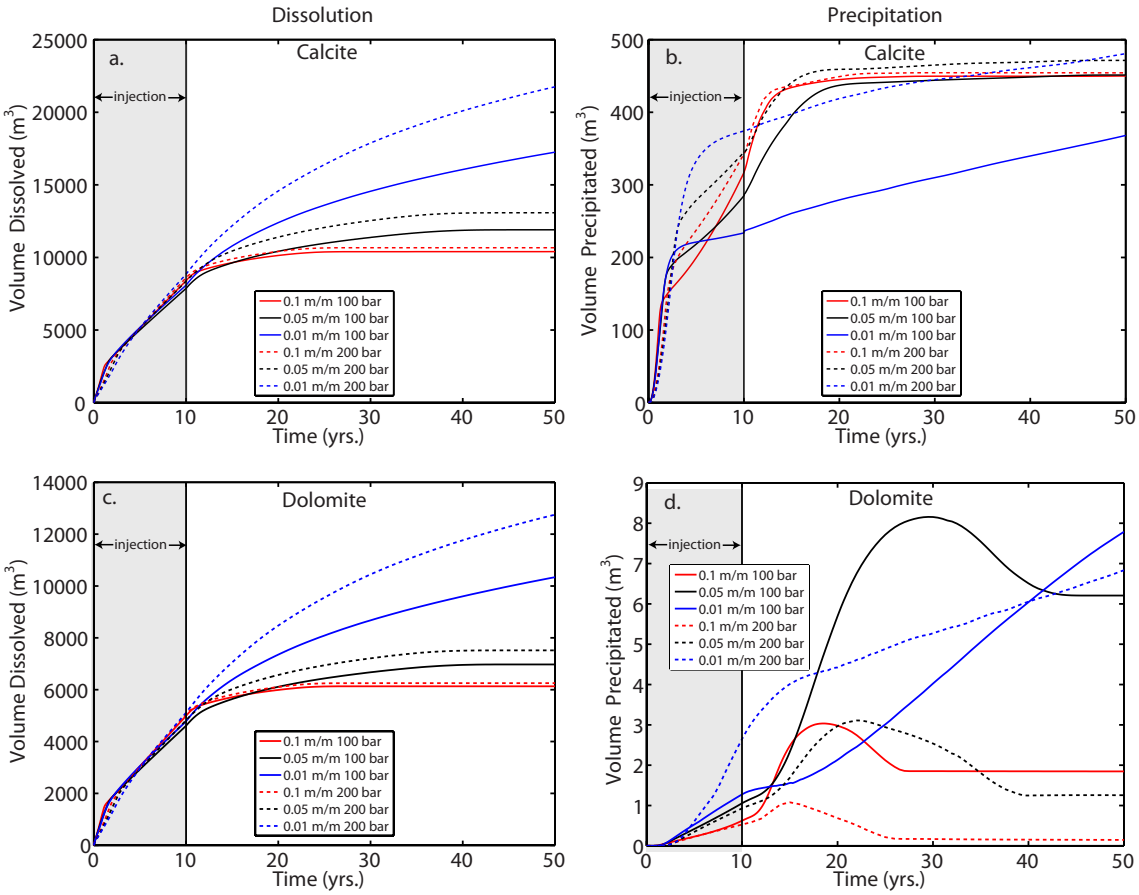

Figure 6.3: Total volumes of calcite (a,b) and dolomite (c,d) dissolution (left column) and precipitation (right column), respectively, resulting from CO_2 injection into CCUS reservoirs. 50°C CO_2 is injected into the simulated 100°C reservoirs at a rate of 50 kg/s for the first 10 years and the reservoirs are then allowed to recover for 40 subsequent years. Simulations are run for three hydraulic head gradients at both 100 and 200 bar reservoir pressures in order to illustrate the effect of pressure (i.e., depth) on CCUS reservoir evolution. Importantly, the volumes of carbonate minerals that dissolve are several orders of magnitude greater than the volumes of carbonate minerals that precipitate in all simulations. To place these figures in perspective, the element volume employed in these simulations is 4000 m^3 and the reservoir volume is 3.6×10^8 m^3.

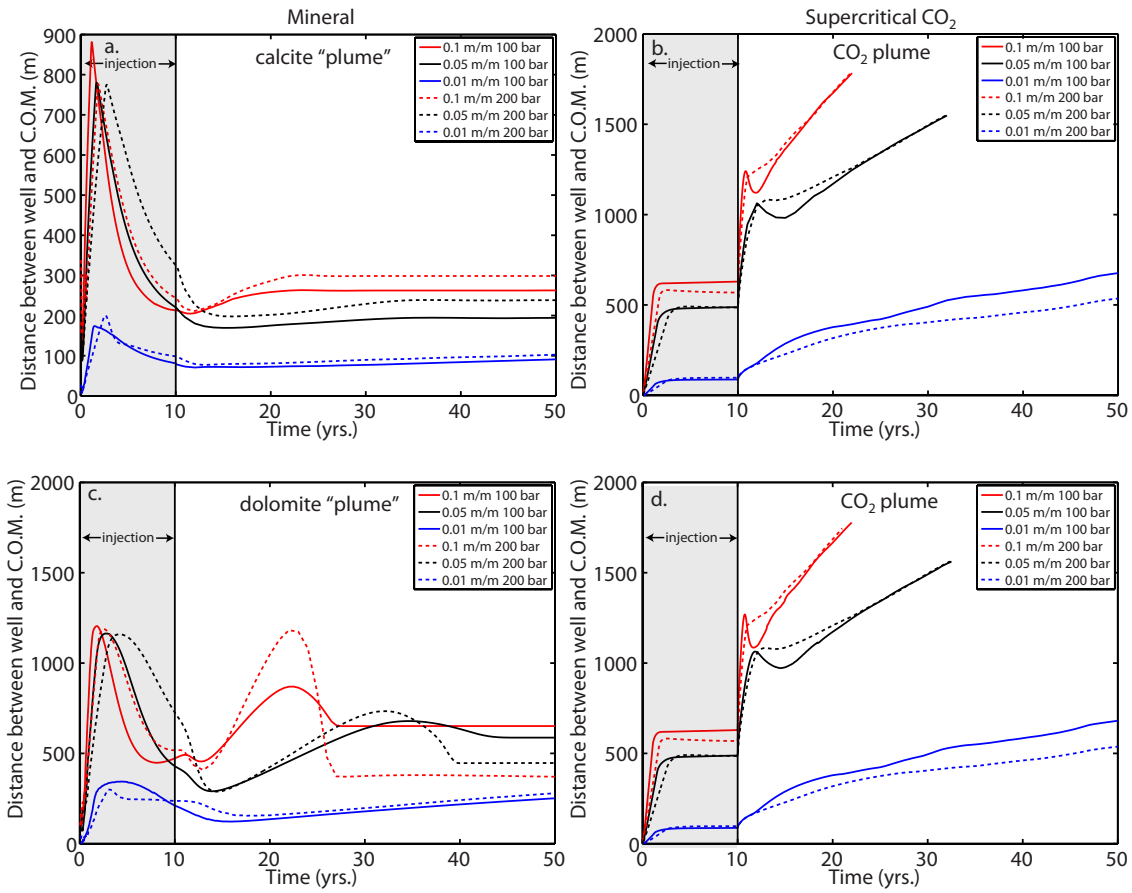

Figure 6.4: Measure of the horizontal distance between the injection well and center of mass (C.O.M) of mineral (a,c) and supercritical CO_2 (b,d) plumes for simulated calcite (a,b), and dolomite (c,d) reservoirs. Simulations are run for three hydraulic head gradients at both 100 and 200 bar reservoir pressures in order to illustrate the effect of pressure (i.e., depth) on CCUS reservoir evolution. Because calcite precipitates at equilibrium and dolomite precipitation is kinetically controlled, the centers of mass of the precipitated calcite "plumes" are considerably closer to the injection well than the analogous dolomite "plume" centers of mass. The supercritical CO_2 plumes tend to establish steady-state configurations during the first several years of injection and gradually exit the reservoir once the injection periods have ended.

reason, the distance downstream from the injection well at which the CO_2 plume center of mass exits the reservoir is different for the 0.01, 0.05, and 0.1 m/m hydraulic head gradient reservoirs (Figs. 6.4, 6.6, and 6.8).

As CO_2 is injected into the reservoir, a small fraction dissolves into the reservoir brine and lowers its pH from the initial, carbonate-buffered value of ∼8.2 to ∼4.4. This lower pH, combined with the higher activity of CO_2(aq) in the CO_2-saturated brine, increases the solubility of the reservoir carbonates such that Mg and Ca concentrations reach ∼12 mmol/kg in the dolomite simulations and Ca concentrations reach ∼34 mmol/kg in the calcite simulations. The region affected by these processes generally follows the outline set by the injected CO_2 plume, except tends to extend further in the downstream direction. In all presented simulations, the volumes of carbonate phases that dissolve as a result of CO_2 injection are much greater than the volumes that precipitate (Fig. 6.3), although the fact that these dissolved volumes are relatively widespread throughout the reservoir suggests that local changes in reservoir porosity will generally not have a significant effect on reservoir permeability. In the cases of both calcite and dolomite, the maximum volume of the mineral that can dissolve is limited by the volume of brine available in the pore space for reaction, the saturation state of that brine with respect to both CO_2 and carbonate phases, and the rate at which the brine is refreshed by non-equilibrated brine. Because the dissolution rates of both phases dictate that the pore fluids equilibrate with the reservoir mineralogy during each time step, the volume of solid that dissolves is transport-limited. In general, the simulated results indicate that the volumes of the carbonate minerals that dissolve during the 10 year injection stage are very similar across all hydraulic head gradient and pressure conditions (Fig. 6.3).

During the CO_2 injection period, an initial, several-year period is required for the supercritical CO_2 plume to reach its steady-state configuration and stabilize (Figs. 6.4, 6.6, and 6.8). Once the CO_2 plume reaches this configuration, it maintains approximately the same shape (except for elongation in the downstream direction) for the duration of the CO_2 injection period and would presumably maintain this configuration as long as the constant CO_2 injection rate persists. After CO_2 injection is halted, the CO_2 plume migrates out of the reservoir such that it exits the reservoirs after ∼ 22 years in the 0.1 m/m head gradient scenario and ∼33 years in the 0.05 m/m scenario. In the 0.01 m/m scenario, the CO_2 plume remains within the simulated reservoirs for the entire 50 years of simulated time.

As the CO_2 plume is reaching its steady-state configuration, carbonate minerals are dissolving and precipitating throughout a large fraction of the reservoir. However, as the CO_2 plume stabilizes, the region where the minerals precipitate begins to concentration in a region close to the well on the downstream side. Notably, the faster rates of calcite precipitation translate to a relatively stable location of the precipitated calcite plume centers of mass at a distance of ∼100-300 m downstream from the injection well. However, in the case of the dolomite reservoir, the centers of mass of the precipitated dolomite plumes are consistently farther downstream from the injection well, and considerably less stable in their locations. The distance between the centers of mass and the injection well in the 0.1 m/m and 0.05 m/m lines plotted in Fig. 6.4 peak two separate times, the first of which is associated with the initial CO_2 injection and the second of which is associated with CO_2 migration out of the system.

After CO_2 injection ceases and the CO_2 begins to migrate out of the reservoir, the volume of mineral that dissolves is largely dependent upon the residence time of the CO_2 and the associated low-pH, high-CO_2 brines in the simulated reservoir. In the high hydraulic head gradient (0.1 m/m and 0.05 m/m) calcite reservoirs, the supercritical CO_2 is quickly pushed out of the reservoir by inflowing fluid and the dissolution process is virtually halted approximately 10 and 20 years, respectively, after the injection is stopped. In the analogous dolomite simulations, as well as the 0.01 m/m head gradient scenarios, the migration of the CO_2 plume out of the reservoir is accompanied by a re-dissolution of a portion of the dolomite that had previously precipitated (Fig. 6.3d).

6.4.3 Delineating the effects of temperature, pressure, injection rate, and reservoir size

Temperature effects

In general, the fraction of our 100°C reservoirs where 50°C CO_2 significantly depresses the temperature is limited to a small region in close proximity to the injection well (Fig. 6.2). The fact that such a minor portion of the reservoir is thermally affected by the cool CO_2 injection suggests that, in actuality, only small portions

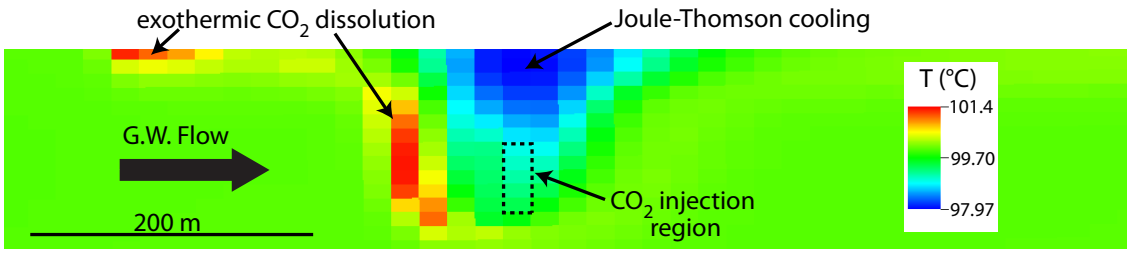

Figure 6.5: Two-dimensional slice parallel to the dominant flow direction along the center of a 200 bar reservoir with a hydraulic head gradient of 0.05 m/m after 5 years of injecting 100°C CO_2 at 50 kg/s. The CO_2 injection location is outlined in a dashed rectangle. Exothermic CO_2 dissolution raises temperature where fresh brine contacts the CO_2 plume and Joule-Thomson cooling lowers temperature in the vicinity of the injection well. Exothermic dissolution is most clearly visible at the upstream edge of the plume, where the majority of fresh brine-CO_2 equilibration is occurring.

of the reservoir experience the enhanced carbonate solubility associated with low-temperature fluid injection. To quantify the volume of mineral dissolution and precipitation that can be directly attributed to the injection of 50°C CO_2 versus 100°C CO_2 into the 100°C reservoirs, we present a second set of 200 bar calcite simulations run at all three hydraulic head gradients with CO_2 injection at this higher temperature. Under these conditions, it is possible to observe the effects of exothermic CO_2 dissolution and Joule-Thomson cooling on reservoir temperature (Fig. 6.5). In the 100°C injection scenarios, Joule-Thomson cooling depresses temperature near the injection well by ∼2-3°C, and exothermic heating increases temperature by ∼1-2°C near the edges of the supercritical CO_2 plume. Similar processes occur in the 50°C injection scenarios, but it is more difficult to delineate the cooling effects. The changes in carbonate solubility associated with these temperature changes (<3°C in all simulations) are considerably smaller than those associated with a transition from 50°C to 100°C.

In general, the comparison between the 50°C and 100°C injection scenarios illustrate that the actual mineral volume changes directly attributable to cool CO_2 injection are relatively minor (Fig. 6.6). During the first three years of injection in the 0.1 and 0.05 m/m hydraulic head gradient scenarios and for the entire duration of injection in the 0.01 m/m hydraulic head gradient scenario, the volumes of calcite precipitation are very similar. This is consistent with dessiccation as the major mode of precipitation during this period and the minor thermal impact that cool CO_2 injection has on the reservoir temperature before the steady-state plume configuration

Table 6.4: Effect of injecting 50 kg/s of CO_2 at 50°C versus 100°C into a 100°C, 200 bar calcite reservoir.

	Calcite dissolved (m^3)†			Calcite precipitated (m^3)†		
Hydraulic head gradient	50°C Inj.	100°C Inj.	Difference♯	50°C Inj.	100°C Inj.	Difference♯
0.01	21750	21400	1.6 %	481	346	39 %
0.05	13080	13300	-1.7 %	471	320	47 %
0.1	10670	10500	1.6 %	454	281	62%

†Values calculated at end of simulation (50 years).
♯Difference is calculated as the 50°C injection results minus the 100°C injection results.

is established (Fig. 6.2). However, once the steady-state plume configuration has been established, the effect of the thermal perturbation on mineral dissolution and precipitation becomes slightly more apparent (Fig. 6.6a,b).

After 50 years of simulated time, the volume of calcite dissolved in both the 50°C and 100°C injection simulations are within ±1.7% of each other (Table 6.4), with the 50°C injection scenario tending to dissolve more calcite, except during the later stages of the 0.05 m/m hydraulic head gradient scenario[1]. The difference in the volumes of calcite dissolved between the 50°C and 100°C injection scenarios tends to approximately correspond toto the additional volumes of calcite precipitated in each scenario. Therefore, thermally-induced calcite precipitation approximately doubles the volume of calcite precipitated in the reservoir. However, because the volume of calcite precipitated is, in all cases, less than 5% of the volume of calcite dissolved, the mineral volume redistribution is strongly dissolution-dominated and permeability changes resulting from calcite precipitation are likely to be practically negligble in both the 50°C and 100°C injection scenarios.

Although it is counter-intuitive to find that cool CO_2 injection does not dramatically impact the volumes of calcite dissolved and precipitated in these comparative simulations, the reason for this behavior becomes clear upon closer examination of the velocity profile within the reservoir (Fig. 6.7). The CO_2-brine relative permeability parameters that we employ dictate that once the CO_2 pore space saturation reaches ∼0.4, the brine relative permeability drops below ∼0.1. In our simulations, where the maximum CO_2 pore space saturation ranges from 0.5 to 0.6, the brine relative permeability becomes sufficiently low such that the calculated brine velocities are ∼0.01% of the background brine velocity (Fig. 6.7). Because of these low brine velocities, CO_2-equilibrated brine is very slow to travel into and out of the CO_2 plume region.

[1] The slightly greater calculated percentage of calcite dissolution in the 100°C reservoir is likely due to boundary effects and the timing of CO_2 exit from the simulated reservoir.

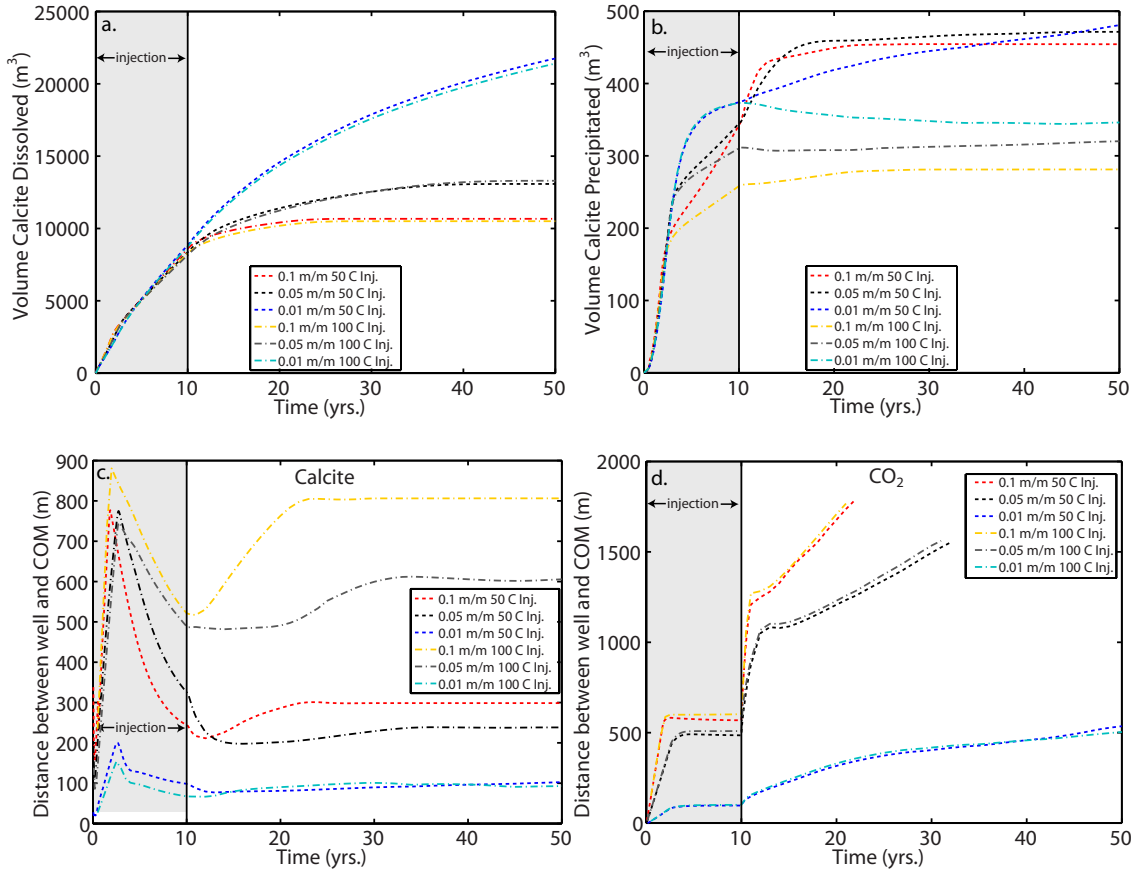

Figure 6.6: Calcite reservoir simulations were run with simulated injection temperatures of 50°C and 100°C in order to delineate the effect of cool CO_2 injection into geothermally warm reservoirs. Injection rate (50 kg/s), duration (10 years, with 40 years of recovery time), and reservoir temperature (100°C) and pressure (200 bars) were held constant through all simulations. The volumes of calcite dissolved and precipitated (a and b, respectively) as well as the horizontal distances between the centers of mass (C.O.M.s) of the CO_2 and precipitated calcite plumes (b and c, respectively) are plotted for comparison. The volumes of calcite dissolved at both injection temperatures are very similar, however the volume of precipitated calcite tends to be higher in the low-temperature injection simulations.

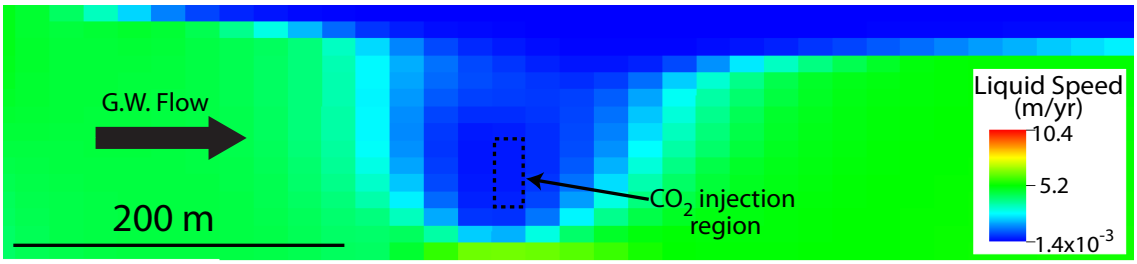

Figure 6.7: Two-dimensional slice parallel to the dominant flow direction down the center of a 200 bar reservoir with a hydraulic head gradient of 0.05 m/m after 5 years of injecting 50°C CO_2 at 50 kg/s. Low brine speeds result from relative permeability effects associated with supercritical CO_2 saturation of pore space.

Pressure effects

The effect of pressure (depth) is examined by running all simulations for both reservoir types at both 100 and 200 bars of pressure, which correspond to approximate depths of ∼1 and ∼2 km, respectively. At temperatures below ∼200°C, pressure has a negligible effect on the thermodynamics of mineral-fluid and aqueous species reactions (e.g., Helgeson, 1969; Sverjensky et al., 1991; Tutolo et al., 2014a, 2015b). Tutolo et al. (2014b) caculated the solubility of dolomite in CO_2-saturated solutions at pressures from 100 to 200 bar and temperatures from 21 to 200 °C and showed that the effect of pressure on dolomite solubility at these conditions is negligible. Because similar processes govern their solubility, calcite is expected to behave similarly. Therefore, we utilize the same thermodynamic database for simulations at both 100 and 200 bars. Nevertheless, CO_2 solubility in aqueous fluids, as well as CO_2 density, are pressure-dependent at the conditions considered here (e.g., Duan and Sun, 2003). PFLOTRAN calculates CO_2 solubility using a subroutine implementation of the Duan and Sun (2003) model, which allows us to examine the particular effects of pressure on CO_2 solubility, CO_2 transport in the aqueous phase, and its effect on mineral solubilities. Similar to other reservoir simulators (e.g., TOUGH2-ECO2N (Pruess and Spycher, 2007)), PFLOTRAN utilizes a database of thermophysical properties in order to calculate other properties of CO_2 such as enthalpy, density, and viscosity.

The density of supercritical CO_2 is strongly pressure-dependent at the temperatures of interest in this study. At low pressure and high temperature, CO_2 density tends to be more gas-like, while at higher pressures it tends to be more liquid-like. An equivalent mass of CO_2 at lower density will tend to fill a greater fraction of the pore space (Tutolo et al., 2014b), which, when substituted into Eqn. 6.3, will yield

higher relative permeabilities of the CO_2 phase. Therefore, the simulated aquifers are more permeable to CO_2 at the lower pressures considered in this study even though the same mass of CO_2 is injected into the reservoirs in both scenarios. In the higher-pressure scenarios, CO_2 is both more soluble and less mobile, and therefore tends to affect the solubility of the carbonate phases to a greater extent. Overall, the effect of pressure on CO_2 and mineral soubilities is more pronounced at lower hydraulic head gradients and related lower flow velocities (Fig. 6.3a,c).

Effects of CO_2 injection rate and reservoir size

An additional set of 200 bar calcite reservoir simulations that were run with an order of magnitude lower CO_2 injection rate (4 kg/s) allows us to explore the effect of injection rate on carbonate CCUS reservoir processes. Because the solubility of CO_2 in the reservoir brines is virtually the same for the 50 kg/s and 4 kg/s injection rate scenarios (ignoring the increased pore-fluid pressure that results from injecting CO_2 into the reservoir), a significantly greater fraction of the injected CO_2 dissolves into the reservoir brine at the lower injection rate. The fact that a smaller volume of CO_2 is being injected leads to even less pronounced thermal perturbations associated with CO_2 injection compared to the 50 kg/s injection rate scenarios.

In general, simulations run with a CO_2 injection rate of 4 kg/s show very similar trends to those run at 50 kg/s. The higher injection rate scenarios tend to dissolve more calcite (Fig. 6.8a), which is consistent with the higher solubility of calcite in CO_2-saturated solutions that are occupying a greater proportion of the reservoir. However, the calculated volumes of calcite precipitation show some interesting trends (Fig. 6.8b). In the 0.01 m/m hydraulic head gradient scenario, the volume of calcite precipitated during the final stages of the 4 kg/s injection period is considerably higher than that precipitated in the 50 kg/s injection scenario. Upon closer examination, it seems likely that this behavior is actually an artifact of the simulated domain size. In the 50 kg/s scenario, the supercritical CO_2 phase reaches the domain boundary sooner than in the 4 kg/s scenario, and, because much of the precipitation is actually occurring through dessiccation at the interface between the injected CO_2 and the reservoir brine, the precipitation is not captured in the higher injection rate scenario. A similar process appears to be occurring in the 0.05 m/m hydraulic head gradient scenarios. Although these results indicate that at least some of the carbonate mineral precipitation is not captured in the presented simulation, it is important to note that

these precipitation processes are occurring in a region far removed from the CO_2 injection well and therefore will be unlikely to impact CO_2 injectivity.

The precipitated calcite and CO_2 plumes tend to behave similarly in regards to their spatial distributions (Fig. 6.8c,d). The precipitated calcite "plume" generally stabilizes in a location further down-gradient from the injection well in the low injection rate scenario (Fig. 6.8c), which is consistent with the behavior of the CO_2 plume (Fig. 6.8d). As might be expected from consideration of the lower total volume of supercritical CO_2 injected into the reservoir, the injected supercritical CO_2 tends to completely exit[2] the simulated domain earlier in the lower injection rate scenarios, as evidenced by the fact that the lines plotted for the 4 kg/s injection rate scenarios tend to end at slightly earlier times than those for the 50 kg/s scenarios (Fig. 6.8d). Because the CO_2 plume stabilizes farther down-gradient in the lower injection rate scenario and much of the calcite dissolution and precipitation generally occurs at the CO_2/brine interface, calcite precipitates closer to the well in the lower injection rate scenario. The 4 kg/s, 0.01 m/m hydraulic head gradient scenario behavior tends to differ from the behavior observed at other hydraulic head gradients, particularly in the calculation of the distance between the calcite plume center of mass and the injection well. This behavior is likely an artifact of the domain size and the timing of the exit of the CO_2 plume, and would likely be more similar to the other scenarios if the domain was of sufficient size. Overall, we can conclude that minor effects of mineral dissolution/precipitation on injectivity are seen for both the 4 kg/s and 50 kg/s CO_2 injection rate scenarios.

6.5 Discussion

Although we present a large number of simulations here, several general processes are characteristic to all of them. Firstly, the magnitude of the thermal perturbation caused by cool CO_2 injection is relatively limited in all scenarios. This limited thermal perturbation is consistent with the fact that the heat capacity of CO_2 is approximately half that of water (Randolph and Saar, 2011a) and it therefore takes a relatively minor amount of the reservoir's geothermal energy to heat the CO_2 up to reservoir temperature. Importantly, this property of CO_2, combined with its higher mobility (i.e., inverse kinematic viscosity), lengthens the period of time that it takes CO_2 to

[2] Note that the reason that the CO_2 plume *completely* exits the simulated reservoirs is an artifact of our usage of 0 for the residual CO_2 saturation (See Sect. 6.3.2).

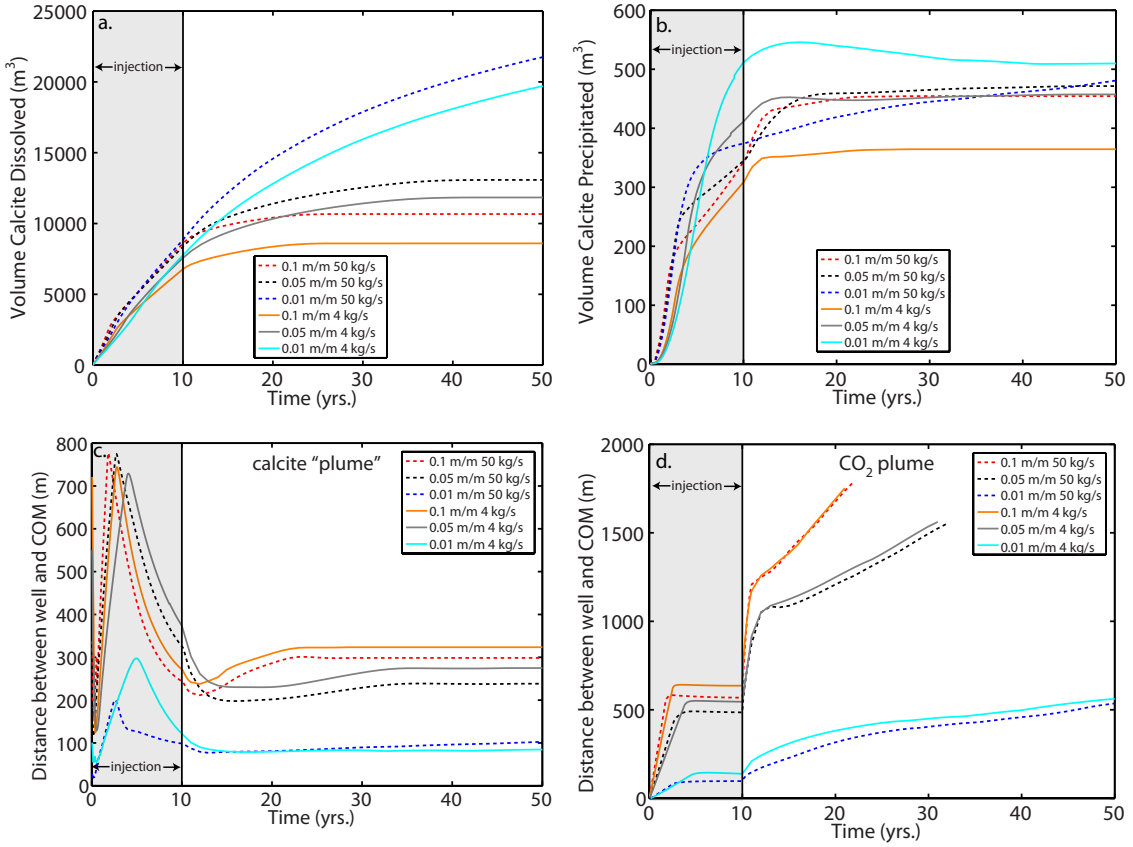

Figure 6.8: Comparison between 200 bar calcite reservoir simulations performed at a lower injection rate (4 kg/s) and those presented in Figs. 6.3 and 6.4. Similar to these figures, the summed volume of calcite dissolved (a) and precipitated (b) as well as the horizontal distance between the injection well and centers of mass of precipitated calcite (c) and CO_2 (d) are presented. The higher injection rate simulations tend to both dissolve and precipitate more calcite than the lower injection rate simulations.

deplete a reservoir's heat and allows CO_2-based geothermal energy extraction to be longer-lived and more efficient than water-based (e.g., Randolph and Saar, 2011a; Garapati et al., 2015).

Upon CO_2 injection, the reservoir brine is displaced and the buoyant CO_2 rises towards the low-permeability cap rock, where it pools and expands areally throughout the reservoir. Except for a region that is a maximum of several tens of meters in diameter surrounding the injection well, most of the CO_2 is located in a pooled plume beneath the impermeable upper boundary of the simulated reservoir. The vertical extent of this CO_2 plume is generally less than about twenty meters, and therefore much of the 150 m depth of the simulated reservoir contains only single phase brine which may or may not be saturated with respect to the supercritical CO_2. However, in thinner reservoirs (e.g., 50 m), CO_2 injection may cause more widespread displacement throughout the reservoir, similar to plug flow (Garapati et al., 2015).

In general, thermally-induced CO_2 exsolution, which was shown to dramatically affect brine relative permeability in a number of laboratory experiments (e.g., Luhmann et al., 2013; Tutolo et al., 2014b) is not readily apparent in any of our simulations. This result is predominantly due to the fact that increases in temperature that affect the CO_2-equilibrated brine occur in close proximity to the much larger supercritical CO_2 plume (Fig. 6.2), and the exsolved CO_2 therefore simply coalesces with the larger plume. The presence of free-phase supercritical CO_2 within the pore space leads to low brine phase velocities within regions with appreciable CO_2 saturations (Fig. 6.7), and therefore the reservoir brine tends to create velocity streamlines that flow around the injection well region and CO_2 plume. The displacement of the brine flow pathways around the CO_2 plume prevents much of the flowing brine from ever thermally equilibrating with the cool, near-well region. Nonetheless, because our results show that the thermally-impacted region of the reservoir grows over the duration of the injection period (Fig. 6.2), it is likely that long-term CCUS operations with low CO_2 injection temperatures relative to the reservoir temperature will become increasingly thermally perturbed over their lifetime.

Another general characteristic of the presented simulations is that dissolution and precipitation tend to occur in the cells near the interface between the CO_2 plume and the reservoir brine. Consistent with the discussion in Sect. 6.4.3, much of the carbonate growth occurs in regions of the reservoir greater than 90°C. This is generally

consistent with the assertion of André et al. (2010) that dessiccation, not thermal processes, accounts for the majority of precipitation when cool CO_2 is injected into carbonate reservoirs. Moreover, the majority of the dissolution processes occur at temperatures slightly greater than 100°C. In these locations, CO_2 is dissolving into the brine and lowering pH, which enhances carbonate solubility, while, at the same time, exothermic heating is raising the brine temperature and thereby slightly counteracting the increase in carbonate solubility.

A final characteristic trait consistent across all presented simulations is the very small magnitudes of mineral volume changes. Even in the simulation with the largest volume of primary mineral dissolution (200 bar, calcite, 0.01 m/m head gradient, see Fig. 6.3), the grid block-averaged porosity across the entire reservoir never increases by more than ∼0.6%. Furthermore, mineral precipitation reactions tend to account for a maximum of ∼0.01% and 0.0001% porosity decreases for the calcite and dolomite scenarios, respectively. The rapid equilibration between the injected CO_2, reservoir brine, and the host mineralogy leads to much of the simulated reservoirs being characterized by a strong transport limitation (i.e., high Damköler number), wherein the extent of dissolution and precipitation and the associated porosity increases and decreases, respectively, are strongly limited by the rate at which pore space brine is refreshed by a far-from equilibrium fluid (e.g., Steefel and Lasaga, 1990; Steefel et al., 2013; Luhmann et al., 2014). The only exception is dolomite precipitation, which occurs considerably more slowly than calcite precipitation. The slow dolomite precipitation kinetics yield a somewhat lower Damköler number and lead to dolomite supersaturation in fluids that dissolve dolomite at low temperature and travel to the higher-temperature portion of the reservoir. Nonetheless, the fact that calcite dissolves and precipitates at equilibrium in all presented simulations shows that this rate limitation does not dramatically affect our overall conclusion that the pore space-filling potential of the carbonate precipitation reactions are generally quite limited. However, the varied style and extent of these changes could potentially have implications for flow, permeability, porosity, and thermal regimes not considered here (see Sect. 6.5.1).

6.5.1 The effect of parameter choice on simulation results

Geochemical kinetics

A number of approximations have been made in the chemical model formulation that may contribute to the overall uncertainty of the simulations presented here. Firstly, although Arvidson and Mackenzie (1999) have made significant strides towards quantifying the rates of dolomite precipitation at conditions relevant to this study, the general process of quantifying precipitation rates is subject to significant uncertainty. The dolomite growth rate parameters we employ were calibrated at dissimilar conditions from those presented here, and the effects of high pCO_2 fluids on dolomite precipitation have not yet been quantified. Furthermore, we ignore crystal nucleation rates and assume a constant mineral specific surface area throughout all runs. The magnitude of the errors introduced due to these approximations are difficult to estimate. Moreover, mineral reactive surface areas are a perpetual source of uncertainty. The value utilized here, while much lower than those measured using B.E.T. measurements (Luhmann et al., 2014), is utilized due to its agreement with the laboratory dissolution experiment of Tutolo et al. (2014b). To test the effect of our chosen value of surface area, additional dolomite simulations were run by inputing the B.E.T. specific surface area reported by Luhmann et al. (2014) for dolomite rock cores, 1020 cm^2/g (Fig. 6.9). Because the rates of geochemical reactions are equivalent to the value of r calculated through Eqn. 6.4 multiplied by the specific surface area, using this higher value effectively increases the dolomite precipitation rates by around fifteen-fold.

In spite of these limitations associated with dolomite growth kinetics, the simulated reservoir remains transport-limited and the solubility of dolomite in the reservoir fluid still places low upper bound limits on the volume of dolomite that can possibly precipitate. In other words, because the dolomite rapidly dissolves and the fluid reaches equilibrium with respect to dolomite, the volume of dolomite that precipitates is predominantly limited by the amount that dissolves and not necessarily the precipitation rate. Even using these high B.E.T. surface areas and associated higher reaction rates cannot dramatically affect the volume of dolomite that precipitates for the range of investigated model parameters.

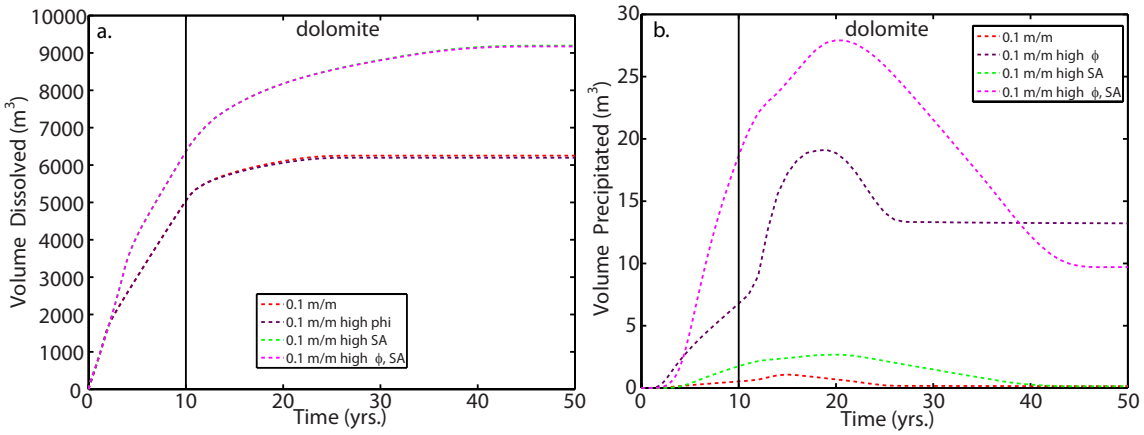

Figure 6.9: Comparison of volumes of dolomite dissolved (a) and precipitated (b) for simulations run using higher input porosity and surface area than the default parameters utilized in all other simulations. The higher porosity increases the instantaneous water-to-rock ratio and therefore more dolomite must dissolve in order for the fluid to equilibrate. This higher dissolved volume has the effect of increasing the volume of dolomite that precipitates, particularly when a higher surface area of the secondary phase is employed (See Sect. 6.5.1.)

Porosity, permeability, and relative permeability

The default porosity that we utilize in our simulations (0.07) is at the lower end of the range of carbonate porosities measured in natural formations (e.g., Schwartz and Zhang, 2003). To examine the effect that porosity, and hence water-to-rock ratio, has on the dissolution and precipitation of carbonate minerals, we present results for the 200 bar, 50°C, 50 kg/s injection dolomite reservoir simulations with a porosity of 0.15 utilizing both the default specific surface area as well as the B.E.T.-measured dolomite specific surface area reported by Luhmann et al. (2014) (Fig. 6.9). As discussed above, the rate of dolomite dissolution is sufficiently rapid at our simulated temperatures that the fluid equilibrates with dolomite between timesteps. Therefore, the higher specific surface area has no effect on the volume of dolomite dissolved during the simulation (Fig. 6.9a). However, the larger porosities increase instantaneous water-to-rock ratios so that more dolomite must dissolve before equilibrium can be reached. The higher porosity therefore has the effect of increasing the volume of dolomite that dissolves and precipitates in the reservoir (Fig. 6.9). Because dolomite precipitation is kinetically limited, the higher surface area has a measurable effect on the precipitated volume of dolomite. However, the volume of dolomite precipitated is

still considerably less than the volume of calcite that precipitates in analagous, lower-porosity simulations (Fig. 6.3), which would therefore be unlikely to affect reservoir injectivity. Notably, a considerable amount of the precipitated dolomite re-dissolves in these simulations, beginning approximately ten years after CO_2 injection stops. At this time, the CO_2 plume has begun to migrate out of the reservoir and the lower brine relative permeability effects associated with the presence of supercritical CO_2 begin to diminish. This higher brine relative permeability and changes in the distribution of the CO_2 plume allow more brine to equilibrate with the CO_2 plume and enhance the solubility of the previously precipitated dolomite.

It is clear from this discussion, and the discussion about velocity profiles in Sect. 6.4.3 above, that the relative permeabilities of the brine and CO_2 phase have a considerable effect on the hydrogeochemical evolution of the simulated CCUS reservoirs. We chose to utilize the relative permeability parameters presented by André et al. (2007), but a considerable body of literature has demonstrated the considerable range of relative permeability parameters associated with different rock types and CO_2-brine flow regimes (e.g., Bennion et al., 2008; Müller, 2011; Krevor et al., 2012; Zuo et al., 2012; Falta et al., 2013; Tutolo et al., 2014b). In particular, a number of studies have shown that exsolved CO_2 can cause interesting and dramatic relative permeability effects (e.g., Luhmann et al., 2013; Falta et al., 2013; Tutolo et al., 2014b). However, variations in the CO_2 and brine relative permeability functions would generally only impact our conclusions if they allowed for high relative permeability of the brine phase even in regions with significant CO_2 saturation, which is generally not the case.

All simulations performed in the present study utilize a single, isotropic value of permeability for the entire simulated reservoir. However, in real carbonate CCUS reservoirs, the geologic history of the reservoir will likely result in significantly anisotropic and heterogeneous permeability fields. The effect that such heterogeneities have on the conclusions of this study are difficult to quantify. However, regardless of the reservoir's permeability structure, the fact that carbonate mineral dissolution and precipitation processes in our simulated reservoirs tend to be strongly transport limited suggests that the calculated volumes of minerals dissolved and precipitated would only be affected if the reservoir permeability were greater than the value we employ.

Mineralogical heterogeneities, well geometry, and reservoir size

Generally, carbonate reservoirs are not entirely composed of dolomite or calcite, and instead are more likely to contain varying abundances of these and other carbonate and silicate minerals. Nonetheless, our results also apply to these mineralogically variable reservoirs. Because calcite never becomes supersaturated in the dolomite simulations we can hypothesize that thermally-induced calcite precipitation is likely to be more prominent than dolomite precipitation in reservoirs containing variable abundances of both calcite and dolomite. This is especially true when one considers the relatively slow rate of dolomite precipitation. Furthermore, variable reservoir thickness and alternate geometry of the injection well(s) may additionally impact the distribution of carbonate mineral dissolution and precipitation in CCUS reservoirs (e.g., MacMinn et al., 2010). If, for example, the reservoir was considerably thinner and a vertical injection well were used, the injected CO_2 would likely occupy a greater proportion of the reservoir than in the presented simulations (Garapati et al., 2015). The more widespread distribution of CO_2 would likely impact the location and quantity of mineral dissolution and precipitation such that greater porosity and permeability changes would occur. If, on the other hand, a horizontal CO_2 injection well drilled perpendicular to the dominant flow direction were utilized, the supercritical CO_2 would likely be less concentrated in the reservoir and correspondingly lower porosity changes would likely occur. In any case, the 21 scenarios that we have presented sample a range of parameters that are likely representative of typical CCUS reservoirs and emphasize that the porosity effects resulting from cool CO_2 injection and coupled carbonate dissolution/precipitation reactions are unlikely to impact CCUS reservoir injectivity.

6.5.2 Comparison with experimental results

A significant amount of research effort has been directed towards quanitfying the porosity and permeability effects of CO_2 injection into carbonate-bearing aquifers. However, in this study, and elsewhere (e.g., Johnson et al., 2004; Xu et al., 2004; Kharaka et al., 2006; Trémosa et al., 2014), the magnitude of these chemical reactions has been put into a more realistic perspective by simultaneously considering the many coupled processes occurring in CCUS reservoirs as CO_2 is introduced and removed from the aquifer. A number of important aspects of the reactive transport approach

utilized in this study allow for these previous results to be put into a more realistic perspective. Specifically, we illustrate that porosity increases and decreases associated with carbonate dissolution and precipitation in our simulated CCUS reservoirs tend to be less substantial than the majority of experimental studies suggest.

As we discuss above, the relatively small mineral volume changes observed in our simulations are mostly related to transport limitations that characterize our simulated CCUS reservoirs. Intuitively, as fluids approach equilibrium with respect to reservoir minerals, their capacity for further reaction diminishes. Luhmann et al. (2014) showed that relatively high water-to-rock mass ratios, on the order of 10 to 50, are required to impact dolomite core permeability through dissolution reactions when the reaction fluid is far-from-equilibrium with respect to dolomite. However, it is important to note that many of their sampled fluids were relatively close to equilibrium with respect to dolomite, the mineral comprising their experimental cores. Therefore, over a length scale of ~ 2.5 cm, a high-temperature experimental fluid was able, in some cases, to reach zero reactivity. If this fluid were then to continue to travel through a much larger-scale dolomite reservoir, it would do so with negligible reactivity and therefore would not be able to dramatically impact the reservoir's injectivity. These processes are characteristic of the transport-limited, high-Damköler number processes we have investigated in our simulations. As we have illustrated, even our highest flow rates did not refresh the reservoir with enough far-from-equilibrium brine to overcome this transport limitation over our simulated time scales, mostly due to the characteristically low relative permeability of the brine phase within the CO_2 plume.

Tutolo et al. (2014b) present a similar experiment to those presented by Luhmann et al. (2014), wherein porosity and dissolution pathways were created as a far-from-equilibrium experimental solution approaches equilibrium with respect to a dolomite core at 21°C and 60°C. However, in the Tutolo et al. (2014b) experiment, the experimental temperature was raised such that the fluid that had been equilibrated with CO_2 at 21°C and dolomite at 60°C was allowed to exsolve CO_2 and precipitate dolomite within the previously created pore space. The fluid was continually recycled through the core, such that, by the time the experiment concluded, a considerable amount of dolomite had re-precipitated in the dissolution pathways previously created at the lower temperatures. In thermodynamic calculations, Tutolo et al. (2014b) suggest that a 1 molal NaCl fluid equilibrated with dolomite and CO_2

at 50°C and 200 bar has the capacity to precipitate ∼0.58 cm^3 dolomite per kg if it is instantaneously transferred to 100°C. Similar calculations show that a 1 molal NaCl fluid equilibrated with calcite and CO_2 at 50°C and 200 bar has the capacity to precipitate ∼0.83 cm^3 calcite per kg. In Fig. 6.10, we plot two simple calculations designed to quantify how these 50°C, carbonate-saturated fluids would impact the porosity of a 100°C rock with an initial porosity of 0.07. These calculations suggest that ∼100 pore volumes would be required to lower the porosity of the reservoir by several percent, with dolomite taking a larger number of pore volumes than calcite. These calculations are lower-bound estimates because they ignore both the transport distance required to increase the fluid temperature from 50° to 100°C and the kinetics of carbonate precipitation. Nonetheless, if these estimates are put into the context of our reservoir-scale simulations, we can begin to see why the impact of cool CO_2 injection is so minor.

At our highest hydraulic head gradient, 0.1 m/m, the Darcy velocity is ∼10.4 m/yr. If, for simplicity, we consider a fully brine-saturated representative elementary volume (REV) of 1 m^3, we can calculate that it would refill approximately 150 times per year at this flow rate. If subjected to the mineral precipitation as calculated in Fig. 6.10, the porosity and permeability would be dramatically lowered within several years. If, on the other hand, the REV contained $\gtrsim$40% supercritical CO_2, relative permeability effects discussed above would cause the REV to be refilled less than once a year. At this rate, it would take hundreds or thousands of years for mineral precipitation to have a substantial effect on porosity. Therefore, the transport limitation associated with relatively fast carbonate reaction rates is made even more severe in CCUS reservoirs by the fact that the relative permeability, and hence velocity of the brine phase in contact with supercritical CO_2, tends to be relatively low. The permeability change resulting from these porosity-reducing reactions would therefore probably not take effect until after the relevant injection period. Even relatively minor amounts of precipitation can potentially negatively impact formation permeability, however, if they concentrate in pore throats. In this specific case, these minor precipitated volumes could potentially impact permeability over a CCUS reservoir lifetime.

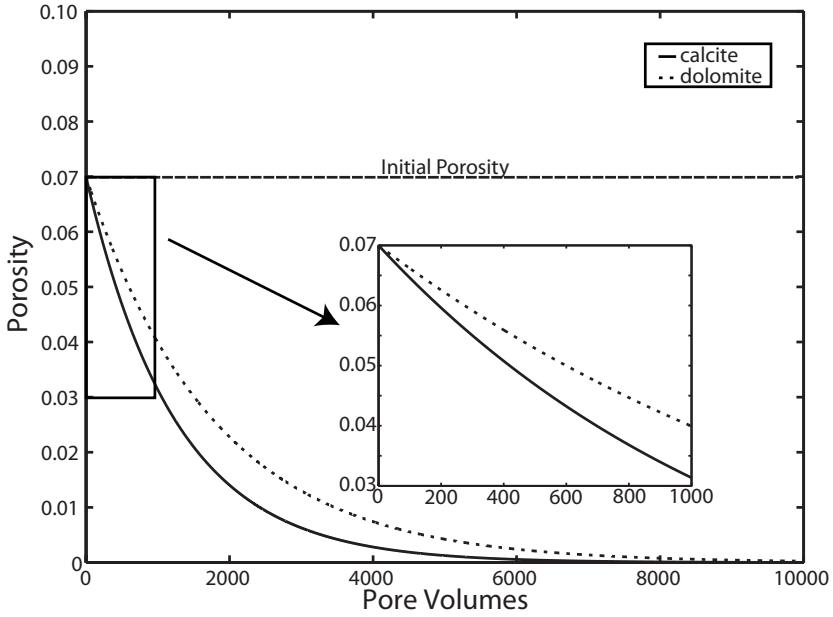

Figure 6.10: Calculation illustrating the effect of dolomite and calcite precipitation on the porosity of a rock with an initial porosity of 0.07. The fluid is assumed to instantaneously transfer from 50°C to 100°C at 200 bar of pressure and deposit 0.58 cm^3/kg (dolomite) or 0.83 cm^3/kg calcite (Tutolo et al., 2014b). Porosity evolution is taken into account such that pore volumes become considerably smaller as the porosity is decreased by mineral precipitation. Note that we utilize pore volumes, which decrease as the volume of precipitated mineral increases, instead of water-to-rock ratios in order to preserve the non-dimensionality of the associated equations.

6.5.3 The utility of reactive transport simulations at reservoir scales

A major conclusion of this study is the benefit of employing reactive transport simulations to upscale experimental results and equilibrium thermodynamic calculations to the field scale. As has been emphasized here, the coupled processes of brine and CO_2 flow, CO_2 dissolution into and exsolution out of brine, mineral dissolution and precipitation, and the transport of solutes and heat are necessary to consider when examining CO_2 injection into carbonate CCUS reservoirs. Only careful examination of all relevant processes in coupled form over (close-to) actual reservoir scales in three dimensions at realistic time scales can reveal these complex processes and their interdependencies. This ultimately requires reactive transport simulations that can put laboratory experiments, that are necessarily conducted over small spatial and temporal scales, as well as field data, which often provide spatially limited information and only a temporal "snapshot", in a more realistic, reservoir-scale framework, both spatially and temporally. Because of their ability to observe the coupled processes of fluid, heat, and aqueous species transport and coupled chemical reactions, reactive transport simulators are a vital tool for the evaluation of CCUS reservoirs. We could not have arrived at the unique conclusions of this study regarding the effect of cool CO_2 injection and CO_2-brine-carbonate mineral reactions in CCUS reservoirs without using this fully coupled, reactive transport approach.

6.6 Conclusions and general implications for CCUS reservoirs

Because carbonate minerals and CO_2 are considerably more soluble at lower temperatures, researchers have hypothesized that cool CO_2 injection can effectively redistribute reservoir porosity and permeability and affect injectivity by dissolving carbonates where cold fluids are injected into the reservoir and precipitating carbonates as the injected fluids heat up during flow away from the injection well. In this study, we examine the coupled effects of cool CO_2 injection and background hydraulic head gradients on reservoir-scale mineral volume changes using the fully coupled, massively parallel reactive transport simulator PFLOTRAN. We examine the effects of temperature, pressure, hydraulic head gradient, and CO_2 injection rate on dissolution and precipitation processes in monomineralic calcite and dolomite CCUS reservoirs. Based

on the 21 low-temperature and isothermal CO_2 injection simulations we present, we provide the following general conclusions:

1. The low heat capacity of CO_2 effectively prevents low-temperature CO_2 injection from decreasing the temperature across large portions of the simulated carbonate reservoirs.

2. The small observed thermal perturbation and generally low relative permeability of brine within supercritical CO_2-saturated pore space result in limited mineral dissolution and precipitation directly attributable to cool CO_2 injection.

3. Relatively high water-to-rock ratios would be required to substantially affect fluid injectivity through thermally-induced mineral dissolution and precipitation, which may occur over much longer CCUS reservoir lifetimes or in materials that maintain sufficiently high brine relative permeability within the CO_2 plume during the CO_2 injection period.

4. Fully coupled, reservoir-scale reactive transport simulations are an effective means of placing laboratory- and field-scale observations into a reservoir-scale context, both spatially and temporally.

Furthermore, in order to examine the effect of our chosen porosity and mineral specific surface area on our conclusions, we present an additional set of simulations run with higher porosity and mineral surface area. Nonetheless, even these simulations illustrate the minor effect that low-temperature CO_2 injection has on reservoir porosity.

Chapter 7

Conclusion

Greenhouse gas emissions and their associated changes to Earth's climate, hydrologic, and ecologic systems remain some of the foremost issues facing society in the twenty-first century. In this thesis, I have explored fundamental and applied aspects of one of the proposed methods for transitioning from a fossil fuel-burning, greenhouse gas-emitting society to a renewable energy-based society: Carbon Capture, Utilization, and Storage (CCUS). During this process, several important themes have developed, and these themes tend to pervade many geoscientific persuits. In particular, I have shown that understanding and predicting the processes that may occur during CCUS operations–and many other geological systems–requires the combination of fundamental data sets from many disparate sources. Successful use of these fundamental data sets, particularly those dealing with the thermodynamics and kinetics of mineral-fluid interactions, necessitates that their users critically examine them prior to incorporating them into their conceptual models. Furthermore, I have emphasized the complexity of the coupling between geochemical processes and hydrogeochemical properties and its importance for understanding how CCUS reservoirs will evolve over their lifetimes and determining the ultimate potential success of such operations. In addition, I have explored the interesting and complex feedbacks between mineral dissolution and precipitation processes, particularly the effect of secondary mineral precipitation rates on primary mineral dissolution rates. This specific and pervasive process remains difficult to predict, and future work should continue to focus on this coupling. Finally, I have repeatedly stressed the vital utility of reactive transport models for producing fully coupled predictions and analyses of relevant processes at the wide range of spatial and temporal scales applicable to CCUS. These simulators show incredible promise for the future of many geoscientific disciplines.

Overall, I have illustrated that CCUS in sandstone and dolomite reservoirs appears to be geochemically feasible from the standpoint of long-term reservoir injectivity and storativity. When considering reservoir-scale results, neither the sandstone nor dolomite reservoirs appear to evolve in such a way as to prevent successful CCUS operations over the time scale of several decades. Nonetheless, the stability of the sealing formations has not been discussed here and future research will be required to examine the potential effects of CO_2 leakage through these formations.

References

Aagaard, P., Helgeson, H. C., 1982. Thermodynamic and kinetic constraints on reaction rates among minerals and aqueous solutions; I. Theoretical considerations. Am. J. Sci. 282 (3), 237–285.

Adams, B. M., Kuehn, T. H., Bielicki, J. M., Randolph, J. B., Saar, M. O., 2014. On the importance of the thermosiphon effect in CPG (CO_2 plume geothermal) power systems. Energy 69, 409–418.

Aja, S. U., Rosenberg, P. E., Kittrick, J. A., 1991. Illite equilibria in solutions: I. Phase relationships in the system K_2O-Al_2O_3-SiO_2-H_2O between 25 and 250° C. Geochim. Cosmochim. Acta 55 (5), 1353–1364.

Alekseyev, V. A., Medvedeva, L. S., Prisyagina, N. I., Meshalkin, S. S., Balabin, A. I., 1997. Change in the dissolution rates of alkali feldspars as a result of secondary mineral precipitation and approach to equilibrium. Geochim. Cosmochim. Acta 61 (6), 1125–1142.

Alexander, S. C., Saar, M. O., 2012. Improved characterization of small "u" for Jacob pumping test analysis methods. Ground Water 50 (2), 256–265.

Allen, D. E., Strazisar, B. R., Soong, Y., Hedges, S. W., 2005. Modeling carbon dioxide sequestration in saline aquifers: Significance of elevated pressures and salinities. Fuel Process. Technol. 86 (14), 1569–1580.

Althaus, E., Karotke, E., Nitsch, K., Winkler, H., 1970. An experimental reexamination of the upper stability limit of muscovite plus quartz. Neues Jahrb. Mineral. Monatsh 7, 325–336.

Anderson, G. M., Crerar, D. A., 1993. Thermodynamics in Geochemistry: The Equilibrium Model. Oxford University Press, New York, NY, USA.

André, L., Audigane, P., Azaroual, M., Menjoz, A., 2007. Numerical modeling of fluid–rock chemical interactions at the supercritical CO_2–liquid interface during CO_2 injection into a carbonate reservoir, the Dogger aquifer (Paris Basin, France). Energy Convers. Manage. 48 (6), 1782–1797.

André, L., Azaroual, M., Menjoz, A., 2010. Numerical simulations of the thermal impact of supercritical CO_2 injection on chemical reactivity in a carbonate saline reservoir. Transport Porous Med. 82 (1), 247–274.

Andreani, M., Gouze, P., Luquot, L., Jouanna, P., 2008. Changes in seal capacity of fractured claystone caprocks induced by dissolved and gaseous CO_2 seepage. Geophys. Res. Lett. 35 (14), L14404.

Apps, J. A., Neil, J., Jun, C.-H., 1988. Thermochemical properties of gibbsite, bayerite, boehmite, diaspore, and the aluminate ion between 0 and 350°C. University of California Lawrence Berkeley Rept., LBL-21482.

Apps, J. A., Neil, J. M., Jun, C. H., 1989. Thermochemical properties of gibbsite, bayerite, boehmite, diaspore, and the aluminate ion between 0 and 350°C. Tech. rep., Nuclear Regulatory Commission, Washington, DC (USA). Div. of Waste Management; Lawrence Berkeley Lab., CA (USA).

Aranovich, L. Y., Newton, R., 1996. H_2O activity in concentrated NaCl solutions at high pressures and temperatures measured by the brucite-periclase equilibrium. Contrib. Mineral. Petr. 125 (2-3), 200–212.

Aranovich, L. Y., Newton, R., 1997. H_2O activity in concentrated KCl and KCl-NaCl solutions at high temperatures and pressures measured by the brucite-periclase equilibrium. Contrib. Mineral. Petr. 127 (3), 261–271.

Archer, D. G., 1991. Thermodynamic properties of the NaBr + H_2O system. J. Phys. Chem. Ref. Data 20 (3), 509–555.

Archer, D. G., 1992. Thermodynamic properties of the NaCl + H_2O system. II. Thermodynamic properties of NaCl (aq), NaCl·2H_2O(cr), and phase equilibria. J. Phys. and Chem. Ref. Data 21 (4), 793–829.

Arnórsson, S., Gunnlaugsson, E., Svavarsson, H., 1983. The chemistry of geothermal waters in Iceland. II. Mineral equilibria and independent variables controlling water compositions. Geochim. Cosmochim. Acta 47 (3), 547–566.

Arnórsson, S., Stefánsson, A., 1999. Assessment of feldspar solubility constants in water in the range of 0° to 350°C at vapor saturation pressures. Am. J. Sci. 299 (3).

Arvidson, R., Mackenzie, F., 1997. Tentative kinetic model for dolomite precipitation rate and its application to dolomite distribution. Aquat. Geochem. 2 (3), 273–298.

Arvidson, R. S., Mackenzie, F. T., 1999. The dolomite problem: control of precipitation kinetics by temperature and saturation state. Am. J. Sci. 299 (4), 257–288.

Bachu, S., 2003. Screening and ranking of sedimentary basins for sequestration of CO_2 in geological media in response to climate change. Environ. Geol. 44 (3), 277–289.

Balashov, V., Guthrie, G., Alexandra Hakala, J., Lopano, C., Donald Rimstidt, J., Brantley, S., 2013. Predictive modeling of CO_2 sequestration in deep saline sandstone reservoirs: Impacts of geochemical kinetics. Appl. Geochem. 30, 41–56.

Barany, R., Kelley, K. K., 1961. Heats and free energies of formation of gibbsite, kaolinite, halloysite, and dickite US Dept. of the Interior. Bureau of Mines 5825, 13 p.

Barbier, E., 2002. Geothermal energy technology and current status: an overview. Renew. Sust. Energ. Rev. 6 (1), 3–65.

Bassett, R. L., Kharaka, Y. K., Langmuir, D., 1979. Critical review of the equilibrium constants for kaolinite and sepiolite. Chemical Modeling in Aqueous Systems: Speciation, Sorption Solubility and Kinetics, American Chemical Society, Washington, 389–400.

Bénézeth, P., Palmer, D. A., Anovitz, L. M., Horita, J., 2007. Dawsonite synthesis and reevaluation of its thermodynamic properties from solubility measurements: Implications for mineral trapping of CO_2. Geochim. Cosmochim. Acta 71 (18), 4438–4455.

Bénézeth, P., Palmer, D. A., Wesolowski, D. J., 2001. Aqueous high-temperature solubility studies. II. the solubility of boehmite at 0.03 m ionic strength as a function of temperature and pH as determined by in situ measurements. Geochim. Cosmochim. Acta 65 (13), 2097–2111.

Bénézeth, P., Stefánsson, A., Gautier, Q., Schott, J., 2013. Mineral solubility and aqueous speciation under hydrothermal conditions to 300°C–the carbonate system as an example. Rev. Mineral. Geochem. 76 (1), 81–133.

Bennion, B., Bachu, S., et al., 2008. Drainage and imbibition relative permeability relationships for supercritical CO_2/brine and H_2S/brine systems in intergranular sandstone carbonate shale and anhydrite rocks. SPE Reservoir Evaluation & Engineering 11 (03), 487–496.

Benson, S. M., Cole, D. R., 2008. CO_2 sequestration in deep sedimentary formations. Elements 4 (5), 325–331.

Berman, R. G., 1988. Internally-consistent thermodynamic data for minerals in the system Na_2O-K_2O-CaO-MgO-FeO-Fe_2O_3-Al_2O_3-SiO_2-TiO_2-H_2O-CO_2. Journal of Petrol. 29 (2), 445–522.

Bethke, C. M., Yeakel, S., 2012. The Geochemist's Workbench Release 9.0 Reaction modeling guide. Aqueous Solutions LLC.

Bevan, J., Savage, D., 1989. The effect of organic acids on the dissolution of K-feldspar under conditions relevant to burial diagenesis. Mineral. Mag 53, 415–425.

Blum, A. E., Stillings, L. L., 1995. Feldspar dissolution kinetics. Rev. Mineral. Geochem. 31 (1), 291–351.

Blunt, M., Fayers, F. J., Orr Jr, F. M., 1993. Carbon dioxide in enhanced oil recovery. Energy Convers. Manage. 34 (9), 1197–1204.

Brantley, S. L., White, A. F., 2009. Approaches to modeling weathered regolith. Rev. Mineral. Geochem. 70 (1), 435–484.

Bricker, O. P., Garrels, R. M., 1967. Mineralogic factors in natural water equilibria. Principles and applications of water chemistry. Wiley, New York, 449–469.

Brooks, R. H., Corey, A. T., 1966. Properties of porous media affecting fluid flow. J. Irrig. Drain. Div. Am. Soc. Civ. Eng. 92(IR2), 61–88.

Brown, D. W., 2000. A hot dry rock geothermal energy concept utilizing supercritical CO_2 instead of water. In: Proceedings of the Twenty-Fifth Workshop on Geothermal Reservoir Engineering, Stanford University, Palo Alto, CA. pp. 233–238.

Brunauer, S., Emmett, P. H., Teller, E., 1938. Adsorption of gases in multimolecular layers. J. Am. Chem. Soc. 60 (2), 309–319.

Burch, T. E., Nagy, K. L., Lasaga, A. C., 1993. Free energy dependence of albite dissolution kinetics at 80°C and pH 8.8. Chem. Geol. 105 (1-3), 137–162.

Busch, A., Alles, S., Gensterblum, Y., Prinz, D., Dewhurst, D., Raven, M., Stanjek, H., Krooss, B., 2008. Carbon dioxide storage potential of shales. Int. J. Greenh. Gas Con. 2 (3), 297–308.

Buscheck, T. A., Sun, Y., Chen, M., Hao, Y., Wolery, T. J., Bourcier, W. L., Court, B., Celia, M. A., Julio Friedmann, S., Aines, R. D., 2012. Active CO_2 reservoir management for carbon storage: Analysis of operational strategies to relieve pressure buildup and improve injectivity. Int. J. Greenh. Gas Con. 6, 230–245.

Buscheck, T. A., Sun, Y., Hao, Y., Wolery, T. J., Bourcier, W., Tompson, A. F., Jones, E. D., Julio Friedmann, S., Aines, R. D., 2011. Combining brine extraction, desalination, and residual-brine reinjection with CO_2 storage in saline formations: Implications for pressure management, capacity, and risk mitigation. Energy Procedia 4, 4283–4290.

Busey, R., Mesmer, R., 1977. Ionization equilibriums of silicic acid and polysilicate formation in aqueous sodium chloride solutions to 300 °C. Inorg. Chem. 16 (10), 2444–2450.

Carroll, S., Hao, Y., Smith, M., Sholokhova, Y., 2013a. Development of scaling parameters to describe CO_2-rock interactions within Weyburn-Midale carbonate flow units. Int. J. Greenh. Gas Con. 16, S185–S193.

Carroll, S., McNab, W., Dai, Z., Torres, S., 2013b. Reactivity of Mt. Simon sandstone and the Eau Claire shale under CO_2 storage conditions. Environ. Sci. Technol. 47 (1), 252–261.

Carroll, S. A., McNab, W. W., Torres, S. C., 2011. Experimental study of cement-sandstone/shale-brine-CO_2 interactions. Geochem. Trans. 12 (1), 9.

Chatterjee, N. D., 1972. The upper stability limit of the assemblage paragonite + quartz and its natural occurrences. Contrib. Mineral. Petr. 34 (4), 288–303.

Chatterjee, N. D., Johannes, W., Leistner, H., 1984. The system CaO-Al_2O_3-SiO_2-H_2O: New phase equilibria data, some calculated phase relations, and their petrological applications. Contrib. Mineral. Petr. 88 (1), 1–13.

Chiquet, P., Daridon, J.-L., Broseta, D., Thibeau, S., 2007. CO_2/water interfacial tensions under pressure and temperature conditions of CO_2geological storage. Energy Convers. Manage. 48 (3), 736–744.

De Ligny, D., Navrotsky, A., 1999. Energetics of kaolin polymorphs. Am. Mineral. 84, 506–516.

DePaolo, D. J., Cole, D. R., 2013. Geochemistry of geologic carbon sequestration: an overview. Rev. Mineral. Geochem. 77 (1), 1–14.

DePaolo, D. J., Cole, D. R., Navrotsky, A., Bourg, I. C., eds., 2013. Geochemistry of geologic CO_2 sequestration. Rev. Mineral. Geochem. 77.

Devidal, J. L., Dandurand, J. L., Gout, R., 1996. Gibbs free energy of formation of kaolinite from solubility measurement in basic solution between 60 and 170°C. Geochim. Cosmochim. Acta 60 (4), 553–564.

Devidal, J.-L., Schott, J., Dandurand, J.-L., 1997. An experimental study of kaolinite dissolution and precipitation kinetics as a function of chemical affinity and solution composition at 150°C, 40 bars, and pH 2, 6.8, and 7.8. Geochim. Cosmochim. Acta 61 (24), 5165–5186.

Ding, K., Seyfried Jr., W., 1990. Activity coefficients of H_2 and H_2S in NaCl solutions at 300°-425°C, 300-500 bars with appliciation to ridge crest hydrothermal systems. Eos 71, 1680.

Ding, K., Seyfried Jr, W. E., Zhang, Z., Tivey, M. K., Von Damm, K. L., Bradley, A. M., 2005. The in situ pH of hydrothermal fluids at mid-ocean ridges. Earth and Planet. Sci. Lett. 237 (1), 167–174.

Dove, P., 1995. Kinetic and thermodynamic controls on silica reactivity in weathering environments. Rev. Mineral. Geochem. 31 (1), 235–290.

Dove, P. M., Crerar, D. A., 1990. Kinetics of quartz dissolution in electrolyte solutions using a hydrothermal mixed flow reactor. Geochim. Cosmochim. Acta 54 (4), 955–969.

Driesner, T., Seward, T., Tironi, I., 1998. Molecular dynamics simulation study of ionic hydration and ion association in dilute and 1 molal aqueous sodium chloride solutions from ambient to supercritical conditions. Geochim. Cosmochim. Acta 62 (18), 3095–3107.

Drummond, S. E., 1981. Boiling and mixing of hydrothermal fluids: Chemical effects on mineral precipitation. PhD Thesis, Pennsylvania State University.

Duan, Z., Møller, N., Weare, J. H., 1992. An equation of state for the CH_4-CO_2-H_2O system: I. pure systems from 0 to 1000° C and 0 to 8000 bar. Geochim. Cosmochim. Acta 56 (7), 2605–2617.

Duan, Z., Sun, R., 2003. An improved model calculating CO_2 solubility in pure water and aqueous NaCl solutions from 273 to 533 K and from 0 to 2000 bar. Chem. Geol. 193 (3), 257–271.

Duan, Z., Sun, R., Zhu, C., Chou, I.-M., 2006. An improved model for the calculation of CO_2 solubility in aqueous solutions containing Na^+, K^+, Ca^{2+}, Mg^{2+}, Cl^-, and $SO_4{}^{2-}$. Mar. Chem. 98 (2), 131–139.

Eberl, D., 2003. User guide to RockJock: A program for determining quantitative mineralogy from X-ray diffraction data, open file report 03-78. United States Geological Survey: Washington, DC.

Eccles, J. K., Pratson, L., Newell, R. G., Jackson, R. B., 2009. Physical and economic potential of geological CO_2 storage in saline aquifers. Environment. Sci. Tech. 43 (6), 1962–1969.

Elliot, T. R., Buscheck, T. A., Celia, M., 2013. Active CO_2 reservoir management for sustainable geothermal energy extraction and reduced leakage. Greenhouse Gas. Sci. Technol. 3 (1), 50–65.

Falta, R. W., Zuo, L., Benson, S. M., 2013. Migration of exsolved CO_2 following depressurization of saturated brines. Greenhouse Gas. Sci. Technol. 3 (6), 503–515.

Farajzadeh, R., Ranganathan, P., Zitha, P. L. J., Bruining, J., 2011. The effect of heterogeneity on the character of density-driven natural convection of CO_2 overlying a brine layer. Adv. Water Resour. 34 (3), 327–339.

Fenter, P., Zapol, P., He, H., Sturchio, N. C., 2014. On the variation of dissolution rates at the orthoclase (001) surface with pH and temperature. Geochim. Cosmochim. Acta 141, 598–611.

Ferrante, M. J., Stuve, J., Richardson, D. W., 1976. Thermodynamic data for synthetic dawsonite. Rep. Invest. (8129).

Fialips, C.-I., Majzlan, J., Beaufort, D., Navrotsky, A., 2003. New thermochemical evidence on the stability of dickite vs. kaolinite. Am. Mineral. 88 (5-6), 837–845.

Fialips, C.-I., Navrotsky, A., Petit, S., 2001. Crystal properties and energetics of synthetic kaolinite. Am. Mineral. 86 (3), 304–311.

Fournier, R., Truesdell, A., 1973. An empirical Na-K-Ca geothermometer for natural waters. Geochim. Cosmochim. Acta 37 (5), 1255–1275.

Franck, E., 1956. Hochverdichteter wasserdampf I. Elektrolytische Leitfähigkeit in KCl-H_2O-Lösungen bis 750°c. Zeitschrift für Physikalische Chemie 8 (1_2), 92–106.

Frank, M. R., Candela, P. A., Piccoli, P. M., 1998. K-feldspar-muscovite-andalusite-quartz-brine phase equilibria: An experimental study at 25 to 60 MPa and 400 to 550 C. Geochim. Cosmochim. Acta 62 (23), 3717–3727.

Frank, M. R., Vaccaro, D. M., 2012. An experimental study of high temperature potassic alteration. Geochim. Cosmochim. Acta 83, 195–204.

Frantz, J. D., Marshall, W. L., 1984. Electrical conductances and ionization constants of salts, acids, and bases in supercritical aqueous fluids: I. Hydrochloric acid from 100 degrees to 700 degrees C and at pressures to 4000 bars. Am. J. Sci. 284 (6), 651–667.

Frantz, J. D., Popp, R. K., 1979. Mineral-solution equilibria–I. An experimental study of complexing and thermodynamic properties of aqueous $MgCl_2$ in the system MgO-SiO_2-H_2O-HCl. Geochim. Cosmochim. Acta 43 (8), 1223–1239.

Freifeld, B., Zakim, S., Pan, L., Cutright, B., Sheu, M., Doughty, C., Held, T., 2013. Geothermal energy production coupled with CCS: A field demonstration at the SECARB Cranfield Site, Cranfield, Mississippi, USA. Energy Procedia 37, 6595–6603.

Freyer, D., Voigt, W., 2003. Crystallization and phase stability of $CaSO_4$ and $CaSO_4$–based salts. Monatshefte für Chemie/Chemical Monthly 134 (5), 693–719.

Fridleifsson, G. O., Elders, W. A., 2005. The Iceland Deep Drilling Project: A search for deep unconventional geothermal resources. Geothermics 34 (3), 269–285.

Friedmann, S. J., 2007. Geological carbon dioxide sequestration. Elements 3 (3), 179–184.

Frink, C., Peech, M., 1962. The solubility of gibbsite in aqueous solutions and soil extracts. Soil Sci. Soc. Am. J. 26 (4), 346–347.

Fu, Q., Lu, P., Konishi, H., Dilmore, R., Xu, H., Seyfried, W., Zhu, C., 2009. Coupled alkali-feldspar dissolution and secondary mineral precipitation in batch systems: 1. New experiments at 200°C and 300 bars. Chem. Geol. 258 (3), 125–135.

Garapati, N., Randolph, J. B., Saar, M. O., 2015. Brine displacement by CO_2, energy extraction rates, and lifespan of a CO_2-limited CO_2-Plume Geothermal (CPG) system with a horizontal production well. Geothermics 55, 182–194.

Garrels, R., Howard, P., 1959. Reactions of feldspar and mica with water at low temperature and pressure. In: 6th Nat. Conf. on Clays and Clay Minerals. Vol. 68. Pergamom, New York, pp. 68–88.

Garrels, R. M., Christ, C. L., 1965. Solutions, minerals, and equilibria. Harper & Row New York.

Garrels, R. M., Mackenzie, F. T., 1967. Origin of the chemical compositions of some springs and lakes. In: Stumm W (chairman) Equilibrium Concepts in Natural Water Systems, Advances in Chem Ser. Vol. 67. ACS Publications, pp. 222–242.

Gaus, I., Audigane, P., André, L., Lions, J., Jacquemet, N., Durst, P., Czernichowski-Lauriol, I., Azaroual, M., 2008. Geochemical and solute transport modelling for CO_2 storage, what to expect from it? Int. J. Greenh. Gas Con. 2 (4), 605–625.

Gaus, I., Azaroual, M., Czernichowski-Lauriol, I., 2005. Reactive transport modelling of the impact of CO_2 injection on the clayey cap rock at Sleipner (North Sea). Chem. Geol. 217 (3), 319–337.

Gautier, J. M., Oelkers, E. H., Schott, J., 1994. Experimental study of K-feldspar dissolution rates as a function of chemical affinity at 150°C and pH 9. Geochim. Cosmochim. Acta 58 (21), 4549–4560.

Giggenbach, W. F., 1988. Geothermal solute equilibria. derivation of Na-K-Mg-Ca geoindicators. Geochim. Cosmochim. Acta 52 (12), 2749–2765.

Gong, Q., Deng, J., Han, M., Yang, L., Wang, W., 2012. Dissolution of sandstone powders in deionised water over the range 50–350°C. Appl. Geochem. 27 (12), 2463–2475.

Gottschalk, M., 1997. Internally consistent thermodynamic data for rock-forming minerals in the system SiO_2-TiO_2-Al_2O_3-CaO-MgO-FeO-K_2O-Na_2O-H_2O-CO_2. Eur. J. Mineral. 9 (1), 175–223.

Gouze, P., Luquot, L., 2011. X-ray microtomography characterization of porosity, permeability and reactive surface changes during dissolution. J. Contam. Hydrol. 120, 45–55.

Gozalpour, F., Ren, S., Tohidi, B., 2005. CO_2 EOR and storage in oil reservoir. Oil Gas Sci. Tech. 60 (3), 537–546.

Gruber, C., Harpaz, L., Zhu, C., Bullen, T. D., Ganor, J., 2013. A new approach for measuring dissolution rates of silicate minerals by using silicon isotopes. Geochim. Cosmochim. Acta 104, 261–280.

Gunnarsson, I., Arnórsson, S., 2000. Amorphous silica solubility and the thermodynamic properties of H_4SiO_4 in the range of 0° to 350°C at Psat. Geochim. Cosmochim. Acta 64 (13), 2295–2307.

Gunter, W., Eugster, H., 1978. Wollastonite solubility and free energy of supercritical aqueous $CaCl_2$. Contrib. Mineral. Petr. 66 (3), 271–281.

Gunter, W., Eugster, H., 1980. Mica-feldspar equilibria in supercritical alkali chloride solutions. Contrib. Mineral. Petr. 75 (3), 235–250.

Gunter, W., Wiwehar, B., Perkins, E., 1997. Aquifer disposal of CO_2-rich greenhouse gases: extension of the time scale of experiment for CO_2-sequestering reactions by geochemical modelling. Mineral. and Petrol. 59 (1-2), 121–140.

Haar, L., Gallagher, J. S., Kell, G. S., 1984. NBS-NRC Steam Tables: Thermodynamics Ans Transport Properties and Computer Programs for Vapor and Liquid States of Water in SI Units. Taylor & Francis.

Haas, H., Holdaway, M., 1973. Equilibria in the system Al_2O_3-SiO_2-H_2O involving the stability limits of pyrophyllite, and thermodynamic data of pyrophyllite. Am. J. Sci. 273 (6), 449–464.

Hajash, A. J., Carpenter, T. D., Dewers, T. A., 1998. Dissolution and time-dependent compaction of albite sand: Experiments at 100°C and 160°C in pH-buffered organic acids and distilled water. Tectonophysics 295 (1), 93–115.

Halbach, H., Chatterjee, N. D., 1984. An internally consistent set of thermodynamic data for twentyone CaO-Al_2O_3-SiO_2-H_2O phases by linear parametric programming. Contrib. Mineral. Petr. 88 (1), 14–23.

Hammond, G., Lichtner, P., Lu, C., 2007. Subsurface multiphase flow and multicomponent reactive transport modeling using high-performance computing. In: Journal of Physics: Conference Series. Vol. 78. IOP Publishing, p. 012025.

Hammond, G., Lichtner, P., Lu, C., Mills, R., 2012. PFLOTRAN: Reactive flow and transport code for use on laptops to leadership-class supercomputers. Ebook: Groundwater Reactive Transport Models, ed. F. Zhang, GT Yeh, and JC Parker, 141–159.

Han, W. S., Stillman, G. A., Lu, M., Lu, C., McPherson, B. J., Park, E., 2010. Evaluation of potential nonisothermal processes and heat transport during CO_2 sequestration. J. Geophys. Res. 115 (B7), B07209.

Hangx, S. J., Spiers, C. J., 2009. Reaction of plagioclase feldspars with CO_2 under hydrothermal conditions. Chem. Geol. 265 (1), 88–98.

Hao, Y., Smith, M., Sholokhova, Y., Carroll, S., 2013. CO_2-induced dissolution of low permeability carbonates. Part II: Numerical modeling of experiments. Adv. Water Resour. 62, 388–408.

Harlow, F. H., Pracht, W. E., 1972. A theoretical study of geothermal energy extraction. J. Geophys. Res. 77 (35), 7038–7048.

Harvie, C. E., Møller, N., Weare, J. H., 1984. The prediction of mineral solubilities in natural waters: The Na-K-Mg-Ca-H-Cl-SO_4-OH-HCO_3-CO_3-CO_2-H_2O system to high ionic strengths at 25°C. Geochim. Cosmochim. Acta 48, 723–751.

Haselton, H., Cygan, G., d'Angelo, W., 1988. Chemistry of aqueous solutions coexisting with fluoride buffers in the system K_2O-Al_2O_3-SiO_2-H_2O-F_2O (1 kbar, 400 degrees-700 degrees C). Econ. Geol. 83 (1), 163–173.

Haselton, Jr., H., Cygan, G., Jenkins, D., 1995. Experimental study of muscovite stability in pure H_2O and 1 molal KCl-HCl solutions. Geochim. Cosmochim. Acta 59 (3), 429–442.

Helgeson, H. C., 1964. Complexing and hydrothermal ore deposition. MacMillan Co., New York.

Helgeson, H. C., 1969. Thermodynamics of hydrothermal systems at elevated temperatures and pressures. Am. J. Sci. 267 (7), 729–804.

Helgeson, H. C., 1992. Effects of complex formation in flowing fluids on the hydrothermal solubilities of minerals as a function of fluid pressure and temperature in the critical and supercritical regions of the system H_2O. Geochim. Cosmochim. Acta 56 (8), 3191–3207.

Helgeson, H. C., Delany, J. M., Nesbitt, H. W., Bird, D. K., 1978. Summary and critique of the thermodynamic properties of rock-forming minerals. Am. J. Sci. 278A (1), 1–229.

Helgeson, H. C., Kirkham, D. H., 1974. Theoretical prediction of the thermodynamic behavior of aqueous electrolytes at high pressures and temperatures: II. Debye-Hückel parameters for activity coefficients and relative partial molal properties. Am. J. Sci. 274 (10), 1199–1261.

Helgeson, H. C., Kirkham, D. H., Flowers, G. C., 1981. Theoretical prediction of the thermodynamic behavior of aqueous electrolytes by high pressures and temperatures: IV. Calculation of activity coefficients, osmotic coefficients, and apparent molal and standard and relative partial molal properties to 600°C and 5 KB. Am. J. Sci. 281 (10), 1249–1516.

Helgeson, H. C., Murphy, W. M., Aagaard, P., 1984. Thermodynamic and kinetic constraints on reaction rates among minerals and aqueous solutions. II. Rate constants, effective surface area, and the hydrolysis of feldspar. Geochim. Cosmochim. Acta 48 (12), 2405–2432.

Hellevang, H., Declercq, J., Kvamme, B., Aagaard, P., 2010. The dissolution rates of dawsonite at pH 0.9 to 5 and temperatures of 22, 60 and 77 C. Appl. Geochem. 25 (10), 1575–1586.

Hellevang, H., Pham, V. T., Aagaard, P., 2013. Kinetic modelling of CO_2–water–rock interactions. Int. J. Greenh. Gas Con. 15, 3–15.

Hellmann, R., 1994. The albite-water system: Part I. The kinetics of dissolution as a function of pH at 100, 200 and 300°C. Geochim. Cosmochim. Acta 58 (2), 595–611.

Hellmann, R., Tisserand, D., 2006. Dissolution kinetics as a function of the Gibbs free energy of reaction: An experimental study based on albite feldspar. Geochim. Cosmochim. Acta 70 (2), 364–383.

Hem, J., Lind, C., 1974. Kaolinite synthesis at 25°C. Science 184 (4142), 1171–1173.

Hemingway, B. S., Haas, J. L., Robinson, J. R., 1982. Thermodynamic properties of selected minerals in the system Al_2O_3-CaO-SiO_2-H_2O at 298.15 K and 1 bar (10^5 Pascals) pressure and at high temperatures. U.S. Geol. Surv. Bull. 1452, 1–70.

Hemingway, B. S., Haselton, H. T., 1994. A reevaluation of the calorimetric data for the enthalpy of formation of some K-and Na-bearing silicate minerals. U.S. Geol. Surv. Open-File Report 94-576, 12p.

Hemingway, B. S., Robie, R., 1977. Enthalpies of formation of low albite ($NaAlSi_3O_8$), gibbsite ($Al(OH)_3$) and $NaAlO_2$; revised values for $\Delta H^\circ_{f,298}$ and $\Delta G^\circ_{f,298}$ of some aluminosilicate minerals. J. Res. U. S. Geol. Surv. 5 (4), 413–429.

Hemingway, B. S., Robie, R. A., Apps, J. A., 1991. Revised values for the thermodynamic properties of boehmite, AlO(OH), and related species and phases in the system Al-HO. Amer. Mineral. 76 (3-4), 445–457.

Hemingway, B. S., Robie, R. A., Kittrick, J. A., 1978. Revised values for the Gibbs free energy of formation of $[Al(OH)^-_{4aq}]$, diaspore, boehmite and bayerite at 298.15

K and 1 bar, the thermodynamic properties of kaolinite to 800 K and 1 bar, and the heats of solution of several gibbsite samples. Geochim. Cosmochim. Acta 42 (10), 1533–1543.

Hemingway, B. S., Sposito, G., 1996. Inorganic aluminum-bearing solid phases. The environmental chemistry of aluminum, 81–116.

Hemley, J., Jones, W., 1964. Chemical aspects of hydrothermal alteration with emphasis on hydrogen metasomatism. Econ. Geol. 59 (4), 538–569.

Hemley, J. J., 1959. Some mineralogical equilibria in the system K_2O-Al_2O_3-SiO_2-H_2O. Am. J. Sci. 257 (4), 241–270.

Hemley, J. J., Montoya, J. W., Marinenko, J. W., Luce, R. W., 1980. Equilibria in the system Al_2O_3-SiO_2-H_2O and some general implications for alteration/mineralization processes. Econ. Geol. 75 (2), 210–228.

Hess, P. C., 1966. Phase equilibria of some minerals in the K_2O-N_2aO-Al_2O_3-SiO_2-H_2O system at 25 degrees C and 1 atmosphere. Am. J. Sci. 264 (4), 289–309.

Hill, V. G., Ellington, A. C., 1961. Chemical characteristics of the ground water resources of Jamaica, WI. Econ. Geol. 56 (3), 533–541.

Hirai, S., Okazaki, K., Tabe, Y., Hijikata, K., Mori, Y., 1997. Dissolution rate of liquid CO_2 in pressurized water flows and the effect of clathrate films. Energy 22 (2), 285–293.

Ho, P. C., Palmer, D. A., 1996. Ion association of dilute aqueous sodium hydroxide solutions to 600°C and 300 MPa by conductance measurements. J. Solution Chem. 25 (8), 711–729.

Ho, P. C., Palmer, D. A., 1997. Ion association of dilute aqueous potassium chloride and potassium hydroxide solutions to 600°C and 300 MPa determined by electrical conductance measurements. Geochim. Cosmochim. Acta 61 (15), 3027–3040.

Ho, P. C., Palmer, D. A., Gruszkiewicz, M. S., 2001. Conductivity measurements of dilute aqueous HCl solutions to high temperatures and pressures using a flow-through cell. J. Phys. Chem. B 105 (6), 1260–1266.

Ho, P. C., Palmer, D. A., Mesmer, R. E., 1994. Electrical conductivity measurements of aqueous sodium chloride solutions to 600°C and 300 MPa. J. Solution Chem. 23 (9), 997–1018.

Hoefner, M., Fogler, H. S., 1988. Pore evolution and channel formation during flow and reaction in porous media. AIChE Journal 34 (1), 45–54.

Holland, T., Powell, R., 1985. An internally consistent thermodynamic dataset with uncertainties and correlations: 2. Data and results. J. Metamorph. Geol. 3 (4), 343–370.

Holland, T., Powell, R., 1990. An enlarged and updated internally consistent thermodynamic dataset with uncertainties and correlations: the system K_2O–Na_2O–CaO–MgO–MnO–FeO–Fe_2O_3–Al_2O_3–TiO_2–SiO_2–C–H_2–O_2. J. Metamorph. Geol. 8 (1), 89–124.

Holland, T. J. B., Powell, R., 1998. An internally consistent thermodynamic data set for phases of petrological interest. J. Metamorph. Geol. 16, 309–344.

Holland, T. J. B., Powell, R., 2011. An improved and extended internally consistent thermodynamic dataset for phases of petrological interest, involving a new equation of state for solids. J. Metamorph. Geol. 29, 333–383.

Huang, W., Keller, W., 1973. Gibbs free energies of formation calculated from dissolution data using specific mineral analysis: III Clay minerals. Am. Mineral. 58, 1023–1028.

Huang, W.-L., 1993. Stability and kinetics of kaolinite to boehmite conversion under hydrothermal conditions. Chem. Geol. 105 (1), 197–214.

Huang, W. L., Longo, J. M., Pevear, D. R., 1993. An experimentally derived kinetic model for smectite-to-illite conversion and its use as a geothermometer. Clay. Clay Miner. 41, 162–162.

Hückel, E., 1925. The theory of concentrated, aqueous solutions of strong electrolytes. Physikalische Zeitschrift 26, 93.

IPCC, 2005. IPCC Special Report on Carbon Dioxide Capture and Storage. Prepared by Working Group III of the Intergovernmental Panel on Climate Change [Metz,

B., O. Davidson, H.C. de Coninck, M. Loos and L.A. Meyer]. Cambridge University Press, Cambridge, UK and New York, USA.

IPCC, 2014. Summary for policymakers. In: Climate change 2014: Impacts, adaptation, and vulnerability. part A: Global and sectoral aspects. Contribution of working group II to the fifth assessment report of the Intergovernmental Panel on Climate Change, [Field, C.B., V.R. Barros, D.J. Dokken, K.J. Mach, M.D. Mastrandrea, T.E. Bilir, M. Chatterjee, K.L. Ebi, Y.O. Estrada, R.C. Genova, B. Girma, E.S. Kissel, A.N. Levy, S. Maccracken, P.R. Mastrandrea, and L.L. White, eds.]. Cambridge University Press, Cambridge, United Kingdom and New York, NY, USA, 1–32.

Ivanov, I., Gusynin, V., 1970. Stability of paragonite in the system SiO_2-$NaAlSi_3O_8$-Al_2O_3-H_2O. Geochem. Int. 7, 578–587.

Jobard, E., Sterpenich, J., Pironon, J., Corvisier, J., Jouanny, M., Randi, A., 2013. Experimental simulation of the impact of a thermal gradient during geological sequestration of CO_2: The COTAGES experiment. Int. J. Greenh. Gas Con. 12, 56–71.

Johnson, J., Nitao, J., Knauss, K., 2004. Reactive transport modelling of CO_2 storage in saline aquifers to elucidate fundamental processes, trapping mechanisms and sequestration partitioning. Geol. Soc. London, Spec. Pubs. 233 (1), 107–128.

Johnson, J. W., Norton, D., 1991. Critical phenomena in hydrothermal systems; state, thermodynamic, electrostatic, and transport properties of H_2O in the critical region. Am. J. Sci. 291 (6), 541–648.

Johnson, J. W., Oelkers, E. H., Helgeson, H. C., 1992. SUPCRT92: A software package for calculating the standard molal thermodynamic properties of minerals, gases, aqueous species, and reactions from 1 to 5000 bar and 0 to 1000 °C. Comput. Geosci. 18 (7), 899–947.

Jørgensen, B. B., Boetius, A., 2007. Feast and famine–microbial life in the deep-sea bed. Nat. Rev. Microbiol. 5 (10), 770–781.

Junglas, P., 2009. Water95: A Matlab implementation of the IAPWS-95 standard for use in thermodynamics lectures. Int. J. Eng. Educ. 25 (1), 3–10.

Kampman, N., Bickle, M., Becker, J., Assayag, N., Chapman, H., 2009. Feldspar dissolution kinetics and Gibbs free energy dependence in a CO_2-enriched groundwater system, Green River, Utah. Earth and Planet. Sci. Lett. 284 (3), 473–488.

Karamalidis, A. K., Torres, S. G., Hakala, J. A., Shao, H., Cantrell, K. J., Carroll, S., 2012. Trace metal source terms in carbon sequestration environments. Environ. Sci. Tech. 47 (1), 322–329.

Kaszuba, J., Janecky, D., Snow, M., 2003. Carbon dioxide reaction processes in a model brine aquifer at 200°C and 200 bars: Implications for geologic sequestration of carbon. Appl. Geochem. 18 (7), 1065–1080.

Kaszuba, J. P., Viswanathan, H. S., Carey, J. W., 2011. Relative stability and significance of dawsonite and aluminum minerals in geologic carbon sequestration. Geophys. Res. Lett. 38 (8).

Kennedy, G. C., 1959. Phase relations in the system Al_2O_3-H_2O at high temperatures and pressures. Am. J. Sci. 257 (8), 563–573.

Kerrick, D., 1972. Experimental determination of muscovite + quartz stability with $P_{H_2O} < P_{total}$. Am. J. Sci. 272 (10), 946–958.

Kerrick, D. M., 1968. Experiments on the upper stability limit of pyrophyllite at 1.8 kb and 3.9 kb water pressure. Am. J. Sci. 266 (3), 204–214.

Kharaka, Y., Cole, D., Hovorka, S., Gunter, W., Knauss, K., Freifeld, B., 2006. Gas-water-rock interactions in frio formation following CO_2 injection: Implications for the storage of greenhouse gases in sedimentary basins. Geology 34 (7), 577–580.

Kharaka, Y. K., 1971. Simultaneous flow of water and solutes through geological membranes: Experimental and field investigations. Ph.D. thesis, University of California, Berkeley.

Kharaka, Y. K., Berry, F. A., 1974. The influence of geological membranes on the geochemistry of subsurface waters from miocene sediments at Kettleman North Dome in California. Water Resour. Res. 10 (2), 313–327.

Kirsch, K., Navarre-Sitchler, A., Wunsch, A., McCray, J. E., 2014. Metal release from sandstones under experimentally and numerically simulated CO_2 leakage conditions. Environ. Sci. Technol. 48 (3), 1436–1442.

Kiseleva, I., Orogodova, L., Krupskaya, V., Melchakova, L., Vigasina, M., Luse, I., 2011. Thermodynamics of the kaolinite-group minerals. Geochem. Int. 49 (8), 793–801.

Kittrick, J. A., 1966. Free energy of formation of kaolinite from solubility measurements. Amer. Mineral. 51, 1457–1466.

Kittrick, J. A., 1970. Precipitation of kaolinite at 25°C and 1 ATM. Clay. Clay Miner. 18, 261–267.

Kittrick, J. A., 1980. Gibbsite and kaolinite solubilities by immiscible displacement of equilibrium solutions. Soil Sci. Soc. Am. J. 44 (1), 139–142.

Klemic, H., Mrose, M. E., 1972. Geologic relations and X-ray crystallography of wavellite from Jackson County, Wisconsin, and their geologic implications. Geological Survey Professional Paper 800, 53.

Kline, W., Fogler, H. S., 1981. Dissolution kinetics: Catalysis by salts. J. Colloid Interface Sci. 82 (1), 103–115.

Knauss, K. G., Wolery, T. J., 1986. Dependence of albite dissolution kinetics on pH and time at 25°C and 70°C. Geochim. Cosmochim. Acta 50 (11), 2481–2497.

Kong, X.-Z., Saar, M. O., 2013. Numerical study of the effects of permeability heterogeneity on density-driven convective mixing during CO_2 dissolution storage. Int. J. Greenh. Gas Con. 19, 160–173.

Kong, X. Z., Tutolo, B. M., Saar, M. O., 2013. DBCreate: A SUPCRT92-based program for producing EQ3/6, TOUGHREACT, and GWB thermodynamic databases at user-defined T and P. Comput. Geosci. 51, 415–417.

Königsberger, E., Königsberger, L., Ilievski, D., 2011. The boehmite solubility gap. Hydrometallurgy 110 (1), 33–39.

Krevor, S., Pini, R., Zuo, L., Benson, S. M., 2012. Relative permeability and trapping of CO_2 and water in sandstone rocks at reservoir conditions. Water Resour. Res. 48 (2).

Lackner, K. S., 2003. A guide to CO_2 sequestration. Science 300 (5626), 1677–1678.

Lagache, M., 1965. Contribution à létude de laltération des feldspaths dans leau entre 100 et 200°C sous diverses pressions de CO_2 et application à la synthèse des mineraux argileux. Bull. Sot. Fr. Miner. Crist. 88, 223 253.

Lammers, L. N., Brown, G. E., Bird, D. K., Thomas, R. B., Johnson, N. C., Rosenbauer, R. J., Maher, K., 2015. Sedimentary reservoir oxidation during geologic co 2 sequestration. Geochim. Cosmochim. Acta 155, 30–46.

Land, L. S., 1998. Failure to precipitate dolomite at 25°C from dilute solution despite 1000-fold oversaturation after 32 years. Aquat. Geochem. 4 (3), 361–368.

Landrot, G., Ajo-Franklin, J., Yang, L., Cabrini, S., Steefel, C., 2012. Measurement of accessible reactive surface area in a sandstone, with application to CO_2 mineralization. Chem. Geol. 318–319, 113–125.

Lasaga, A. C., 1981. Rate laws of chemical reactions. Rev. Mineral. 8.

Lasaga, A. C., Soler, J. M., Ganor, J., Burch, T. E., Nagy, K. L., 1994. Chemical weathering rate laws and global geochemical cycles. Geochim. Cosmochim. Acta 58 (10), 2361–2386.

Lebron, I., Suarez, D., 1998. Kinetics and mechanisms of precipitation of calcite as affected by PCO_2 and organic ligands at 25°C. Geochim. Cosmochim. Acta 62 (3), 405–416.

Leverett, M. C., 1940. Capillary behavior in porous solids. Trans. AIME, Petr. Eng. Div. 142, 152–169.

Li, L., Salehikhoo, F., Brantley, S. L., Heidari, P., 2014. Spatial zonation limits magnesite dissolution in porous media. Geochim. Cosmochim. Acta 126, 555–573.

Li, Z., Dong, M., Li, S., Huang, S., 2006. CO_2 sequestration in depleted oil and gas reservoirs–caprock characterization and storage capacity. Energy Convers. Manage. 47 (11), 1372–1382.

Lichtner, P. C., Hammond, G. E., Lu, C., Karra, S., Bisht, G., Andre, B., Mills, R. T., Kumar, J., 2013. PFLOTRAN User Manual.

Liu, F., Lu, P., Griffith, C., Hedges, S., Soong, Y., Hellevang, H., Zhu, C., 2012. CO_2-brine-caprock interaction: Reactivity experiments on Eau Claire shale and a review of relevant literature. Int. J. Greenh. Gas Con. 7, 153–167.

Lo Ré, C., Kaszuba, J. P., Moore, J. N., McPherson, B. J., 2014. Fluid–rock interactions in CO_2-saturated, granite-hosted geothermal systems: Implications for natural and engineered systems from geochemical experiments and models. Geochim. Cosmochim. Acta 141, 160–178.

Lu, C., Lichtner, P. C., 2005. PFLOTRAN: Massively parallel 3-D simulator for CO_2 sequestration in geologic media. In: DOE-NETL Fourth Annual Conference on Carbon Capture and Sequestration.

Lu, J., Partin, J. W., Hovorka, S. D., Wong, C., 2010. Potential risks to freshwater resources as a result of leakage from CO_2 geological storage: a batch-reaction experiment. Environ. Earth Sci. 60 (2), 335–348.

Lu, M., Connell, L. D., 2008. Non-isothermal flow of carbon dioxide in injection wells during geological storage. Int. J. Greenh. Gas Con. 2 (2), 248–258.

Lu, P., Fu, Q., Seyfried Jr, W. E., Hedges, S. W., Soong, Y., Jones, K., Zhu, C., 2013. Coupled alkali feldspar dissolution and secondary mineral precipitation in batch systems–2: New experiments with supercritical CO_2 and implications for carbon sequestration. Appl. Geochem. 30, 75–90.

Lu, P., Fu, Q., Seyfried Jr, W. E., Hereford, A., Zhu, C., 2011. Navajo sandstone–brine–CO_2 interaction: implications for geological carbon sequestration. Environment. Earth Sci. 62 (1), 101–118.

Lu, P., Konishi, H., Oelkers, E., Zhu, C., 2015. Coupled alkali feldspar dissolution and secondary mineral precipitation in batch systems: 5. Results of K-feldspar hydrolysis experiments. Chinese Journal of Geochemistry 34 (1), 1–12.

Luhmann, A. J., Kong, X.-Z., Tutolo, B. M., Ding, K., Saar, M. O., Seyfried, Jr., W. E., 2013. Permeability reduction produced by grain reorganization and accumulation of exsolved CO_2 during geologic carbon sequestration: A new CO_2 trapping mechanism. Environ. Sci. Tech. 47 (1), 242–251.

Luhmann, A. J., Kong, X.-Z., Tutolo, B. M., Garapati, N., Bagley, B. C., Saar, M. O., Seyfried Jr, W. E., 2014. Experimental dissolution of dolomite by CO_2-charged brine at 100°C and 150 bar: Evolution of porosity, permeability, and reactive surface area. Chem. Geol. 380, 145–160.

Luquot, L., Andreani, M., Gouze, P., Camps, P., 2012. CO_2 percolation experiment through chlorite/zeolite-rich sandstone (Pretty Hill Formation–Otway Basin–Australia). Chem. Geol. 294, 75–88.

Luquot, L., Gouze, P., 2009. Experimental determination of porosity and permeability changes induced by injection of CO_2 into carbonate rocks. Chem. Geol. 265 (1), 148–159.

MacMinn, C. W., Szulczewski, M. L., Juanes, R., 2010. CO_2 migration in saline aquifers. Part 1. capillary trapping under slope and groundwater flow. J. Fluid Mech. 662, 329–351.

Maher, K., Steefel, C. I., White, A. F., Stonestrom, D. A., 2009. The role of reaction affinity and secondary minerals in regulating chemical weathering rates at the Santa Cruz Soil Chronosequence, California. Geochim. Cosmochim. Acta 73 (10), 2804–2831.

Majzlan, J., Navrotsky, A., Casey, W. H., 2000. Surface enthalpy of boehmite. Clays and Clay Minerals 48 (6), 699–707.

Malik, Q. M., Islam, M., et al., 2000. CO_2 injection in the Weyburn field of Canada: Optimization of enhanced oil recovery and greenhouse gas storage with horizontal wells. In: SPE/DOE Improved Oil Recovery Symposium. Society of Petroleum Engineers.

Manning, C. E., 2013. Thermodynamic modeling of fluid-rock interaction at mid-crustal to upper-mantle conditions. Rev. Mineral. Geochem. 76 (1), 135–164.

Markham, A. E., Kobe, K. A., 1941. The solubility of carbon dioxide and nitrous oxide in aqueous salt solutions. J. Am. Chem. Soc. 63 (2), 449–454.

Marshall, W. L., Franck, E., 1981. Ion product of water substance, 0–1000°C, 1–10,000 bars new international formulation and its background. J. Phys. Chem. Ref. Data 10 (2), 295–304.

May, H., Klnniburgh, D., Helmke, P. A., Jackson, M., 1986. Aqueous dissolution, solubilities and thermodynamic stabilities of common aluminosilicate clay minerals: Kaolinite and smectites. Geochim. Cosmochim. Acta 50 (8), 1667–1677.

May, H. M., Helmke, P. A., Jackson, M. L., 1979. Gibbsite solubility and thermodynamic properties of hydroxy-aluminum ions in aqueous solution at 25°C. Geochim. Cosmochim. Acta 43 (6), 861–868.

McGrail, B. P., Schaef, H. T., Ho, A. M., Chien, Y.-J., Dooley, J. J., Davidson, C. L., 2006. Potential for carbon dioxide sequestration in flood basalts. J. Geophys. Res 111, B12201.

Merino, E., 1975. Diagenesis in Tertiary sandstones from Kettleman North Dome, California–II. Interstitial solutions: Distribution of aqueous species at 100°C and chemical relation to the diagenetic mineralogy. Geochim. Cosmochim. Acta 39 (12), 1629–1645.

Mills, R. T., Hammond, G. E., Lichtner, P. C., Sripathi, V., Mahinthakumar, G. K., Smith, B. F., 2009. Modeling subsurface reactive flows using leadership-class computing. In: Journal of Physics: Conference Series. Vol. 180. IOP Publishing, p. 012062.

Molins, S., Trebotich, D., Steefel, C. I., Shen, C., 2012. An investigation of the effect of pore scale flow on average geochemical reaction rates using direct numerical simulation. Water Resour. Res. 48 (3).

Møller, N., 1988. The prediction of mineral solubilities in natural waters: A chemical equilibrium model for the Na-Ca-Cl-SO_4-H_2O system, to high temperature and concentration. Geochim. Cosmochim. Acta 52 (4), 821–837.

Montoya, J. W., Hemley, J. J., 1975. Activity relations and stabilities in alkali feldspar and mica alteration reactions. Econ. Geol. 70 (3), 577–583.

Mualem, Y., 1976. A new model for predicting the hydraulic conductivity of unsaturated porous media. Water Resour. Res. 12 (3), 513–522.

Mukhamet-Galeev, A., Zotov, A., 1992. Relative stability of kaolinite and dickite. In: Thermodynamics of natural processes, symposium, Novosiibirsk, Russia, 13-20 September.

Müller, N., 2011. Supercritical CO_2-brine relative permeability experiments in reservoir rocks–Literature review and recommendations. Transport Porous Med. 87 (2), 367–383.

Nagy, K. L., Blum, A. E., Lasaga, A. C., 1991. Dissolution and precipitation kinetics of kaolinite at 80°C and pH 3: The dependence on solution saturation state. Am. J. Sci. 291 (7), 649–686.

Nagy, K. L., Cygan, R. T., Hanchar, J. M., Sturchio, N. C., 1999. Gibbsite growth kinetics on gibbsite, kaolinite, and muscovite substrates: Atomic force microscopy evidence for epitaxy and an assessment of reactive surface area. Geochim. Cosmochim. Acta 63 (16), 2337–2351.

Nagy, K. L., Lasaga, A. C., 1992. Dissolution and precipitation kinetics of gibbsite at 80 °C and pH 3: The dependence on solution saturation state. Geochim. Cosmochim. Acta 56 (8), 3093–3111.

Nagy, K. L., Lasaga, A. C., 1993. Simultaneous precipitation kinetics of kaolinite and gibbsite at 80°C and pH 3. Geochim. Cosmochim. Acta 57 (17), 4329–4335.

Navarre-Sitchler, A., Steefel, C. I., Yang, L., Tomutsa, L., Brantley, S. L., 2009. Evolution of porosity and diffusivity associated with chemical weathering of a basalt clast. J. Geophys. Res.-Earth 114 (F2).

Navarre-Sitchler, A. K., Maxwell, R. M., Siirila, E. R., Hammond, G. E., Lichtner, P. C., 2013. Elucidating geochemical response of shallow heterogeneous aquifers to CO_2 leakage using high-performance computing: implications for monitoring of CO_2. Adv. Water Resour., 45–55.

Nielsen, A. E., 1984. Electrolyte crystal growth mechanisms. J. Cryst. Growth 67 (2), 289–310.

Noiriel, C., Luquot, L., Madé, B., Raimbault, L., Gouze, P., Van Der Lee, J., 2009. Changes in reactive surface area during limestone dissolution: An experimental and modelling study. Chem. Geol. 265 (1), 160–170.

Nordstrom, D. K., Munoz, J. L., 1994. Geochemical Thermodynamics. Blackwell Scientific.

Oelkers, E. H., Cole, D. R., 2008. Carbon dioxide sequestration a solution to a global problem. Elements 4 (5), 305–310.

Oelkers, E. H., Helgeson, H. C., 1990. Triple-ion anions and polynuclear complexing in supercritical electrolyte solutions. Geochim. Cosmochim. Acta 54 (3), 727–738.

Oelkers, E. H., Helgeson, H. C., 1991. Calculation of activity coefficients and degrees of formation of neutral ion pairs in supercritical electrolyte solutions. Geochim. Cosmochim. Acta 55 (5), 1235–1251.

Oelkers, E. H., Helgeson, H. C., 1993a. Calculation of dissociation constants and the relative stabilities of polynuclear clusters of 1 : 1 electrolytes in hydrothermal solutions at supercritical pressures and temperatures. Geochim. Cosmochim. Acta 57 (12), 2673–2697.

Oelkers, E. H., Helgeson, H. C., 1993b. Multiple ion association in supercritical aqueous solutions of single electrolytes. Science 261 (5123), 888–891.

Oelkers, E. H., Helgeson, H. C., Shock, E. L., Sverjensky, D. A., Johnson, J. W., Pokrovskii, V. A., 1995. Summary of the apparent standard partial molal gibbs free energies of formation of aqueous species, minerals, and gases at pressures 1 to 5000 bars and temperatures 25 to 1000°C. J. Phys. Chem. Ref. Data 24 (4), 1401–1560.

Oelze, M., von Blanckenburg, F., Bouchez, J., Hoellen, D., Dietzel, M., 2015. The effect of Al on Si isotope fractionation investigated by silica precipitation experiments. Chem. Geol.

Oldenburg, C. M., 2007. Joule-Thomson cooling due to CO_2 injection into natural gas reservoirs. Energy Convers. Manage. 48 (6), 1808–1815.

Orville, P. M., 1963. Alkali ion exchange between vapor and feldspar phases. Am. J. Sci. 261 (3), 201–237.

Pabalan, R. T., Pitzer, K. S., 1987. Thermodynamics of concentrated electrolyte mixtures and the prediction of mineral solubilities to high temperatures for mixtures in the system Na-K-Mg-Cl-SO_4-OH-H_2O. Geochim. Cosmochim. Acta 51 (9), 2429–2443.

Pacala, S., Socolow, R., 2004. Stabilization wedges: solving the climate problem for the next 50 years with current technologies. Science 305 (5686), 968–972.

Palandri, J., Kharaka, Y., 2004. A compilation of rate parameters of water-mineral interaction kinetics for application to geochemical modeling. Tech. rep., DTIC Document.

Palmer, D. A., Bénézeth, P., Wesolowski, D. J., 2001. Aqueous high-temperature solubility studies. I. the solubility of boehmite as functions of ionic strength (to 5 molal, NaCl), temperature (100–290 C), and pH as determined by in situ measurements. Geochim. Cosmochim. Acta 65 (13), 2081–2095.

Palmer, D. A., Wesolowski, D. J., 1992. Aluminum speciation and equilibria in aqueous solution: II. The solubility of gibbsite in acidic sodium chloride solutions from 30 to 70 °C. Geochim. Cosmochim. Acta 56 (3), 1093–1111.

Parks, G. A., 1972. Free energies of formation and aqueous solubilities of aluminum hydroxides and oxide hydroxides at 25°C. Amer. Mineral. 57 (7), 1163–1189.

Patterson, S. H., Roberson, C. E., 1961. Weathered basalt in the eastern part of Kauai, Hawaii. USGS Professional Paper 424, 195–198.

Pačes, T., 1978. Reversible control of aqueous aluminum and silica during the irreversible evolution of natural waters. Geochim. Cosmochim. Acta 42, 1487–1493.

Pester, N. J., Ding, K., Seyfried, W. E., 2014. Magmatic eruptions and iron volatility in deep-sea hydrothermal fluids. Geology, G35079–1.

Peters, C., 2009. Accessibilities of reactive minerals in consolidated sedimentary rock: An imaging study of three sandstones. Chem. Geol. 265 (1), 198–208.

Pitzer, K. S., 1973. Thermodynamics of electrolytes. I. Theoretical basis and general equations. J. Phys. Chem. 77 (2), 268–277.

Pitzer, K. S., Pabalan, R. T., 1986. Thermodynamics of NaCl in steam. Geochim. Cosmochim. Acta 50 (7), 1445–1454.

Plummer, L., Parkhurst, D., Wigley, T., 1979. Critical review of the kinetics of calcite dissolution and precipitation. Chemical Modeling in Aqueous Systems: American Chemical Society, Washington, 537–573.

Plyasunov, A. V., Shock, E. L., 2001. Correlation strategy for determining the parameters of the revised Helgeson-Kirkham-Flowers model for aqueous nonelectrolytes. Geochim. Cosmochim. Acta 65 (21), 3879–3900.

Pokrovskii, V. A., 1999. Calculation of the standard partial molal thermodynamic properties and dissociation constants of aqueous HCl° and HBr° at temperatures to 1000° C and pressures to 5 kbar. Geochim. Cosmochim. Acta 63 (7), 1107–1115.

Pokrovskii, V. A., Helgeson, H. C., 1995. Thermodynamic properties of aqueous species and the solubilities of minerals at high pressures and temperatures; the system Al_2O_3-H_2O-NaCl. Am. J. Sci. 295 (10), 1255–1342.

Pokrovskii, V. A., Helgeson, H. C., 1997. Calculation of the standard partial molal thermodynamic properties of KCl° and activity coefficients of aqueous KCl at temperatures and pressures to 1000°C and 5 kbar. Geochim. Cosmochim. Acta 61 (11), 2175–2183.

Pokrovsky, O. S., Golubev, S. V., Schott, J., 2005. Dissolution kinetics of calcite, dolomite and magnesite at 25 °C and 0 to 50 atm pCO_2. Chem. Geol. 217 (3), 239–255.

Pokrovsky, O. S., Golubev, S. V., Schott, J., Castillo, A., 2009. Calcite, dolomite and magnesite dissolution kinetics in aqueous solutions at acid to circumneutral pH, 25 to 150°C and 1 to 55 atm pCO_2: New constraints on CO_2 sequestration in sedimentary basins. Chem. Geol. 265 (1), 20–32.

Pokrovsky, O. S., Schott, J., 2001. Kinetics and mechanism of dolomite dissolution in neutral to alkaline solutions revisited. Am. J. Sci. 301 (7), 597–626.

Polzer, W., Hem, J., 1965. The dissolution of kaolinite. J. Geophys. Res. 70 (24), 6233–6240.

Popp, R. K., Frantz, J. D., 1979. Mineral solution equilibria–II. An experimental study of mineral solubilities and the thermodynamic properties of aqueous $CaCl_2$ in the system CaO-SiO_2-H_2O-HCl. Geochim. Cosmochim. Acta 43 (11), 1777–1790.

Popp, R. K., Frantz, J. D., 1980. Mineral-solution equilibria III. the system Na_2O-Al_2O_3-SiO_2-H_2O-HCl. Geochim. Cosmochim. Acta 44 (7), 1029–1037.

Porter, M. L., Wildenschild, D., 2010. Image analysis algorithms for estimating porous media multiphase flow variables from computed microtomography data: a validation study. Computational Geosciences 14 (1), 15–30.

Powell, R., Holland, T., 1985. An internally consistent thermodynamic dataset with uncertainties and correlations: 1. Methods and a worked example. J. Metamorph. Geol. 3 (4), 327–342.

Powell, R., Holland, T., 1993. The applicability of least squares in the extraction of thermodynamic data from experimentally bracketed mineral equilibria. Am. Mineral. 78, 107–112.

Pruess, K., 2006. Enhanced geothermal systems (EGS) using CO_2 as working fluid-A novel approach for generating renewable energy with simultaneous sequestration of carbon. Geothermics 35 (4), 351–367.

Pruess, K., Spycher, N., 2007. ECO2N–a fluid property module for the TOUGH2 code for studies of CO_2 storage in saline aquifers. Energy Convers. Manage. 48 (6), 1761–1767.

Quist, A. S., Marshall, W. L., 1968. Electrical conductances of aqueous sodium chloride solutions from 0 to 800° and at pressures to 4000 bars. J. Phys. Chem. 72 (2), 684–703.

Rafal'skiy, R., Prisyagina, N., Kondrushin, I., 1990. Reaction of microcline-perthite with aqueous solutions at 150 and 250°C. Geochem. Int. 27 (9-12), 56.

Randall, M., Failey, C. F., 1927. The activity coefficient of non-electrolytes in aqueous salt solutions from solubility measurements. The salting-out order of the ions. Chem. Rev. 4 (3), 285–290.

Randolph, J. B., 2011. Coupling geothermal energy capture with carbon dioxide sequestration in naturally permeable, porous geologic formations– a novel approach for expanding geothermal energy utilization. Ph.D. thesis, University of Minnesota.

Randolph, J. B., Saar, M. O., 2011a. Combining geothermal energy capture with geologic carbon dioxide sequestration. Geophys. Res. Lett. 38 (10), L10401.

Randolph, J. B., Saar, M. O., 2011b. Coupling carbon dioxide sequestration with geothermal energy capture in naturally permeable, porous geologic formations: Implications for CO_2 sequestration. Energy Procedia 4, 2206–2213.

Randolph, J. B., Saar, M. O., 2011c. Impact of reservoir permeability on the choice of subsurface geothermal heat exchange fluid: CO_2 versus water and native brine. In: GRC Transactions. Vol. 35. pp. 521–526.

Rayward-Smith, W., Woods, A. W., 2011. Some implications of cold CO_2 injection into deep saline aquifers. Geophys. Res. Lett. 38 (6), L06407.

Reed, M. H., 1997. Hydrothermal alteration and its relationship to ore fluid composition. Geochemistry of hydrothermal ore deposits 3, 303–365.

Reesman, A., Keller, W., 1968. Aqueous solubility studies of high-alumina and clay minerals. Am. Mineral 53, 929–942.

Rimstidt, J. D., 1997. Quartz solubility at low temperatures. Geochim. Cosmochim. Acta 61 (13), 2553–2558.

Robie, R. A., Hemingway, B. S., 1991. Heat capacities of kaolinite from 7 to 380 K and of DMSO-intercalated kaolinite from 20 to 310 K the entropy of kaolinite $Al_2Si_2O_5(OH)_4$. Clay. Clay Miner. 39 (4), 362–386.

Robie, R. A., Hemingway, B. S., 1995. Thermodynamic properties of minerals and related substances at 298.15 K and 1 bar (10^5 Pascals) pressure and at higher temperatures. US Geol. Survey Bull. 2131, 461–461.

Robie, R. A., Hemingway, B. S., Fisher, J. R., 1978. Thermodynamic properties of minerals and related substances at 298. 15 k and 1 bar (10^5 pascals) pressure and at higher temperatures. Tech. rep., Geological Survey, Washington, DC (USA).

Robie, R. A., Waldbaum, D. R., 1968. Thermodynamic Properties of Minerals and Related Substances at 298.150 K (25.00 C) and One Atmosphere (1.013 Bars) Pressure and at Higher Temperatures. US Government Printing Office.

Ruan, B., Xu, R., Wei, L., Ouyang, X., Luo, F., Jiang, P., 2013. Flow and thermal modeling of CO_2 in injection well during geological sequestration. Int. J. Greenh. Gas Con. 19, 271–280.

Saar, M. O., 2011. Review: Geothermal heat as a tracer of large-scale groundwater flow and as a means to determine permeability fields. Hydrogeol. J. 19 (1), 31–52.

Saar, M. O., Manga, M., 1999. Permeability-porosity relationship in vesicular basalts. Geophys. Res. Lett. 26 (1), 111–114.

Saar, M. O., Manga, M., 2004. Depth dependence of permeability in the Oregon Cascades inferred from hydrogeologic, thermal, seismic, and magmatic modeling constraints. J. Geophys. Res. 109 (B4).

Saar, M. O., Randolph, J. B., Kuehn, T. H., the Regents of the University of Minnesota, 2012. Carbon dioxide-based geothermal energy generation systems and methods related thereto. U.S. Patent No. 8,316,955.

Saar, M. O., Randolph, J. B., Kuehn, T. H., the Regents of the University of Minnesota, 2013. Carbon dioxide-based geothermal energy generation systems and methods related thereto. Canada Patent No. 2.753.393.

Saar, M. O., Randolph, J. B., Kuehn, T. H., the Regents of the University of Minnesota, 2014a. Carbon dioxide-based geothermal energy generation systems and methods related thereto. European Patent No. 2406562.

Saar, M. O., Randolph, J. B., Kuehn, T. H., the Regents of the University of Minnesota, Heat Mining Company, L., 2014b. Carbon dioxide-based geothermal energy generation systems and methods related thereto. U.S. Pending Patent No. WO2014015307-A1.

Saccocia, P. J., Seyfried, Jr., W. E., 1994. The solubility of chlorite solid solutions in 3.2 wt% NaCl fluids from 300–400 C, 500 bars. Geochim. Cosmochim. Acta 58 (2), 567–585.

Salehikhoo, F., Li, L., Brantley, S. L., 2013. Magnesite dissolution rates at different spatial scales: The role of mineral spatial distribution and flow velocity. Geochim. Cosmochim. Acta 108, 91–106.

Schulte, M. D., Shock, E. L., Wood, R. H., 2001. The temperature dependence of the standard-state thermodynamic properties of aqueous nonelectrolytes. Geochim. Cosmochim. Acta 65 (21), 3919–3930.

Schwartz, F. W., Zhang, H., 2003. Fundamentals of Ground Water. Wiley New York: 576 p.

Schweda, P., 1990. Kinetics and mechanisms of alkali feldspar dissolution at low temperatures. PhD Thesis, Medd./Miner. Inst. (Stockholm): 99p.

Scislewski, A., Zuddas, P., 2010. Estimation of reactive mineral surface area during water–rock interaction using fluid chemical data. Geochim. Cosmochim. Acta 74 (24), 6996–7007.

Selley, R., 1982. An introduction to sedimentology. Academic Press, 417 p.

Seyfried, Jr., W., Ding, K., Berndt, M., 1991. Phase equilibria constraints on the chemistry of hot spring fluids at mid-ocean ridges. Geochim. Cosmochim. Acta 55 (12), 3559–3580.

Seyfried, W. J., Pester, N. J., Ding, K., Rough, M., 2011. Vent fluid chemistry of the rainbow hydrothermal system (36°N, MAR): Phase equilibria and in situ pH controls on subseafloor alteration processes. Geochim. Cosmochim. Acta 75 (6), 1574–1593.

Shade, J. W., 1974. Hydrolysis reactions in the SiO_2-excess portion of the system K_2O-Al_2O_3-SiO_2-H_2O in chloride fluids at magmatic conditions. Econ. Geol. 69 (2), 218–228.

Shao, H., Kukkadapu, R. K., Krogstad, E. J., Newburn, M. K., Cantrell, K. J., 2014. Mobilization of metals from Eau Claire Siltstone and the impact of oxygen under geological carbon dioxide sequestration conditions. Geochim. Cosmochim. Acta 141, 62–82.

Sharygin, A. V., Wood, R. H., Zimmerman, G. H., Balashov, V. N., 2002. Multiple ion association versus redissociation in aqueous NaCl and KCl at high temperatures. J. Phys. Chem. B 106 (28), 7121–7134.

Shinohara, H., Fujimoto, K., 1994. Experimental study in the system albite-andalusite-quartz-NaCl-HCl-H_2O at 600°C and 400 to 2000 bars. Geochim. Cosmochim. Acta 58 (22), 4857–4866.

Shiraki, R., Brantley, S. L., 1995. Kinetics of near-equilibrium calcite precipitation at 100°C: An evaluation of elementary reaction-based and affinity-based rate laws. Geochim. Cosmochim. Acta 59 (8), 1457–1471.

Shock, E. L., Helgeson, H. C., 1988. Calculation of the thermodynamic and transport properties of aqueous species at high pressures and temperatures: Correlation algorithms for ionic species and equation of state predictions to 5 KB and 1000°C. Geochim. Cosmochim. Acta 52 (8), 2009–2036.

Shock, E. L., Oelkers, E. H., Johnson, J. W., Sverjensky, D. A., Helgeson, H. C., 1992. Calculation of the thermodynamic properties of aqueous species at high pressures and temperatures. effective electrostatic radii, dissociation constants and standard

partial molal properties to 1000°C and 5 kbar. J. Chem. Soc., Faraday Trans. 88 (6), 803–826.

Siirila, E. R., Navarre-Sitchler, A. K., Maxwell, R. M., McCray, J. E., 2012. A quantitative methodology to assess the risks to human health from CO_2 leakage into groundwater. Adv. Water Resour. 36, 146–164.

Simmons, S. F., Browne, P. R., 2000. Hydrothermal minerals and precious metals in the broadlands-ohaaki geothermal system: Implications for understanding low-sulfidation epithermal environments. Econ. Geol. 95 (5), 971–999.

Singh, A., Baumann, G., Henninges, J., Görke, U.-J., Kolditz, O., 2012. Numerical analysis of thermal effects during carbon dioxide injection with enhanced gas recovery: A theoretical case study for the Altmark gas field. Environ. Earth Sci. 67 (2), 497–509.

Smith, M. M., Sholokhova, Y., Hao, Y., Carroll, S. A., 2012. Evaporite caprock integrity: An experimental study of reactive mineralogy and pore-scale heterogeneity during brine-CO_2 exposure. Environment. Sci. Tech. 47 (1), 262–268.

Smith, M. M., Sholokhova, Y., Hao, Y., Carroll, S. A., 2013. CO_2-induced dissolution of low permeability carbonates. Part I: Characterization and experiments. Adv. Water Resour. 62, 370–387.

Spycher, N., Pruess, K., 2005. CO_2-H_2O mixtures in the geological sequestration of CO_2. II. partitioning in chloride brines at 12–100°C and up to 600 bar. Geochim. Cosmochim. Acta 69 (13), 3309–3320.

Spycher, N. F., Reed, M. H., 1988. Fugacity coefficients of H_2, CO_2, CH_4, H_2O and of H_2O-CO_2-CH_4 mixtures: a virial equation treatment for moderate pressures and temperatures applicable to calculations of hydrothermal boiling. Geochim. Cosmochim. Acta 52, 739–749.

Stauffer, F., Kong, X.-Z., Kinzelbach, W., 2009. A stochastic model for air injection into saturated porous media. Adv. Water Resour. 32 (8), 1180–1186.

Steefel, C. I., Lasaga, A. C., 1990. Evolution of dissolution patterns: Permeability change due to coupled flow and reaction. In: ACS symposium series. Vol. 416. Oxford University Press, pp. 212–225.

Steefel, C. I., Molins, S., Trebotich, D., 2013. Pore scale processes associated with subsurface CO_2 injection and sequestration. Rev. Mineral. Geochem. 77 (1), 259–303.

Stefánsson, A., 2001. Dissolution of primary minerals of basalt in natural waters: I. calculation of mineral solubilities from 0 °C to 350 °C. Chem. Geol. 172 (3), 225–250.

Stefánsson, A., Bénézeth, P., Schott, J., 2013. Carbonic acid ionization and the stability of sodium bicarbonate and carbonate ion pairs to 200°C–a potentiometric and spectrophotometric study. Geochim. Cosmochim. Acta, 600–611.

Strandh, H., Pettersson, L. G., Sjöberg, L., Wahlgren, U., 1997. Quantum chemical studies of the effects on silicate mineral dissolution rates by adsorption of alkali metals. Geochim. Cosmochim. Acta 61 (13), 2577–2587.

Sverdrup, H. U., 1990. The kinetics of base cation release due to chemical weathering. Vol. 245. Lund University Press Lund, Sweden.

Sverjensky, D. A., Hemley, J. J., D'Angelo, W. M., 1991. Thermodynamic assessment of hydrothermal alkali feldspar-mica-aluminosilicate equilibria. Geochim. Cosmochim. Acta 55 (4), 989–1004.

Sverjensky, D. A., Shock, E. L., Helgeson, H. C., 1997. Prediction of the thermodynamic properties of aqueous metal complexes to 1000°C and 5 kb. Geochim. Cosmochim. Acta 61 (7), 1359–1412.

Swift, A. M., Anovitz, L. M., Sheets, J. M., Cole, D. R., Welch, S. A., Rother, G., 2014. Relationship between mineralogy and porosity in seals relevant to geologic CO_2 sequestration. Environmental Geosciences 21 (2), 39–57.

Syverson, D. D., Borrok, D. M., Seyfried, Jr., W. E., 2013. Experimental determination of equilibrium Fe isotopic fractionation between pyrite and dissolved Fe under hydrothermal conditions. Geochim. Cosmochim. Acta, 170–183.

Tagirov, B., Schott, J., 2001. Aluminum speciation in crustal fluids revisited. Geochim. Cosmochim. Acta 65 (21), 3965–3992.

Tagirov, B., Schott, J., Harrichourry, J.-C., Salvi, S., 2002. Experimental study of aluminum speciation in fluoride-rich supercritical fluids. Geochim. Cosmochim. Acta 66 (11), 2013–2024.

Tagirov, B., Zotov, A., Akinfiev, N., 1997. Experimental study of dissociation of HCl from 350 to 500°C and from 500 to 2500 bars: Thermodynamic properties of $HCl^{\circ}_{(aq)}$. Geochim. Cosmochim. Acta 61 (20), 4267–4280.

Takemura, F., Yabe, A., 1999. Rising speed and dissolution rate of a carbon dioxide bubble in slightly contaminated water. J. Fluid Mech. 378, 319–334.

Tanger, J., Helgeson, H. C., 1988. Calculation of the thermodynamic and transport properties of aqueous species at high pressures and temperatures; revised equations of state for the standard partial molal properties of ions and electrolytes. Am. J. Sci. 288 (1), 19–98.

Tao, Z., Clarens, A., 2013. Estimating the carbon sequestration capacity of shale formations using methane production rates. Env. Sci. Tech. 47 (19), 11318–11325.

Teng, H. H., Dove, P. M., De Yoreo, J. J., 2000. Kinetics of calcite growth: Surface processes and relationships to macroscopic rate laws. Geochim. Cosmochim. Acta 64 (13), 2255–2266.

Tester, J. W., Anderson, B. J., Batchelor, A., Blackwell, D., DiPippo, R., Drake, E., Garnish, J., Livesay, B., Moore, M., Nichols, K., et al., 2006. The future of geothermal energy. Impact of Enhanced Geothermal Systems (EGS) on the United States in the 21st Century, Massachusetts Institute of Technology, Cambridge, MA, 372.

Theye, T., Chopin, C., Grevel, K.-D., Ockenga, E., 1997. The assemblage diaspore + quartz in metamorphic rocks: a petrological, experimental and thermodynamic study. J. Metamorph. Geol. 15 (1), 17–28.

Trémosa, J., Castillo, C., Vong, C. Q., Kervévan, C., Lassin, A., Audigane, P., 2014. Long-term assessment of geochemical reactivity of CO_2 storage in highly saline aquifers: Application to Ketzin, In Salah and Snøhvit storage sites. Int. J. Greenh. Gas Cont. 20, 2–26.

Tutolo, B. M., Kong, X.-Z., , Saar, M. O., Seyfried, Jr., W. E., 2014a. Internal consistency in aqueous geochemical data revisited: Applications to the aluminum system. Geochim. Cosmochim. Acta 133, 216–234.

Tutolo, B. M., Luhmann, A. J., Kong, X.-Z., , Saar, M. O., Seyfried, Jr., W. E., 2014b. Experimental observation of permeability changes in dolomite at CO_2 sequestration conditions. Environ. Sci. Tech. 48 (4), 2445–2452.

Tutolo, B. M., Luhmann, A. J., Kong, X.-Z., Saar, M. O., Seyfried, W. E., 2015a. CO_2 sequestration in feldspar-rich sandstone: Coupled evolution of fluid chemistry, mineral reaction rates, and hydrogeochemical properties. Geochim. Cosmochim. Acta 160, 132–154.

Tutolo, B. M., Schaen, A. T., Saar, M. O., Seyfried, Jr., W. E., 2015b. Implications of the redissociation phenomenon for mineral-buffered fluids and aqueous species transport at elevated temperatures and pressures. Appl. Geochem. 55, 119–127.

Usdowski, H., Barnes, H., 1972. Untersuchungen über das gleichgewicht zwischen k-feldspat, quarz und muskovit und die anwendung auf fragen der gesteinsbildung bei tieferen temperaturen. Contrib. Mineral. Petr. 36 (3), 207–219.

U.S.G.S., G. C. D. S. R. A. T., 2013. National assessment of geologic carbon dioxide storage resources–results. U.S.G.S. Circular 1386, 41.

Van Genuchten, M. T., 1980. A closed-form equation for predicting the hydraulic conductivity of unsaturated soils. Soil Sci. Soc. Am. J. 44 (5), 892–898.

Wagner, W., Pruss, A., 2002. The IAPWS formulation 1995 for the thermodynamic properties of ordinary water substance for general and scientific use. J. Phys. Chem. Ref. Data 31 (2), 387–536.

Walther, J. V., 1997. Determination of activity coefficients of neutral species in supercritical H_2O solutions. Geochim. Cosmochim. Acta 61 (16), 3311–3318.

Washton, N. M., Brantley, S. L., Mueller, K. T., 2008. Probing the molecular-level control of aluminosilicate dissolution: A sensitive solid-state NMR proxy for reactive surface area. Geochim. Cosmochim. Acta 72 (24), 5949–5961.

Wesolowski, D. J., 1992. Aluminum speciation and equilibria in aqueous solution: I. The solubility of gibbsite in the system Na-K-Cl-OH-Al$(OH)_4$ from 0 to 100°C. Geochim. Cosmochim. Acta 56 (3), 1065–1091.

Wesolowski, D. J., Palmer, D. A., 1994. Aluminum speciation and equilibria in aqueous solution: V. Gibbsite solubility at 50 C and pH 3–9 in 0.1 molal NaCl solutions (a general model for aluminum speciation; analytical methods). Geochim. Cosmochim. Acta 58 (14), 2947–2969.

White, A., Blum, A., Bullen, T., Vivit, D., Schulz, M., Fitzpatrick, J., 1999. The effect of temperature on experimental and natural chemical weathering rates of granitoid rocks. Geochim. Cosmochim. Acta 63 (19), 3277–3291.

White, A. F., Brantley, S. L., 2003. The effect of time on the weathering of silicate minerals: Why do weathering rates differ in the laboratory and field? Chem. Geol. 202 (3), 479–506.

White, A. F., Peterson, M. L., 1990. Role of reactive-surface-area characterization in geochemical kinetic models. Chemical Modeling of Aqueous Systems II (eds DC Melchoir and RL Bassett) Chap 35, 461–475.

Whitney, D. L., Evans, B. W., 2010. Abbreviations for names of rock-forming minerals. Amer. Mineral. 95, 185–187.

Williams-Jones, A. E., Heinrich, C. A., 2005. 100th anniversary special paper: vapor transport of metals and the formation of magmatic-hydrothermal ore deposits. Econ. Geol. 100 (7), 1287–1312.

Williams-Jones, A. E., Migdisov, A. A., Samson, I. M., 2012. Hydrothermal mobilisation of the rare earth elements–a tale of ceria and yttria. Elements 8 (5), 355–360.

Wintsch, R. P., Merino, E., Blakely, R. F., 1980. Rapid-quench hydrothermal experiments in dilute chloride solutions applied to the muscovite-quartz-sanidine equilibrium. Am. Mineral. 65 (9-10), 1002–1011.

Wolery, T., Sutton, M., 2013. Evaluation of thermodynamic data. Tech. rep., Lawrence Livermore National Laboratory (LLNL), Livermore, CA.

Wolery, T. J., 1992. EQ3/6: A software package for geochemical modeling of aqueous systems: Package overview and installation guide (version 7.0). Lawrence Livermore National Laboratory.

Woodland, A. B., Walther, J. V., 1987. Experimental determination of the solubility of the assemblage paragonite, albite, and quartz in supercritical H_2O. Geochim. Cosmochim. Acta 51 (2), 365–372.

Wright, J., Lindsay Jr, W., Druga, T., 1961. The behavior of electrolytic solutions at elevated temperatures as derived from conductance measurements. Tech. rep., Westinghouse Electric Corp. Bettis Atomic Power Lab., Pittsburgh.

Wunsch, A., Navarre-Sitchler, A. K., Moore, J., Ricko, A., McCray, J. E., 2013. Metal release from dolomites at high partial-pressures of CO_2. Appl. Geochem. 38, 33–47.

Xie, Z., Walther, J. V., 1993. Quartz solubilities in NaCl solutions with and without wollastonite at elevated temperatures and pressures. Geochim. Cosmochim. Acta 57 (9), 1947–1955.

Xu, T., Apps, J., Pruess, K., 2003. Reactive geochemical transport simulation to study mineral trapping for CO_2 disposal in deep arenaceous formations. J. Geophys. Res. 108 (B2), 2071.

Xu, T., Apps, J., Pruess, K., Yamamoto, H., 2007. Numerical modeling of injection and mineral trapping of CO_2 with H_2S and SO_2 in a sandstone formation. Chem. Geol. 242 (3), 319–346.

Xu, T., Apps, J. A., Pruess, K., 2004. Numerical simulation of CO_2 disposal by mineral trapping in deep aquifers. Appl. Geochem. 19 (6), 917–936.

Xu, T., Sonnenthal, E., Spycher, N., Pruess, K., 2006. TOUGHREACT–a simulation program for non-isothermal multiphase reactive geochemical transport in variably saturated geologic media: Applications to geothermal injectivity and CO_2 geological sequestration. Comput. Geosci. 32 (2), 145–165.

Yang, L., Steefel, C. I., 2008. Kaolinite dissolution and precipitation kinetics at 22 °C and pH 4. Geochim. Cosmochim. Acta 72 (1), 99–116.

Yardley, B. W., 2005. 100th anniversary special paper: metal concentrations in crustal fluids and their relationship to ore formation. Econ. Geol. 100 (4), 613–632.

Yardley, B. W., Bodnar, R. J., 2014. Fluids in the continental crust. Geochem. Perspec. 3 (1), 1–123.

Yoo, S.-Y., Kuroda, Y., Mito, Y., Matsuoka, T., Nakagawa, M., Ozawa, A., Sugiyama, K., Ueda, A., 2013. A geochemical clogging model with carbonate precipitation rates under hydrothermal conditions. Appl. Geochem. 30, 67–74.

Zerai, B., Saylor, B., Matisoff, G., 2006. Computer simulation of CO_2 trapped through mineral precipitation in the Rose Run Sandstone, Ohio. Appl. Geochem. 21 (2), 223–240.

Zhang, G., Spycher, N., Xu, T., Sonnenthal, E., Steefel, C., 2006. Reactive geochemical transport modeling of concentrated aqueous solutions: Supplement to TOUGHREACT user's guide for the Pitzer ion-interaction model.

Zhao, R., Cheng, J., 2014. Non-isothermal modeling of CO_2 injection into saline aquifers at a low temperature. Environmental Earth Sci., 1–10.

Zhou, X., Burbey, T. J., 2014. Fluid effect on hydraulic fracture propagation behavior: a comparison between water and supercritical CO_2-like fluid. Geofluids 14 (2), 174–188.

Zhu, C., Lu, P., 2009. Alkali feldspar dissolution and secondary mineral precipitation in batch systems: 3. Saturation states of product minerals and reaction paths. Geochim. Cosmochim. Acta 73 (11), 3171–3200.

Zhu, C., Lu, P., Zheng, Z., Ganor, J., 2010. Coupled alkali feldspar dissolution and secondary mineral precipitation in batch systems: 4. Numerical modeling of kinetic reaction paths. Geochim. Cosmochim. Acta 74 (14), 3963–3983.

Zimmerman, G., Arcis, H., Tremaine, P., 2012. Limiting conductivities and ion association constants of aqueous NaCl under hydrothermal conditions: Experimental data and correlations. J. Chem. Eng. Data 57 (9), 2415–2429.

Zotov, A., Mukhamet-Galeev, A., Schott, J., 1998. An experimental study of kaolinite and dickite relative stability at 150-300 c and the thermodynamic properties of dickite. Am. Mineral. 83, 516–524.

Zuo, L., Krevor, S., Falta, R. W., Benson, S. M., 2012. An experimental study of CO_2 exsolution and relative permeability measurements during CO_2 saturated water depressurization. Transport Porous Med. 91 (2), 459–478.

Appendix A

Overview of data examined during the composition of Chapter 2

In composing this study, a large number of experimental and field measurements of mineral solubilities, phase equilibria, heat capacities, and enthalpies were considered. We have included a list of the studies considered during preparation of the presented data set in Table A.1. The studies are classified as 1) "calorimetry"; 2) "solubility," which indicates measurements of equilibrium between only the listed mineral and the experimental fluid; and 3) "phase equilbria," which indicates measurements of equilibrium between the listed mineral, the experimental fluid, and at least one other mineral. See the referenced studies for details on experimental conditions and mineral phases. Final decision on whether to include thermodynamic data from a particular study were based on the following criteria:

1) Has equilibrium been demonstrated between the focus mineral, an aqueous solution, and at least one other mineral in the reaction matrix?

2) Are experimental parameters (temperature, pressure, ionic strength) amenable to the derivation of thermodynamic properties without introducing undue uncertainty?

3) Are the results of the study in reasonable agreement with other studies at similar conditions?

4) Can "summed" reactions, such as those described in Sect. 2.5.2, be employed using the experimental data?

Preference was given to experimental datasets where equilibrium was demonstrated at multiple T-P conditions in order to provide decreased uncertainty on calculated results. Note that the criteria for inclusion in the present study require that data be obtained from measurements of solution composition and not, for example,

T-P bracketing of crystal growth. Quartz is excluded from this table because its thermodynamic properties and solubility have been studied in extensive detail and it was accepted as an anchor mineral here. For a review of these solubility measurements, see the recent reviews of Rimstidt (1997) or Stefánsson (2001). The solubilities of boehmite and gibbsite have been examined in a much larger number of studies than are included in this table; however, examination of the majority of these references reveals that they are all in relatively clear agreement. Reviews of Al hydroxide solubility studies can be found in Parks (1972), Apps et al. (1988), Pokrovskii and Helgeson (1995), Tagirov and Schott (2001). For minerals where no calorimetric study is given, the analysis relied upon Robie and Hemingway (1995) and references therein.

Table A.1: Experimental studies considered

Reference	Method	T-P Range
Albite		
Burch et al. (1993)	Solubility	80°C, Psat
Arnórsson et al. (1983)	Phase Equilibria	21-250°C, Psat
Merino (1975)	Phase Equilibria	100°C, 150 bars
Montoya and Hemley (1975)	Phase Equilibria	25-500°C, 1000 bars
Saccocia and Seyfried (1994)	Phase Equilibria	300-500°C, 500 bars
Woodland and Walther (1987)	Phase Equilibria	350-500°C, 1000-2500 bars
Tagirov et al. (2002)	Phase Equilibria	400-350°C, 500-1000 bars
Orville (1963)	Phase Equilibria	350-700°C, 2000 bars
Popp and Frantz (1980)	Phase Equilibria	500-700°C, 1000 bars
Shinohara and Fujimoto (1994)	Phase Equilibria	600°C, 400-2000 bars
Andalusite		
Hemley et al. (1980)	Phase Equilibria	340-500°C, 1000-2000 bars
Sverjensky et al. (1991)	Phase Equilibria	400-550°C, 1000-2000 bars
Montoya and Hemley (1975)	Phase Equilibria	400-500°C, 1000 bars
Haselton et al. (1995)	Phase Equilibria	400-500°C, 1000 bars
Frank et al. (1998)	Phase Equilibria	400-550°C, 250-600 bars
Shinohara and Fujimoto (1994)	Phase Equilibria	600°C, 400-2000 bars
Boehmite		
Hemingway et al. (1991)	Calorimetry	25°C,1 bar
Majzlan et al. (2000)	Calorimetry	25°C, 1 bar
Palmer et al. (2001)	Solubility	100-290°C, Psat
Bénézeth et al. (2001)	Solubility	100-290°C, Psat
Königsberger et al. (2011)	Solubility	95°C, 1 bar
Bénézeth et al. (2007)	Phase Equilibria	150-200°C, Psat
Hemley et al. (1980)	Phase Equilibria	200-300°C, 1000 bars
Hemley (1959)	Phase Equilibria	400°C, 1000 bars
Dawsonite		
Ferrante et al. (1976)	Calorimetry	25-204°C, Psat
Bénézeth et al. (2001)	Phase Equilibria	25-200°C, Psat
Diaspore		
Apps et al. (1989)	Solubility	25-350°C, Psat
Hemley et al. (1980)	Phase Equilibria	200-390°C, 1000-2000 bars
Gibbsite		
Frink and Peech (1962)	Solubility	25°C, 1 bar
May et al. (1979)	Solubility	25°C, 1 bar
Palmer and Wesolowski (1992)	Solubility	30-70°C, 1 bar
Wesolowski and Palmer (1994)	Solubility	50°C, Psat
Nagy and Lasaga (1992)	Solubility	80°C, Psat

Helgeson et al. (1978)	Phase Equilibria	25°C, 1 bar
Muscovite		
Montoya and Hemley (1975)	Phase Equilibria	25-500°C, 1000 bars
Usdowski and Barnes (1972)	Phase Equilibria	30-300°C, Psat
Wintsch et al. (1980)	Phase Equilibria	200-500°C, 2000 bars
Sverjensky et al. (1991)	Phase Equilibria	300-550°C, 1000-2000 bars
Haselton et al. (1995)	Phase Equilibria	400-500°C, 1000-6000 bars
Shade (1974)	Phase Equilibria	400-500°C, 1000 bars
Frank et al. (1998)	Phase Equilibria	400-550°C, 250-600 bars
Gunter and Eugster (1980)	Phase Equilibria	600-670°C, 1000-2000 bars
K-feldspar		
Arnórsson et al. (1983)	Phase Equilibria	21-250°C, Psat
Merino (1975)	Phase Equilibria	100°C, 150 bars
Usdowski and Barnes (1972)	Phase Equilibria	30-300°C, Psat
Wintsch et al. (1980)	Phase Equilibria	200-500°C, 2000 bars
Sverjensky et al. (1991)	Phase Equilibria	300-600°C, 1000-2000 bars
Haselton et al. (1995)	Phase Equilibria	400-500°C, 1000-6000 bars
Shade (1974)	Phase Equilibria	400-500°C, 1000 bars
Frank et al. (1998)	Phase Equilibria	400-550°C, 250-600 bars
Gunter and Eugster (1980)	Phase Equilibria	600-670°C, 1000-2000 bars
Kaolinite		
De Ligny and Navrotsky (1999)	Calorimetry	25°C
Fialips et al. (2001)	Calorimetry	25°C
Fialips et al. (2003)	Calorimetry	25°C
Kiseleva et al. (2011)	Calorimetry	25°C
Barany and Kelley (1961)	Calorimetry	25°C
Hemingway et al. (1978)	Calorimetry	25-800°C
Robie and Hemingway (1991)	Calorimetry	25-107°C
Yang and Steefel (2008)	Solubility	22°C, 1 bar
Polzer and Hem (1965)	Solubility	25°C, 1 bar
Reesman and Keller (1968)	Solubility	25°C, 1 bar
Huang and Keller (1973)	Solubility	25°C, 1 bar
May et al. (1986)	Solubility	25°C, 1 bar
Kittrick (1966)	Solubility	25°C, 1 bar
Kittrick (1980)	Solubility	25°C, 1 bar
Devidal et al. (1996)	Solubility	60-170°C, Psat
Nagy et al. (1991)	Solubility	80°C
Mukhamet-Galeev and Zotov (1992)	Solubility	200-300°C, Psat
Zotov et al. (1998)	Solubility, Phase Equilibria	150-300°C, Psat
Helgeson et al. (1978)	Phase Equilibria	25°C, 1 bar
Montoya and Hemley (1975)	Phase Equilibria	25-300°C, Psat and 1000 bars

Huang et al. (1993)	Phase Equilibria	200-275°C
Sverjensky et al. (1991)	Phase Equilibria	300°C, 1000 bars
Hemley et al. (1980)	Phase Equilibria	200-300°C, 1000, 2000 bars
Hemley (1959)	Phase Equilibria	200-300°C, 1000 bars
Orville (1963)	Phase Equilibria	350-700°C, 2000 bars
Paragonite		
Montoya and Hemley (1975)	Phase Equilibria	200-500°C, 1000 bars
Saccocia and Seyfried (1994)	Phase Equilibria	300-500°C, 500 bars
Tagirov et al. (2002)	Phase Equilibria	400-450°C, 500-1000 bars
Pyrophyllite		
Hemley et al. (1980)	Phase Equilibria	200-450°C, 1000-2000 bars
Montoya and Hemley (1975)	Phase Equilibria	300-400°C, 1000 bars
Sverjensky et al. (1991)	Phase Equilibria	300-400°C, 1000 bars

Appendix B

Validation of the activity coefficient formulation utilized in Chapter 3

To test the accuracy and correct implementation of Debye-Hückel activity coefficient models in the present study, we compare them with another published, calibrated model (Archer, 1992). Because it is based on a modified form of the Pitzer ion-interaction model (Pitzer, 1973; Archer, 1991), the Archer (1992) model is formulated based upon I, the stoichiometric ionic strength of the solution and we must therefore derive a relationship between the two ionic strength scales in order to yield a meaningful comparison.

In NaCl-dominated solutions where H^+ and OH^- contribute negligibly to ionic strength, we can assume:

$$\bar{I} = \mathrm{m}_{\mathrm{Na}^+} \tag{B.1}$$

and

$$I = \mathrm{m}_{\mathrm{Na}}. \tag{B.2}$$

Further, by defining $\gamma_\pm$ as the activity coefficient on the stoichiometric ionic strength scale (i.e., those reported by Archer (1992)) and keeping in mind that a_{Na^+} must be consistent regardless of whether the activity model is employing I or $\bar{I}$, we can write:

$$\gamma^*_\pm \mathrm{m}_{\mathrm{Na}^+} = \gamma_\pm \mathrm{m}_{\mathrm{Na}}. \tag{B.3}$$

Lastly, by plugging Eqs. B.1 and B.2 into Eq. B.3, we have:

$$\gamma_\pm I = \gamma^*_\pm \bar{I}, \tag{B.4}$$

which allows us to compare values of $\gamma^*_\pm$ calculated using Eq. 3.3 with values of $\gamma_\pm$ calculated using the Archer (1992) model.

Comparisons between values calculated from Eq. 3.3 using both the Helgeson (1969) and Oelkers and Helgeson (1990) parameters and those calculated from the parameterization of Archer (1992) indicate varying degrees of agreement and disagreement over the range of calculated temperatures and ionic strengths (Fig. B.1). At lower temperatures, the Helgeson (1969) formulation agrees well with the Archer (1992) formulation up to NaCl molalities of $\sim$1, and the Oelkers and Helgeson (1990)

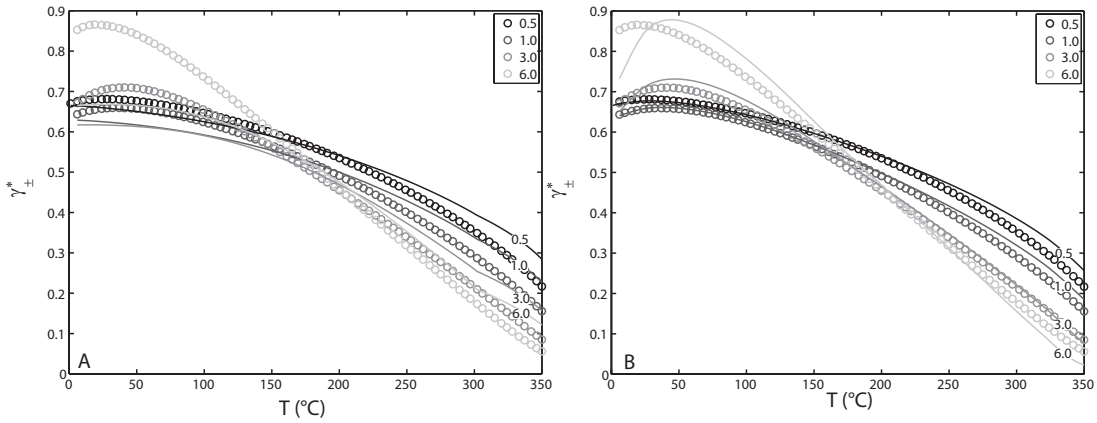

Figure B.1: Comparison between calculations of mean ionic activity coefficients for 0.5, 1, 3, and 6 molal NaCl solutions using extended Debye-Hückel equations parameterized by Helgeson (1969) (A) and Helgeson et al. (1981) (B) (lines) and Archer (1992) (symbols) for equivalent true ionic strengths (see text).

parameters are in agreement up to NaCl molalities of ∼3. At higher temperatures, both formulations are in better agreement with the Archer (1992) calculations, and the Oelkers and Helgeson (1990) parameters appear to be in very good agreement with the Archer (1992) calculations up to 6 molal NaCl. This conclusion is in accord with the assertion by Helgeson and Kirkham (1974) that the dielectric constant of water and values of parameters in Eq. 3.3 change in such a way as to extend the region of applicability of Debye-Hückel theory to progressively more concentrated solutions with increasing temperature and/or decreasing pressure.

The Helgeson (1969) calibration of Eq. 3.3, which is implemented in many geochemical speciation codes (e.g., EQ3/6 (Wolery, 1992), PFLOTRAN (Hammond et al., 2012), and the Geochemist's Workbench (Bethke and Yeakel, 2012)), was limited by the relatively few experimental measurements available at the time it was produced. The Helgeson (1969) calibration was therefore superceded by the Oelkers and Helgeson (1990) formulation, which employed experimental data acquired over a much wider range of temperature, pressure, and concentration conditions. Nonetheless, although the Oelkers and Helgeson (1990) formulation yields activity coefficients in significantly better agreement with the Archer (1992) formulation and is therefore more accurate, it has been shown that the error in mineral solubility calculations resulting from even the relatively large inter-model variations in $\gamma^*_\pm$ shown in Fig. B.1 is relatively minor (e.g., Manning, 2013). Therefore, either the Helgeson (1969) or Oelkers and Helgeson (1990) parameters may be used without introducing undue uncertainty in speciation calculations. In this study, we employ the Oelkers and Helgeson (1990) parameters for all relevant calculations.

Appendix C

Supporting information for Chapter 4

Table C.1: K-feldspar dissolution rates

Time (min)	ΔG_{rxn} (kJ/mol)	Rate (K) (mol/cm^2/s)	Rate (Si) (mol/cm^2/s)	Average Rate (mol/cm^2/s)
Recycling Experiment				
496	-22.1	2.4×10^{-13}	2.5×10^{-13}	2.5×10^{-13}
1,871	-19.2	2.2×10^{-13}	2.1×10^{-13}	2.1×10^{-13}
4,139	-15.8	1.1×10^{-13}	1.2×10^{-13}	$1.2\times10^{-}13$
9,050	-10.7	6.1×10^{-14}	6.6×10^{-14}	6.4×10^{-14}
16,894	-7.3	4.2×10^{-14}	4.3×10^{-14}	4.3×10^{-14}
26,404	-6.2	3.3×10^{-14}	3.5×10^{-14}	3.4×10^{-14}
36,664	-6.5	2.2×10^{-14}	2.1×10^{-14}	2.2×10^{-14}
46,771	-6.0	1.6×10^{-14}	1.3×10^{-14}	1.4×10^{-14}
61,110	-2.0	8.8×10^{-15}	2.3×10^{-14}	1.6×10^{-14}
72,505	-1.2	1.0×10^{-14}	1.5×10^{-14}	1.2×10^{-14}
Single Pass 1 "steady state"	-18.35	4.1×10^{-13}	2.7×10^{-13}	3.4×10^{-13}
Single Pass 2 "steady state"	-18.35	3.8×10^{-13}	2.3×10^{-13}	3.1×10^{-13}
Average		4.0×10^{-13}	2.5×10^{-13}	3.2×10^{-13}

Appendix D

Supporting Information for Chapter 5

D.1 Experimental Details

The experimental rock core was cut from an outcrop sample collected in Layton Canyon, South Dakota, USA. Prior to the experiment, the core was placed in an ultrasonic bath for ∼5 seconds to remove loose particles, rinsed with deionized water, and dried at 60°C. Deionized water flowed through the core for three days at 21°C and experimental pressures to measure the core's initial, pre-experiment permeability. During the experiment, the fluid was recirculated through the core at a flow rate of 0.05 mL/min from 0-75, 168-190, and 198-650 hours and 0.1 mL/min from 75-148 and 151-168 hours. Flow rate was 0.4 mL/min from 148-151 hours during fluid sample collection and 0.1, 0.15, 0.2, or 0.25 mL/min from 190-198 hours to confirm laminar flow. The changes in flow rate at lower T do not affect the conclusions of this study because they all occurred during the low-T portion of the experiment, which only served as a fluid-rock equilibration step.

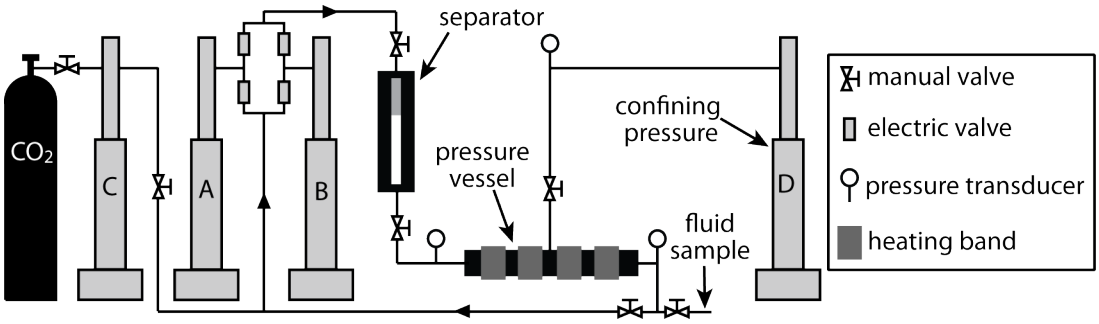

Figure D.1: Experimental setup used in the variable T experiments (after Luhmann et al. Luhmann et al. (2013)).

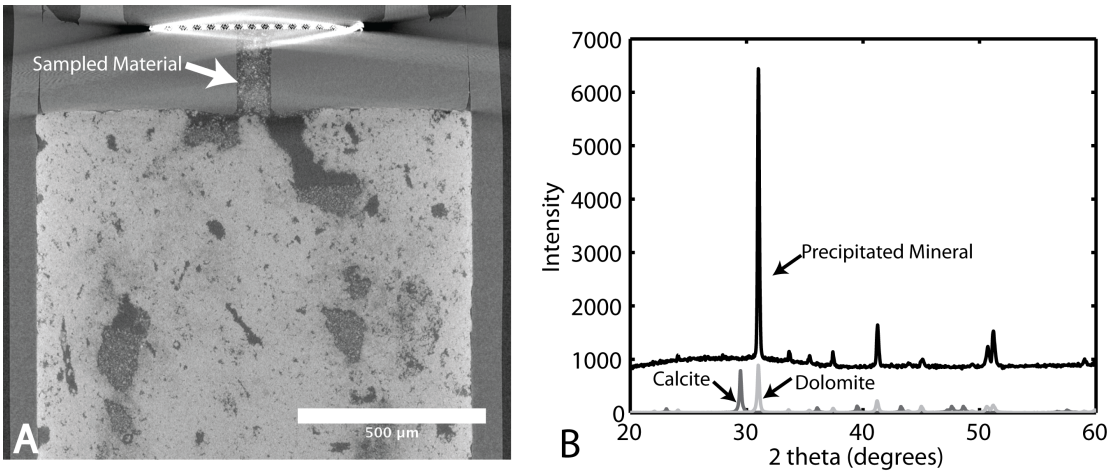

Figure D.2: A. XRCT image indicating the sampling location for the precipitated material analyzed using X-ray Diffraction (XRD). B. XRD pattern of mineral precipitate recovered from within the Teflon orifice in the dolomite experiment. Standard patterns from Eberl (2003) for calcite and dolomite are shown for reference.

D.2 Analytical Methods

X-ray Computed Tomography (XRCT) data and imagery were obtained at the University of Minnesota (UMN) XRCT facility, using a 3073 x 3889 pixel Dexela detector. A total of 900 radiographs were obtained at 0.6 frames per second with a 50 kV beam and 496 μA tube current. The imaged volume was reconstructed at 11.5 μm^3 voxel size with the efXCT software package from North Star Imaging. Pore volumes, porosity, and precipitate volume were calculated by separating each individually from the reconstructed volume and summing them to obtain a total voxel volume. Post-experiment, the core was prepared for Scanning Electron Microscopy (SEM) by sawing horizontally across the core at a distance of 2.5 mm from the upstream end. The saw was operated without water to limit disruption of internal structure of the core. The sample was subsequently sprayed with pressurized air before entering the SEM chamber to ensure that any dust was removed from the sample face.

With the aid of the XRCT imagery, a precipitated phase (dolomite) was located within the Teflon endcap on the upstream end of the core (Fig. D.2 A). The precipitated phase was carefully extracted from within the endcap orifice to avoid contamination from the rock core, and prepared for X-Ray Diffraction (XRD) analysis on a Rigaku Miniflex XRD instrument in the UMN X-ray Mineralogy Laboratory.

The fluid sample shown in Fig. D.3 and a sample of the Madison dolomite were analyzed using inductively coupled plasma optical emission spectrometry (ICP-OES) for major dissolved cations and major oxides. The Mg-Ca ratio measured for Madison dolomite sample (0.96) indicates that the sample is nearly stoichiometric dolomite. Cation 2σ accuracies are generally better than 3%.

D.3 Relative Permeability Calculations

The modified Darcy equations for both water and CO_2 Stauffer et al. (2009),

$$\frac{Q_w}{A} = \frac{kk_{rw}}{\mu_w}\frac{\Delta P_w}{L} \tag{D.1}$$

and

$$\frac{Q_{CO_2}}{A} = \frac{kk_{CO_2}}{\mu_{CO_2}}\frac{\Delta P_w + P_c}{L}, \tag{D.2}$$

can be combined to yield,

$$\frac{Q_w}{Q_{CO_2}} = \frac{k_{rw}}{k_{CO_2}}\frac{\mu_{CO_2}}{\mu_w}\frac{\Delta P_w}{\Delta P_w + P_c}, \tag{D.3}$$

where $Q_i (i = w, CO_2)$ is the volumetric flow rate, μ_i is the dynamic viscosity, k_{ri} is the relative permeability, ΔP_w is the pressure difference for water phase, P_c is the capillary pressure, k is the intrinsic permeability, and A and L are the cross-sectional area and the length of the core, respectively. By assuming that exsolved CO_2 and water within the core behave according to the modified Darcy's law for two-phase flow Stauffer et al. (2009), and that water relative permeability behaves according to the Brooks-Corey model (Brooks and Corey, 1966), the relative permeabilities of water (k_{rw}) and CO_2 (k_{rCO_2}), the Leverett function, J, and the capillary pressure, P_c, can be calculated Leverett (1940):

$$k_{rw} = S_w^{3+2/\lambda}, \tag{D.4}$$

$$J = S_w^{-1/\lambda}, \tag{D.5}$$

and

$$P_c = \sigma\sqrt{\frac{\phi}{k}}J(S_w), \tag{D.6}$$

respectively, where S_w is water saturation, σ is the interfacial tension (set here to 0.03 N/m Chiquet et al. (2007), λ is pore size distribution index (set here to 4) and ϕ is the porosity. Given the measured values of Q_w and ΔP_w, S_w can be calculated using Eqns. (D.1) and (D.4). The mass balance equation for CO_2 can be written as

$$(Q_w E_{CO_2} - Q_{CO_2})\, dt = -\Delta S_w V_{pore}, \tag{D.7}$$

where E_{CO_2} is the unitless (volume/volume) CO_2 exsolution capacity, V_{pore} is the total pore volume, and ΔS_w is the water saturation difference during time step dt. This mass balance, together with Eqns. (D.3) and (D.6), allows for calculation of k_{rCO_2}.

D.4 Fluid Chemistry Calculations

The revised Helgeson-Kirkham-Flowers (HKF) equations of state were employed in the calculation of standard molal thermodynamic properties of aqueous species Tanger and Helgeson (1988), and H_2O thermodynamic properties were calculated according to the algorithms implemented in SUPCRT92 Johnson et al. (1992). Thermodynamic properties utilized in speciation and solubility

calculations performed in this study are included in Table D.1. Shock and Helgeson Shock and Helgeson (1988) standard state thermodynamic properties and equation of state parameters were chosen for CO_2(aq) because they produced solubility predictions in significantly better agreement with an independent, calibrated model Duan and Sun (2003) than the newer HKF parameters reported by Schulte et al. Schulte et al. (2001) and Plyasunov and Shock Plyasunov and Shock (2001). Other aqueous species properties and parameters represent the most up-to-date properties from the literature (Table D.1).

Charged species activity coefficients are calculated according to the "B-dot" extended Debye-Hückel equation, which provides a reasonable approximation of activity coefficients in solutions of ionic strengths up to several molal for NaCl-dominated fluids Helgeson (1969); Helgeson and Kirkham (1974). Neutral species (including CO_2(aq)) activity coefficients are calculated according to the Drummond Drummond (1981) formulation, which is parameterized for CO_2 solubility in solutions up to 6 molal NaCl over the range 0°C - 400°C. CO_2 fugacity coefficients are calculated according to the Duan et al. Duan et al. (1992) equation of state, which was shown by Allen et al. Allen et al. (2005) to be more accurate for predicting CO_2 fugacities over the range of pressure and temperature conditions applicable to geologic CO_2 storage than the Spycher and Reed Spycher and Reed (1988) equation.

Changes in fluid concentration of the elements Ca and Mg during passes through the core, ΔC, can be modeled according to:

$$\Delta C \times Q = A \times r, \tag{D.8}$$

where Q is the fluid flow rate, A is the total reacting surface area, and r is the rate constant for the stoichiometric dissolution of dolomite. In order to model the low-T core-fluid interactions, the far from equilibrium, 25°C, 50 bar pCO_2 value of r ($10^{-9.4}$ mol/cm^2/s) calculated using the equation presented by Pokrovsky et al. Pokrovsky et al. (2009) was used. The use of this rate constant is justified by the low dependence of 25°C dolomite dissolution rates on pCO_2 at $pCO_2 \gtrsim 5$ atmPokrovsky et al. (2009) and the far from equilibrium nature of the measured fluid concentrations (Fig. D.3 A). The Ca and Mg concentrations in Fig. D.3 A were determined by analyzing a fluid sample taken from the line downstream of the pressure vessel (Fig. D.1). The reacting surface area parameter was then adjusted to ensure agreement between the modeled concentration and the sampled concentration (Fig. D.3 B) The initial core mass was 11.6 g, and this requires a reacting surface area of ∼70.5 cm^2/g in order to match the sampled concentration (Fig. D.3). Although this number is small compared with measured dolomite physical surface areas, it is consistent with whole-rock dissolution kinetics Wunsch et al. (2013) in that only a small portion of the rock is expected to react with the flowing fluid, particularly after flow pathways are short-circuited.

The 400 mL of reaction fluid were circulated through the reaction vessel from Pump A, through the separator and reaction vessel, and into Pump B (Fig. D.1). Once Pump B became full, the electronic valves were switched so that fluid from Pump B was injected into the separator while Pump A was refilled. The separator contained 140 mL of CO_2-saturated water until 169 hours, when some of the CO_2 within the separator was bled off to leave 180 mL of water in the vessel. Note that, because the experimental fluid is injected directly from the separator into the reaction vessel, the reacting fluid remains far from dolomite saturation (∼ 19 mmolal Mg) during the 21°C stage

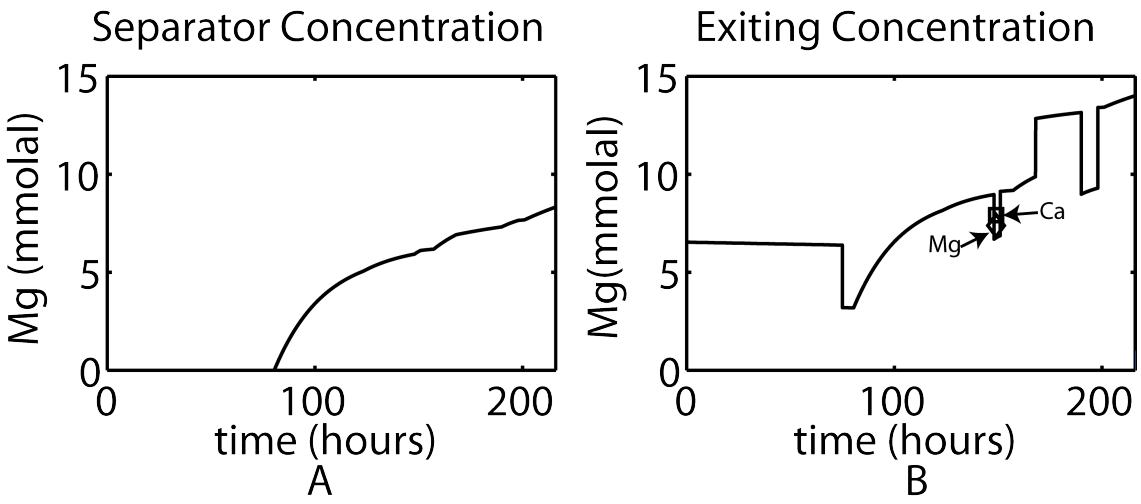

Figure D.3: A. Separator concentration and B. Concentration of fluid exiting the reaction vessel, both calculated using the kinetic model. Symbols labled Ca and Mg in B. represent analyzed concentrations.

of the experiment (Fig. D.3A). Rapid changes in the modeled exit concentration result from the different flow rates used during this portion of the experiment, and more gradual changes result from the modeled change in total surface area. Surface area is assumed to be removed proportional to the mass of stoichiometric dolomite removed, i.e., the specific reactive surface area is kept constant but the total surface area decreases somewhat over the modeled time period. The kinetic model assumes that the fluid in all vessels is well mixed, which is allowable due to the low concentrations and slow flow rate through the separator. Although we have not performed the calculations here, 50°C reaction rates are rapid enough to allow for total equilibration of all reaction fluid during the 50°C portion of the experiment Pokrovsky et al. (2009).

Table D.1: HKF equation of state (aqueous species) and Maier-Kelley heat capacity (minerals) parameters and standard state thermodynamic properties used in this study.

Species	$\Delta\overline{G}^\circ_f$	$\Delta\overline{H}^\circ_f$	$\overline{S}^\circ_{P_r,T_r}$	a_1 (10^1)	a_2 (10^{-2})	a_3	a_4(10^{-4})	c_1	c_2(10^{-4})	$\omega_{P_rT_r}$(10^{-5})
CO_2(aq)	-92250.	-98900.	28.100	6.2466	7.4711	2.8136	-3.0879	40.0325	8.8004	-0.0200
Ca^{++}	-132120.	-129800.	-13.50	-0.1947	-7.2520	5.2966	-2.4792	9.00	-2.522	1.2366
CaCO3(aq)	-262850.	-287390.	2.500	-0.2100	-8.295	9.010	-2.436	-11.783	-9.152	-0.038
$CaHCO3^+$	-273830.	-294350.	16.000	3.706	1.267	5.252	-2.831	41.722	8.336	0.308
$HCO3^-$	-140282.	-164898.	23.53	7.5621	1.1505	1.2346	-2.8266	12.9395	-4.7579	1.2733
Na+	-62591.	-57433.	13.96	1.8390	-2.2850	3.2560	-2.726	18.18	-2.981	0.3306
Cl^-	-31379.	-39933.	13.56	4.0320	4.8010	5.5630	-2.847	-4.40	-5.714	1.4560
Mg^{++}	-108505.	-111367.	-33.00	-0.8217	-8.5990	8.3900	-2.390	20.80	-5.892	1.5372
$MgCl^+$	-139700.	-150933.	-19.	2.223	-2.3505	6.6669	-2.6818	28.6016	2.058	0.8449
$MgHCO3^+$	-250200.	-275750.	-3.000	3.271	0.206	5.669	-2.788	47.284	9.340	0.599
NaCl(aq)	-92910.	-96160.	28.	5.0364	4.5189	3.9669	-2.9658	10.798	-1.3031	-0.038
$CaCl^+$	-163100.	-168607.	4.5	2.7148	-1.1497	6.1949	-2.7314	20.8839	0.5241	0.4862
$CaCl_2$(aq)	-194000.	-211060.	6.	6.2187	7.4058	2.8322	-3.0851	23.961	3.272	-0.038
Mineral	Formula	$\Delta\ \overline{G}^\circ_f$	$\Delta\ \overline{H}^\circ_f$	$S^\circ_{P_r,T_r}$	$V^\circ_{P,T}$	a	$b \times 10^3$	$c \times 10^{-5}$		
dolomite	$MgCa(CO_3)_2$	-517760.0	-556631.0	37.090	64.365	41.557	23.952	-9.884		
CO_2(g)	CO_2	-94254.0	-94051.0	51.085	0.0	10.57	2.10	-2.06		